



HAL
open science

Enregistrement des événements extrêmes dans les sédiments, à l'est de Taiwan

Rémi Lehu

► **To cite this version:**

Rémi Lehu. Enregistrement des événements extrêmes dans les sédiments, à l'est de Taiwan. Sciences de la Terre. Université Montpellier II - Sciences et Techniques du Languedoc; Université Nationale Centrale (JhongLi, Taïwan), 2014. Français. NNT : 2014MON20133 . tel-01661529

HAL Id: tel-01661529

<https://theses.hal.science/tel-01661529>

Submitted on 12 Dec 2017

HAL is a multi-disciplinary open access archive for the deposit and dissemination of scientific research documents, whether they are published or not. The documents may come from teaching and research institutions in France or abroad, or from public or private research centers.

L'archive ouverte pluridisciplinaire **HAL**, est destinée au dépôt et à la diffusion de documents scientifiques de niveau recherche, publiés ou non, émanant des établissements d'enseignement et de recherche français ou étrangers, des laboratoires publics ou privés.

THÈSE

Pour obtenir le grade de
Docteur

Délivré par **UNIVERSITE MONTPELLIER 2**

Préparée au sein de l'école doctorale SIBAGHE
Et de l'unité de recherche Géosciences Montpellier-
UMR5243

Spécialité : **Géologie marine**

Présentée par **Rémi LEHU**

**Enregistrement des événements extrêmes
dans les sédiments marins, à l'est de
Taiwan**

Soutenue le 10/11/2014 devant le jury composé de

Mr. Chris GOLDFINGER, PR, Oregon State Univ. (USA)	Examineur
Mr. Shu-Kun HSU, PR, NCU (Taiwan)	Directeur
Mr. Serge LALLEMAND, DR, Univ. Montpellier II	Directeur
Mr. Andrew T. LIN, PR, NCU (Taiwan)	Examineur
Mr. Gueorgui RATZOV, MCF, Géoazur, Univ. Sophia-Antipolis	Examineur
Mr. Lionel SIAME, MCF, CEREGE, Univ. Aix- Marseille	Rapporteur
Mr. Chih-Chieh SU, MCF, NTU (Taiwan)	Rapporteur

NATIONAL CENTRAL UNIVERSITY- TAIWAN
COLLEGE OF EARTH SCIENCES

A dissertation for the Degree of Doctor of Philosophy

Speciality : Marine Geology



**Record of extreme events in marine
sediments, offshore eastern Taiwan**

Presented and defended by

Rémi LEHU

Defended on November 10th 2014, in front of the committee members composed by:

Chris GOLDFINGER	-	PR, Oregon State University, USA	<i>Examinator</i>
Shu-Kun HSU	-	PR, NCU, Taiwan	<i>Director</i>
Serge LALLEMAND	-	RD, University of Montpellier 2	<i>Director</i>
Andrew T LIN	-	PR, NCU, Taiwan	<i>Examinator</i>
Gueorgui RATZOV	-	APR, Geoazur, Nice	<i>Examinator</i>
Lionel SIAME	-	APR, CEREGE, Aix en Provence	<i>Reviewer</i>
Chih-Chieh SU	-	APR, IONTU, Taiwan	<i>Reviewer</i>

Record of extreme events in marine sediments, offshore eastern Taiwan

摘要

台灣是現在世界上最活躍的年輕的造山帶之一。從二十世紀初至今已有超過二十幾次的規模七(M_w 7)以上地震發生於此，然而是否有超過規模八(M_w 8)以上的大地震仍存有問題和爭議。本論文利用長其地震記錄來評估發生大地震的情形，同時本論文也藉由近年來發展迅速的方法，通過研究重力岩芯沉積記錄為基礎，探討歷史長期地震活動情況。本論文首先探討了台灣東部的沉積體系，瞭解沉積形態特徵，沉積相和研究海底斜坡的演化進程,同時注意近期內的沉積影響因素。我們的研究結果顯示當地有許多不同的沉積體系正在進行，而且對台灣東側岸外坡產生影響，同時濁流作為侵蝕作用的主要因素，佔據了當地沉積紀錄的60%。濁流主要受到構造運動和氣候運動這兩個重要控制因素影響，當濁流同時有構造運動相結合，可能事地震晃動所導致，因而形成內陸斜坡盆地。在氣候因素的影響下，濁流可能在盆地及內陸河域導致特大洪澇或颱風。其次是應用古地震學中兩個時間軸上以濁流岩紀錄為根本的方法。我們先通過測試並調整濁流沉積物和地震形成之間的對應關聯，一旦校正後我們將時間序列前調至最近的三次濁積岩層形成時間，分別是西元2001年、西元1950年以及西元1928年。我們將地下加速度，震級，震源通過經驗關係相連，分別驗證了沉積岩和三個地震的關聯性，分別是2013年12月10日的成功地震(M_w 6.8)，1951年11月24日的台東地震(M_w 7.1)以及1935年9月4日的綠島地震(M_w 7.0)。年代測定以及時間建構模型為過去的3000年來提供了極端地質事件代表。經過比對不同誘發因素對濁流形成的影響，我們得到的結論是地震是濁流形成的主要機制。本論文研究為全新世極端事件重新排序做了良好開端。

Enregistrement des événements extrêmes dans les sédiments marins, à l'est de Taïwan

Résumé

La chaîne de Taïwan représente l'une des zones les plus actives au monde. Depuis le début du XX^e siècle, plus d'une vingtaine de séismes $\geq M_w$ 7 ont affecté l'île. Cependant la probabilité d'occurrence de séismes plus importants ($\geq M_w$ 8) est toujours matière à débat. Dans un tel contexte il apparaît donc important d'obtenir des enregistrements plus anciens pour évaluer l'occurrence de tel événements. La paleosismologie marine, basée sur l'enregistrement des dépôts issus de la sédimentation gravitaire, apparaît comme une alternative sérieuse afin d'illuminer l'histoire de la sismicité sur des périodes anciennes. Ce travail de thèse apporte de nouvelles contraintes sur l'histoire sismique au large à l'est de Taïwan au cours des derniers 3000 ans.

La première partie de ce travail consiste à caractériser les systèmes sédimentaires récents. Cette étape fut essentielle pour la compréhension des processus, faciès sédimentaires et les facteurs de contrôle de la sédimentation qui régissent l'évolution de la pente sous-marine. Ces résultats ont montré que l'est de Taïwan est caractérisé par une grande variabilité de processus et que les courants de turbidité dominant l'enregistrement sédimentaire. Les courants de turbidité sont générés par deux facteurs distincts: l'activité tectonique/sismique et l'activité climatique.

La deuxième partie de ce travail est consacrée à l'approche paleosismique en utilisant les dépôts de turbidites comme marqueurs des paleoseismes. Pour ce faire, nous avons dans un premier temps testé et validé l'approche à l'échelle du siècle dernier. Ensuite une fois calibré, nous avons pu étendre les séries temporelles à l'échelle de l'Holocène. Nous avons daté les trois plus récents événements turbiditiques autour de 2001 ± 3 AD, 1950 ± 5 AD et 1928 ± 10 AD. En utilisant des relations empiriques intégrant magnitude, distance et valeur du "peak ground acceleration", nous avons pu calibrer la source sismique et ainsi corrélérer ces trois turbidites à trois séismes instrumentaux: le séisme de Chengkong (12/10/2003) (M_w 6.8), le séisme de Taitung (11/24/1951) (M_w 7.1) et le séisme de Lutao (9/4/1935) (M_w 7.0). Au-delà du siècle dernier, les datations et modèles d'ages nous permettent d'établir une partie de la chronologie des événements extrêmes sur une période de 3000 ans et d'estimer un temps de retour pour des événements de l'ordre $\geq M_w$ 7. Les résultats ont toutefois montré que ces temps de retour sont nettement supérieurs à ceux connus sur le siècle dernier, ce qui suggère que tous les séismes ne sont pas enregistrés par les dépôts sédimentaires marins.

Ce travail de thèse a donc permis de montrer que les dépôts issus de la sédimentation événementielle peuvent être considérés comme marqueurs de la sismicité et que cette approche peut constituer un outil complémentaire pour les études portant sur le risque sismique.

Record of extreme events in marine sediments, offshore eastern Taiwan

Abstract

Taiwan is a young mountain belt, known as one of the most active area in the world. Since the beginning of the 20th century more than twenty $\geq M_w 7$ earthquakes have struck the island. However, the occurrence of larger events ($\geq M_w 8$) is still a matter of debate. In this framework it is of key importance to obtain longer record in order to evaluate the occurrence of large past earthquakes. The sub-aqueous paleoseismology, based on the record of the sedimentary gravity deposits, appears as a serious alternative to approach this thematic and is a rapidly advancing field that has the potential to illuminate the long-term history of seismicity.

The first part of this work was to investigate the present sedimentary systems off east Taiwan, essential to understand the morphosedimentary features, sedimentary facies and processes governing the evolution of the submarine slope, and the controlling factors of the recent sedimentation. Our results showed that the offshore slope east Taiwan is affected by a variety of sedimentary systems and processes, and that turbidity currents appear as the main erosional processes covering nearly 60% of the sedimentary record. Turbidity currents are generated by distinct controlling factors such as tectonic and climatic activity that enabled us to define two end-members relative to turbidity currents initiation: Turbidity currents preconditioned by tectonic activity and triggered by earthquakes shaking and likely deposited into intra-slope basin and turbidity currents driven by climatic activity such as extreme floods or typhoons, generated in basin directly connected with onland rivers.

The second part consisted to apply a paleoseismic approach, based on turbidites record, at two time-scales. First, we tested and validated the method by correlating turbidites deposits with instrumental earthquakes. Then, once calibrated we extended the time-series back in time. We dated the three most recent turbidites layers circa 2001 ± 3 AD, 1950 ± 5 AD and 1928 ± 10 AD. Using empirical relationship that link peakground acceleration, distance and magnitude to calibrate the seismic sources, we correlate these three turbidites with instrumental earthquakes: the Chengkong Earthquake 12/10/2003 ($M_w 6.8$), the 11/24/1951 Taitung Earthquake ($M_w 7.1$) and the 9/4/1935 Lutaio Earthquake ($M_w 7.0$) respectively. Applying criteria to discriminating the different triggering mechanisms for turbidity current generation, we propose that earthquakes are the main triggering mechanisms. Dating and age modeling provided a part of the chronology of extreme events since the last 3000 years and allowed us to estimate return time for earthquakes $M_w \geq 6.8$.

This work represents a good starting-point for future investigations in order to better assess Holocene time series of extreme events.

Acknowledgments

As Jim Morrison wrote some years ago..."This is the end"... and after these 3 years I realize that completing a PhD is an incredible-crazy-exhausting-exciting adventure. I have been lucky enough to be accompanied, supported, encouraged and motivated in so many ways by so many persons and I cannot be anything but grateful to all these people that with their time and dedication, their expertise, their laughs, good sense of humor, their love and friendship had inspired me to accomplish this work.

First of all, my profound respect and gratefulness go to my two advisors: Shu-kun Hsu and Serge Lallemand.

Laoshi, I would like to express my gratitude for the continuous help and support since the first day I arrived in Taiwan and during key moments of my research, for his expertise and for all the assistance he provided.

This work would not have been possible without Serge Lallemand; to whom I owe my deepest thankfulness to for his endless guidance, patience, his dedication and wise counsels during these years, always leading me to give my best. I would like also to highlight, beside his role in the academics, his human values that he spreads. Thanks also go to the committee members to accept to judge my work: Chris Goldfinger, Lionel Siame and Don Su, Andrew Lin and Gueorgui Ratzov.

I also thank the "Paleosismo_Taiwan Team", Nathalie Babonneau and Gueorgui Ratzov for their extreme kindness, help, discussions, numerous Skype, reading, writing, re-reading, and advises during my Ph.D, I learned a lot from your experiences.

Andrew Lin is also thanked for his kindness, his constant help provided to realize my research and discussion all those years.

Thanks go now to the Marine Geophysical Research crew, for their great help and enthusiasm; as well, very special and big thanks to the administrative staff for their outstanding support (we know how challenging it was to solve some issues...).

The great people from the Laboratory of Géosciences of Montpellier, thanks to all of you. Special thanks to Yannick C. and Antoine P. my dear fellas that are also seeing the light at the end of the tunnel. What a nice time spent in the lab with you, thanks for all those conversations while fishing (tons of Daurade) or while having a "petit Ricard" after the football games or for the break at 4 pm (hehe); I wish you guys good luck for the very last end and we will have a triple celebration in Montpellier!!

To those who became more than friends during these years in Taiwan, thanks for your friendship and your support, for the good talks with coffee, the long nights of music, crazy parties, and laughs, for sharing and understanding, thanks, gracias, dziekuje xie-xie my friends, Lucas M., Slawek G., Olimpia G., Mama Helena G. and Matt (sometimes Julien) my best Taiwanese friend. To my lifetime friends: Tonio (almost the end for your too my "Slop"), Teber, Tamago, Antoine (le fou), Theo, Pablo, Mathieu, Peo, Vinc; my "core" (yeah...) friends, thanks for being my brothers, my accomplices, for always being there despite the distance, for crossing the world (or half of it) to come in Taiwan, for every time spent in "Les Cevennes" our fief, in Paris or when far away just talking through Skype...

My family, especially to my parents for their incomparable support, for teaching me with an exceptional life example and for giving me the independence and freedom to accomplish what I wanted to do; to both of you my deepest love and truly admiration. To my brother and sister, Julien and Caroline, stay yourself and enjoy this world as much as you can :)

Finally for the most important person on this planet, the most amazing woman I have met, my lovely wife Irene; thank you for your support, your love, your positivism, your confidence, your smiles, your kindness, your generosity, your understanding, you encouragements, you constant help; also for the good moments, the bad ones, for all these adventures lived together, for all these years spent together and the coming ones. Let's move now to the next adventure...

Contents

1	Introduction	1
1.1	Research motivations and objectives	3
1.1.1	Aims	3
1.1.2	Objectives	5
1.2	An introduction to the geology of Taiwan	5
1.2.1	Generalities	5
1.2.2	Topography	8
1.2.3	Regional climate	9
1.2.4	Seismicity	10
1.3	Thesis plan	15
I	Sedimentary processes offshore eastern Taiwan	17
2	Background	19
2.1	Submarine sedimentary gravity processes and deposits	21
2.1.1	Mass slide	21
2.1.2	Gravity flows	24
2.1.2.1	Laminar flows	24
2.1.2.2	Turbulent flows	25
2.1.2.3	Evolution and transformation of gravity flows	27
2.1.3	Turbiditic systems architecture	28
2.1.3.1	Canyons and gullies	30
2.1.3.2	Channels-levees complexes	31
2.1.3.3	Lobes	32
2.1.4	Controlling factors of turbiditic systems	33
2.1.5	Initiation of turbidity currents	35
2.2	Study area and coring strategy	37
2.3	Coring sites	39
3	Deep-sea sedimentation offshore eastern Taiwan: facies and processes characterization	51
3.1	Introduction	55
3.2	Regional settings	55
3.2.1	Geological context	55
3.2.2	Regional climate, drainage systems and sediment discharge	56
3.2.3	Submarine morphology	57
3.2.4	Seismic activity	57
3.3	Materials and methods	58
3.3.1	Bathymetry, acoustic and seismic data	58
3.3.2	Cores material	58
3.4	Description of sedimentary features revealed by geophysical data	58
3.4.1	The southern sector	59

3.4.2	The central sector	61
3.4.3	The northern sector	62
3.5	Characterization and classification of lithofacies	63
3.5.1	End-members lithofacies	63
3.5.2	Turbidites facies	65
3.6	Discussion and conclusion	67
3.6.1	Erosional sedimentary processes	67
3.6.2	Control factor and sediment provenance of turbidity currents	70
3.7	Acknowledgments	73
II	Testing a paleoseismological approach offshore eastern Taiwan	89
4	Background	91
4.1	Turbidites deposits as a marker of paleoseismicity	93
4.2	Datings proxies	96
4.2.1	The last century sedimentation: ^{210}Pb and ^{137}Cs proxies	96
4.2.2	Radiocarbon ^{14}C : Dating, age calibration and reservoir age	99
5	Historical reconstruction of paleo-earthquakes using ^{210}Pb, ^{137}Cs and ^{241}Am turbidite chronology and radiocarbon reservoir age estimation off East Taiwan	103
5.1	Introduction	107
5.2	Setting and analytical methods	108
5.3	Results and discussion	109
5.3.1	Identifying and dating turbidite layers in core	109
5.3.2	Linking turbidites and earthquakes events	111
5.3.3	Modern reservoir age estimation	112
5.4	Conclusion	113
5.5	Aknowledgment	114
6	2,700 years of seismicity recorded offshore eastern Taiwan by turbidites deposits	123
6.1	Introduction	127
6.2	Regional settings	129
6.2.1	Geological and seismic context	129
6.2.2	Sedimentology	129
6.3	Materials and methods	130
6.3.1	Core site location	130
6.3.2	Cores analysis	130
6.3.3	Criteria for turbidites events identification and delimitation	131
6.3.4	Radiometric datings and age model	131
6.3.5	Event's terminology	133
6.4	Turbidites identification	133
6.5	Chronostratigraphy	135
6.6	Discussion	136
6.6.1	Turbidites correlation	136
6.6.2	From turbidites to earthquakes	138

6.6.3	Estimation of earthquake sources and magnitudes, and recurrence intervals	141
6.7	Conclusion	143
6.8	Acknowledgments	144
7	A ~3,000 years-old super-event revealed by marine deposits east of Taiwan: paleo- landslide, earthquake, tsunami or typhoon ?	163
7.1	Introduction	167
7.2	Geological, oceanic and atmospheric setting	167
7.3	Core sampling strategy, data and results	171
7.3.1	Sampling strategy	171
7.3.2	Methods	171
7.3.3	Core description	172
7.3.4	Age model	173
7.4	Discussion	175
7.4.1	Age of shells vs age of sediment	175
7.4.2	Possible origin of the anomalous deposit	175
7.4.3	Hydro-dynamical tests	179
7.5	Conclusion	180
7.6	Acknowledgments	181
	Appendices	182
	Tsunami generation	182
	Propagation model	182
	Run-up height estimations	183
8	General conclusions	195
8.1	Summary	197
8.2	Concluding remarks	200
8.3	Perspectives	202
	Bibliography	205
	Appendices	227
A	Morphosedimentary facies map offshore east Taiwan	229
B	Technical sheets	233
C	Coring site KS06: Morphology and core analysis	241
D	Coring sites KAS03/KR03: Morphology and core analysis	253
E	Coring sites KS08/KS09: Morphology and core analysis	263
F	¹⁴C and ²¹⁰Pb sampling	273
G	The P-Sequence in OxCal	277

List of Figures

1.1	Magnitude 8 and greater earthquake since the 20 th century, (Source USGS). . .	3
1.2	Plate tectonics and geodynamic of Eastern Asia. The thick lines represent plate boundaries. White arrow indicates the relative motion of the PSP	6
1.3	A) Geodynamic context of Taiwan. The thick lines represent the main deformation fronts. Index: MT: Manila Trench; MAW: Manila Accretionary Wedge; SCS: South China Sea; CCM: Chinese Continental Margin; CP: Coastal Plain; CeR: Central Range; CoR: Coastal Range; RT: Ryukyu Trench; RAW: Ryukyu Accretionary Wedge; LVF: Longitudinal Valley Fault. The white arrow represents the ongoing convergence rate from Seno et al. (1993). B) GPS velocity field relative to Paisha, Penghu for the period between 1993 and 1999, (after Hsu et al., 2009)	7
1.4	Geological map of Taiwan, showing the main structural units and their boundaries (LF= Lishan Fault and LVF=Longitudinal Valley Fault) (modified from Huang et al., 2006)	8
1.5	Profiles across Taiwan showing both subaerial and submarine reliefs. DEM 100m gridded, from courtesy of Stephane Dominguez.	9
1.6	Left, satellite image of the Morakot typhoon at its peak (source CWB); Right, Impact of typhoon Morakot, an example of one of several typhoon-triggered landslides	10
1.7	Example of disasters that occurred during the last century in Taiwan. Left, broken bridge after the Chi-Chi earthquake in 1999. Right, copy a newspaper of 1935 showing damages after the Hsinchu earthquake that occurred the same year (Kuo-Fong Ma, personal communication).	11
1.8	A: Seismicity of Taiwan $M_L > 3$ for the period 1991-2008. Data from Central Weather Bureau; B: Perspective view showing the two subduction and the collision zone. The seismicity is concentrated on the subduction zone and the collision zone. The red box shows the study area for this work (Courtesy from Serge Lallemand and Jacques Malavieille)	12
1.9	Earthquakes magnitude 7 and greater recorded over the instrumental period. . .	13

2.1	Perspective diagram showing the different types of deep-sea sedimentary processes: From hemipelagite sedimentation to mass transports processes. (after Shanmugam, 2003)	22
2.2	Global classification of offshore mass movements. Red boxes emphasize the sedimentary processes approached and described in this work (modified after Mulder and Cochonat, 1996)	22
2.3	Idealistic model of A: Slide and B: Slump (after Stow et al., 1996).	23
2.4	The Bouma sequence (1962) and its extensions for the low-density turbidity currents (Stow and Shanmugam, 1980) and high-density currents (after Lowe, 1982)	26
2.5	Sequence and facies of an hyperpycnal deposit according to the charge and discharge of the river during flood (after Mulder et al., 2003)	28
2.6	Possible evolution of mass transport processes relative to space and time (after Middleton and Hampton, 1973)	29
2.7	Evolution from a mass slide to gravity flow (i.e turbidity current) (after Shanmugam et al., 1994)	29
2.8	Theoretical depositional model for channelized systems and non-channelized systems (after Shanmugam, 2000).	30
2.9	Bathymetric 3D map of the Danube canyon (after Popescu et al., 2004)	32
2.10	Example of A: subdued gully system showing 3.5kHz profile (left) and shaded relief map (right); B: Angular gully form showing 3.5kHz profile (left) and shaded relief map (right) (after Mountjoy et al., 2009)	33
2.11	Genetic model of channel-levee complexes (after Eschard et al., 2003).	34
2.12	Model of triggering mechanisms of mass movements showing interactions between origin, cause, flow and deposit. Red boxes emphasizes the processes that will be developed in this work, from the origin to the deposit (modified after Pouderoux, 2011).	36
2.13	A: perspective view of eastern Taiwan viewed from the east. The three dashed-lined boxes show the three zones chosen for this work. B: DEMs showing zooms of the coring site; colored dots show the sedimentary cores collected during OR1-1013 and OR1-1048. The yellow dot corresponds to the box-core from the study of Huh et al. (2004)	40

2.14	A: DEM of the Ryukyu arc core site; B: slope gradient map of the core site, lines show bathymetric profiles shown in D; C: closer view on DEM of the KS09 and KS08 location; D: bathymetric profiles of the core sites, showing the surrounding slopes adjacent KS09 and KS08 sites.	41
2.15	A: chirp profiles across KS08 and KS09 sites; B: perspective view of the core site, lines show the chirp profiles shown in A; C: perspective view showing slope failures on KS09 and KS08 sites.	42
2.16	A: Detailed DEM of KS06 site, red dot show the coring site, lines display seismic profiles shown in Fig.2.17; B: bathymetric profiles across the core site, showing the surrounding slopes on KS06 site; C: slope gradient map around KS06 site.	44
2.17	A: MCS profile and chirp profile across KS06 site. B: perspective view of KS06 site, showing the slope instabilities in that area.	45
2.18	A: detailed DEM of the core site, red dots show the core locations and lines location of seismic profiles shown in Fig.2.19; B: perspective view of the core site to highlight the isolated topographic high where was collected KR03 and the isolated terrace where was taken KAS03; C: slope gradient map of the core site. The lines show bathymetric profiles; D: Bathymetric profiles S-N and W-E respectively of the core site.	46
2.19	A: MCS profile across the topographic high where we selected KR03 site to record the background sedimentation. Note the 1.5 km sediment pile that layered above the basement (probably the volcanoclastic series of the Luzon arc). B: chirp profile across KAS03 and KR03 core sites.	47
2.20	Southern Longitudinal Trough coring site. A: DEM showing the turbiditic system developed in the trough, with channel-levees complex; B: DEM viewed from the east, showing the gullied slope from where the sediment transit from the onland rivers. The three core sites are represented by the red dots; C: chirp profile across the KC03A core site, showing high energy reflector at sea-bottom and stratified reflectors in depth.	49
2.21	Map showing the objective for coring operations for the two surveys OR1-1013 and OR1-1048. We show sites that were successful, other that failed during coring and abandoned sites.	50

- 3.1 A: Geodynamic context of Taiwan and plate boundaries, the box represents a zoom on the study area shown in B. CCM= Chinese Continental Margin, HR= Hsuechan Range, DF= Deformation Front, LF= Lishan Fault, LVF= Longitudinal Valley Fault, CP= Coastal Plain, CR= Central Range, HP= Hengchun Peninsula, SCS= South China Sea, MT= Manila Trench, CoR= Coastal Range; B: Recent sedimentary systems offshore eastern Taiwan showing the main active canyons and the actual drainage system. In yellow boxes are represented the river discharge in Mt/yr (after Liu et al., 2008). HB=Hoping Basin, HR=Hoping Rise, NB=Nanao Basin, NR= Nanao Rise, ENB=East Nanao Basin, HpC=Hoping Canyon, HC=Hualien Canyon, CC=Chimei Canyon, SLT= Southern Longitudinal Trough, TC=Taitung Canyon. 77
- 3.2 Location of seismic, CHIRP profiles and cores materials. 78
- 3.3 A. Backscatter imagery of the southern sector. The circles represent the sedimentary cores. Boxes indicate zoom on high resolution DEM; B: Morphosedimentary mapping based on backscatter imagery, seismic and CHIRP data and high resolution DEM. The annotated circles represent the east coast rivers: 1. Xuhai river, 2. Daren river, 3.Dawu river, 4. Nangxi river, 5. Jinlun river, 6.Taimali river, 7.Zhiben river, 8.Taiping river, 9.Beinan river, 10.Donghe river; C: CHIRP profile across the SLT, showing acoustic facies of sedimentary levee; D: high resolution DEM across the SLT showing the well-developed channel-levee system. 79
- 3.4 A: Zoom on high resolution DEM showing submarine landslides affecting the Taitung Canyon (L4), the slope of the Luzon Arc (L3, L2) and the Huatung Ridge (L1); B: Seismic reflection profil across the Taitung Canyon (S2), showing the slope affected landslides on the Luzon Arc and the Huatung ridge. The levee of the Taitung Canyon are also well observable. 80
- 3.5 A: Backscatter imagery of the central sector; B: Mapping of the central sector, using backscatter imagery, seismic data and bathymetry data. Annotated circles represent all the rivers identified in that sector. 9. Beinan river, 10.Donghe river, 11. Sanxiantan river, 12.Wushibi river, 13.Baxiandong river, 14.Xiukuluan river, 15. Hualien river, 16. Liwu river. 81
- 3.6 A:High resolution DEM showing area affected by landslides on the deforming Luzon arc; B: Seismic reflection profiles and CHIRP profile displaying seismic facies of landslide and stratified units of the basin-fill sediment respectively. . . . 82

3.7	A: High resolution DEM showing the Chimei turbiditic system with landslide affecting the northern flank of the deep sea fan and bathymetric highs; B: CHIRP profiles imaging the bathymetric high.	83
3.8	A: Backscatter imagery of the northern sector; B: Mapping of the northern sector using backscatter imagery, seismic profiles and high resolution DEM. Annotated circles represent east coast rivers identified. 16. Liwu river, 17. Hoping river, 18. Nanao river.	84
3.9	High resolution DEM on the Ryukyu arc area showing landslides affecting the slope of the arc. B: CHIRP profiles displaying sedimentary levees.	85
3.10	Sedimentological description of cores.	86
3.11	Characterization of sedimentary facies using grain size distribution, X-Rays and chemical analysis.	87
3.12	Photography and relative composition (%) of the different turbidites facies identified corresponding to the coarser beds of turbidites sequences (fraction $>150 \mu\text{m}$).	88
4.1	Characteristic features of seismoturbidites and comparison with "normal turbidites" (after Nakajima and Kanai, 2000).	93
4.2	Data for turbidites in Santa Monica basin cores, showing the difference of volume between earthquake-generated turbidites and "normal turbidites" (after Gorsline et al., 2000).	94
4.3	Example the synchronicity of turbidite deposits (modified after Goldfinger et al., 2007). The map shows the location of cores in different turbiditic systems. In the bottom is shown the correlation (on the latitudinal axis on the map) of turbidites on 5 different turbiditic systems, one color represents one correlated event, a paleo-earthquake.	95
4.4	A: Disintegration chain of the ^{226}Ra after Bourdon (2003); B: Pathways by which ^{210}Pb reaches aquatic sediments (after Oldfield and Appleby, 1984).	97
4.5	On the left : decay curve of $^{210}\text{Pb}_{ex}$ function of the accumulated sedimentary mass. On the right the CF:CS applied to the whole profile (after Sabatier, 2009).	98
4.6	^{137}Cs deposition density in the northern and southern hemispheres calculated from fission production amounts with the atmospheric model.	99

4.7	A: Principle of radiobarcon measurement on terrestrial organisms (source www.http://radiocarbon.pl/); B: Example of calibration of ^{14}C age. Because of uncertainty of ^{14}C age, calendar age (cal. AD) are expressed only in terms of probability distribution.	100
4.8	Sea surface reservoir ^{14}C ages $R(t)$ for modern sample on core KS06B (see chapter 5 for details on the results) calculated by subtracting the atmospheric ^{14}C estimated for the ^{210}Pb from the measured apparent ^{14}C ages of foraminifera. This gives a $R(t)$ value. The deviance from the global mean reservoir age (ΔR) is then obtained by subtracting the marine model value from the measured apparent ^{14}C age of the foraminifera (see chapter 5 for details on the results and discussion). .	101
4.9	The mean ΔR value in the western Pacific. Arrows represent the current: a) North Equatorial current, b) Kuroshio current, c) Kuroshion countercurrent current, d) Oyashio current, e) East Sakhalin current, f) Liman current, g) North Korea Cold current, h) Tsushima Warm current, i) Soya Warm current (modified after Yoneda et al., 2007).	102
5.1	General map of Taiwan showing geodynamical setting and strong magnitude earthquakes ($M_w > 6.8$) over the 100 years. Major onland faults are represented, DF= Deformation Front, LVF= Longitudinal Valley Fault.	116
5.2	Sedimentological analysis of KS06-B and turbidites events identification, using grain size distribution, photo, X-rays, median grain size and geochemical elements (Ca and Fe).	117
5.3	A: ^{210}Pb , ^{137}Cs and ^{241}Am activity profiles. Blue dots represent sample from continuous sedimentation (hemipelagite) whereas red crosses represent samples from instantaneous sedimentation (i.e turbidite event). B: Methodology used to reconstruct depositional model to estimate sedimentation rate and turbidites layers age.	118
5.4	Distance from earthquakes correlated with turbidites events to site KS06.	119
5.5	Sea surface reservoir ^{14}C ages $R(t)$ for modern sample on core KS06-B calculated by subtracting the atmospheric ^{14}C estimated for the ^{210}Pb from the measured apparent ^{14}C ages of foraminifera. This gives a $R(t)$ value. The deviance from the global mean reservoir age (ΔR) is then obtained by subtracting the marine model value from the measured apparent ^{14}C age of the foraminifera.	120

5.6	A: General map of Taiwan showing the ΔR values around the Taiwan area (this study and Yoneda et al., 2007). In light grey: the mean path of the Kuroshio current (after Hsin et al., 2008). The red star shows the core location; B: Upwelling zone northward Lutao island evidenced by satellite image and sea-water temperature (after Chang et al., 2013)	121
6.1	A: General geodynamic setting of Taiwan. Onland are represented the two major fault zones are DF: Deformation Front and LVF: Longitudinal Valley Fault. The black arrow shows the plate convergence component. Green dots represent the instrumental seismicity over the 20 th century with corresponding numbers listed in Table 6.1; B: morpho-tectonic map of the study area. Blue dashed-lines represent drainage systems from rivers to offshore channels. In blue are represented the major submarine canyon east Taiwan. Red dots represent the studied cores locations. SLT= Southern Longitudinal Trough; TC= Taitung Canyon; CC=Chimei Canyon; HC=Hualien Canyon; HpC=Hoping Canyon; N.B= Nanao Basin; H.B= Hoping Basin.	151
6.2	Close bathymetric view of the Ryukyu forearc zone. Red dots are cores from the present study. Purple dot represents the core location of the study of Huh et al. (2004).	152
6.3	Bathymetric map representing a zoom on the Luzon volcanic arc zone. Red dots are the cores studied in the present paper.	153
6.4	X-rays imagery (given with equivalent colors of gray tones), lithological description, median grain size, geochemical composition (Sr, Ca and Fe) of the studied sections of the OR1-1013 and OR1-1048 cores from the Ryukyu forearc zone. Turbidite numbers are depicted for each core. Red line marks the 12 μ m threshold in the grain size.	154
6.5	X-rays imagery (given with equivalent colors of gray tones), lithological description, median grain size, geochemical composition (Sr, Ca and Fe) of the studied sections of the OR1-1013 and OR1-1048 cores from the Luzon volcanic arc zone. Turbidite numbers are depicted for each core. Red line marks the 12 μ m threshold in the grain size.	155
6.6	Activity-depth profiles of ²¹⁰ Pb _{ex} and ¹³⁷ Cs in boxcore KS06-B	156

- 6.7 Methodology used for ^{14}C age modeling, using the P_sequence in OxCal program:
 1. All turbidites sequences are virtually removed to build hemipelagite model; 2. ^{14}C date are calibrated. Input parameters to generate the age model are the uncalibrated ^{14}C ages and respective ΔR correction with their corresponding corrected depths. Age model are built using the P_Sequence (a Bayesian model of deposition) implemented in the computer program OxCal 4.2 that assimilates sedimentation as a random process (Ramsey, 2008). The regularity of sedimentation is determined by the k parameter (see text for details). Sequence boundary indicates the boundary of the depositional model. Each turbidites layers are then inserted in the age model and their ages modeled. 157
- 6.8 Oxcal age models from the four studied cores, showing the sedimentation rate of hemipelagite through time and turbidites ages modeled. The k parameter is used to define the regularity of the sedimentation rate along the core. Since hemipelagite is assumed roughly constant rate, the highest k parameter was chosen for each core. All ages are plotted with their 1 and 2σ age range. 158
- 6.9 A. Age correlation of turbidites from the RF cores and LA cores. Colored rectangles represent turbidites modeled ages at 1σ projected on time axis. Two types of correlation are proposed: zone scale correlation (black rectangle) considering synchronous turbidites between two cores within one zone and margin scale correlation i.e, synchronous turbidites between at least two cores within the two zones (RF+LA); B. Age correlation over the 20^{th} based on ^{210}Pb and ^{137}Cs between box-core BC-18 and KS06-B. Rectangles represent events with their uncertainties projected on time axis. Stars represent candidates earthquakes that correlate the turbidites events. 159
- 6.10 Chronostratigraphic event correlation from all the studied cores offshore eastern Taiwan showing local events labeled Rx and Lx, and regional events labeled Mx. 160

6.11 A. Map showing radius in which an M_w8 earthquake will trigger slope failures. Circles have been centered on the turbidite source areas. At 100 km radius peak ground acceleration 0.1g is reached for such earthquakes. The 0.1 g corresponds to the threshold for slope failures generation. Note that no overlap is possible between the two sites, suggesting that an earthquake M_w8 cannot be recorded in both KS06-B and BC-18 cores; B. Same as A for M_w7 earthquake. The value of 0.1 g is reached at 50 km radius. Note that there is no overlap between the two circles, suggesting that it is not possible to record the same M_w7 events in both coring sites BC-18 and KS06-B. Reversed triangles represents coring sites. Green dots are the seismic event recorded over the instrument period and listed in Table1.161

6.12 A. As shown in figure 7, the circles represent the impact of a M_w8 earthquake on slope instabilities. The circles have been drawn around the turbidite source areas. The black areas correspond to the possible local scale events correlations showing the relative areas in which a M_w8 earthquake should occurred to trigger synchronous turbidites within a single zone. Red areas corresponds to the overlap of three cores and suggests that to record synchronous turbidites between three cores within the two zones, a M_w8 earthquake should occur within this area; B. Idem as A but for a M_w7 earthquake. We note that regional event cannot be recorded for a M_w7 earthquake. 162

7.1 General map of the Ryukyu and Luzon subduction zones overlapping in Taiwan. The numbers in the arrows indicate the relative subduction rates in mm/yr. The bold dates are major tsunami events described in the litterature (see the text for further details). In light grey : the mean path of the Kuroshio current (after **Hsin et al., 2008**) 187

7.2 Topographic and bathymetric map of the studied area based on ACT swath mapping (**Lallemand and Tsien, 1997**). Isobaths every 100 m. H.R. = Hsiukiulian River, T.H. = Takangkou High, C.H. = Changping High. S1 to S6 are candidate submarine landslides. Red dotted lines are suspected scars. K1 and K2 are knickpoints of the Chimei Valley. 188

7.3 KR03 core logs : MS = Magnetic susceptibility, X-ray, d50 median grain size, Fe content, visual description and radiocarbon sampling in orange. 189

7.4	Top of core KR03 (upper 17 cm) with ^{137}Cs and $^{210}\text{Pb}_{ex}$ measurements and modeled ages (see text for further details).	190
7.5	Detailed description of anomalous sequence of core KR03. Grain size distribution stacked with depth, core layers interpretation with purple dots marking the radiocarbon samples, HP = hemipelagite, P1 to P4 = silty layers, T = top anomalous layer with shells and wood fragments, XR = X-ray, Mean = mean grain size, d50 = median grain size. Radiocarbon ages are indicated in bold letters. Modeled ages are specified in parentheses as well as the dated material.	191
7.6	A: undetermined Veneroida bivalves external sides, B: bivalves internal sides, C: wood debris, D: silty fraction	192
7.7	Results of hydro-dynamic modeling for S4 submarine landslide source. The paths of drifters D1 to D10 are computed during 5 days after initial input. Two drifters start from each D point, one at 15 m depth and one at sea bottom. The position of other sources S1 to S6 is shown on the map even if the drifters's paths are not indicated for all sources. It helps to locate the sources with respect to the run-ups computed at 3 coastal locations. KR03 located the core site at 1,200 m depth. See the text and Appendices A, B, C for further details.	193
A.1	Morphosedimentary facies map offshore eastern Taiwan based on imagery, bathymetry and seismic data	231
B.1	Principle of the Box-Corer	235
B.2	Principle of the Piston and Gravity-Corer	236
B.3	Principle of the Geotek Multi Sensor Core Logger	237
B.4	Principle of the Coulter LS13-320	238
B.5	Principle of the ITRAX Core scanner	239
B.6	Principle of the foraminifera picking	240
C.1	Seismic, chirp profiles and source of instabilities.	243
C.2	Grain size analysis of KS06-B	244
C.3	Grain size analysis of KS06-P	245
C.4	XRF analysis of KS06-B and P	246
C.5	Detailed analysis of turbidites layers-I	247
C.6	Detailed analysis of turbidites layers-II	248

C.7	Detailed analysis of turbidites layers-III	249
C.8	Detailed analysis of turbidites layers-IV	250
C.9	Detailed analysis of turbidites layers-V	251
D.1	Seismic profiles across KR03 site	255
D.2	Seismic profiles across KR03 site	256
D.3	Chirp profiles across KR03 and KAS03 sites	257
D.4	Grain size analysis of core KAS03	258
D.5	Grain size analysis of core KR03	259
D.6	XRF analysis of core KAS03	260
D.7	XRF analysis of core KR03	261
E.1	Seismic profile across KS09 and KS08	265
E.2	Chirp profiles across KS08 and KS09, and slope instabilities around core sites . .	266
E.3	Grain size analysis of core KS09	267
E.4	Grain size analysis of core KS08	268
E.5	XRF analysis of core KS09 and KS08	269
E.6	Detailed analysis of turbidites layers-I	270
E.7	Detailed analysis of turbidites layers-II	271
E.8	Detailed analysis of turbidites layers-III	272
F.1	^{14}C and ^{210}Pb sampling	275
G.1	Example of P-Sequence code in OxCal for KS06G core	278

List of Tables

1.1	$M_w \geq 6.8$ earthquakes recorded over the instrumental period (20 th century) in the studied area. References for the location origin: 1. Engdahl and Villaseñor (2002); 2; Theunissen et al. (2010); 3. Cheng and Yeh (1989); 4. Chen and Tsai (2008); Cheng et al. (1996); 5. Wu et al. (2008). (*) M'_w : equivalent moment magnitude determined by Theunissen et al. (2010).	14
2.1	Cores collected during the OR1-1013 and OR1-1013 surveys	48
3.1	List of available seismic lines in the study area. 1:(Schnürle et al., 1998b); 2:(McIntosh and Nakamura, 1998); 3:(Wang and Chiang, 1998); 4:(Font et al., 2001); 5:(Hetland and Wu, 2001); 6:(Wang et al., 2004); 7:(McIntosh et al., 2005); 8:(Font and Lallemand, 2009); 9:(Lallemand et al., 1997b); 10:(Lallemand et al., 1999); 11:(Malavieille et al., 2002); 12:(Ramsey et al., 2006); 13:(Lallemand et al., 2013).	76
3.2	List of the sedimentary cores used in this study; 1:(Bentahila et al., 2008), 2:(Huang et al., 1992), 3: (Huh et al., 2004)	76
5.1	¹⁴ C dates of modern prep-bomb foraminifera samples in KS06-B and their reservoir ages.	115
6.1	$M_w \geq 6.8$ earthquakes recorded over the instrumental period (20 th century) in the studied area. References for the location origin: 1. Engdahl and Villaseñor (2002); 2; Theunissen et al. (2010); 3. Cheng and Yeh (1989); 4. Chen and Tsai (2008); Cheng et al. (1996); 5. Wu et al. (2008). (*) M'_w : equivalent moment magnitude determined by Theunissen et al. (2010).	145
6.2	Location of the studied cores, AMS radiocarbon data and sample age calibrations based on the Marine13 curve. (*) Corrected ages with the local reservoir correction of $\Delta R = 86 \pm 40$ based on Yoneda et al. (2007).	147
6.3	Activity-depth profiles of ²¹⁰ Pb _{ex} and ¹³⁷ Cs in KS06-B core.	149
6.4	Calibrated ages of the turbidite events. Calibration is based on Marine13 included in OxCal 4.2 calibration software. Turbidite ages are modeled using the P_Sequence model of deposition implemented in OxCal 4.2 (Ramsey, 2008). (**) Ages obtained with ²¹⁰ Pb _{ex} and ¹³⁷ Cs dating.	150

7.1	Input and output parameters of TOPICS simulations for 8 different submarine landslides sources S1 to S62. Parameters are described in Appendices A and B. .	185
7.2	Nearest grid points used for the run-up computation at the Holocene "Malaulau" terrace, Changping and Takangkou locations along the coast. L is the distance from the shore in meters.	185
7.3	Run-up computations using the analytical solution of (Choi et al., 2011) at the shore ($x = 0$) extrapolated from the last grid points ($x = L$) accounting for the slope between the shore and the last grid point. t_{at} is the arrival time (hour, minutes) of the wave at the last grid point.-means that the run-up computed is negative. The inaccuracy of grid resolution in these areas and the small amplitude of waves causes a retreat of the sea, following by small waves but the elevation induced by these waves wasn't higher than 0.	186

Introduction

Contents

1.1	Research motivations and objectives	3
1.2	An introduction to the geology of Taiwan	5
1.3	Thesis plan	15

1.1 Research motivations and objectives

1.1.1 Aims

Human society can be severely impacted by several kinds of natural phenomena, such as earthquakes, climate changes, catastrophic storms, tsunamis, etc. Therefore, understanding the nature and frequency of such geological processes is now a major and fundamental issue for making better natural hazard assessments. Over the 20th century, since the rapid development of technical methods able to record the seismicity, a great number of large earthquakes have struck the Earth (Fig.1.1). The largest ever recorded was the 1960 Valdivia earthquake (Chile) with a moment magnitude M_w 9.5. More recently the 2004 Sumatra and the 2011 Tohoku earthquakes (M_w 9.1 and M_w 9 respectively) have produced large tsunamis with consequent damages and human casualties. Therefore, for the next decades and centuries, one of the biggest challenge will be, using a large panel of scientific approaches, to better constrain the occurrence of such natural disasters.

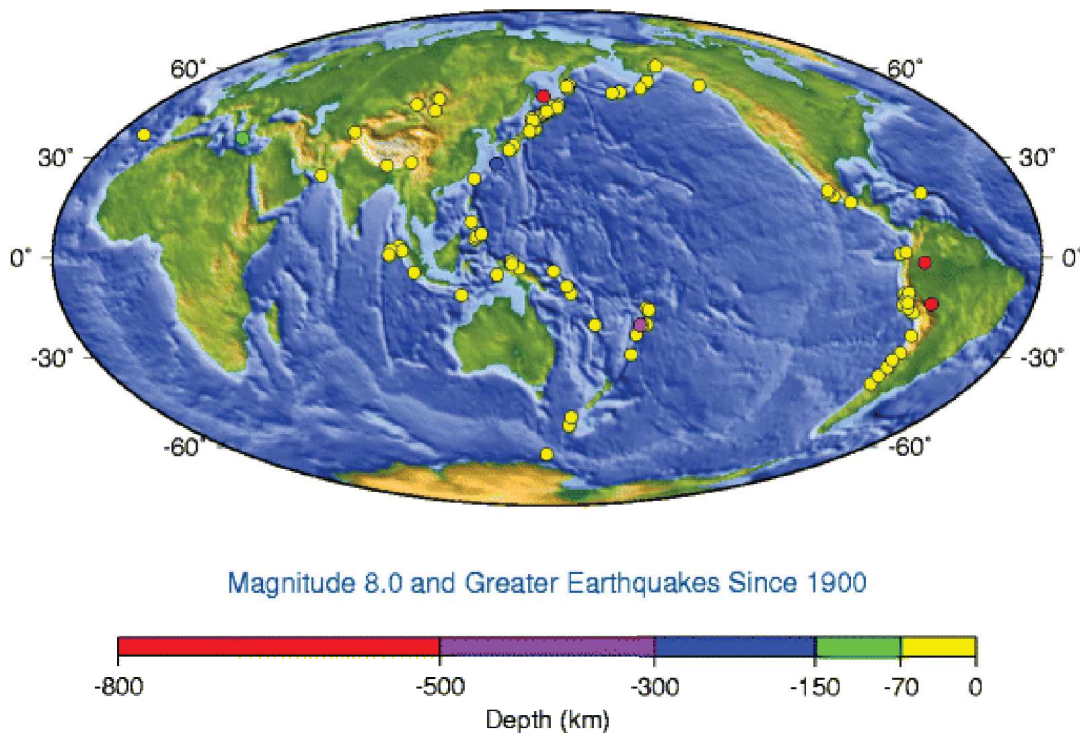


Figure 1.1: Magnitude 8 and greater earthquake since the 20th century, (Source USGS).

One possible key is the sub-aqueous paleoseismology based on the record of **the sedimentary gravity deposits**. This recent approach (developed since the nineties), appears as a serious alternative to approach this thematic and is a rapidly advancing field that has the potential to

illuminate the long-term history of seismicity, patterns of recurrence, the strength of shaking, rupture area and segmentation of fault systems (Goldfinger et al., 2003; Goldfinger, 2011). Subaqueous investigations offer the advantage of site to site correlation, and longer time spans than typically possible with onshore paleoseismology investigation.

Active margins such as subduction zones, are the best environment to study sedimentary gravity processes, especially turbidity currents, that constitute the essential process that fill out deep oceanic basins. Active margins, with their high bathymetry gradient, the development of turbiditic systems and high sediment supply from the eroded mountain belts confer a great record of sedimentary events with high resolution. Since the 1929 Grand Banks earthquake (that triggered slope failures and turbidity currents that broke several telecommunications cables), it is known that large earthquakes are the main agents responsible of submarine landslides and may produce gravity flows transported along the slope towards the deep oceanic basins. The product of the instabilities, initially mass transport deposits, may rapidly evolve into turbidity currents. Several authors have used mass transport deposits and turbidites as a marker of the instrumental, historical and paleo seismicity (Adams, 1990; Beck et al., 2007; Blumberg et al., 2008; Carrillo et al., 2006; Chapron et al., 1999; Goldfinger et al., 2003; Huh et al., 2004; Gràcia et al., 2010; Polonia et al., 2013; Ratzov et al., 2010).

When the turbidite sequences are well defined among the sedimentary archives, it is possible to date them and build stratigraphical time-series. It has also been demonstrated by several authors that, using paleoseismology on turbidites, it is possible to recover about 18,000 years of seismic cycles (Goldfinger et al., 2003; Ratzov et al., 2010; Poudoux et al., 2012). However this approach remains challenging and must be carefully employed. In fact, different triggers may instigate turbidity currents. Among them, earthquakes but also extreme climatic events such as typhoons. It is thus crucial to discriminate these two kinds of turbidites. Therefore robust criteria must be established to discriminate between the different triggering mechanisms.

The Taiwan mountain belt, known as one of the most active area in the world, has suffered, since the beginning of the instrumental record (on the 20th century) 22 earthquakes with a magnitude of greater than seven. Therefore, the instrumental record shows that great earthquakes have illustrated the need of longer records to evaluate occurrence of seismic event through longer span of time, but also what are the possibilities that larger events (an earthquake of magnitude 8 and greater) occur in Taiwan?

Beside abundant geological and geophysical studies found in the literature, dealing with a large panel of geological problems, it appears that the study of sub-aqueous sedimentary gravity

processes as marker of paleo-earthquakes, has not been really investigate yet. Indeed, only one study about the record of instrumental earthquakes based on turbidites records, has been carried out (Huh et al., 2004) offshore eastern Taiwan. This study could attest for the reliability of the method and highlight the great potential of a paleoseismological approach in such an active context.

1.1.2 Objectives

This work is thus articulated around four objectives in order to provide new constrains on seismic chronology over the Holocene:

- Collect a new sedimentary data set (i.e sedimentary cores) in strategic areas detailed thereafter (Indeed so far few sedimentary data are available or exist offshore eastern Taiwan).
- Understand the recent sedimentary processes offshore eastern Taiwan providing an analysis of the recent sedimentary systems, sedimentary facies, to characterize deposits (i.e turbidites) and the controlling factors of recent submarine sedimentation (tectonic forcing vs climate forcing).
- Test the reliability and the validity of a paleoseismological approach over the instrumental period.
- Once calibrated over the instrumental-scale, extend the time-series of seismic event over a larger span of time applying discriminant criteria to eliminate the possible other trigger mechanisms (i.e large flood induced by typhoons).

1.2 An introduction to the geology of Taiwan

1.2.1 Generalities

Taiwan mountain belt at the cross-road of two subduction zones. The island seats at the extremity of the south Ryukyu subduction zone (linking Japan to Taiwan) and the Manila subduction zone (between The Philippines and Taiwan). This area forms the northeastern tip of the Philippine Sea Plate (PSP) adjacent to the Eurasian Plate (EP) (Fig.1.2). The Taiwan mountain belt results of the rapid and oblique convergence of the Luzon arc carried by the PSP with respect to the passive Chinese continental margin (Fig.1.2, 1.3) (Biq, 1972; Suppe,

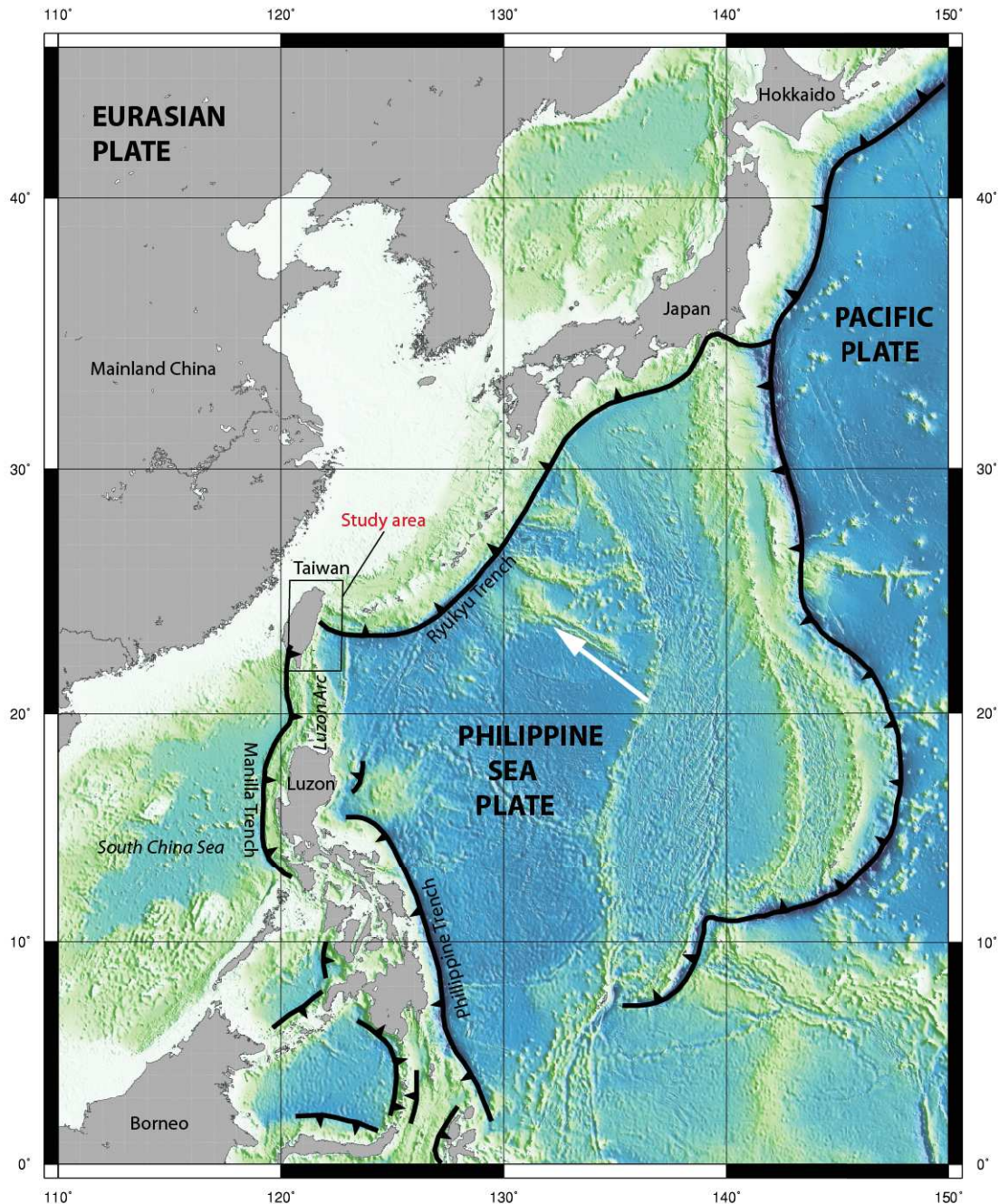


Figure 1.2: Plate tectonics and geodynamic of Eastern Asia. The thick lines represent plate boundaries. White arrow indicates the relative motion of the PSP

1984). Plate kinematics predicts about 80 mm/yr of convergence between these two plates (Seno et al., 1993) (Fig.1.3B). The orogen links two subduction systems dipping with opposite vergence: to the South the Manila subduction zone and to the east the Ryukyu subduction zone (Fig.1.3). South of Taiwan, the South China Sea is being subducted eastwards beneath the PSP, building an accretionary wedge progressively uplifted above the sea level. To the northeast, the PSP slab is retreating southwardly beneath the Eurasian margin, resulting on the

opening of the Okinawa back-arc domain and the collapse of the northern part of the Taiwan mountain belt. Thus, the Taiwan orogen is located at the junction of those two opposite-dipping subduction systems and marks the interactions between them. Consequently, the deformation is characterized by a very high rate of seismicity onland and offshore eastern Taiwan (Hsu, 1961).

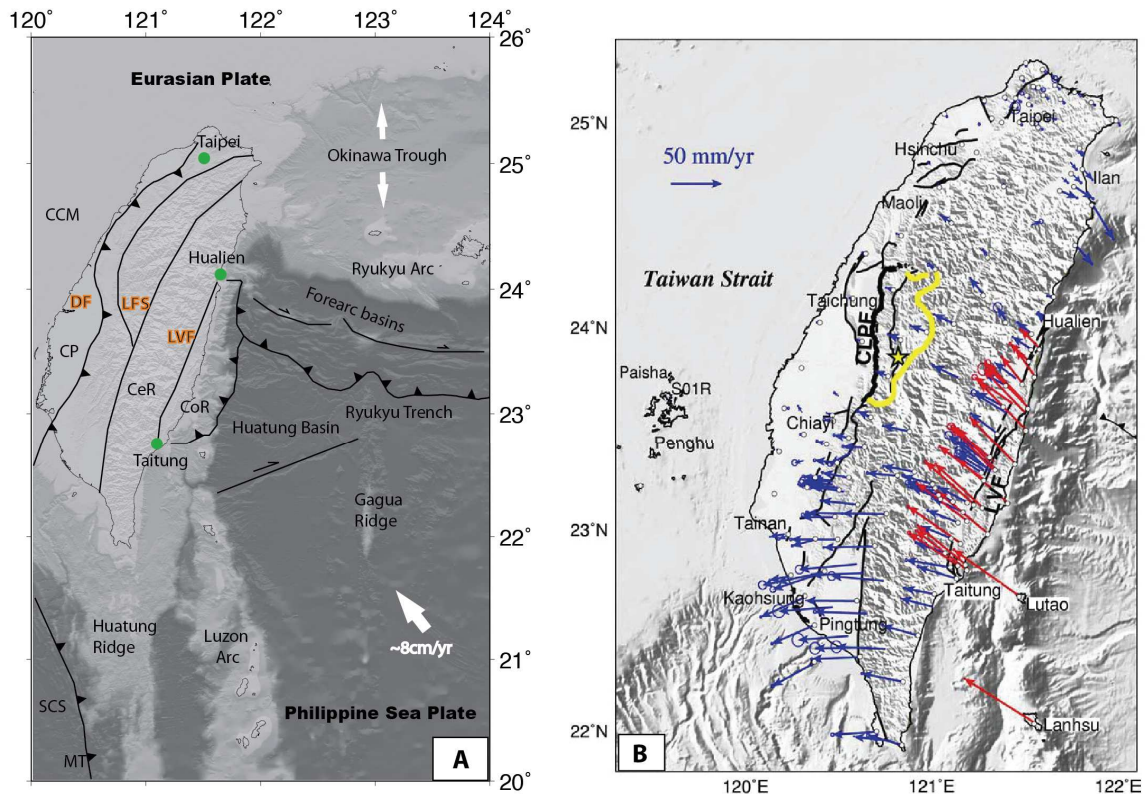


Figure 1.3: A) Geodynamic context of Taiwan. The thick lines represent the main deformation fronts. Index: MT: Manila Trench; MAW: Manila Accretionary Wedge; SCS: South China Sea; CCM: Chinese Continental Margin; CP: Coastal Plain; CeR: Central Range; CoR: Coastal Range; RT: Ryukyu Trench; RAW: Ryukyu Accretionary Wedge; LVF: Longitudinal Valley Fault. The white arrow represents the ongoing convergence rate from Seno et al. (1993). B) GPS velocity field relative to Paisha, Penghu for the period between 1993 and 1999, (after Hsu et al., 2009)

The geologic setting of the Taiwan collision belt can be summarized as follow: the sedimentary cover of the Chinese continental margin (Fig.1.4) was accreted in the northwest part of the island, and it is still accreting in the southwest, against a backstop formed by the Pre-Tertiary rocks of the Central Range (Malavieille et al., 2002). The Central Range includes the Eocene and Miocene metamorphic Backbone Range. The Lishan Fault (LF on Fig.1.4), west of the

subduction wedge, is a west dipping reverse fault, which separates the western Backbone Range from the Eocene-Oligocene units of the Hsüehshan Range forming the slate and sandstone belt. The Central Range is bounded to the east by the Longitudinal Valley, which separates the Central Range from the Coastal Range (Fig.1.4) and represents the northernmost segment of the Luzon volcanic arc (Malavieille et al., 2002).

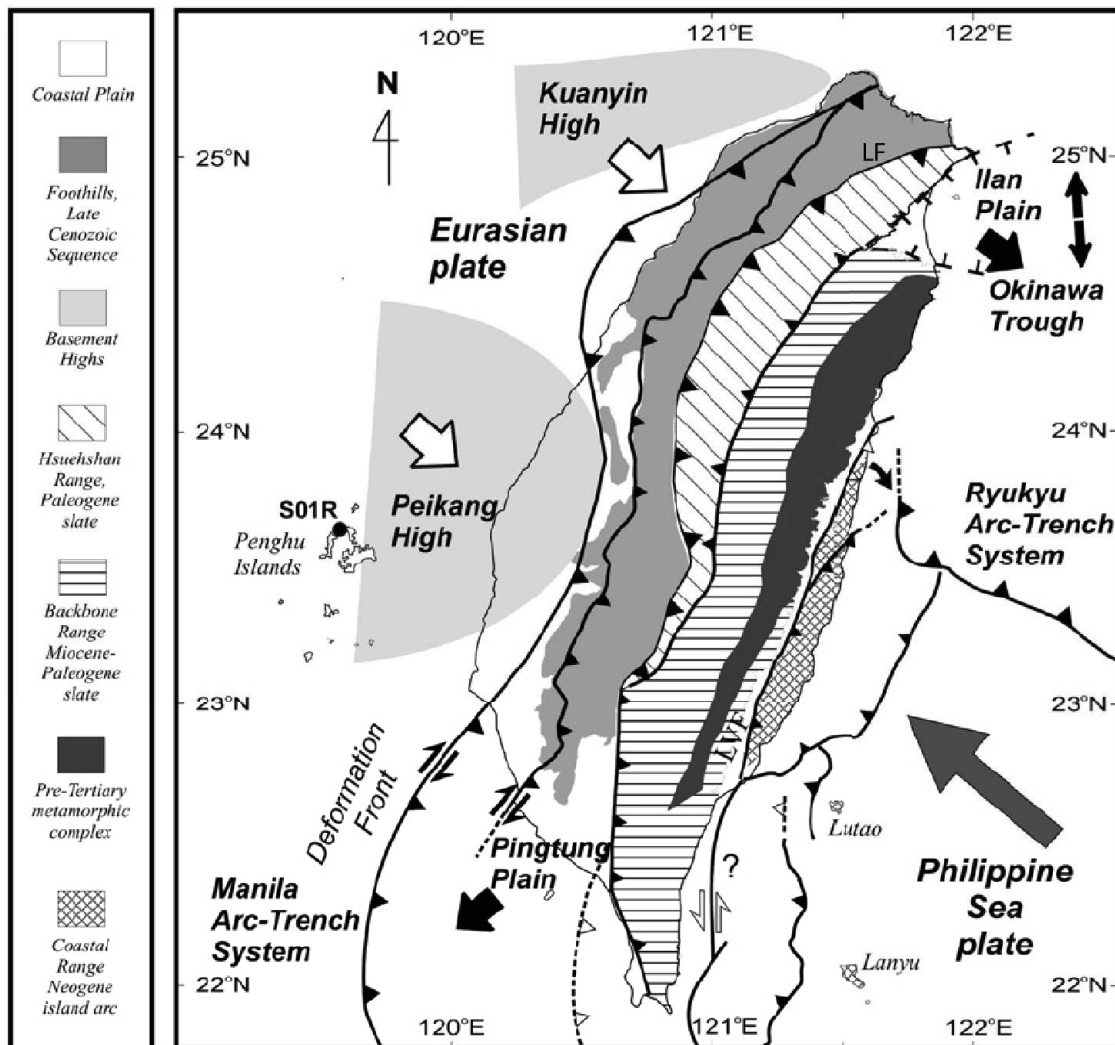


Figure 1.4: Geological map of Taiwan, showing the main structural units and their boundaries (LF= Lishan Fault and LVF=Longitudinal Valley Fault) (modified from Huang et al., 2006)

1.2.2 Topography

Topography sculpted by submarine processes is subsequently uplifted above sea level and forms a template on which subaerial relief develops. In turn, the products of sub-aerial erosion are transported into the submarine landscape and may drive its topographic evolution by erosion

and/or deposition. The sub-aerial and submarine landscapes are intrinsically linked (Ramsey et al., 2006). The plate obliquity has led the collision to propagate southward over the past 5 Myr.

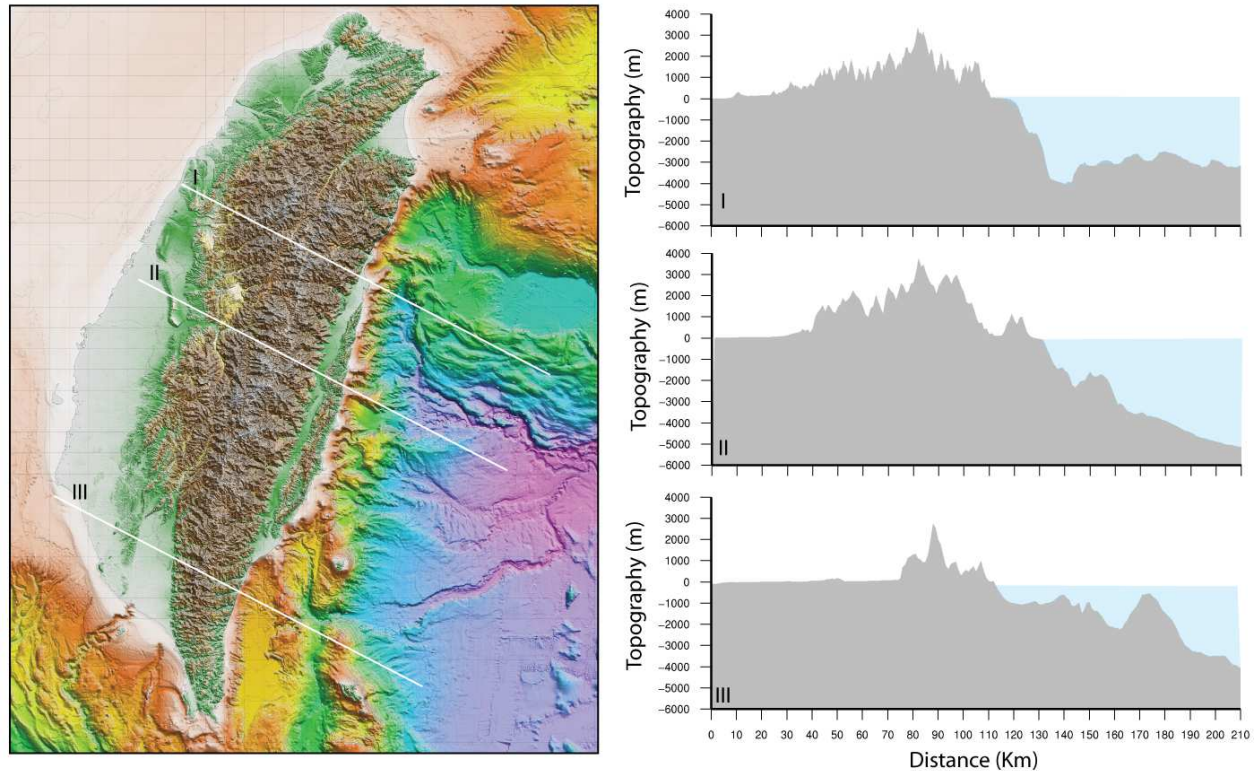


Figure 1.5: Profiles across Taiwan showing both subaerial and submarine reliefs. DEM 100m gridded, from courtesy of Stephane Dominguez.

The ongoing uplift rates on the order of $5\text{-}6\text{ mm.yr}^{-1}$, and locally up to 1 cm.yr^{-1} (Peng et al., 1977; Chen and Liu, 2000; Hsieh et al., 2004; Liew et al., 1993; Wang and Burnett, 1990), combined with wet and stormy climate induce, for the emerged part reliefs reaching up to 3950m above sea level. Consequently, this merges to produce erosion rate among the highest of the world (Dadson et al., 2003; Siame et al., 2011; Derrieux et al., 2014). In the submerged part, the topography extends down to 6000 m below sea level (Fig.1.5).

1.2.3 Regional climate

Taiwan is positioned within what has been called the "typhoon Alley" (Liu et al., 2008). On average, three or four typhoons impact the island annually. As such, Taiwan receives not only abundant precipitations due to its southern Asian monsoon climate, but also periodically heavy rains during typhoons (Wu et al., 1999; Lin et al., 2002; Galewsky et al., 2006; Liu et al., 2008).

The Morakot Typhoon in 2009 was the worst event of the last 50 years (Fig.1.6). The storm produced accumulated rainfall of 2777 mm (Ge et al., 2010) which triggered 12,697 landslides (Wu et al., 2011; Tsou et al., 2011) and exceptional flooding in southern Taiwan. The Morakot typhoon caused 700 casualties and catastrophic damages (Fig.1.6). With high relief, steep gradients, important tectonic activity, heavy rainfalls and frequent typhoons, Taiwan is generally recognized as having the highest sediment production in the world as 7 of the 10 global rivers with the highest sediment yield are in Taiwan (Li, 1976; Milliman and Syvitski, 1992; Chen et al., 2004; Dadson et al., 2004; Liu et al., 2008). Taiwanese rivers presently discharge more than 300Mt of sediments to the surrounding ocean each year and more than 30% of the total sediment from Taiwanese rivers is discharged at hyperpycnal concentrations (Dadson et al., 2005; Kao and Milliman, 2008; Liu et al., 2008).



Figure 1.6: Left, satellite image of the Morakot typhoon at its peak (source CWB); Right, Impact of typhoon Morakot, an example of one of several typhoon-triggered landslides

1.2.4 Seismicity

The seismicity in Taiwan is concentrated in the collision zone, the Ryukyu subduction zone and the Manila subduction zone (Fig.1.8) According to the geological context, the seismicity rate is extremely high (Fig.1.8). Destructive earthquakes have significantly struck the island repeatedly.

During the last century, more than 20 $M_w > 6.8$ earthquakes have been recorded (Table 6.1). Onland, the greatest occurred in 1999 with a magnitude M_w 7.6 leaving catastrophic damages and casualties (Fig.1.7). Offshore, the greatest event ever recorded in the Ryukyu margin (former estimated magnitude 8), has been re-estimated with a magnitude M_w 7.7 (Theunissen et al., 2010, Fig.1.9). Such a high seismic rate will consequently produce slope instabilities and play an important role the driving mechanisms of the actual offshore sedimentary processes.

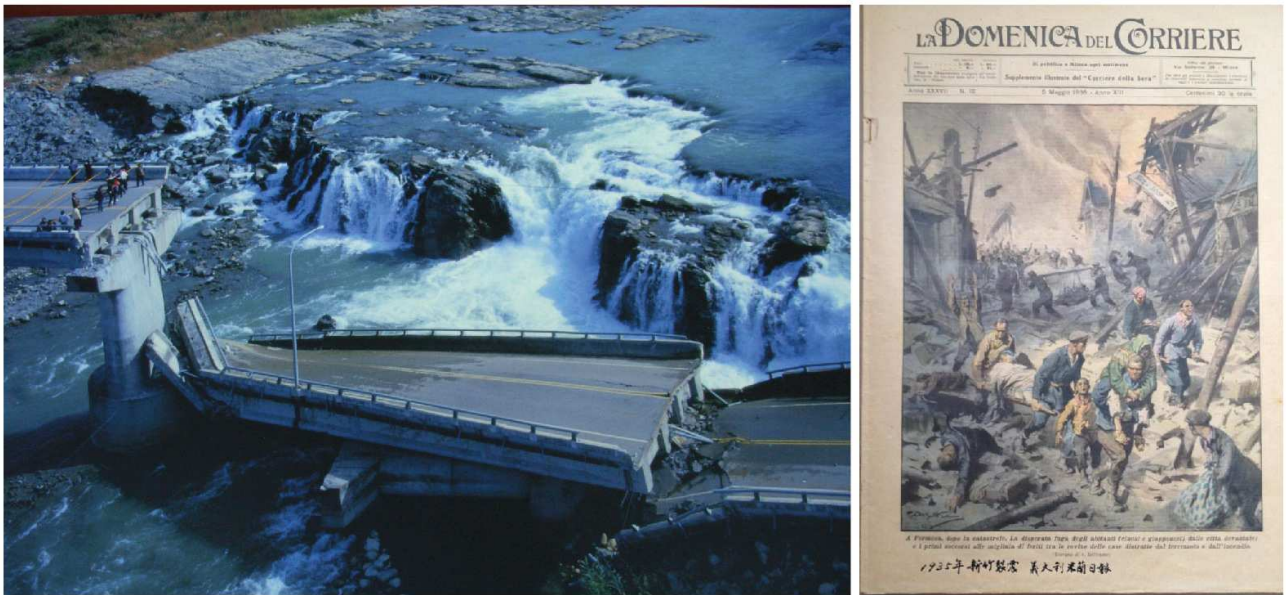


Figure 1.7: Example of disasters that occurred during the last century in Taiwan. Left, broken bridge after the Chi-Chi earthquake in 1999. Right, copy a newspaper of 1935 showing damages after the Hsinchu earthquake that occurred the same year (Kuo-Fong Ma, personal communication).

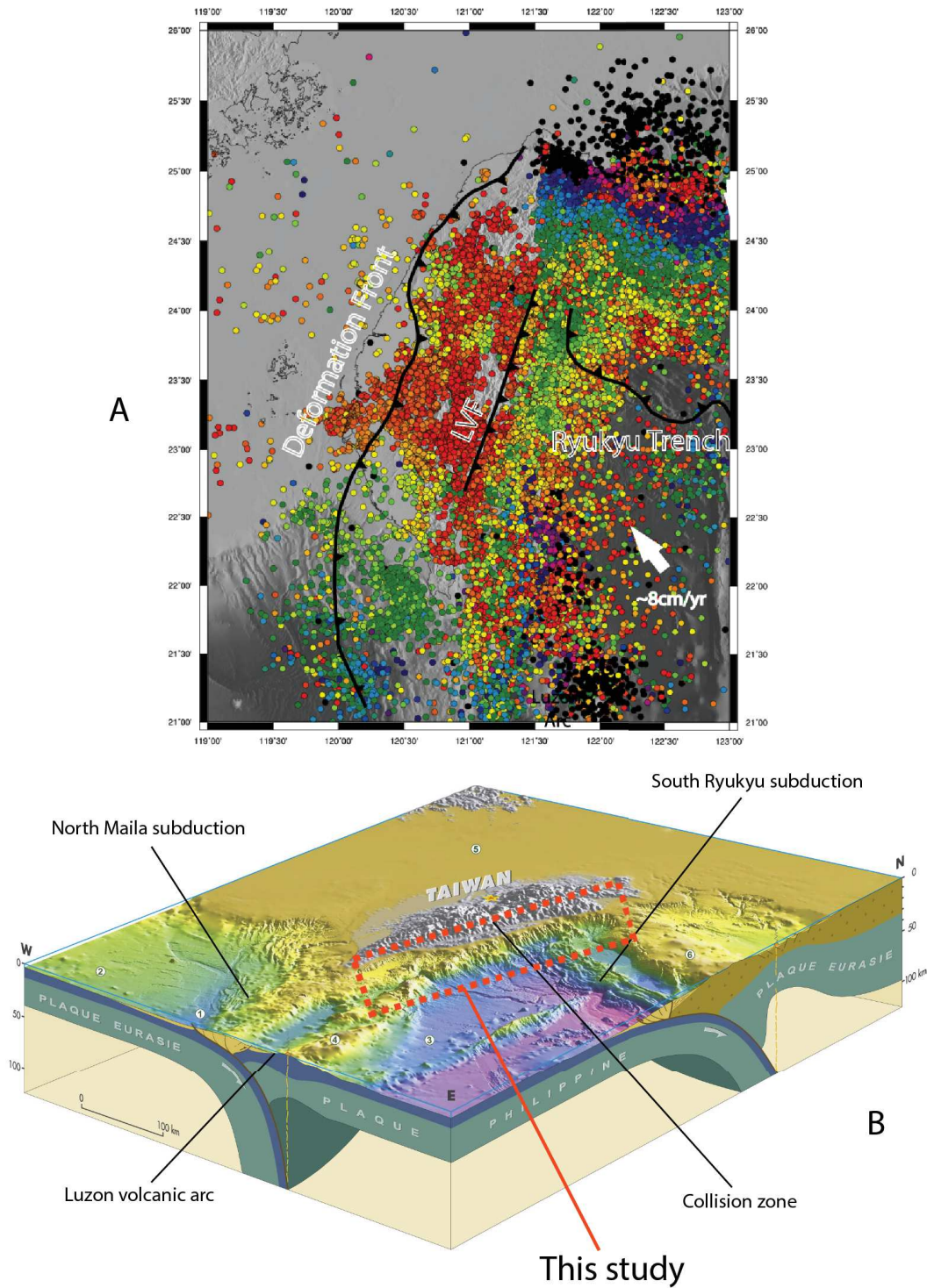


Figure 1.8: A: Seismicity of Taiwan $M_L > 3$ for the period 1991-2008. Data from Central Weather Bureau; B: Perspective view showing the two subduction and the collision zone. The seismicity is concentrated on the subduction zone and the collision zone. The red box shows the study area for this work (Courtesy from Serge Lallemand and Jacques Malavieille)

Eq. number	Date (yy/mm/dd)	Lon.(°)	Lat. (°)	Depth (km)	M_w' (*)	Loc. origin references
1	1915/2/28	123.50	23.60	0	7.5	1
2	1919/12/20	122.50	22.50	35	6.9	1
3	1920/6/5	122.22	24.29	35	7.7	2
4	1921/4/2	123.00	23.00	35	7.1	1
5	1922/9/1	122.04	24.50	35	7.3	1
6	1922/9/14	122.64	24.370	35	7	1
7	1935/9/4	121.55	22.50	20	7	3
8	1935/4/20	120.82	24.35	5	6.9	3
9	1947/9/26	123.00	24.75	110	7.3	1
10	1951/10/21	121.72	23.87	4	7.1	4
11	1951/11/24	121.35	23.27	36	7.1	4
12	1951/10/22	121.72	24.07	1	6.9	4
13	1951/10/22	121.95	23.82	18	6.9	4
14	1957/2/23	121.80	23.80	30	7.1	3
15	1959/4/26	122.79	24.68	126	7.5	1
16	1963/2/13	122.06	24.35	35	7.1	1
17	1966/3/12	122.69	24.30	28	7.5	1
18	1972/1/25	122.32	22.54	10	7.3	1
19	1978/7/23	121.32	22.35	6	7.2	3
20	1986/11/14	121.83	23.99	15	7.3	3
21	1999/9/20	120.80	23.85	6	7.6	5
22	2002/3/31	122.16	24.16	16	7	5
23	2003/12/10	121.38	23.07	21	6.8	5

Table 1.1: $M_w \geq 6.8$ earthquakes recorded over the instrumental period (20th century) in the studied area. References for the location origin: 1. Engdahl and Villaseñor (2002); 2. Theunissen et al. (2010); 3. Cheng and Yeh (1989); 4. Chen and Tsai (2008); Cheng et al. (1996); 5. Wu et al. (2008). (*) M_w' : equivalent moment magnitude determined by Theunissen et al. (2010).

1.3 Thesis plan

After this **first introductory chapter**, the manuscript has been organized into two part based on the previous observations and in order to reach the objectives of this work.

The first part entitled **Sedimentary processes offshore eastern Taiwan**, will deal with the two first objectives: 1) To collect new sedimentary data in strategic areas and 2) understand the recent sedimentary systems offshore east Taiwan. This part has been thus cut into two chapters: the **second chapter** presents 1) a global overview of the notions and concepts of the sedimentary gravity processes and their deposits and 2) the coring strategy as well as the presentation of the coring sites. **The third chapter** will concern the deep-sea sedimentation and sedimentary facies offshore eastern Taiwan. Using several dataset such as geophysical data and sedimentological data, this work proposes to characterize the sedimentary facies and associated sedimentary processes. The erosional potential offshore eastern Taiwan and the controlling factors of recent sedimentation in such active area will be discussed.

The second part entitled **Testing a paleoseismological approach offshore eastern Taiwan**, will deal with the two last objectives of this study. **The fourth chapter** presents 1) the background relative to turbidites as a marker of paleoseismology and 2) the dating proxies used in this thesis (^{210}Pb and ^{137}Cs for the last century and ^{14}C for the late Holocene). Then **chapter five** presents the results of a study relative to the dating of turbidites and correlation with instrumental earthquakes from the last century using ^{210}Pb and ^{137}Cs proxies. Furthermore, we will discuss how to estimate a crucial parameter for ^{14}C age corrections and why it may be variable. **The chapter six**, will cover the paleoseismological study conducted, offshore east Taiwan, showing the results including all the sedimentary and dating analysis necessary to build robust age models for each core. We will then demonstrate, using discriminant criteria, the seismic character of the turbidites deposits. Then the frequency, source and magnitude of earthquakes for the last 2,700 years will be discussed. **Chapter 7**, will present the results of study about an original deposit we found in our core dataset. In this chapter, we intend to interpret this marine deposit, supported by sedimentological analysis, dating and current modeling, as a result of a super event that occurred 3,000 years ago. The possible scenario to explain the origin of this anomalous deposit will be discussed.

Finally, the last chapter of this thesis, **chapter 8**, will expose a summary of the major results and conclusions, concluding remarks on several points and the possible perspectives.

Part I

Sedimentary processes offshore eastern Taiwan

Background

Contents

2.1	Submarine sedimentary gravity processes and deposits	21
2.2	Study area and coring strategy	37
2.3	Coring sites	39

2.1 Submarine sedimentary gravity processes and deposits

Gravity processes occur at any scale and affect all types of continental margin (passive and active). They are able to transport sediment from the continental shelves to the abyssal plains under the influence of the gravity (Fig.2.1). Nevertheless these processes have never been observed directly but mainly detected by their impact on human infrastructures such as cable failures (Hsu et al., 2008; Genesseeaux et al., 1980). The study and analysis of the gravity sedimentary processes and their associated deposits are essential for the understanding of the construction and the evolution of continental margins. In the case of active margin context, they may represent invaluable sedimentary archives to decipher the history of the margin. The literature provides abundant studies and classifications according to the rheology, motion, duration or deposits (Middleton and Hampton, 1973; Stow et al., 1996; Hampton et al., 1996; Mulder and Cochonat, 1996; Mulder and Alexander, 2001). These processes are distinguished into two main categories relative to the motion mechanisms of the transported materials (Fig.2.2):

- Mass slide (Motion not due to pore fluid): *creeping, block gliding/rock avalanche, slide (translational and rotational)*
- Gravity flow (Triggering and motion due to pore fluid): *laminar and turbulent regimes*

2.1.1 Mass slide

The mass slides are characterized by homogenous sedimentary volumes displaced along a basal shear surface. They may travel over a limited distance from few hundred meters to several kilometers. Their resulting deposits are often called **Mass-Transport deposits (MTDs)** defined as sedimentary, stratigraphic successions that are remobilized and transported downslope by gravitational processes as non-Newtonian rheological units (*N.B: In the following review, only the sedimentary processes used in this thesis will be described*).

- **Translational slide (i.e slide)**, corresponds to a sedimentary mass displacement following a translational shear surface (Fig.2.3A). This process is observable at different scales of size and displacement (Stow et al., 1996). Slides display very low internal deformation because of the high cohesion of the sedimentary mass.
- **Rotational slide (i.e slump)**, (Fig.2.3B), corresponds to a sedimentary mass movement on a basal shear surface limited by rupture plans and by a headwall scarp ranging from

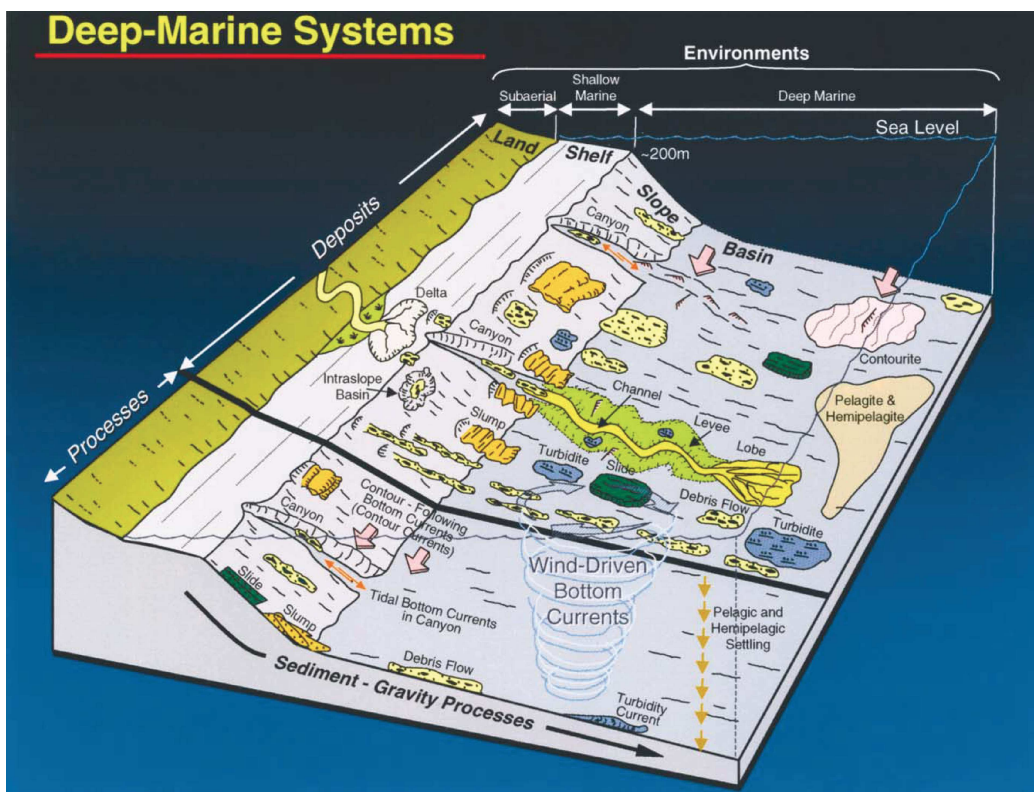


Figure 2.1: Perspective diagram showing the different types of deep-sea sedimentary processes: From hemipelagite sedimentation to mass transports processes. (after Shanmugam, 2003)

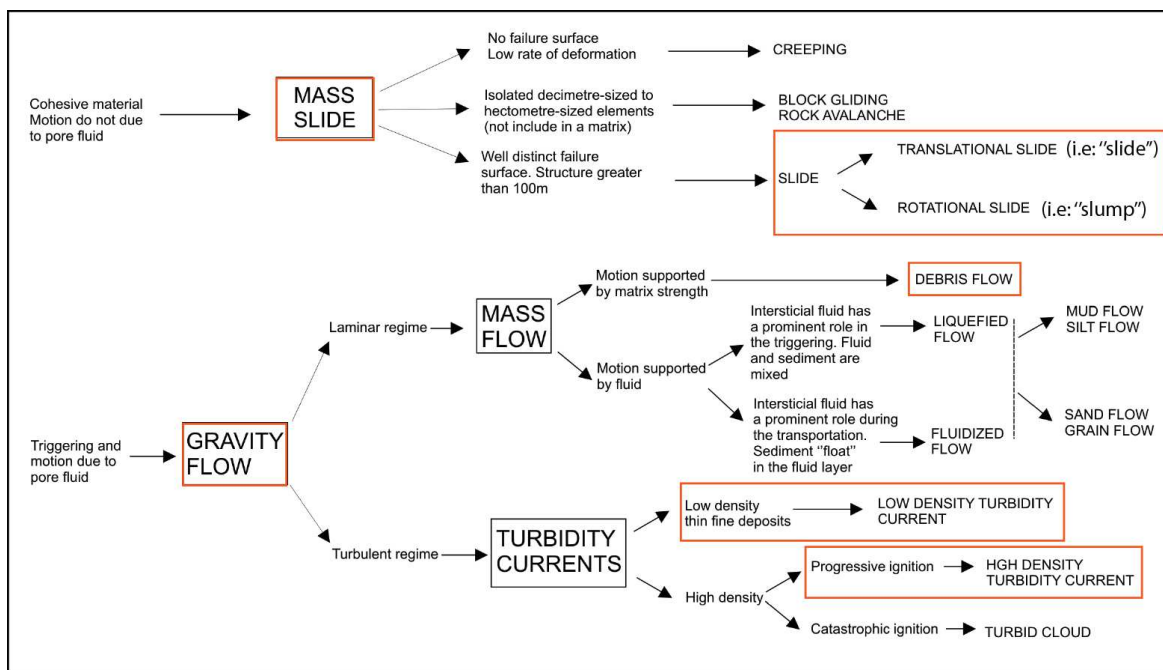


Figure 2.2: Global classification of offshore mass movements. Red boxes emphasize the sedimentary processes approached and described in this work (modified after Mulder and Cochoat, 1996)

several meters to several hundreds meters (Mulder and Cochoat, 1996). This sedimentary process occurs at any scales on a gentle slope (surfaces involve sometimes more than 100km^2). Unlike translational slides, rotational slides display important and heterogeneous internal deformation. The deformation occurs when the shear stress reach a critical limit.

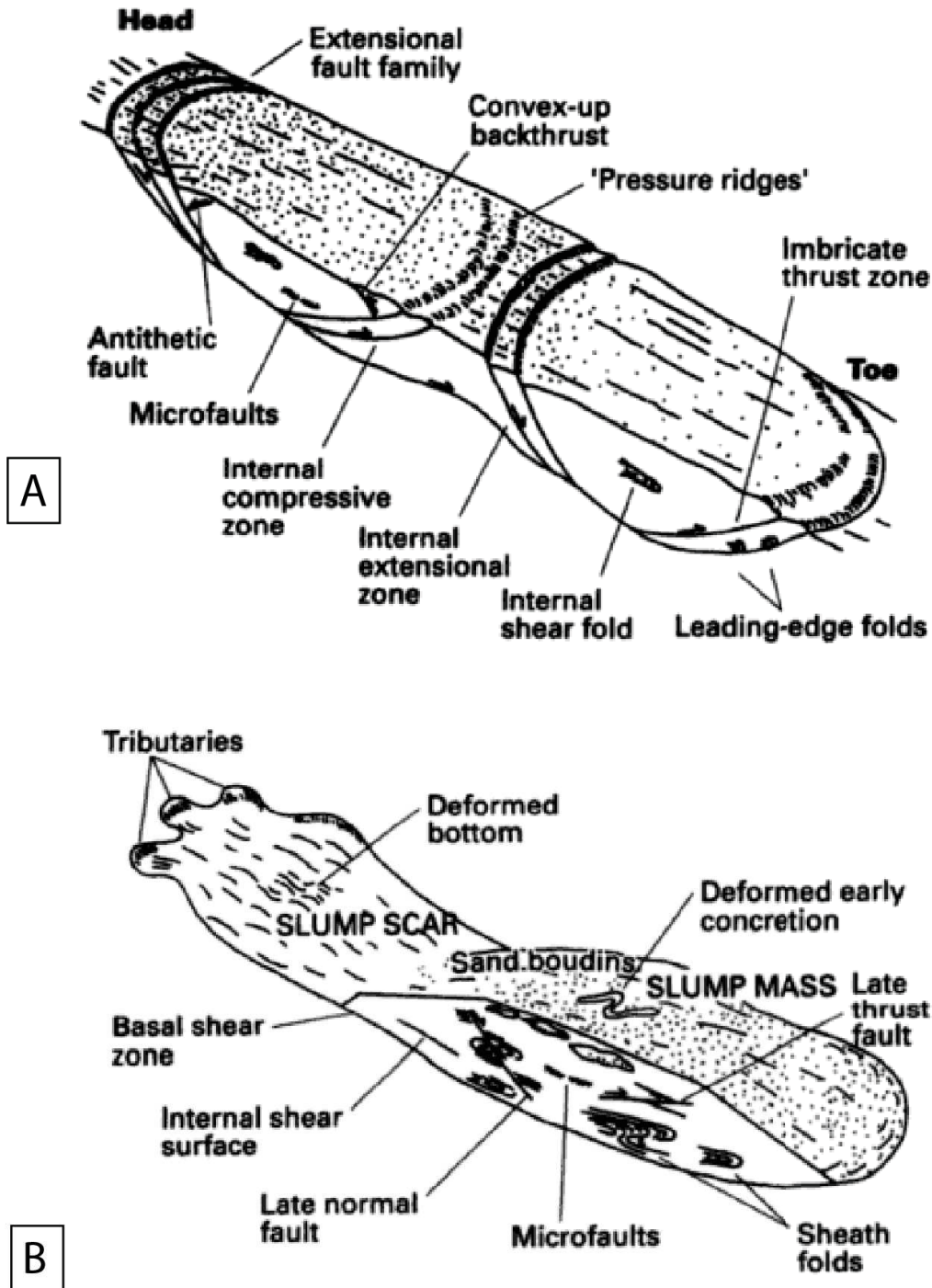


Figure 2.3: Idealistic model of A: Slide and B: Slump (after Stow et al., 1996).

2.1.2 Gravity flows

The motion of gravity flows results from the difference between the mix of sediment/fluid and the surrounding fluid (i.e sea water). Authors distinguish two hydraulic mechanisms: laminar flows and turbulent flows (Mulder and Cochonat, 1996). The distinction between those two mechanisms depends of by the Reynold number (Re), characteristic of the flow regime (the Reynolds number is the ratio between inertial and viscous forces): **laminar** if $Re < 500$, transitional if $500 < Re < 2000$ and **turbulent** if $Re > 2000$. The variation of the Re parameter may lead to a flow evolution from laminar to turbulent flow regime (for example if the viscosity decreases). Mulder and Alexander (2001), proposed a classification of gravity flows according to the dominant grain support mechanisms: 1) matrix strength support, 2) grain-to-grain support, 3) turbulent support (*N.B: As previously mentioned, only the processes and deposits used in this work are described*).

2.1.2.1 Laminar flows

Laminar flows are characterized by high sediment concentration and high viscosity that avoid the development of turbulent flow regime. The sediment concentration is basically $>9\%$ so that the flow has a non-Newtonian fluid behavior. The transport of laminar flows is mainly supported by a clay matrix, grain-to-grain interaction mechanisms, buoyancy and friction (Mulder and Alexander, 2001). The distinction between the different styles of laminar flows is based on sediment concentration, matrix and the presence of fluid (i.e water). Thus, three kind of flow are distinguished: **debris flow**, fluidized flows and liquefied flows.

Debris flows: They are made of a plastic matrix of cohesive material and not liquefiable (generally silt and clay) containing rock fragments and water (Postma, 1986; Mulder and Cochonat, 1996; Mulder and Alexander, 2001). Deposition occurs when the shear rate does not reach the yield strength. When shear rate decreases, the flow "freezes" due do its high cohesion (Rodine and Johnson, 1976; Mulder and Cochonat, 1996). The cohesive matrix (presence of clay) avoids the transformation of debris flow into turbulent flow even if the volume of sediment and the slope are important. The events may be considerably catastrophic and consequently travel over few hundreds kilometers away from the source.

Debris flow deposits, debrites, are often conglomerates with a possible inverse grading. They form massive beds with some blocks transported at the top of the flow. The seafloor morphol-

ogy is a typical hummocky surface. On seismic profile debrites have usually low amplitude to transparent reflectors displaying a chaotic facies.

2.1.2.2 Turbulent flows

Turbulent flow is defined as a flow where the turbulence is the main particle transport mechanism. The theoretical sediment concentration is low (<9% of sediment concentration). The flow is assimilated to a Newtonian fluid (Mulder and Alexander, 2001). Unlike laminar flows, that can be easily observed onland (e.g. landslides, debris flows etc.), turbulent flows are only found in sub-aqueous environment and consequently difficult to observe and monitor. The first studies and observations of such processes started at the dawn of the 20th century with Forel (1887) on the Leman lake at the Rhône river mouth. From the mid 20th century, the experiments of Kuenen and Migliorini (1950) helped developing the concept of turbiditic sedimentation. They demonstrated the existence of turbidity currents and their capacity to transport sediment from shallow water to deep sea environments. Among turbulent flows, it is possible to distinguish: the turbidity currents (*sensu lato*), the turbidity surge and hyperpycnal flow:

- Turbulent flows are classified according to the volume of sediment involved in the flow (Mulder and Alexander, 2001): 1) **Turbidity current (*sensu lato*)** are constantly fed by sediment incorporated during the transport and 2) **Turbidity surges** that involve a finite volume of sediment:

1) The turbidity current *sensu lato*, is continuously maintained by incorporation of eroded material during the flow. Therefore, turbidity currents (*sensu lato*) may have a lifetime from several hours to several weeks.

2) Turbidity surge corresponds to flow with a finite volume of sediment and no sediment incorporation during flow motion. Consequently, these flows have a relative short lifetime ranging from several hours to several days. However, the deposits from turbidity surges may be difficult to differentiated from other fine-grained deposits such as pelagite, hemipelagite or contourites deposits because of their fine-grained composition. These deposits may also be eroded by other kind of gravity flows because of their thin thickness or later homogenized by bioturbation (Mulder and Alexander, 2001).

The deposits that result from the turbulent flows are termed **turbidites**, displaying a normal grading sequence with sometimes sedimentary structures (ripples, cross-laminae ...). Bouma (1962) proposed an idealistic sequence of a turbidity current and a relative repar-

tition of sedimentary facies on a deep-sea fan. This sequence, called **Bouma sequence** contains a succession of five facies (from T_a to T_e) above an erosional base. Unfortunately, this ideal sequence is rarely fully observed because of the potential erosion at the base of the sequence or because of the position on the deep-sea fan (Bouma, 1962). The Bouma sequence introduced the concept of "energy loss" during the flow of turbidity currents but does not take into account the dynamic processes responsible for the sedimentary structures observed in the sequence. Therefore, the Bouma sequence cannot justify the observed diversity of turbidites deposits. Thus, several studies intended to fill this gap and proposed new models and classifications. Stow and Shanmugam (1980) proposed a model relative to low density turbidity currents (high content of fine grained sediments) and Lowe (1982) proposed a classification that corresponds to high density turbidity currents (higher content of coarse materials). Together with the Bouma sequence, these models cover a broader spectrum of turbiditic systems (Fig.2.4).

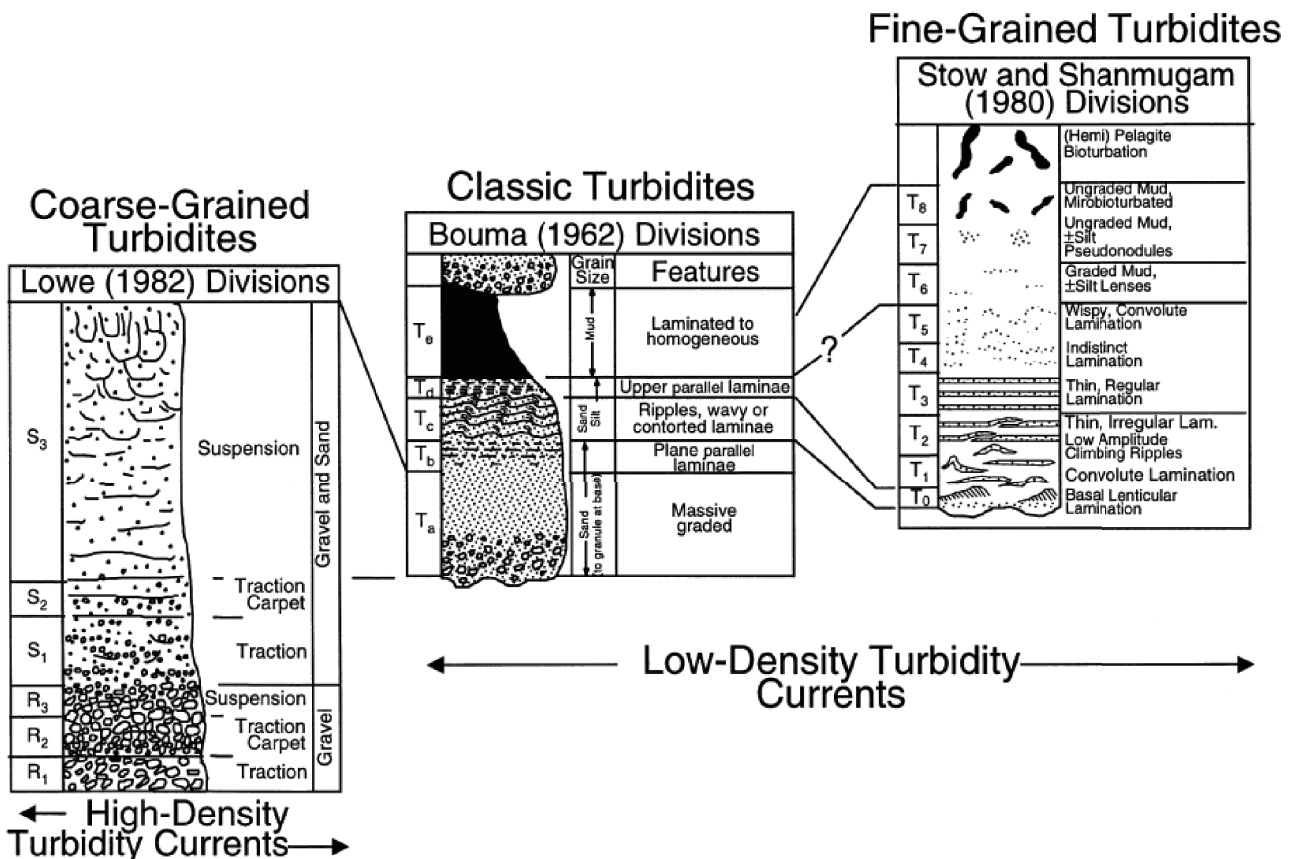


Figure 2.4: The Bouma sequence (1962) and its extensions for the low-density turbidity currents (Stow and Shanmugam, 1980) and high-density currents (after Lowe, 1982)

- Hyperpycnal flows are produced at the river mouths when the density of the fluid becomes greater than the surrounding water (e.g, ocean water $1,025 \text{ g.ml}^{-1}$). Rivers are the main transport agent of sediment from continent to ocean bringing 85% of the total load of the sediment to the global ocean (20 billions of tons per year) (Milliman and Syvitski, 1992). The rivers loads are supplied as suspended load (64%) or dissolved load (18%). At rivers mouths, flow evolution depends on the density contrast between the flow (ρ_f) and the surrounding water (ρ_w). The hyperpycnal flow is also defined as a turbulent flow. They occur generally during large climatic events such as flood or storm (e.g. typhoons in the case of Taiwan). When they reach the head of canyons, they changed into gravity flows and may transport the sediment load toward deep basin or subduction trenches (Mulder and Syvitski, 1995). Although the characteristics are similar to the classic turbidity currents, their duration is longer and the dynamics follows the sediment charge/discharge of the river which can be observed in the sedimentary records (Fig.2.5). For the charge phase, the grading is increasing from the base of the turbidites. In contrast, during the discharge phase the grading is decreasing (Mulder et al., 2003). When the event is strong enough, the turbulent flow may be considerably erosive and the base of the sequence may be truncated (Fig.2.5). It becomes then difficult to differentiate the hyperpycnites (deposits resulting from the hyperpycnal flows) from the Bouma sequences of "classic" turbidites.

2.1.2.3 Evolution and transformation of gravity flows

The mechanisms previously described are idealistic ones. The mechanisms involved may change between the time of transportation and deposition. The dynamics of a gravity flow (transport, erosion and deposition) lead to the incorporation of a fluid and sediment but it also involves the destructure of the sediment. The first model of spatial evolution for gravity flow was proposed by the Middleton and Hampton (1973) (Fig.2.6). Mulder and Alexander (2001) highlighted the fact that the classification of gravity flows is relatively complex because of their possible transformation between the source where they are triggered and the place where they are deposited (up to several hundreds of kilometers). Shanmugam et al. (1994) suggested an evolution from a mass slide (i.e slide, slump etc.) to a gravity flow (such as laminar flow that evolve to a turbulent flow (Fig.2.7). Several mechanisms can thus alternate during the same transport and the deposit will reflect the final and punctual mass movement. This model is later confirmed by Piper et al. (1999), evidencing transformations from slides to debris flow and

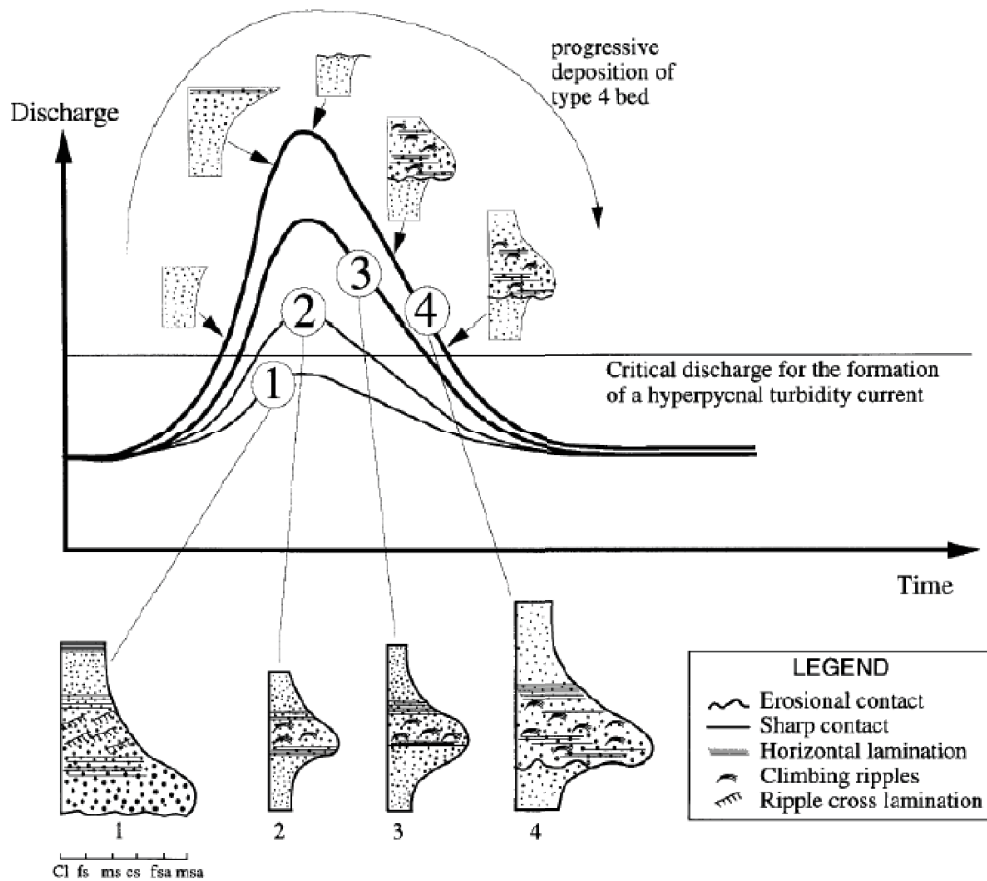


Figure 2.5: Sequence and facies of a hyperpycnal deposit according to the charge and discharge of the river during flood (after Mulder et al., 2003)

finally into turbulent flows in the east Canadian margin.

A slide will evolve into a debris flow if 1) the sediment mass has a clay content, 2) if during the sliding phase the grain agitation is high enough to destruct the sliding mass and 3) if there is water incorporation during the flow. The progressive destruction of the slide will facilitate the water incorporation that will reduce the strength and then generate internal displacements. The debris flow is created. The transition between laminar flow and turbulent flow will need a dilution of the laminar flow (Hampton, 1972).

2.1.3 Turbiditic systems architecture

Turbiditic systems have been discovered tardily and represent important financial interest for oil exploration. As such, they have been extensively studied during the last decades. The improvements of technical methods, highly supported by the oil exploration, have favored the relatively good knowledge of the deep-sea turbiditic systems. However the actual concepts and

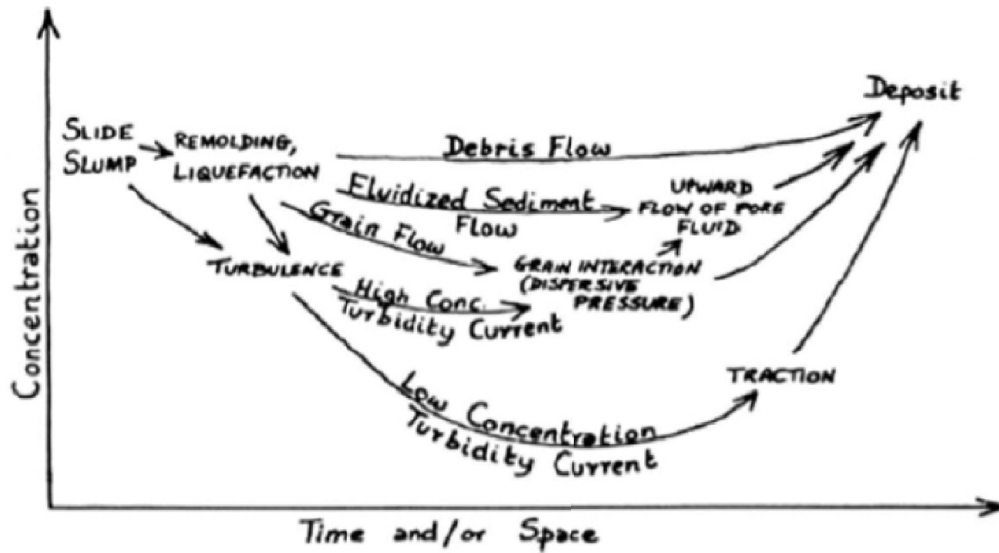


Figure 2.6: Possible evolution of mass transport processes relative to space and time (after Middleton and Hampton, 1973)

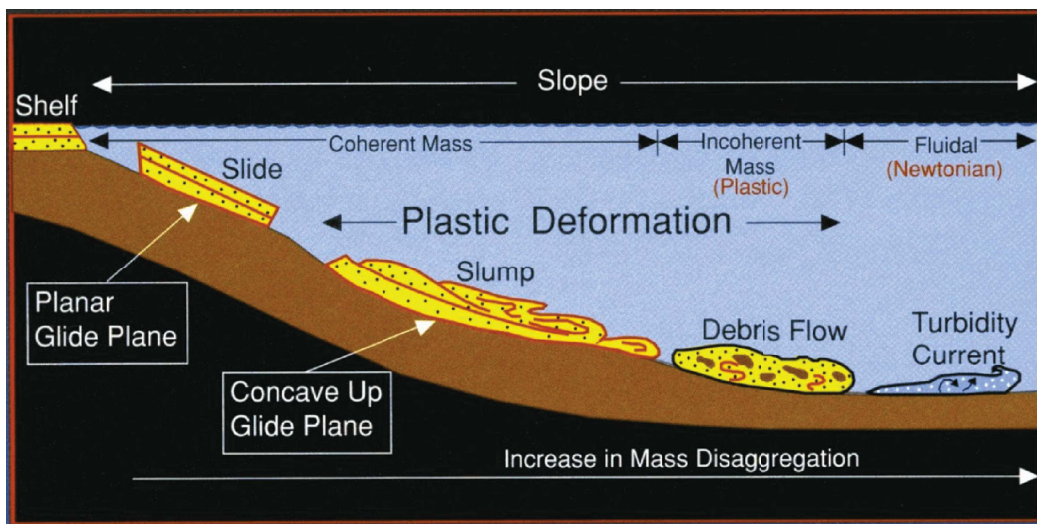


Figure 2.7: Evolution from a mass slide to gravity flow (i.e turbidity current) (after Shanmugam et al., 1994)

hypothesis suffer from a lack of direct observations. They are only available on the ancient systems based on seismic profiles.

Turbiditic systems correspond to systems that transport and accumulate sediments from the continental shelf to the abyssal plains. Their high sedimentation rate and high sediment accumulation may represent important hydrocarbon reservoirs. Also, the sedimentary flow dynamics that shape these systems are usually initiated by extreme events (earthquakes, storms) and may represent natural hazards for offshore infrastructures (e.g, telecommunication cables breaks off western Taiwan after the 2006 Pingtung earthquake) or coastal hazards (e.g, tsunami). Sev-

eral morphological units are produced according to two types of turbiditic systems: channelized system and non-channelized system (Fig.2.8).

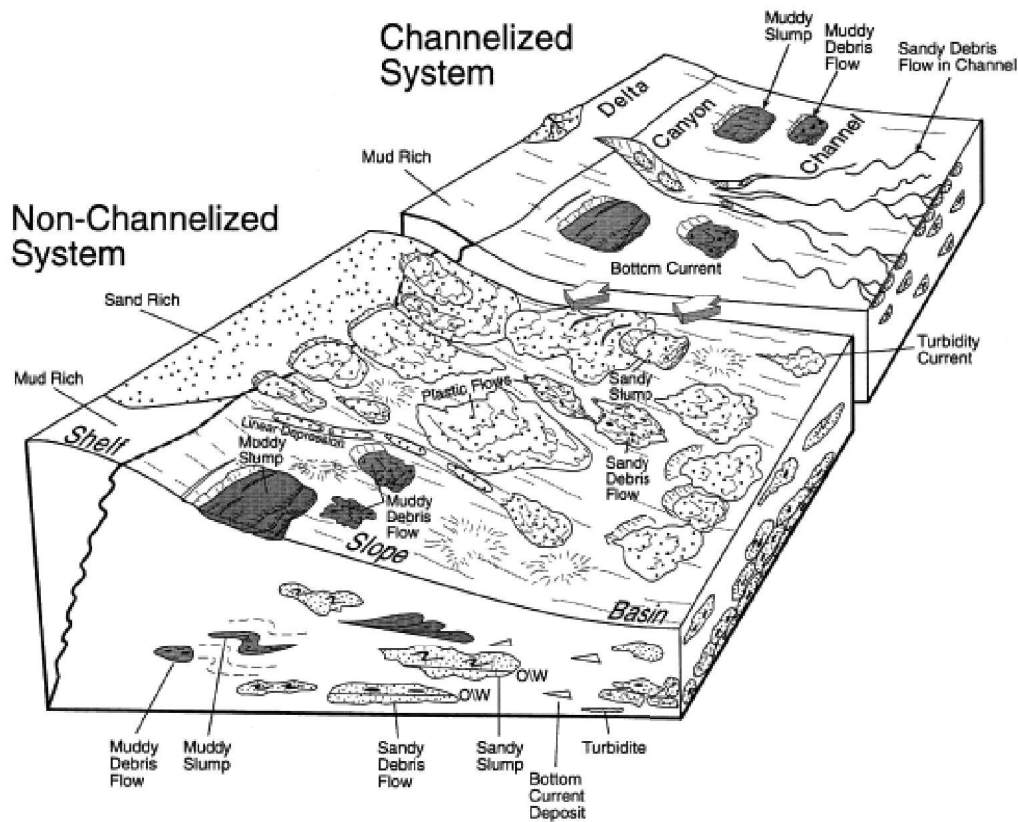


Figure 2.8: Theoretical depositional model for channelized systems and non-channelized systems (after Shanmugam, 2000).

Non-channelized systems are generally generated by punctual and local slope failures. Thus, the sediment supply is not high or constant enough to build a well developed turbiditic system. These systems include three zones: 1) a failure zone with one or several headscarp, 2) a bypass zone and 3) a depositional zone that is often assimilated to a depositional lobe. They are generally known as slope apron (Reading and Richards, 1994). Conversely, if the sediment supply is constant and high enough (e.g connection to a river mouth), the system evolves into a channelized system. The sediment flows are channelized from a canyon to channel system to finally reach a depositional zone (i.e, distal lobe). These systems belong to submarine fan and ramp defined by Reading and Richards (1994).

2.1.3.1 Canyons and gullies

Many studies have been carried out since the discover of the **submarine canyons**. These erosional features, ensure the transfer of sediment toward the abyssal plains. They have a

characteristic V-shape morphology, usually found between 500 m to 3000 m water depth and are up to 100 km long (Normark and Carlson, 2003) (Fig.2.9). A submarine canyon usually have an upstream part called **head** that constitutes the zone of intense erosion on the continental slope and able to incise the continental shelf. Submarine canyons may be fed in their upstream reaches by a gully network or immature erosional features on the continental slope (Fig.2.10). The main part of a submarine canyon called **body** constitutes the zone between the head and the bottom of the slope or the trench in the case of an active margin. The length of the body is variable and may reach several hundred kilometers. The morphology is characterized by a decrease of the slope compared to the head with an average of 2° (Gaudin, 2006; Arzola et al., 2008). The incision is V-shaped and progressively evolve downstream to a U-shape. The relief of the incision may reach more than 1000 m (e.g, Taitung Canyon, offshore eastern Taiwan). The slopes of the flanks are usually steep and reach up to 45° , with an average of 25° . The most upstream part of a submarine canyon corresponds to the **outlet** (Fig.2.9). The outlet is characterized by a valley usually wider than the body of the canyon and a progressive decrease of the slope reaching up to 0.5° (Babonneau et al., 2002). Downstream, the outlet may develop a channel-levee system and/or distal lobes (Galloway, 1998).

Gullies, are relatively linear with narrow width submarine valleys (from 100 to 200 m) (Fig.2.10). They are located on the continental shelf or the continental slope. They are usually not connected to a fluvial system. Where erosion dominates these features, may spatially evolve with time. Their origin are often attributed to instabilities on the edge of the continental shelf such as **slides** or **turbidity currents** (Izumi, 2004).

2.1.3.2 Channels-levees complexes

Channel-levee system is the area where erosion and deposition processes interact (Fig.2.11). It is usually developed downstream of the outlet of submarine canyon.

Deep-sea channel morphology is controlled by erosion and deposition by turbidity currents. Two types of channels may be observed: incising channels (erosive) (e.g. Zaire, Babonneau et al., 2002) and constructive (aggrading) (e.g. Amazon, Flood et al., 1991). Erosive channels are V-shaped, with small or no existent levees because the sediment spilling is not important enough to build them. The morphology of depositional channel is highly influenced by the nature of the transported sediment (Piper and Normark, 2009). The channels that transport coarse material (sand or gravel), are wide and straight. In general they do not build levees. In contrast, the channels that transport fine-grained material are narrow and sinuous (or meandered). They are

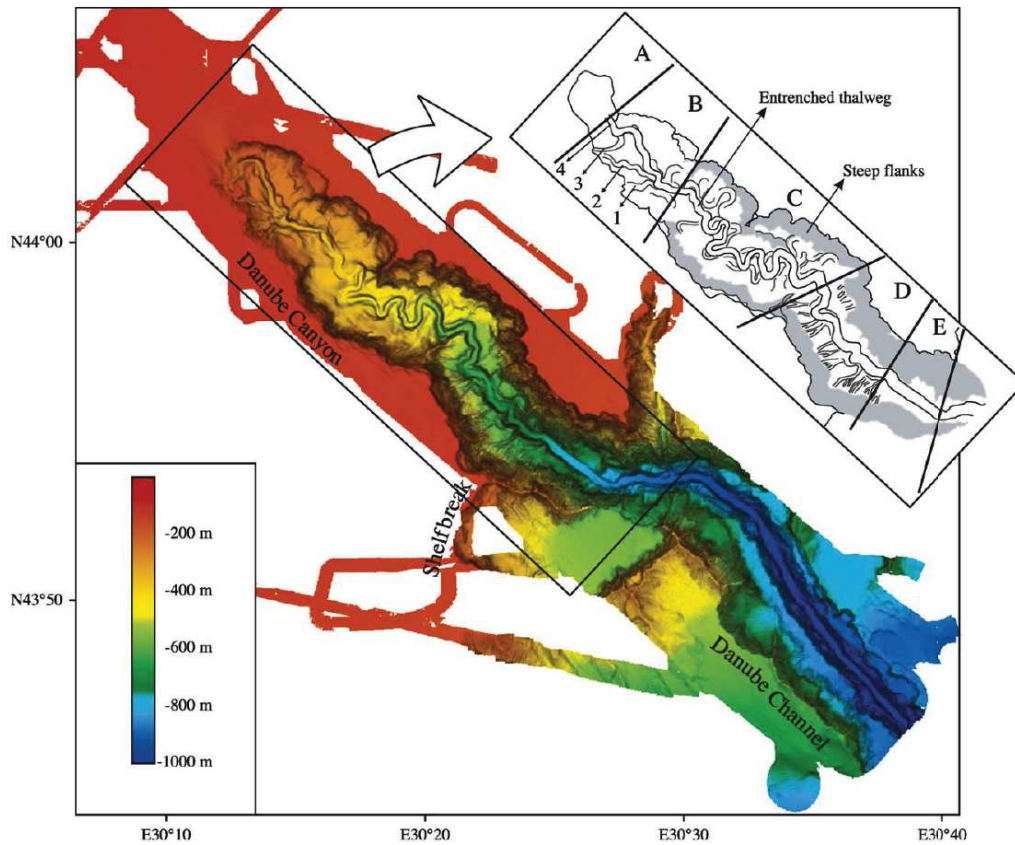


Figure 2.9: Bathymetric 3D map of the Danube canyon (after Popescu et al., 2004)

deeply incised and build well-developed levees.

Sedimentary levees are built by overspilling of the fine fraction of a turbidity current. Their extension may reach 50 km from the channel axis. The levees are asymmetric on their flanks. The internal flank (channel side) display a steep slope experiencing erosional processes. The external flanks of the levee, display gentle slopes and correspond to depositional processes. Sedimentary levees are often characterized by sedimentary waves (Normark et al., 2002). The levees constitute a complete record of turbiditic events and are good archives to investigate turbiditic systems.

2.1.3.3 Lobes

Lobes represent the distal part of the turbiditic systems. They are mainly built by sand accumulation because of the loss of the fine grain fraction deposited in the complexes described above. These complexes formations may be also built by accumulation of sub-lobes sometimes channelized (Bonnell, 2005).

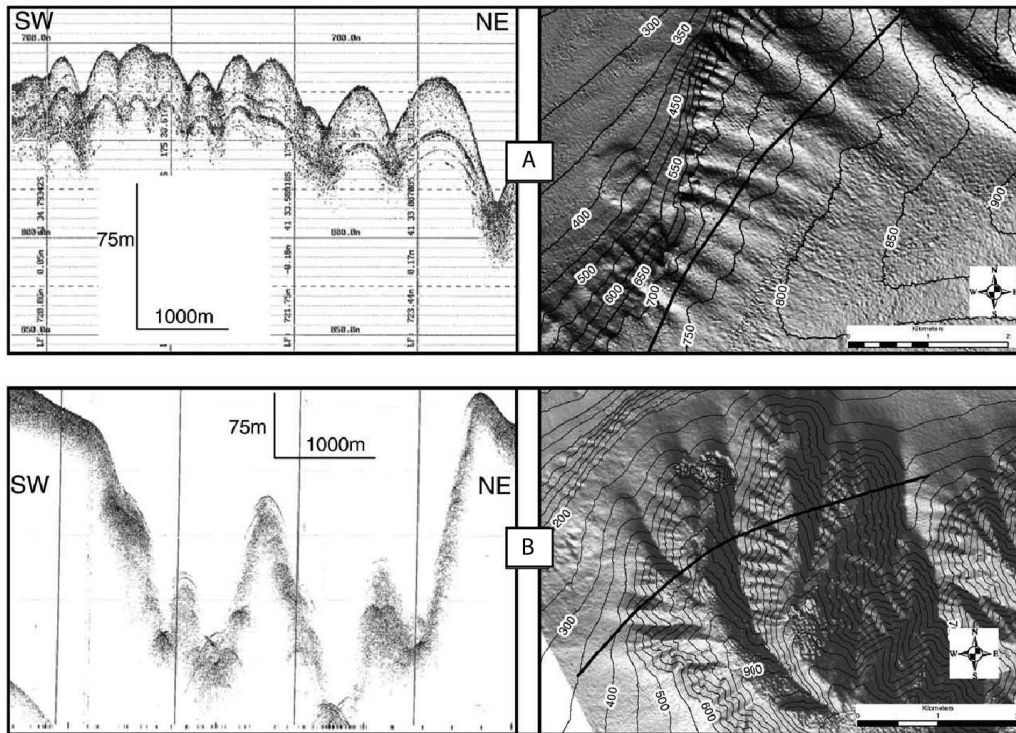


Figure 2.10: Example of A: subdued gully system showing 3.5kHz profile (left) and shaded relief map (right); B: Angular gully form showing 3.5kHz profile (left) and shaded relief map (right) (after Mountjoy et al., 2009)

2.1.4 Controlling factors of turbiditic systems

Several factors influenced the development of the turbiditic systems. Stow et al. (1985) consider four factors: tectonics, nature of sediment supply, climate and sea-level variations. These parameters interact and may be variable in space and time. They lead to build turbiditic systems with variable architectures, geometries and sedimentary facies. Although these parameters are difficult to quantify, they confer a better understanding of the architecture of these systems (Bouma, 2000).

The **tectonic activity** will affect the whole turbiditic system from the source to the abyssal plain. Tectonics is a first order factor that will influence the type and nature of sediment. It will influence the uplift rate, the denudation and erosion rates, the onland drainage network, and also the morphology of the drainage basin. A "young" and active mountain belt characterized by a high surrection rate, will favor important erosion and important volume of sediment supply from the drainage basin. This supply will be even higher if the reliefs are under the action of a "humid" climate (i.e tropical climate). A characteristics of the drainage basin is the

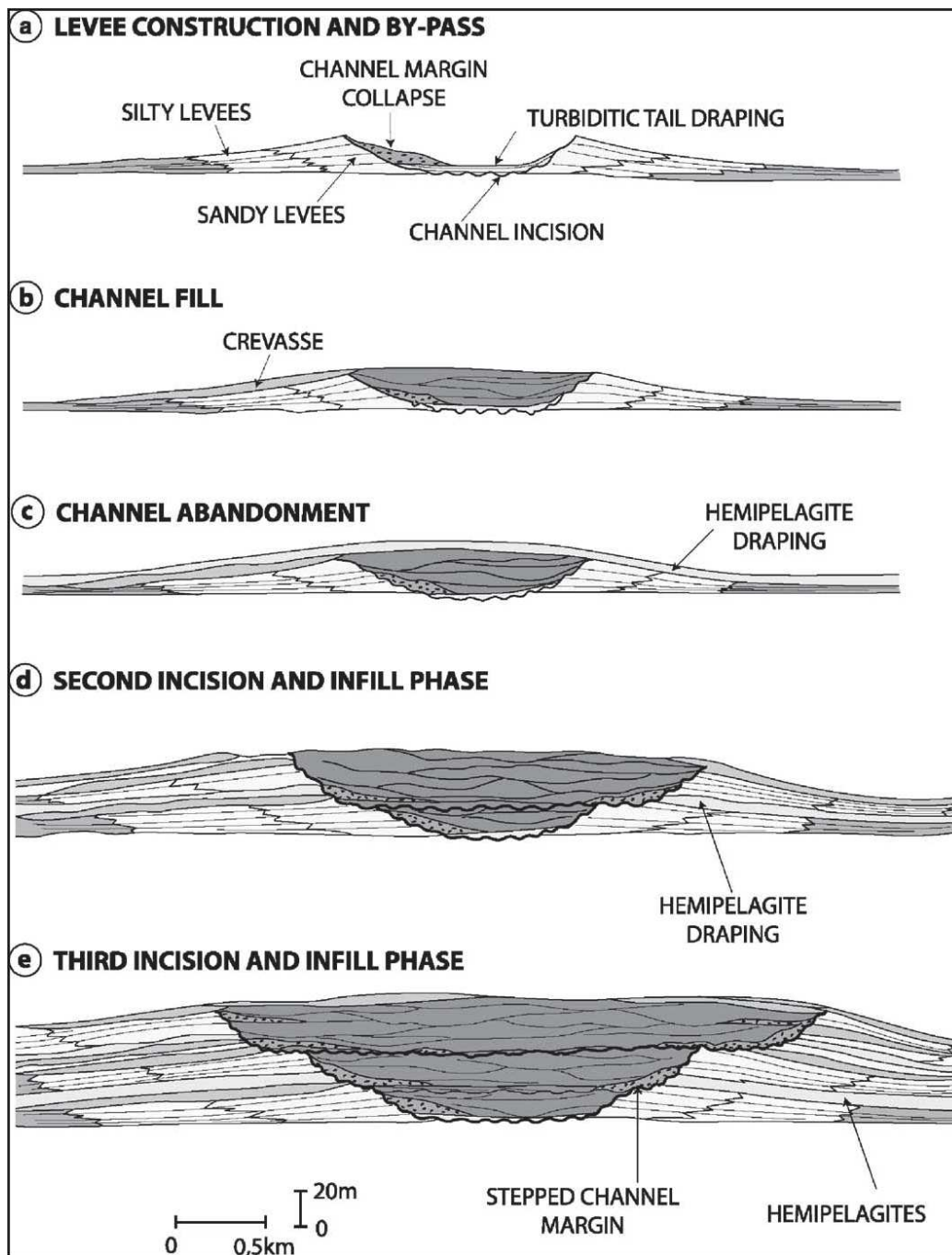


Figure 2.11: Genetic model of channel-levee complexes (after Eschard et al., 2003).

distance between the source (relief) of the river outlet and the slope. A sedimentary source close to the coastline will reduce the capacity of sediments to accumulate in the continental domain (i.e. active margins). This configuration is prone to the development of turbiditic systems that mainly transport coarse material (Bouma, 2000). In contrast, in large continental domain where the distance source/slope is important, sediments accumulate in the continental domain (i.e passive margins). In such contexts, the turbiditic systems built are fine-grained rich (Bouma, 2000). The brutal variations of the drainage basin dynamic are also respon-

sible of important changes in the nature and volume of sediment supply to the turbiditic system.

At the river mouth, sediments shall transit through the continental shelf before they reach the deep-sea domain. The width of the continental shelf and also the presence of submarine canyons are thus determinant factors. The continental shelf is more or less developed according to the type of the margins. In the case of active margins, the continental shelf is usually narrow and favor the direct input of sediment supply to the slope. In contrast, in the case of passive margins, continental shelves are wider and well developed, consequently limiting the propagation of sediment to the slope. Submarine canyons will also facilitate the supply to the turbiditic systems. The supply is continuous from the river mouth to the head of the canyon. Most of the turbiditic systems are developed in confined basins in active margins in opposition to the large deep-sea fan systems developed in the passive margins. Regional tectonics is often involved in the genesis of these confined basins. For example, in the fore-arc domain of the active margins, the tectonics provide a regular and abundant supply in the confined basins where turbidites sequences are accumulated.

The **climate** has a significant influence on the erosion of the reliefs, transport and sea-level variations. [Litchfield and Berryman \(2005\)](#), propose that the nature and the volume of sediment are directly linked to climatic variations that affect the drainage basins. During glaciation, the erosion of the relief is favored because of the weak vegetal cover. However, the sediments are accumulated in the fluvial systems to build aggradational terraces. In contrast, during interglacial periods and despite a developed vegetal cover, the incision of the rivers and transport of sediments are favored. Therefore, a significant volume of sediments are transported to the turbiditic systems. Beside long-scale climatic events, punctual phenomena may also provide a large amount of sediments (i.e large storms, typhoons..) and generate for example, hyperpycnal activity that directly supply turbidite systems ([Mulder et al., 2003](#)).

2.1.5 Initiation of turbidity currents

Mass movements may be triggered in response to catastrophic events such as earthquakes, floods, tsunamis. When analyzing the sedimentary archives, it is possible to extract the chronology relative to these extreme events. Turbidites appear to be the most interesting deposits because they are extremely sensitive to the extreme events mentioned above. Pale-

oseismic and paleoclimatic archives are thus available (Beck, 2009; Goldfinger et al., 2003). The main triggering mechanism for mass movements are synthesized in the figure Fig.2.12. A turbidite may be triggered either by a turbidity current *sensu lato* that evolved from a slope failure (Middleton and Hampton, 1973; Piper et al., 1999), either by a density current (i.e hyperpycnal flow) (Mulder and Alexander, 2001). Slope instabilities (slope failure, such as slides or slumps) are known to evolve to turbidity currents (Piper et al., 1999). They occur in deep-sea environment below the continental shelf. The stability of the slope will depend in the first order, on the slope gradient and the nature of the sediments.

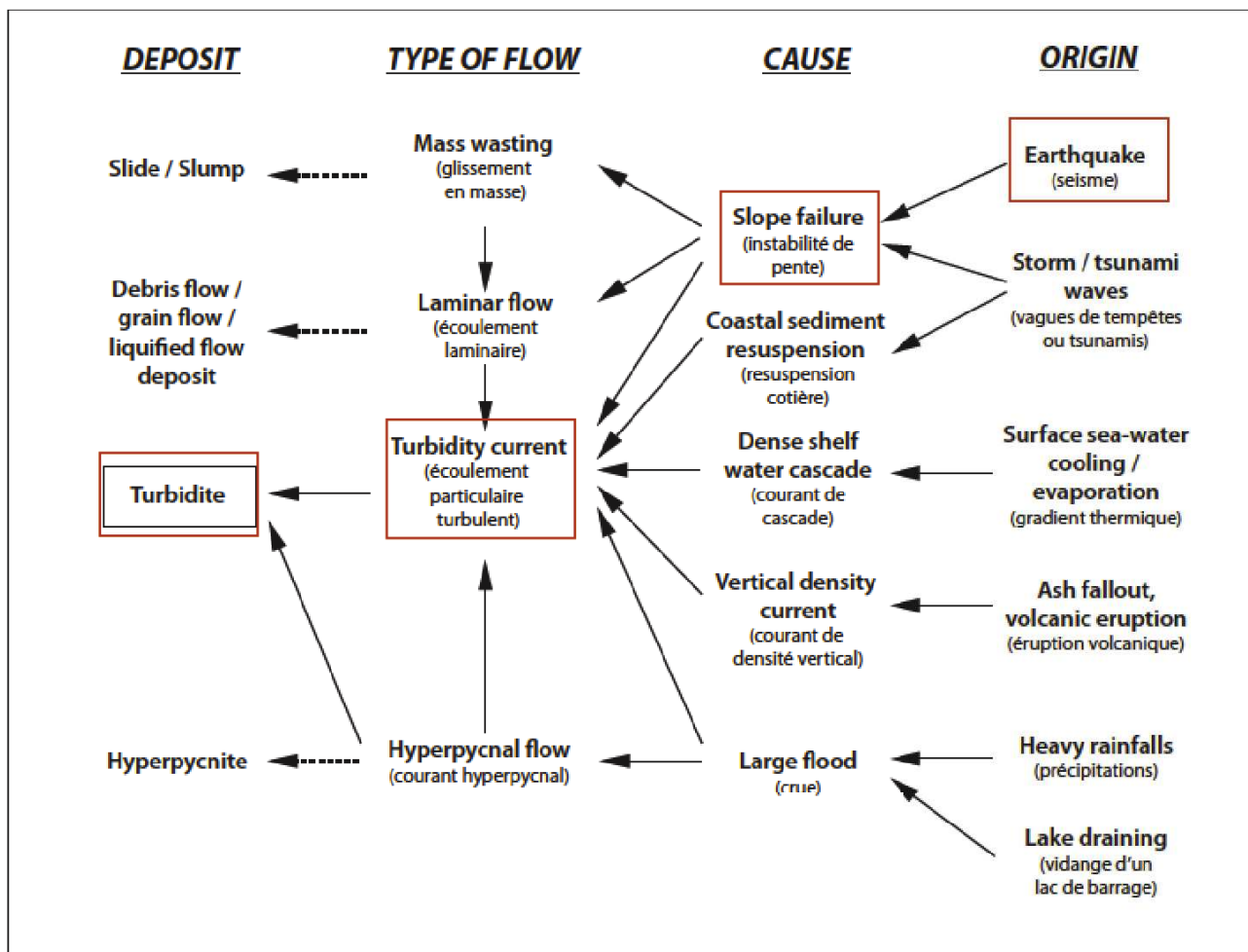


Figure 2.12: Model of triggering mechanisms of mass movements showing interactions between origin, cause, flow and deposit. Red boxes emphasize the processes that will be developed in this work, from the origin to the deposit (modified after Poudroux, 2011).

Earthquakes are considered as the main trigger mechanisms for slope instabilities. Turbidity currents have been associated to instrumental and historical earthquakes affecting active margins, *e.g.* Taiwan, (Huh et al., 2004); Japan, (Noda et al., 2008); Cascadia margin, (Goldfinger

et al., 2003); South Portugal, (Gràcia et al., 2010); Greece, (Polonia et al., 2013); New-Zealand (Pouderoux et al., 2012; Barnes et al., 2013). These examples suggested that a large earthquake (i.e, $M > 6.8$) is necessary to trigger mass failure and turbidity currents. However, more than the magnitude, the intensity or the *Peak Ground Acceleration* (PGA) on the continental slope will control its instability during an earthquake. The PGA depends on the magnitude and the distance to the epicenter (Lee and Edwards, 1986). The PGA threshold will also depend on the nature of the substratum (e.g. site effects, sediments vs rocks) and may have a value comprised between 0.08 and $0.6g$ (g is the gravitational acceleration) (Dan et al., 2009; Lee et al., 1999; Huh et al., 2004; Noda et al., 2008; Strasser et al., 2007).

2.2 Study area and coring strategy

According to the previous observations and in regard of the possible triggering mechanisms of mass movements, it appeared crucial to carefully choose the study area and the cores locations in order to reach up our objectives.

We thus aimed to sample offshore eastern Taiwan because it is prone to study mass movements relative to seismic activity: a) it is the most active area (most of the magnitude 7 earthquakes occurred in that area), then susceptible to trigger slope instabilities, b) the submarine morphology displays steep slope gradients, essential parameter to generate instabilities, c) the sediment supply is extremely high ($\sim 150 \text{ Mt.yr}^{-1}$, Liu et al., 2008).

Then, using several types of available data (bathymetry, back-scatter imagery, 3.5 kHz, Multi-Channel Seismics), we first have determined core sites fitting our objectives but also satisfying logistical criteria (such as maximum depth of surveying). We divided our sampling into three types of targeted sites:

- **Reference cores sites:** in order to get well-preserved records of the hemipelagic sedimentation we chose an area without influences from both typhoons and earthquakes (high bathymetric point, sites distant from canyon system or subject to instabilities).
- **Paleoclimatological cores sites:** to obtain the record of turbidites triggered by typhoons, we chose areas located on levees systems of canyons or channels where the accumulation of sediment is the greatest and well preserved from the remobilization of sediments

initiated by earthquake shaking.

- **Paleoseismological cores sites:** to obtain the record of paleo-seismicity, we select areas able to trap sediments originated from instabilities triggered by seismic events. We thus favor areas such as perched basins adjacent to steep slopes sheltered from terrestrial input.

When selecting the cores locations, we also took into consideration the depth of the sites. First all sites greater than 4000 m deep were excluded. Indeed, the Carbonate Compensation Depth (CCD), is the depth in the oceans below which the rate of calcium carbonate is behind the rate of solvation, thus no CaCO_3 is preserved. The CCD depends on the solubility of CaCO_3 which is determined by the temperature, pressure, chemical composition and oceanographic conditions of the oceanic waters. Nowadays, the in the Pacific Ocean the CCD is about 3500-4500 m with local variations, except beneath the equatorial upwelling zone where it reaches about 5000 m. The CCD will thus preclude the possibility for dating the hemipelagic fraction using ^{14}C dating. At such a depth, the foraminifera tests (organisms used for ^{14}C) will be affected by CaCO_3 dissolution.

We also excluded, in respect to logistical criteria, sites greater than 3000 m below sea-level. In fact, we initially planned to conduct a survey using a deep-two side-scan sonar, in order to acquire complementary chirp data to help in the coring site selection process. Equipment such as deep-tow side-scan sonar may be only used down to 3000 m below sea-level and has to be maintained 30-50 meters above the seafloor. Unfortunately, for technical reasons this survey have not been conducted.

2.3 Coring sites

We will further consider three study zones (Fig.2.13): 1) The Ryukyu forearc zone, 2) the Luzon volcanic arc zone and 3) the Southern Longitudinal Trough (Fig.2.13).

1. **The Ryukyu forearc zone** corresponds to the forearc basin of the western termination of the Ryukyu subduction zone. This area suffers from an intense tectonic and seismic activity (Malavieille et al., 2002; Theunissen et al., 2010; Lallemand et al., 2013). We thus focused on sampling to maximize the record of paleo-earthquakes. For that purpose, we selected isolated sites and enough from major continental sediments supply. Two cores sites have been selected: **KS09** is located on an isolated terrace at the bottom of the slope of the Ryukyu arc (Fig.2.14), at 2900 m water depth. The slope of the arc uphill of this site reaches $\sim 6-7^\circ$. In KS09 acoustic facies are characterized by deformed and stratified reflectors on the chirp line, suggesting sediment deposition and accumulation (Fig.2.15A). Because of the intense tectonic and seismic activity, this area is prone to slope instabilities as seen on Fig.2.15. Indeed, superficial submarine landslides affect the slope of the Ryukyu arc. We thus considered that KS09 site is a good candidate fitting the objective of the record of paleo-earthquakes. Site **KS08** is located at 2800 m below sea-level, northward KS09, on an isolated terrace adjacent to the slope of Ryukyu arc (Fig.2.14). The slope of the Ryukyu arc near that site, is dipping about $\sim 11^\circ$ (Fig.2.14). The acoustic facies of KS08 site display stratified reflectors also suggesting sediment deposition and accumulation. Slope failures also affect the slope of the Ryukyu arc in that area as shown in the Fig.2.15. As such, KS08 has been selected as a candidate for the record of paleo-earthquakes. Also, **KS08** is located near the site **BC18** of Huh et al. (2004) (Fig.2.13). Their study has shown that in that area it is possible to record paleo-earthquakes using turbidite records. Therefore, we selected KS08 site in order to be calibrated our results with those of Huh et al. (2004).

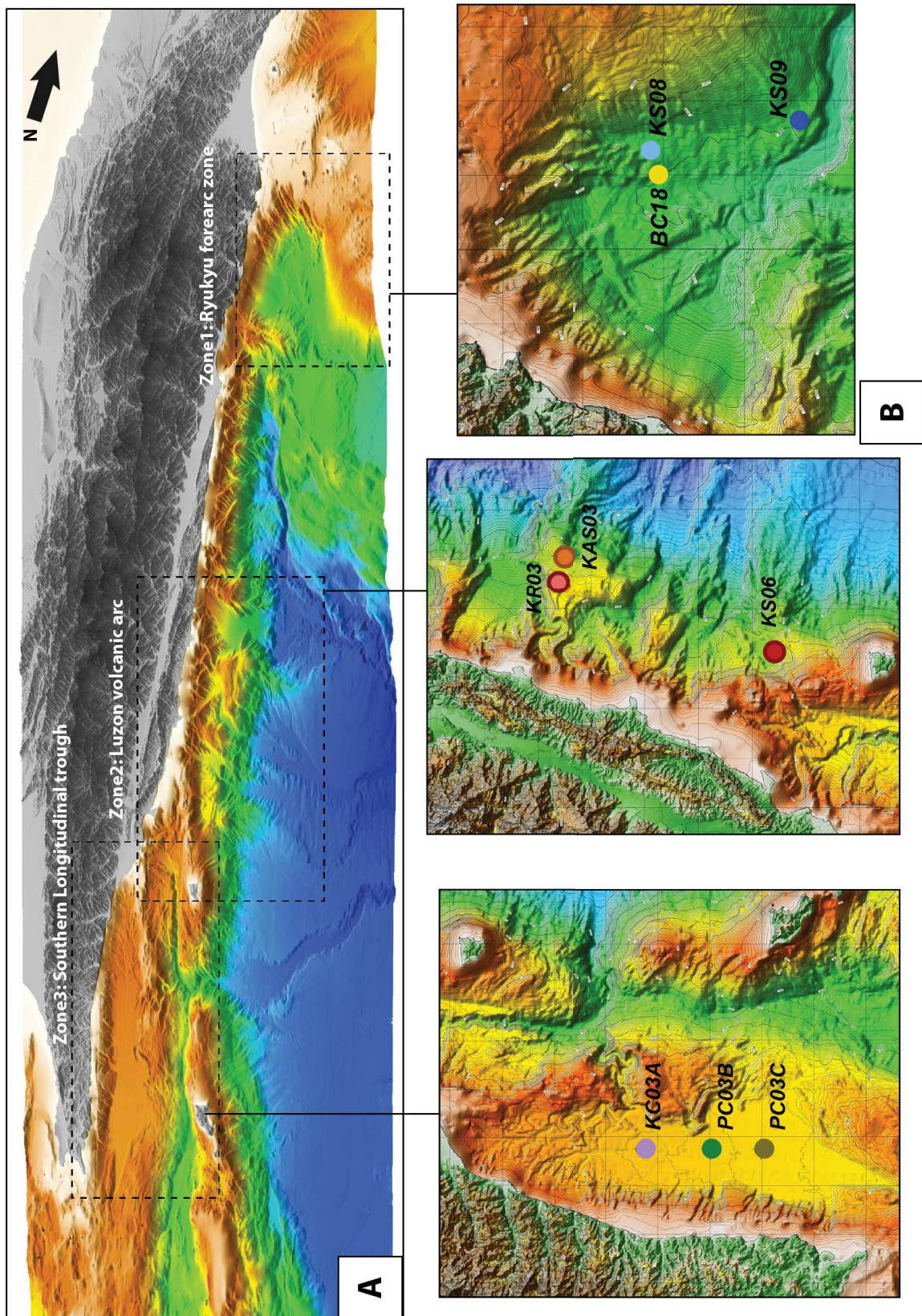


Figure 2.13: A: perspective view of eastern Taiwan viewed from the east. The three dashed-lined boxes show the three zones chosen for this work. B: DEMs showing zooms of the coring site; colored dots show the sedimentary cores collected during OR1-1013 and OR1-1048. The yellow dot corresponds to the box-core from the study of Huh et al. (2004).

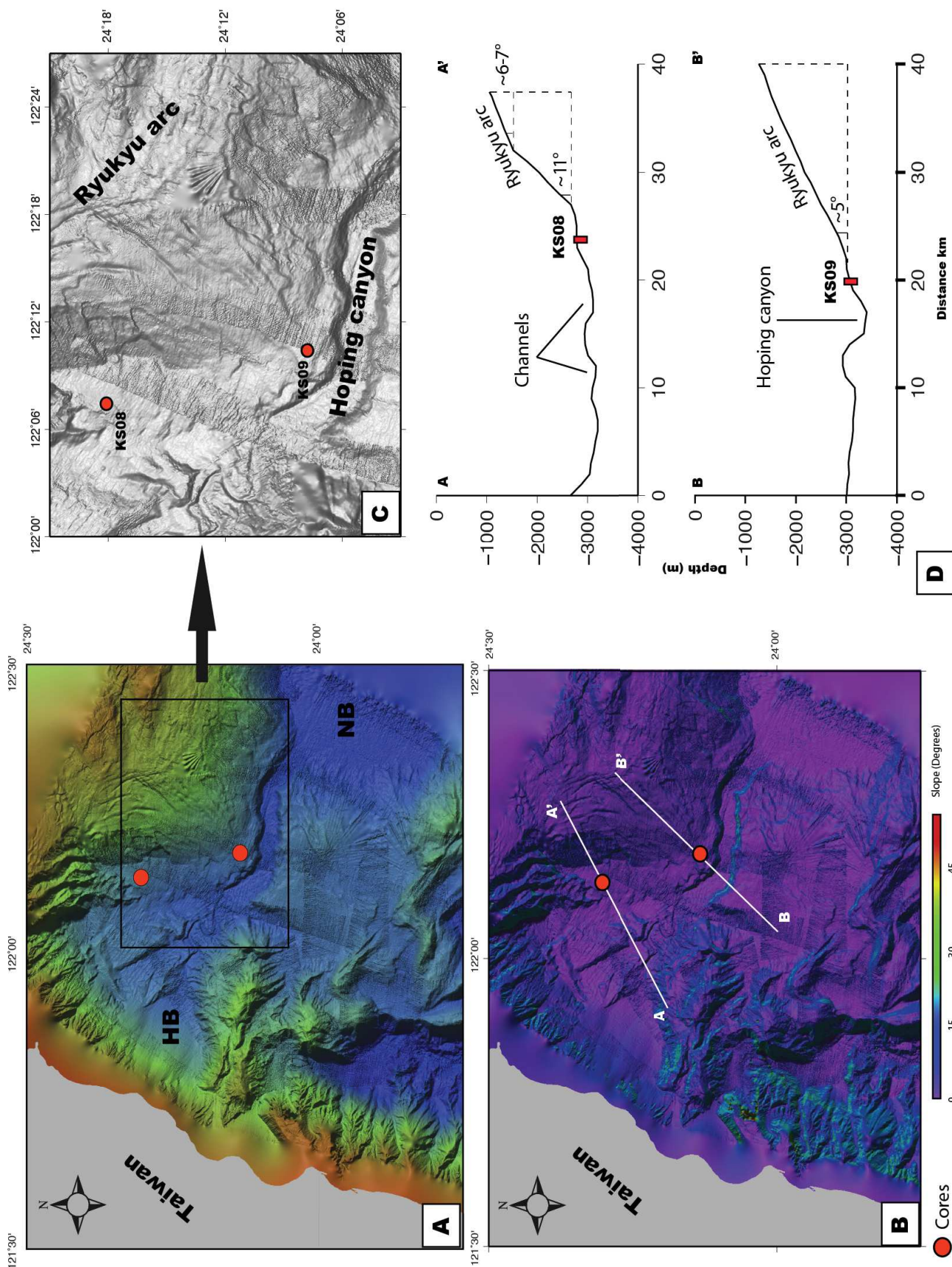


Figure 2.14: A: DEM of the Ryukyu arc core site; B: slope gradient map of the core site, lines show bathymetric profiles shown in D; C: closer view on DEM of the KS09 and KS08 location; D: bathymetric profiles of the core sites, showing the surrounding slopes adjacent KS09 and KS08 sites.

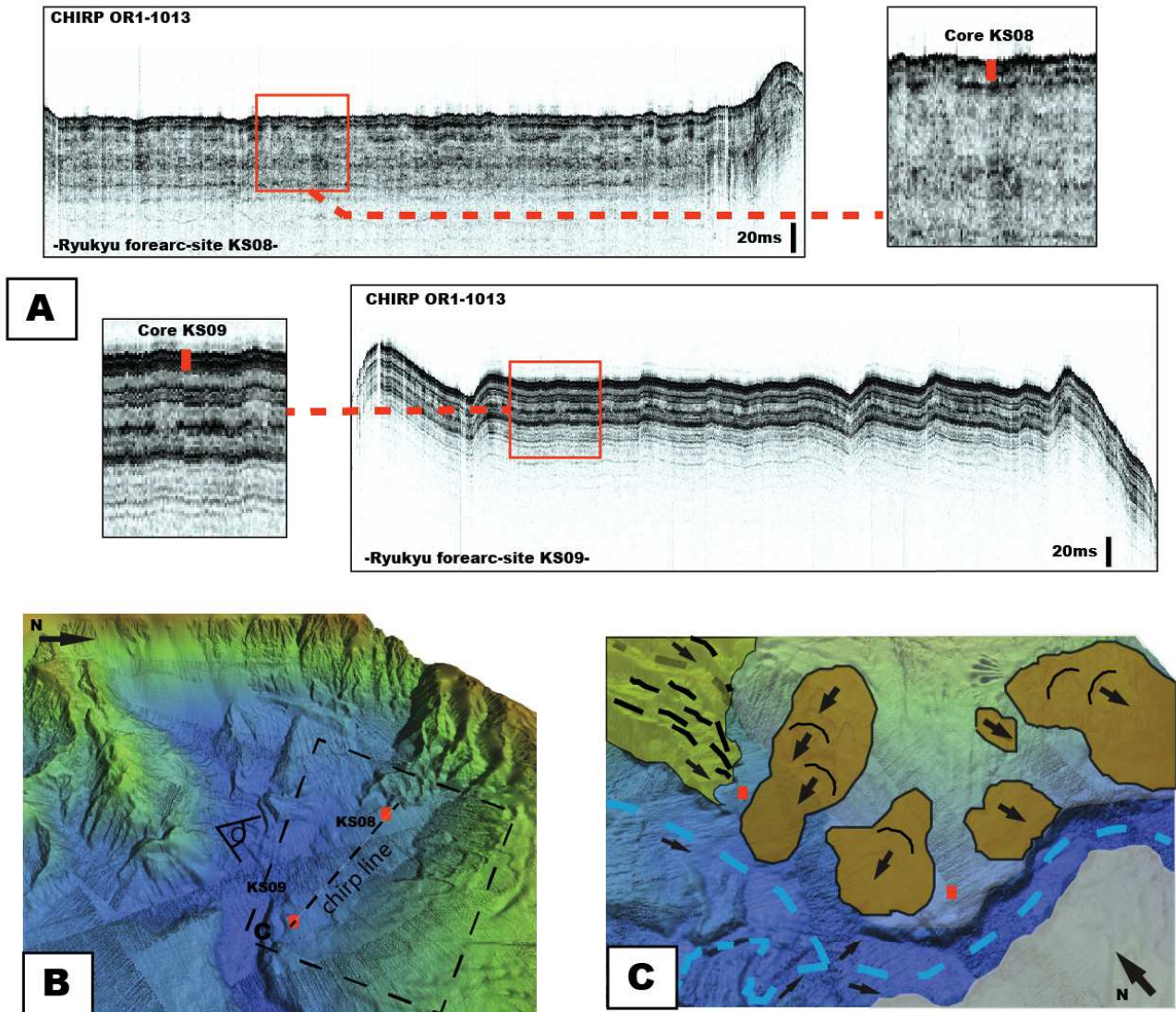


Figure 2.15: A: chirp profiles across KS08 and KS09 sites; B: perspective view of the core site, lines show the chirp profiles shown in A; C: perspective view showing slope failures on KS09 and KS08 sites.

2. **The Luzon volcanic arc zone** corresponds to the well developed collision zone of the Luzon arc with the Chinese continental margin. There, we selected sites to obtain the record of paleo-earthquakes and also to obtain the record of the background sedimentation (reference core). **KS06** is located northward Lutao Island, in an small isolated basin at mid-slope of the colliding Luzon arc (Fig.2.16). The seafloor at that site is reaching 1947 meters water-depth. The basin is completely disconnected from any major drainage system (Fig.2.16). The slopes surrounding the basin range from 8 to 17° (Fig.2.16). Seismic and chirp profiles acquired across the basin express strong reflector at seabottom and well-stratified reflectors in depth indicating basin fill sediments (Fig.2.17). Since this area is very active, we suspect that this site is prone to slope instabilities triggered by earthquakes as identified northward KS06 site on Fig.2.17 and may constitutes a suitable location for paleoseismic purposes.

About 50 km northward, **KR03** is located on a bathymetric high between canyons at 1205 m water depth. Therefore, this site should not be affected by the path of turbidity currents (Fig.2.18). Seismic profile shows stratified reflector suggesting sediment accumulation reaching about 1,5 kilometers thick above the basement of the colliding Luzon arc (Fig.2.19). **KR03** site thus represents a good candidate for the record of background sedimentation. Five-hundred meters downslope, **KAS03** is located on a isolated terrace at 1700 m water-depth (Fig.2.18). This site is sheltered from the paths of terrestrial input and should mainly record slope instabilities of the surrounding slope triggered by earthquakes. Five cores were retrieved from these 3 coring sites during the OR1-1013 and OR1-1048, using piston corer, gravity corer and box-corer (Fig.2.13, Table 2.1).

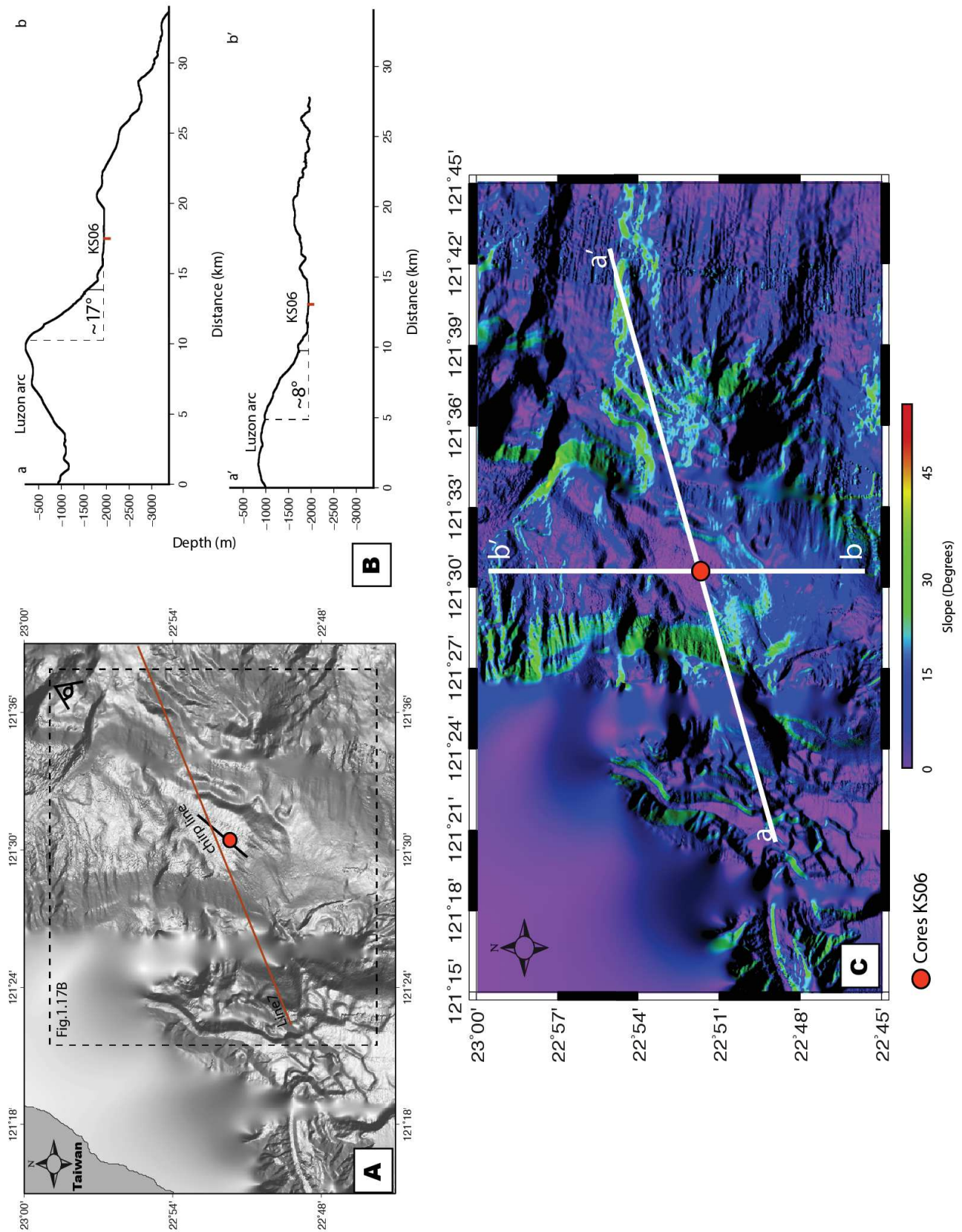


Figure 2.16: A: Detailed DEM of KS06 site, red dot show the coring site, lines display seismic profiles shown in Fig.2.17; B: bathymetric profiles across the core site, showing the surrounding slopes on KS06 site; C: slope gradient map around KS06 site.

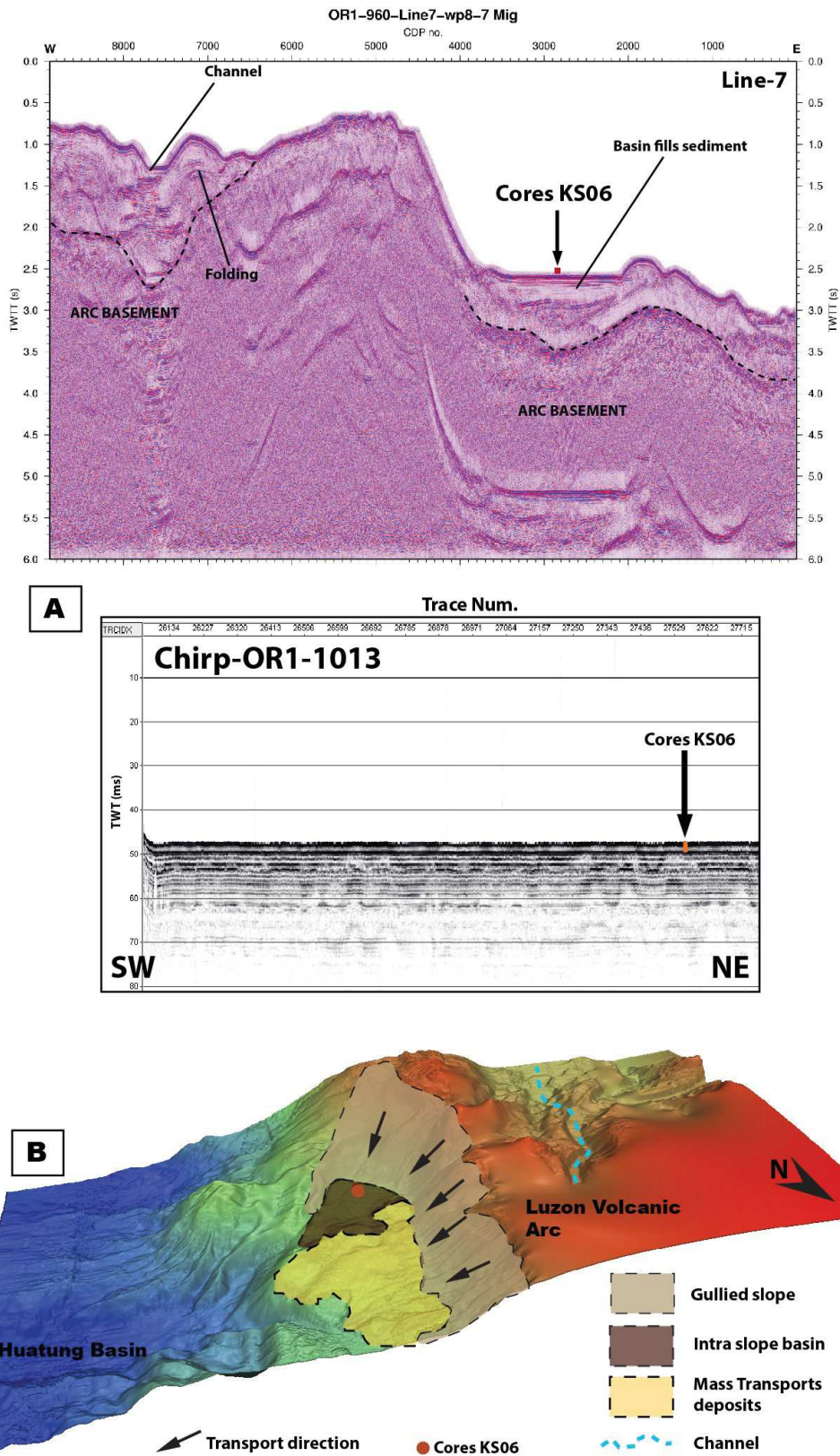


Figure 2.17: A: MCS profile and chirp profile across KS06 site. B: perspective view of KS06 site, showing the slope instabilities in that area.

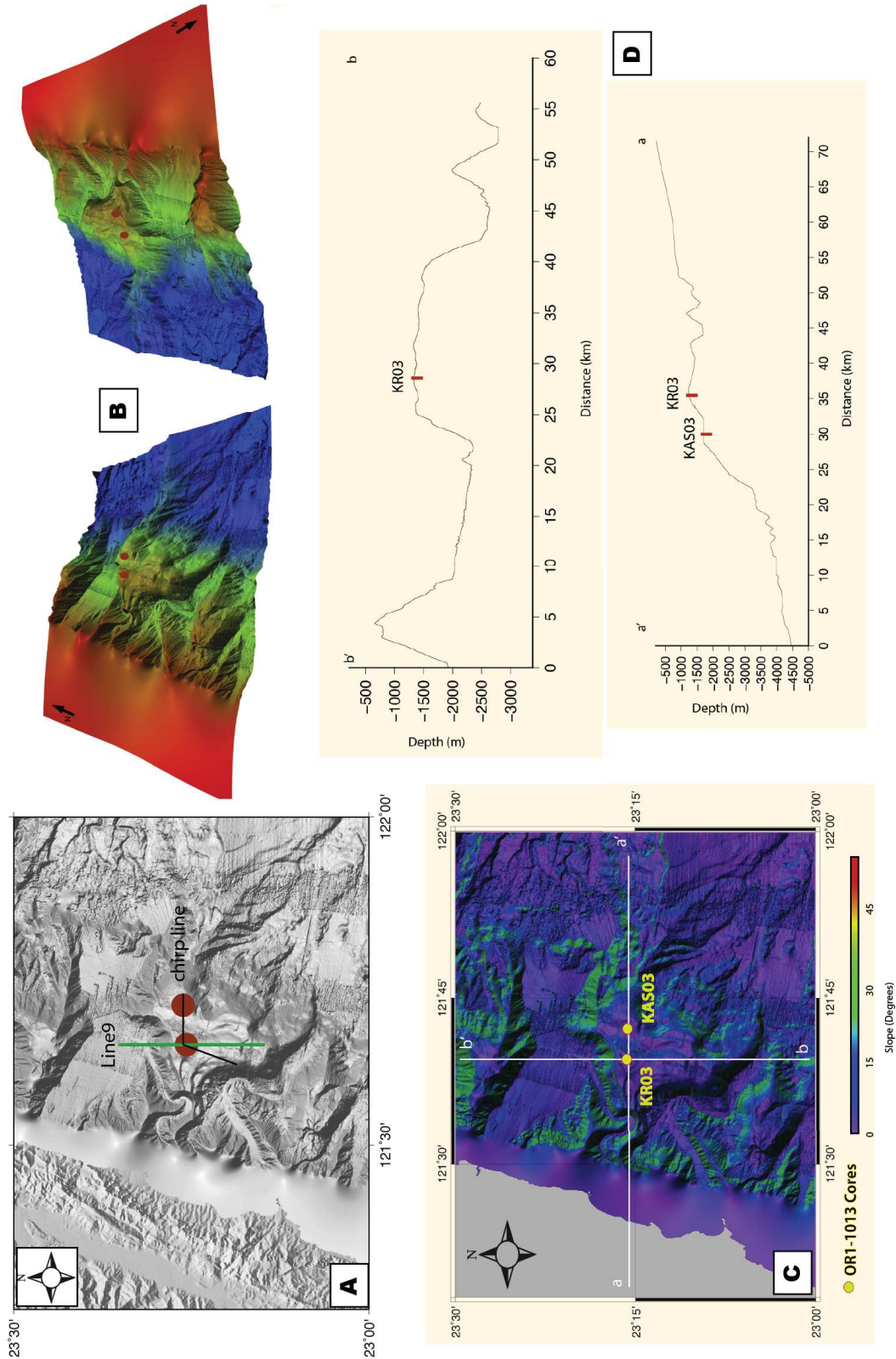


Figure 2.18: A: detailed DEM of the core site, red dots show the core locations and lines location of seismic profiles shown in Fig.2.19; B: perspective view of the core site to highlight the isolated topographic high where was collected KR03 and the isolated terrace where was taken KAS03; C: slope gradient map of the core site. The lines show bathymetric profiles; D: Bathymetric profiles S-N and W-E respectively of the core site.

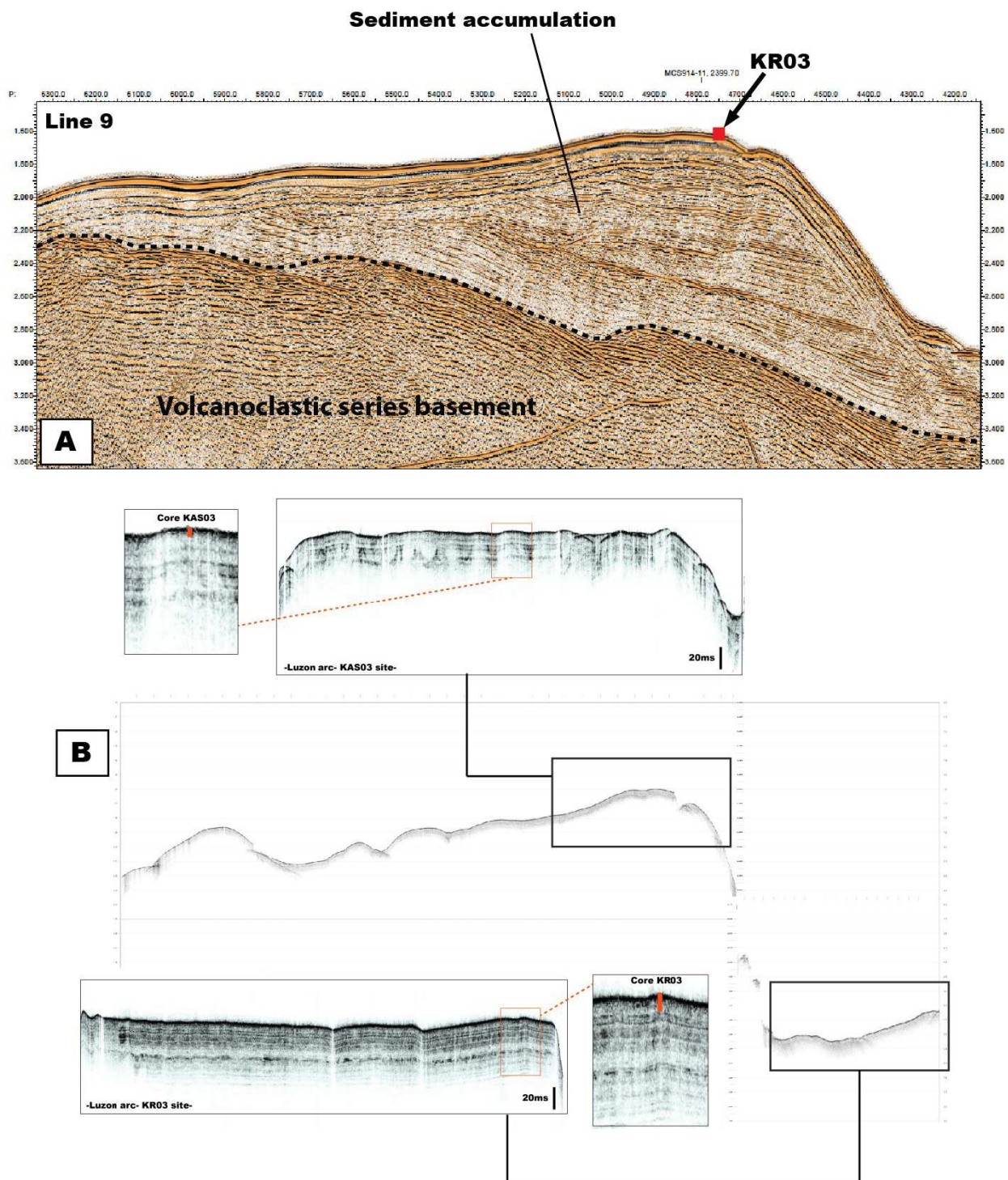


Figure 2.19: A: MCS profile across the topographic high where we selected KR03 site to record the background sedimentation. Note the 1.5 km sediment pile that layered above the basement (probably the volcanoclastic series of the Luzon arc). B: chirp profile across KAS03 and KR03 core sites.

3. **The Southern Longitudinal Trough** (SLT hereafter) represents a proximal orogenic basin (Malavieille et al., 2002). There, we selected sites to mainly obtain the record of climatic events such as turbidites deposited after storms or typhoons. The SLT is directly connected and fed by rivers onland from both its northern part and the gullied slope on the eastern part (Fig.2.20B). The SLT is characterized by a turbiditic system with well developed channel-levees complexes (Fig.2.20). We selected three sites that represent good candidates to record past climatic events. These sites are located between 1160 m and 1272 meters water depth. **KC03A** site is located on a sedimentary levee whereas **PC03B and C** are located on the continuity of the main axial channel (Fig.2.20).

Note:

Following the coring strategy described above, we collected in total ten cores between the two cruises, OR1-1013 and OR1-1048 (Table 2.1). Other sites were basically selected, but failed during the cruises (Fig.2.21) either for logistical problems (i.e, breaking of the trigger mechanism from the piston cores), seafloor conditions (i.e, sea bottom too rough, sand etc..) or were simply abandoned because of sea conditions (i.e, sea too rough because of an approaching typhoon leading to the impossibility of deploying coring equipment). During cruise OR1-1013 ~60% of the cored sites were successful. During OR1-1013 we only cored one site due to the extreme bad sea conditions consequent to a typhoon (Fig.2.21).

Core	Longitude	Latitude	Depth (mbsl)	Length (cm)
KS08-P	122°08'	24°19'	2800	91
KS09-P	122°11'	24°08'	2900	98
KAS03-P	121°42'	23°15'	1700	157
KR03-P	121°38'	23°15'	1205	398
KS06-G	121°30'	22°51'	1947	212
KS06-P	121°30'	22°51'	1947	152
KS06-B	121°30'	22°51'	1947	36
KC03A-P	121°04'	22°19'	1160	212
PC01B-P	121°04'	22°12'	1229	212
PC01C-P	121°04'	22°6'	1272	212

Table 2.1: Cores collected during the OR1-1013 and OR1-1013 surveys

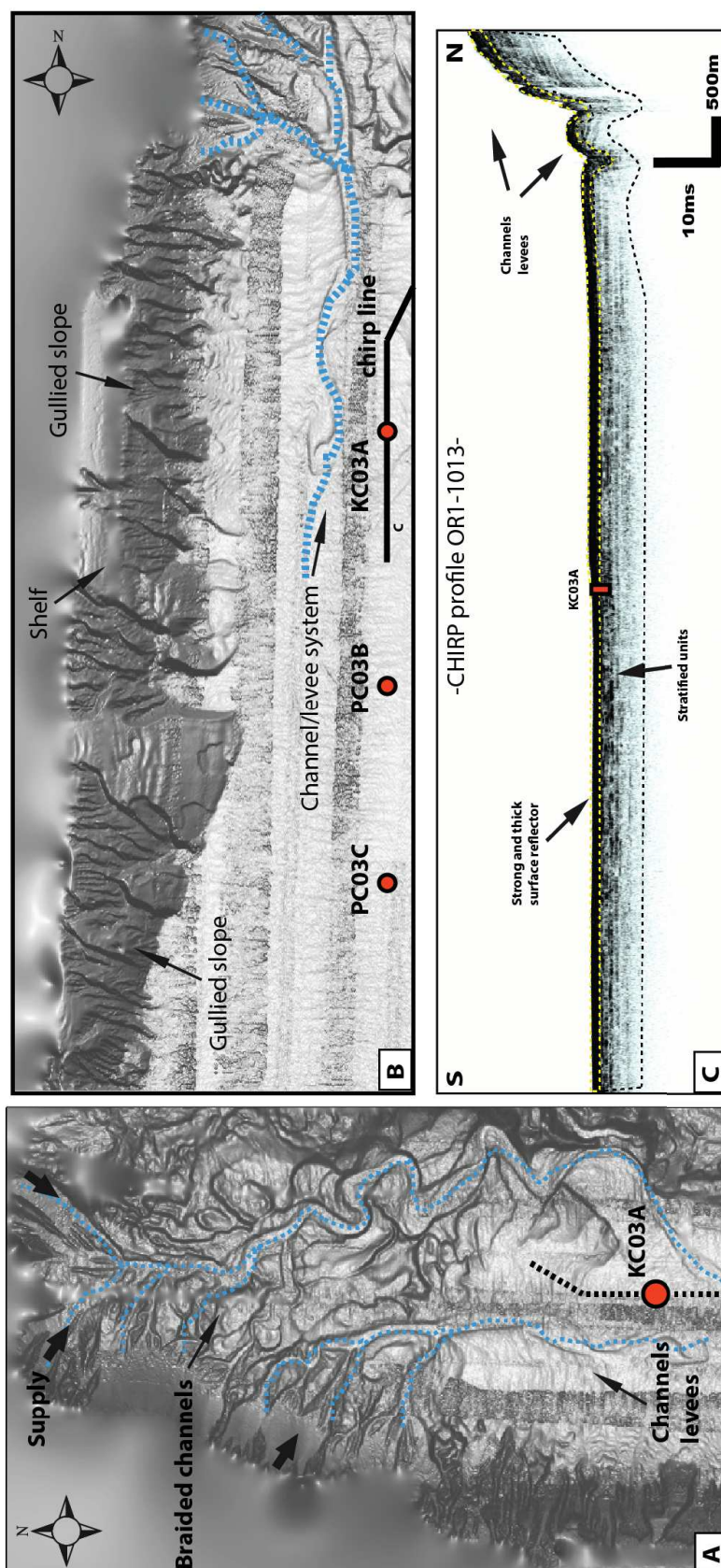


Figure 2.20: Southern Longitudinal Trough coring site. A: DEM showing the turbiditic system developed in the trough, with channel-levees complex; B: DEM viewed from the east, showing the gullied slope from where the sediment transit from the onland rivers. The three core sites are represented by the red dots; C: chirp profile across the KC03A core site, showing high energy reflector at sea-bottom and stratified reflectors in depth.

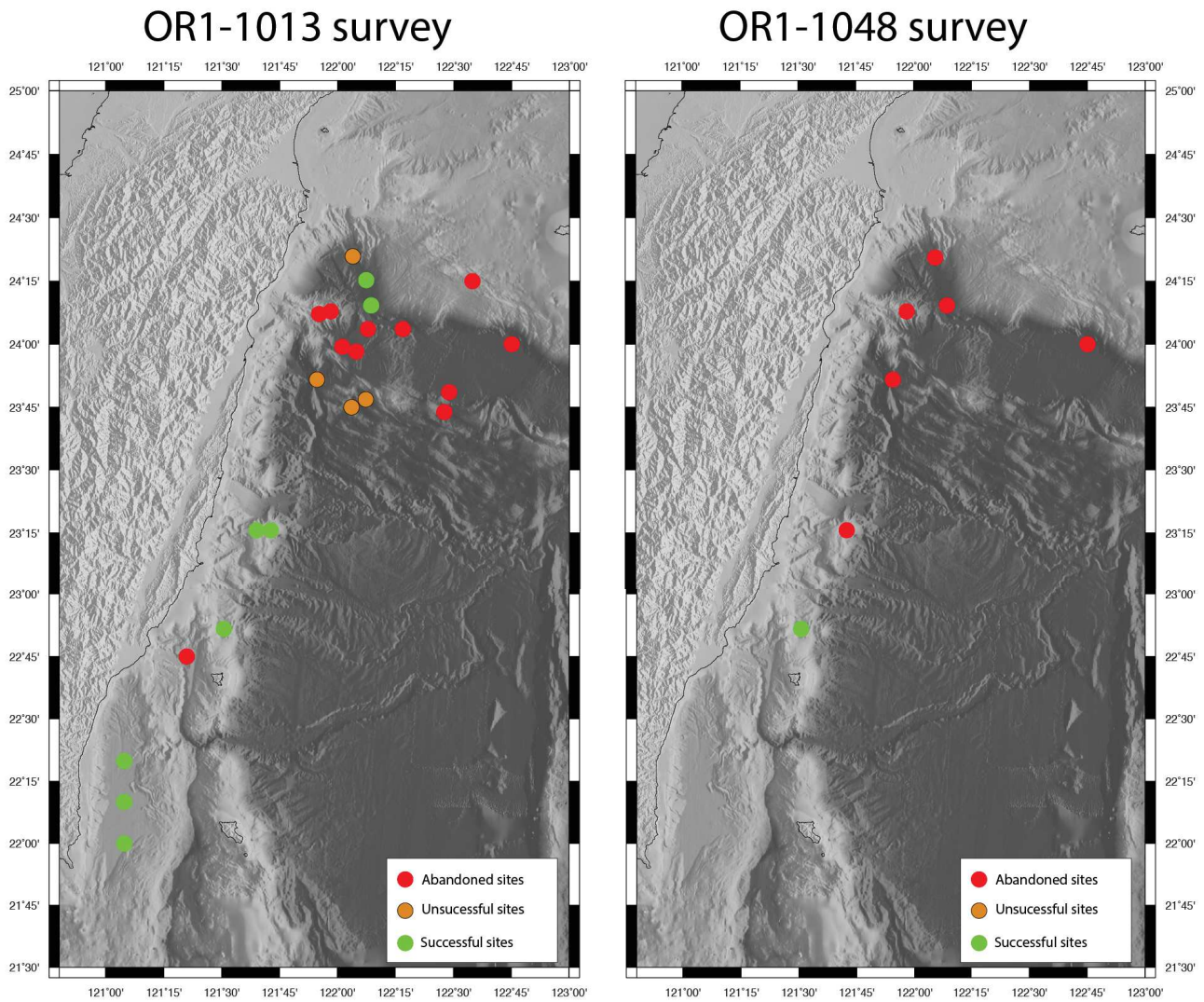


Figure 2.21: Map showing the objective for coring operations for the two surveys OR1-1013 and OR1-1048. We show sites that were successful, other that failed during coring and abandoned sites.

Deep-sea sedimentation offshore eastern Taiwan: facies and processes characterization

Contents

3.1	Introduction	55
3.2	Regional settings	55
3.3	Materials and methods	58
3.4	Description of sedimentary features revealed by geophysical data	58
3.5	Characterization and classification of lithofacies	63
3.6	Discussion and conclusion	67
3.7	Acknowledgments	73

Deep-sea sedimentation offshore eastern Taiwan: facies and processes characterization

Paper under review in Marine Geology

REMI LEHU (1,2), SERGE LALLEMAND (1), SHU-KUN HSU (2), NATHALIE BABONNEAU (3), GUEORGUI RATZOV (4), ANDREW T.LIN (2), LAURENT DEZILEAU (1)

1. *Géosciences Montpellier, Montpellier, France*

2. *Department of Earth Sciences, National Central University, Zhongli, Taiwan (R.O.C)*

3. *Domaines Oceaniques, IUEM, Brest, France*

4. *GéoAzur Laboratory, Nice Sophia-Antipolis University, France*

[*Corresponding author: lehu@gm.univ-montp2.fr](mailto:lehu@gm.univ-montp2.fr)

Abstract

Recent sedimentary facies and processes along the offshore slope of east Taiwan are investigated using a large set of geophysical and sedimentological data. The Taiwan orogen is often considered as one of the most tectonically active regions in the world and also experiences from important climatic activity with an average of four typhoons per year.

We have mapped in details the morphosedimentary features and characterized the sedimentary facies along offshore eastern Taiwan. There, we show that the slope is driven by a variety of erosional processes from slump/slide masses to turbidity currents. Mass movements such as slides or mass transport deposit (MTDs) are ubiquitous and affect the whole east coast off Taiwan. The trigger mechanisms likely range from slope instabilities due to oversteepening induce by tectonic uplift, mass wasting related to earthquakes shaking and failure relative to sediment overloading due to climatic-controlled pulses of sediment supply. Cores investigation indicate that alternating hemipelagite, turbidite and debrite facies are characteristics of the sedimentary records. Our results show that along offshore east Taiwan the relative proportion of these three end-members represent about 20% of hemipelagites, 20% of debrites and about 60% of turbidites. We thus consider that turbidity currents represent an important sedimentary process that governs the slope morphology off east Taiwan. Detailed core investigations, such as grain size analysis, chemical and mineralogical composition, revealed that turbidites facies range from thin fine-grained turbidites to thick massive turbidites facies. The detailed analysis of turbidites beds allow us discussing the controlling factors of turbidity currents generation. We propose that at least two end-members are characteristics in our turbidites records in term of controlling factor:

- 1) Turbidity currents likely generated by tectonic and earthquakes shaking.
- 2) Turbidity currents likely generated by climatic activity such as typhoon-induced floods.

Keywords: Offshore eastern Taiwan, Morphosedimentary features, Sedimentary processes, Turbidites

3.1 Introduction

At active margin scale, gravity flows are ubiquitous and represent the main erosional agent that control the slope morphology and governs sediment dispersal in the oceanic realm (Masson *et al.*, 2006). According to the literature, gravity flows range from massive debris avalanche i.e, New Zealand, (Collot *et al.*, 2001), slide/slumps, cohesive debris flow, fluidized flows, (Mulder and Cochonat, 1996; Mulder and Alexander, 2001) and turbulent flows such as turbidity currents (Bouma, 1962; Mulder and Alexander, 2001). The sedimentary processes result in a variety of deposits (slumps, MTDs, Turbidites) and are triggered or facilitated by a wide range of factors. These include tectonic forcing (uplift and slope oversteepening, earthquakes) and climatic forcing (catastrophic floods, sea-level variations, wave loading, storms, sediment overloading), or a combined effect of both forcing (Einsele, 1996; Locat and Lee, 2002; Piper and Normark, 2009).

The Taiwan mountain belt, known as one of the most active place in the world, represents a key place to investigate such sedimentary processes because it displays a variety of morphological settings, an intense tectonic and seismic activity, and high sedimentation rates (Huh *et al.*, 2004, 2006). Since the last decades, the Taiwan area has been well studied with abundant tectonic and geophysical investigations but it appears that only few studies focused on morphosedimentary processes. Because of a lack of "ground-truth" data it is still uncertain to provide a clear assessment about the erosional processes that shape the seafloor offshore eastern Taiwan and their controlling factors. Using a compilation of a large preexisting geophysical dataset and a newly acquired sedimentological data we aim to characterize the variability of sedimentary facies in such an active context. This work at providing new considerations on recent sedimentary processes and tentatively reply to the following question: what are the controlling factors of such sedimentary processes offshore eastern Taiwan?

3.2 Regional settings

3.2.1 Geological context

The Taiwan mountain belt results from the rapid and oblique convergence of the Luzon arc carried, by the Philippine Sea Plate, and the passive Chinese continental margin (CCM, Fig.3.1)(Biq, 1972; Suppe, 1984). Plate kinematics predicts about 80 mm/yr of convergence between these two plates (Seno *et al.*, 1993). The orogen links two subduction systems dipping with opposite vergence: to the South the Manila subduction zone and to the east the Ryukyu

subduction zone (Fig.3.1A). South of Taiwan, the South China Sea is being subducted eastwards beneath the Philippine Sea plate, building an accretionary wedge progressively uplifted above the sea level. To the northeast, the Philippine Sea Plate slab is retreating southwards beneath the Eurasian margin resulting on the opening of the Okinawa back-arc domain and the collapse of the northern part of the Taiwan mountain belt. Thus, the Taiwan orogen is located at the junction of those two opposite-dipping subduction systems and marks the interactions between them. Consequently, the deformation is characterized by a very high rate of seismicity onland and offshore eastern Taiwan (Hsu, 1961).

3.2.2 Regional climate, drainage systems and sediment discharge

Taiwan is positioned within what has been called the "Typhoon Alley" (Liu et al., 2008). On average, three or four typhoons impact the island annually. As such, Taiwan receives not only abundant precipitation due to its southern Asian monsoon climate, but periodically heavy rains during typhoons (Wu et al., 1999; Lin et al., 2002; Galewsky et al., 2006; Liu et al., 2008). The Morakot Typhoon (2009) resulted in the worst event of the last 50 years. The storm produced accumulated rainfall of 2777mm during the event (Ge et al., 2010). This historic amount of rain within short period of time triggered 12,697 landslides (Wu et al., 2011; Tsou et al., 2011) and exceptional flooding in Southern Taiwan. The Typhoon Morakot left 700 casualties and catastrophic damages.

The east flank of the Central Range is drained by rivers, incising the geological units. The Coastal Range, elongating along the east coast of Taiwan, plays a role of dam for the rivers so that the rivers are captured. The runoff collected along the Longitudinal Valley (Fig.3.1B) is diverted around the northern and southern edges of the Coastal Range in the Hualien and Beinan rivers respectively. The Hsiukuluan river is the only drainage cutting through the Coastal Range. Northeast of Taiwan, the Hoping and the Liwu rivers (Fig.3.1B) are the major rivers collecting the runoff from the Central Range. In Southeastern of Taiwan, the Taimali River and smaller rivers (e.g Jinlun river, Nongxi river, Dawu river and Daren river, see Fig.3.1B for location) convey most of the runoff from the Hengchun Peninsula (Fig.3.1B).

With high relief, steep gradients, important tectonic activity, heavy rainfall and frequent typhoons, Taiwan is generally recognized as having the highest sediment production in the world as 7 of the 10 global rivers with the highest sediment yield are in Taiwan (Li, 1976; Milliman and Syvitski, 1992; Chen et al., 2004; Dadson et al., 2004; Liu et al., 2008). Taiwanese

rivers presently discharge more than 300Mt of sediments to the surrounding ocean each year and more than 30% of the total sediment from Taiwanese rivers is discharged at hyperpycnal concentrations (Dadson et al., 2005; Kao and Milliman, 2008; Liu et al., 2008).

3.2.3 Submarine morphology

The morphology off eastern Taiwan displays a complex interaction between onshore and offshore processes in a context of high tectonic activity and extreme tropical rainfalls. The shelf is typically less than 10km wide, with a slope break around 100m water-depth. The slope displays steep slope gradients varying (15 to 20°) and is deeply incised by systems of gullies and canyons (Fig.3.1B). Downslope, they merge to form a dendritic channel pattern transferring sediments to deep oceanic basins (Ramsey et al., 2006). The submarine slope also exhibits seafloor escarpments associated to tectonic structures such as thrusts and folds (Malavieille et al., 2002). The drainage systems involve three major submarine canyons offshore eastern Taiwan collecting the sedimentary discharge from the Central Ranges and the Coastal Range; from the north to the south, the Hualien Canyon, the Chimei Canyon and the Taitung Canyon respectively (Fig.3.1B). The Hualien and Taitung canyons exhibits a similar V-shape valley in the upstream part, deep incision with relief neighboring 500 m and are known to receive significant amounts of river sediment at hyperpycnal flow (Dadson et al., 2005). In contrast, the Chimei submarine valley does not cut the slope into a narrow and steep valley floor but undergoes considerable sediment-filled depression with a 5° slope (Ramsey et al., 2006). Beside large canyons and gullies systems, there are numerous channels sculpting the slope across the eastern coast. These systems eventually merge with the three larger canyons mentioned above and seem not to be connected with sub-aerial drainage systems. Their morphological characteristics, extensively described by Ramsey et al. (2006), suggest that marine erosional processes such as submarine landslides, debris flows or turbidity currents might be responsible in the development of such channels systems.

3.2.4 Seismic activity

The seismicity rate is extremely high on both onland and offshore Taiwan. Destructive earthquakes have significantly struck the island repeatedly. During the last century, 22 $M_w > 7$ earthquakes have been recorded. Offshore, the greatest event ever recorded in the Ryukyu margin, has been reestimated with a magnitude M_w 7.7 (Theunissen et al., 2010). Such seismic activity will have necessarily direct influences on shaping the offshore morphology and consequently on

the driving mechanisms of the actual offshore sedimentary processes discussed in this paper.

3.3 Materials and methods

3.3.1 Bathymetry, acoustic and seismic data

Multibeam bathymetry and side-scan backscatter imagery were obtained during the ACT (Active Collision Taiwan) survey in 1996 on board of the *R/V L'Atalante* (Lallemand and Tsien, 1997) (Fig.3.2) using a SIMRAD EM12-Dual and EM950 (for depths shallower than 300 m) multibeam systems that enable swath mapping and backscatter imagery. Bathymetry and backscatter imagery provide respectively information on seafloor morphology and its variation of acoustic properties and nature. Chirp seismic reflection data have been recorded during the OR1-1013 survey in September 2012 allowing us characterizing the seismic facies of the first meters below the seafloor. Moreover a set of multi-channel seismic reflection lines acquired during several cruises between 1993 and 2021 is used in this study (Fig.3.1, 3.2).

3.3.2 Cores material

A total of ten cores were collected and analyzed off eastern Taiwan during the OR1-1013 and the OR1-1048 surveys (Fig.3.2, 3.2). Sedimentary descriptions were done for all the cores, with a particular attention to grain size distribution variation and turbidite/hemipelagite differentiation. Sediment cores were sampled from 2 to 0.5 cm interval for grain size analyses using a Coulter laser micro-granulometer LS13 320 (size range from $0.4\mu\text{m}$ to 2 mm). In addition, in order to enhance the core coverage of the study area, complementary cores collected from several surveys have been used (Fig.3.2): 7 box-cores collected on board *R/V Ocean Researcher I* (1989) (Huang et al., 1992); 5 cores collected during the OR1-960 survey and 1 box-core from OR1-687 (Huh et al., 2004).

3.4 Description of sedimentary features revealed by geophysical data

Detailed mapping based on Digital Elevation Model (DEM hereafter), backscatter imagery and seismic data (MCS and chirp data) allows identifying three sectors with distinct morpho-sedimentary features: The southern, central and northern sectors (Fig.3.2). This mapping

enables to assess the relative distribution of sedimentary structures that might be related to processes controlling erosion and deposition in such an active context.

3.4.1 The southern sector

The Taitung canyon is the most prominent sedimentary feature offshore eastern Taiwan. The canyon indents the upper slope, bends along the Luzon Arc, crosses it and incises the Huatung Basin to finally ends in the Ryukyu Trench (Fig.3.1B). The shape of the Taitung canyon allows a division into three distinct segments S1, S2 and S3 respectively (Fig.3.3B):

-S1 oriented E-W, corresponds to the head of the canyon (Fig.3.4). It is 4 km wide, runs from 500 m water depth down to 1000 m and is directly fed by the major Beinan River onland and a small river from the Coastal Range (Fig.3.1B, River 9 on Fig.3.3B and River 10 Fig.3.5B). The canyon bed exhibits a high reflectivity (Fig.3.3A).

-S2, oriented N-S, runs from 1500 m water depth down to 3000 m in its southern extremity. It has a rough, sinuous and narrow (~ 2 km wide) bed with a V-shape incision and is characterized by a highly reflective seafloor (Fig.3.3B, 3.4B). Well-developed canyon levees are observable on both banks of S2 (Fig.3.4B). One tributary canyon (C1) oriented E-W, meanders and incises the sedimentary Huatung ridge (Fig.3.3B). The canyon C1 also exhibits a strong reflectivity (Fig.3.3A).

- The pathway of S3 changes to E-W, cutting through the Luzon Arc between the volcanic islands of Lutao and Lanyu before incising the Huatung Basin (Fig.3.1, 3.3). Where crossing the Luzon Arc, the canyon shows a narrow (~ 4 km wide) V-shape incision, up 1500m-deep. In the Huatung Basin, the upper part of S3 is fan shaped and its channel width decreases from 14 km down to 7,2 km downstream (Schnurle et al., 1998). The floor of the canyon appears to be very rough as shown by the strong to moderate reflectivity of the acoustic imagery (Fig.3.3A). In the Huatung Basin, levees are built on both side of the canyon (Fig.3.3B).

The Southern Longitudinal Trough (hereafter called SLT) is a proximal orogenic basin developed in a forearc position (Malavieille et al., 2002). This basin is elongated following a N-S direction (Fig.3.1,3.3). It is about 90km long and 15km wide. The SLT is bounded to the west by the structural slope of the Hengchun peninsula and to the east by the sedimentary Huatung ridge (Fig.3.1B). A narrow shelf (less than 5km) fringes the SLT (Fig.3.1B). Below the 100m isobath, the slope dip changes abruptly from a gently dipping shelf ($\sim 1-2^\circ$) to a steep slope ($\sim 20^\circ$). A network of E-W trending gullies erode the western slope of the SLT and feed the

basin with sediment (Fig.3.1B). Gullies form a badland topography and show a high reflectivity (Fig.3.3A). They are observed at different scales from tens of meters to several hundreds meters. Gullies coalesce and extend into the SLT floor.

We identify channel-levees complexes on the SLT seafloor. Narrow channels from the western and northern slopes of the SLT fed by the Taimali and smaller rivers from the Hengchun peninsula respectively develop in this area (Fig.3.1B, 3.3B). They form a complex braided channels system flanked by sedimentary levees (Fig.3.3A.). Two main channels (Ch1 and Ch2 on Fig.3.3A) are identified running parallel to the western slope of the SLT. The channel Ch1 is 20 km long and linear and characterized by a low reflectivity (Fig.3.3A). It is mainly fed by the Jinlun (river 5 on 3.3B). Other tributary channels fed by smaller onland rivers (e.g. River 1, 2, 3, and 4 on Fig.3.3B) merge to the main channel Ch1 (Fig.3.3B). Channel Ch2 is 30 km long sinuous and meandering in its upper part, becoming linear downstream (Fig.3.3A, Fig.3.3D). It is mainly fed from north to south by the Taiping, the Zhiben and Taimali rivers (Rivers 8, 7 and 6 respectively, 3.3B). Ch2 is also characterized by a low reflectivity (Fig.3.3A). Downstream, the two channels Ch1 and Ch2 finally merge and end 15 km afterward, into a sedimentary lobe identified by a low (to moderate) reflectivity (Fig.3.3A). Well-developed sedimentary levees (<100m-high) flank the channels and exhibit a moderate reflectivity (Fig.3.3A). On echo-sounder profile sedimentary levees are characterized by a continuous and high amplitude sea-bottom reflector evolving into a stratified echo-facies with depth (Fig.3.3C) The slope is affected by a variety of mass movement, including slide/slumps, mass transport deposits (MTDs hereafter) or turbidites as defined by (Hampton et al., 1996); Mass movements in the form of slumps or MTDs are observable in shallow sediment on (i) the northernmost part of the Huatung ridge (L1 on Fig.3.3B, 3.4A, and B), (ii) the slope of the Luzon Arc (L3 and L2, on Fig.3.3B, 3.4A) and (iii) the southern wall of the segment 3 of the Taitung canyon (L4 on Fig.3.3B, 3.4A).

(i) The northernmost edge of the Huatung ridge exhibits a submarine landslide as shown by the seismic profile on 3.4B. The slide L1 is characterized by a steep scarp marked by an arcuate shape, and by chaotic reflectors packages interpreted as slumped materials (Fig.3.4B).

(ii) ~25km-wide arcuate scars displaying a steep slope (~20-30°) affect the western and the eastern slope (Slide L2 and L3) of the Luzon Arc (Fig.3.4A, B). The chaotic reflector packages at the base of the scars supports slope failures (Fig.3.4B).

(iii) Slides on canyons flanks are common (Mountjoy et al., 2009). The southern flank of the Taitung canyon in the segment 3 shows a ~30 km-large scar and a gullied slope (L4) supporting

a collapse of the canyon levee (Fig.3.4A).

3.4.2 The central sector

The central sector corresponds to the well developed collision zone of the Luzon Arc with the Chinese continental margin (Malavieille et al., 2002). It includes the Coastal Range and its submerged eastern flank, the western edge of the Ryukyu accretionary wedge and the abyssal Huatung Basin (Fig.3.1). A prominent canyon, the Hualien canyon (C8 on Fig.3.5B) flows mainly N-S, through the Ryukyu accretionary wedge and then eastward to join the Ryukyu Trench (Fig.3.1B, 3.5). We divided this canyon into three segments, S1 to S3: -S1 trends NW-SE and then sharply turns southwards (Fig.3.5B). It corresponds to the major canyon head, fed by the Liwu river (River 16 in Fig.3.5B). S1 is V-shaped, wide (~ 4 -5km) and displays a high reflectivity (Fig.3.5A). - S2 located at river mouth south of Hualien, corresponds to a tributary that trends E-W and sharply turns southward where it merges with S3 (Fig.3.5B). It is fed by the Hualien river (River 15 Fig.3.5B) and all its tributary rivers draining the northernmost tip of the Longitudinal Valley. S2 is V-shaped, narrow (~ 1 -2 km) and is highly reflective (Fig.3.5A). - S3 is oriented N-S and flows through the Ryukyu accretionary wedge. It has a V-shape morphology. The northern part of S3 is wide (~ 6 km) and becomes meandering and more narrow in its central and southern parts (between 1 km and 3 km respectively) (Fig.3.5B). It expresses a strong reflectivity on backscatter imagery (Fig.3.5B). Sedimentary levee developed on the western flank of S3 are characterized by a low to moderate reflectivity (Fig.3.5A).

The Chimei "Canyon" (C7) (Fig.3.1B, 3.5, 3.7A) incises the offshore eastern slope of the Coastal Range. This flat sea-floored "valley" has a wide (~ 10 km) and U-shape morphology. It is fed by the only river cutting through the Coastal Range, the Hsiukuluan river and by a tributary from the Coastal Range (Rivers 14 and 13 respectively, Fig.3.5B). The canyon C6 (Fig.3.5) meanders and joins the Chimei valley on its southern flank. It has a V-shape incision and is characterized by high reflectivity. It does not seem connected to any particular rivers from the Coastal Range. The Chimei valley seafloor expresses a high reflectivity on backscatter imagery (Fig.3.5A). On the eastern edge of the Chimei valley, two meandering channels: Ch3 connected to C6 and Ch4 connected to C7, develop with their associated sedimentary levees (Fig.3.5B and 3.6A). Bathymetric highs with moderate reflectivity are visible on the southern and northern flanks of the Chimei Valley (Fig.3.5A and 3.7A). On chirp profile, these relieves

display stratified reflectors (Fig.3.7B). Other canyons C3, C4 and C5 also incise the Huatung basin. They are characterized by a wide (between 2 and 5km), V-shape morphology and express high reflectivity on backscatter imagery. These canyons, except C4 that is connected to two small rivers onland from the Coastal Range (Rivers 11 and 12, Fig.3.5B), are not fed by onland rivers. Associated canyon levees develop on the northern and southern flank of these canyons. They are characterized by a moderate to low reflectivity (Fig.3.5B). Erosive features such as submarine valleys incising the offshore slope of the Coastal Range (Fig.3.6A and 3.7B) have been extensively described by (Ramsey et al., 2006). These features are characterized by high reflectivity on backscatter imagery suggesting intense erosion and steep slopes (Fig.3.5A). Mass-movements also affect the seafloor of the Coastal Range (L5, L6 and L7, Fig.3.5B, 3.6 and 3.7A). Landslides L5 and L6 are characterized by head scarps on seismic lines 5 and 7 (Fig.3.6B) as well as transparent and chaotic reflectors packages suggesting slumped or slid masses, or buried mass transport deposits (Fig.3.6B). A small-perched basin is observable on the Luzon Arc (Fig.3.6A). Chirp profile across the basin expresses strong reflector at seabottom and well-stratified reflectors in depth, showing basin fill sediments (Fig.3.6B) not affected by the large scale slumped deposit observed immediately northward. Finally, downslope the Chimei Valley a slope failure with a well defined slope scarp is observed southward the channels-levees system described above (L7 on Fig.3.5 and 3.6A).

3.4.3 The northern sector

The northern sector corresponds to an area of well developed collision including the western termination of the Ryukyu accretionary wedge, forearc basins and the Ryukyu arc. From west to east, we distinguish the Hopping Basin (HB) and the Nanao Basin (NB) respectively (Fig.3.1, 3.8). This area experiences from both intense tectonic and seismic activity (Lallemand et al., 2013; Malavieille et al., 2002; Theunissen et al., 2010; Wu et al., 2009; Hetland and Wu, 2001).

The Hopping Canyon (HC hereafter) incises the northern sector (Fig.3.8, 3.9). This Canyon (C9). It crosses the forearc domain ensuring the sediment transit between the two forearc basins HB and NB. The HC runs mainly NW-SE, exhibits a U-shaped morphology and is ~3-4 km wide. The HC canyon starts from the southeastern edge of the HB, runs almost parallel to the Ryukyu arc and finally reaches the NB that is characterized by a moderate reflectivity on acoustic imagery. The HC canyon is structurally controlled by faults cutting through the entire margin (Font and Lallemand, 2009). In contrast with the other canyons previously described,

the HC displays a low reflectivity on backscatter imagery (Fig.3.8A). Canyon levees are identified on chirp profile on its northern and southern flanks (Fig.3.8B, 3.9) and are characterized by moderate reflectivity. The western slope of the HB is strongly eroded and affected by gullies. They ensure the sediment transit from two rivers onland (rivers 17 and 18) to the offshore basins. They are characterized by a very strong reflectivity on the acoustic imagery (Fig.3.8A). Downstream, and connected to the head of the HC, a channel-levees system develops in the HB. Three main channels Ch5, 6 and 7 respectively incise the steep ($\sim 18-20^\circ$) and eroded western slope of the HB. Ch5 and Ch6 are connected with major rivers (Rivers 17 and 18 respectively on Fig.3.8B) whereas Ch7 seems not being connected to any river. All the channels have built sedimentary levees characterized by moderate reflectivity on acoustic imagery and by stratified reflectors on chirp profile (Fig.3.8B, 3.9). The HB is bordered on its southern edge by an uplifting sedimentary ridge (Malavieille et al., 2002) that is characterized by moderate reflectivity on backscatter imagery (Fig.3.8A). The northeastern part of this sector is characterized by the western termination of the Ryukyu arc that expresses a moderate reflectivity on backscatter imagery (Fig.3.8A). The slope of the Ryukyu arc is affected by several mass-movements mapped L8, L9 and L10 respectively (Fig.3.8B, 3.9). Arcuate scarp shapes are recognizable above landslides L8, L9 and L10 but not well defined, as shown on DEM on Fig.3.9. Other landslide (L11) affects the western slope of the Hopping Basin and is characterized by a high reflectivity on backscatter imagery (Fig.3.8A, 3.8B)

3.5 Characterization and classification of lithofacies

In this section, we describe the variability of sedimentary facies along the offshore eastern Taiwan. We intend to address and characterize the lithofacies based on both sedimentological data studies such as visual description, grain size variation, chemical composition and sand fraction content (Fig.3.10 and 3.11), and preexisting cores analysis found in the literature.

3.5.1 End-members lithofacies

We propose three end-member lithofacies distinguished and qualified as following:

Facies I: Hemipelagic sedimentation.

Facies I (Fig.3.11) is composed of homogeneous clay with low content of silty sediment ($<20\%$) and contains diluted foraminifera and sometimes bioturbations. Inconspicuous laminations are

present but do not correspond to grain-size changes. Hemipelagites in core are usually characterized by the finest grain size ($< 10\mu\text{m}$). This facies is interpreted as the background sedimentation of deep offshore environment.

Hemipelagite facies may be present either with alternating resedimented units such as turbidites sequences (Fig.3.11), or in isolated places that are prone to sediment accumulation. As a good example, the core KR03 located on a top of a bathymetric high (Fig.3.5B, 3.7) is mainly composed by homogeneous clay and thus dominated by hemipelagic deposits (Fig.3.10). In the low reflective Taitung Trough mapped on Fig.3.3B, pelagic mud seems to dominate as described by (Huang et al., 1992). No sedimentary records are available to characterize the low reflective Huatung Basin mapped on 3.3B. Nevertheless, its acoustic and seismic signatures suggest that it is mainly characterized by Facies I. We thus consider that Facies I cover about 20% of the study area.

Facies II: Turbidites.

Facies II together with Facies I, dominate the sedimentary record. Turbidites are recognized by their coarser grain size and a typical fining upward trend (Fig.3.11), defined by the Bouma sequence (Bouma, 1962) and the classification of (Stow and Shanmugam, 1980). In our cores, turbidite thickness ranges from 1 to about 30 cm (described in previous section). Turbidites are usually interbedded with hemipelagites (Facies I) or stacked. The basal boundaries are easily identified from a change to coarser-grain size and darker color of the sediment. All the cores are characterized by Facies II and found in different sedimentary settings. We consider according to our results, that Facies II represents 60% of the sedimentary coverage off east Taiwan.

Facies III: Debrites.

Following the description of Huang et al. (1992), debrites consist of chaotic material, angular rock detritus, pebbles and blocks. The Huatung ridge and the head of the Taitung Canyon (Segment 1 on Fig.3.3B) are characterized by the Facies III. Sampled core on the Huatung ridge revealed the presence of sandstone and mudstone blocks within a mudstone matrix (Huang et al., 1992), that could explain the high reflectivity of the Huatung ridge (Fig.3.3A). As described by Huang et al. (1992), sediment samples cored at the head of the Taitung Canyon contained angular metamorphic detritus that could also explain its high reflectivity on backscatter imagery. This chaotic composition within a matrix supported texture also suggests a mass transport deposit or slump/slid masses (Mulder and Alexander, 2001). We suppose, that the slided masses mapped

on Fig.3.3 and Fig.3.5, are associated to debrite deposits. According to our observations and data analysis, Facies III covers about 20% of the study area.

3.5.2 Turbidites facies

According to visual description, grain size analysis, chemical and mineralogical composition, four main turbidites facies can be defined:

- *TI*: thin silty-clay lithogenic turbidites
- *IIIa*: thin silty to fine sand lithogenic turbidites
- *IIIb*: thin silty to fine sand biogenic turbidites
- *III*: thick to massive, fine sand to coarse sand lithogenic turbidites

***TI*: Thin silty-clay lithogenic turbidites.**

TI corresponds to re-sedimented deposits. It consists of 0.5-10 cm fining upward silty-clay sequences interbedded with Facies I. *TI* differs from Facies I (hemipelagite) by being darker in color and coarser in grain size compared to the hemipelagic sedimentation. The contact with hemipelagite is sharp and there is no evidence of basal erosion. The progressive grain-size evolution of the top of the silty-clay laminae indicates that they could correspond to thin and fine-grained turbidites. Chemical signature (evidenced by XRF) data, shows both slight positive anomalies in Fe and negative in Ca, on the coarser beds. The lithogenic fraction dominates the composition of the sand fraction (65%) (Fig.3.11). The lithogenic fraction is composed by metamorphic rock fragments (40%), quartz grains (30%), slate (25%) and micas (5%). The other 35% of the coarser fraction are constituted by biogenic material with benthic foraminifera (1%), vegetal remnants (5%), sponge spiculae (45%) and planktonic foraminifera (49%). Silty-clay turbidite may be interpreted as the subdivision T4 or T7 corresponding to low-density turbidity current defined by Stow and Shanmugam (1980). *TI* has been observed on cores KAS03, KS08 and KS09 (Fig.3.10, 3.7 and 3.9 for cores location).

***III*: Thin silty to fine sand turbidites.**

III also corresponds to re-sedimented deposits. It is composed of 1 to 15 cm thick fining upward silty to fine sand sequences (Fig.3.10, 3.11). The basal contact is usually sharp but in some cases there are evidences of erosional contact. *III* is composed of a succession of silty to fine sand

turbidites alternating with thin hemipelagic intervals (Facies I) (Fig.3.10).

TIIa: Thin silty to fine sand lithogenic turbidites. Chemical analysis reveals positive Ca anomalies and negative Fe anomalies in coarser beds. The composition of the coarser fraction is mainly of lithogenic material (75%). The lithogenic fraction is composed by metamorphic rock fragments (20%), quartz (30%), slate (45%) and micas (5%). The other 25% of the coarser fraction are constituted by biogenic material with benthic foraminifera (1%), vegetal remnants (5%), sponge spiculae (45%) and planktonic foraminifera (49%). This turbidite facies may be assimilated to the subdivision Tb or Tc defined by Bouma (1962) and characteristic of low-density turbidity current. This facies is present in the cores KS09, KAS03 and KC03A (Fig.3.10, Fig3, 3.7 and 3.9 for cores location), ORI-960-C5-G, ORI-969-3-P (Fig.3.4A) as well as VM33-95 collected on the southern levee of the Taitung Canyon (Segment 3 on Fig.3.3B).

TIIb: Thin silty to fine sand biogenic turbidites. Chemical analysis reveals very clear positive Ca anomalies anticorrelated with negative Fe anomalies (relative to background signal, i.e Facies I) on coarser beds. In contrast with *TIIa*, the coarser fraction is composed by relatively high concentration of biogenic material (70%). This fraction contains mainly planktonic foraminifera (60%), sponge spicules (25%), benthic foraminifera (5%), plant remnants (5%) and other remnant organisms (5%). The lithogenic material is mainly constituted by feldspars plagioclase (60%), biotite (30%) and quartz (10%). This particular turbidite facies could also correspond to the subdivision Tb and Tc of the Bouma sequence (Bouma, 1962) that indicates a low-density turbidity flow. Facies *TIIb* has been observed only to core KS06 (Fig.3.6 for core location).

TIII: Thick to massive, fine sand to coarse sand lithogenic turbidites.

TIII is characterized by a clear graded sand layer at the turbidite base, fining upward to silty sequences, usually > 15 cm thick (Fig.3.10). Chemical analysis show negative Ca and positive Fe anomalies (relative to the hemipelagic signal) on coarser beds. The coarser fraction is only composed of lithogenic material. We relate this turbidite facies to the subdivision Ta or Tb defined as medium-density turbidity current by Bouma (1962). This facies is characteristic of cores collected in the Southern Longitudinal Trough: KC03, P01B and P01C. The sedimentary cores described by (Huang et al., 1992) (Fig.3.3 for cores location) in the same area suggest that they are also characterized by facies *TIII* sometimes interbedded with very thin sequences of Facies I.

3.6 Discussion and conclusion

3.6.1 Erosional sedimentary processes

The analysis of morphosedimentary features and sedimentary facies show that off east Taiwan is characterized by three end-members facies, hemipelagite, turbidite and debrite, showing a relative proportion of the study area of about 20%, 60% and 20% respectively. As discussed by Ramsey et al. (2006), erosional processes are the major sedimentary processes that shape the continental slope offshore of eastern Taiwan.

As such, submarine mass movements are the leading processes in sediment mass transfer, sediment distribution and consequently in shaping the slope morphology. Mass movements are ubiquitous in both active and passive margins (Hampton et al., 1996; Locat and Lee, 2002; Lee and Pradhan, 2007; Chiu and Liu, 2008; Hsu et al., 2008). In term of triggering mechanisms, many studies indicate that earthquake shaking is the greatest trigger for slope failure initiation in active margin context (Hampton et al., 1996). Beside that, long-term factor such as tectonic oversteepening, overloading, oceanic conditions and climatic conditions play a key role in preconditioning submarine slopes to collapse (Hampton et al., 1996; Locat and Lee, 2002; Masson et al., 2006; Strasser et al., 2011).

Offshore Taiwan, the particular seismic, tectonic and climatic active context is prone to initiate mass movements. For example offshore southwestern Taiwan, Chiu and Liu (2008) and Hsu et al. (2008) have shown that both the talus of the passive Chinese continental margin (CCM on 3.1A) and accretionary wedge (Fig.3.1A) undergo slope failures. Moreover, Hsu et al. (2008) reported that several communication cables deployed on the seafloor of the Manila accretionary wedge broke right after several slumps and turbidity currents initiated during the Pingtung earthquake in 2006. Our morphosedimentary analysis revealed that slope failure impacts also the offshore east coast of Taiwan. The size and style of failure vary from submarine landslides to turbidity currents (Fig.3.3, 3.4, 3.5, 3.6, 3.8, 3.9, 3.10).

Mass wasting Eastern Taiwan

Mass wasting mainly affect (i) the flanks of the Taitung canyon, (ii) the slope of the deforming Luzon Arc, (iii) the deforming Huatung ridge, (iv) the flank the ancient Chimei deep sea fan deposit and (v) the Ryukyu margin, including the Ryukyu arc and the Hopping Basin.

(i) The failure style affecting the wall of the Taitung canyon (L4 on segment 3, Fig.3.3B and Fig.3.4A) suggests slided masses. These slides have moved from the walls down to the canyon

floor and may have probably evolved into gravity flow such as debris flow or turbidity currents. On tectonically active context, mass wasting often triggered by earthquake shaking or tectonic activity can be significant processes in controlling the evolution of a submarine canyon (Hampton et al., 1996; McAdoo and Watts, 2004). In fact, Schnurle et al. (1998) and Sibuet et al. (2004) have shown that the Taitung Canyon is tectonically controlled by active strike-slip fault in the oceanic basement. However, the presence of well developed sedimentary levees on both flanks of the canyon shows that climatic-controlled pulses of sediment supply is also a non-negligible parameter controlling the evolution of the Taitung Canyon. We thus suggest that mass wasting in the Taitung Canyon results from the combined effect of tectonic and climatic forcings.

(ii) On the slope of the Luzon Arc the failure style includes slumps, slides and mass transport deposits (Fig.3.4, 3.6). The failure style shows relatively short displacements from where they originate (Fig.3.4, 3.6). Slope failures (L2, L3 and L6 on Fig.3.3, 3.6) were identified on the vicinity of the transition between two tectonic domains: a southern tectonic domain where the Luzon Arc is being deformed and a northern tectonic domain that is characterized by the well-developed accretion of the Luzon Arc onto the Taiwan orogen (Malavieille et al., 2002). We thus propose that slope failures in that highly active area is likely controlled by tectonic trigger mechanisms including earthquakes.

(iii) In the same area as described above, the sedimentary Huatung Ridge also faces slope instabilities, characterized by similar failure style previously discussed such as slided masses (L1, Fig.3.3,3.4). Here, we suggest that the triggering mechanisms are mainly tectonic including seismic activity, but a climatic forcing cannot be ruled out from massive terrestrial sediment discharge in the Taitung Canyon. A plausible scenario would be first related to overloading sediment due to the proximal sediment supply and then tectonic activity that initiate the mass wasting.

(iv) On the Chimei deep sea fan, we observed that its southern flank had collapsed displaying a well defined scar (L7 on Fig.3.5 and 3.7). Based on previous morphology studies (Malavieille et al., 2002) we speculate that there, a preexisting fan accumulated sediment discharges from both the Hualien Canyon and the Chimei Valley (or a former canyon) outlets. Then because of the both effect of important sediment discharges down the canyons and tectonic uplift, the deep sea fan reached the critical angle of instabilities to finally collapse.

(v) The Ryukyu margin offshore NE Taiwan is the place where the deformation is paroxysmal (Lallemand et al., 2013). Our analysis shows that the Ryukyu forearc domain is also affected by slope instabilities. There, sliding morphology differs from those previously described. In fact as

identified on high resolution DEM, the failure scarps are not well expressed on the Ryukyu Arc slope suggesting superficial slope failures. The trigger mechanisms proposed are tectonic activity and seismic shaking since the area displays a very high seismicity rate. Similarly, according to the steep slope morphology, and high reflective acoustic facies, the whole offshore slope of the Central Range is affected by important mass wasting processes such as debris flow or slided masses (Fig.3.8). Here the trigger mechanism is also due to geological processes. In fact, we consider that the main triggering mechanism is an earthquake after a long-term process such as slope oversteepening (preconditioning factor) in the wake of the Luzon arc subducting beneath the Central Range (Lallemand et al., 2013).

Turbidity currents

The mapping of recent morphosedimentary features using acoustic, seismic data and sedimentological data shows that turbidity currents are ubiquitous in different sedimentary systems such as (i) large turbiditic systems, (ii) confined intra-slope basins and (iii) canyon levees that have been built by turbidites deposits.

(i) *Large turbiditic systems:* Acoustic imagery and sedimentological data of mass-movements deposits in the SLT suggest that, here, the major gravitational process is likely turbidity currents rather than other processes (i.e debris flow). Thus, the SLT is recognized and interpreted as a turbiditic system, where turbiditic channels, sedimentary levees and lobe deposits develop. The high reflective gullied slopes of the SLT, the short shelf-break and the direct connection of major rivers with the SLT show that this area can be considered as a by-pass region for gravity flows. The two sinuous and meandered turbiditic channels Ch1 and Ch2 that develop in the continuity of rivers 1 to 9 (Fig.3.3B) have the capacity of overflow and consequently contribute to the upbuilding of sedimentary levees (Fig.3.3C and D). The different types of turbidites deposits found in cores KC03A, PC01B and PC01C (Fig.3.10) indicate that the type and energy of the passing flows were variable with consequently different capacity to erode and/or deposit.

Likewise, the Hoping Basin (HB) expresses similar features and is also interpreted as a turbiditic system. The extremely short shelf and the intensively eroded gullied slope of the western slope of the HB also indicate that this area represents a by-pass zone for gravity flows. Downslope the Chimei Valley, a similar turbiditic system also develops including two meandered channels (Ch3 and Ch4 Fig.3.5,3.7) and associated sedimentary levees (Fig3.5,3.7).

(ii) *Confined intra-slope basins:* Turbidity currents also affect the slope of small confined basin for example at site KS06 (Fig.3.5B, 3.6). Both seismic and sedimentological data have shown

that this basin, located southward of a slope failure area, is able to records turbidites deposits interbedded with hemipelagic sediments (Fig.3.10). This intra-slope basin does not indicate any trace of recent or buried turbidite channels nor sedimentary levees (Fig.3.6). Moreover, this basin is not connected to onland input suggesting that, here, the slope may not play the role of by-pass sediment but that turbidity currents should be triggered on the slope itself.

(iii) *Canyon levees*: Finally, it is suggested that channels and canyons are often incised by the course of turbidity currents whereas spillover deposition of fine-grained sediments led to the formation of sedimentary levees (Shepard and Dill, 1966). The flanks of the Taitung Canyon and the Hoping Canyon show well-developed sheet-like turbidites that build sedimentary levees (Fig.3.4B and 3.9B).

3.6.2 Control factor and sediment provenance of turbidity currents

An important question remaining to be addressed is, "which factor control the generation of turbidity currents?" It is known that turbidity currents usually involve great floods (Mulder et al., 2003; St-Onge et al., 2004a; Beck, 2009), tsunamis (Shanmugam, 2006), storm waves (Mulder and Alexander, 2001; Puig et al., 2004), volcanism (Schneider et al., 2001) and large earthquakes (Goldfinger et al., 2003; St-Onge et al., 2004a; Poudroux et al., 2012). Moreover, mechanisms recognized as "long-term" preconditioning or facilitating factors, have been proposed such as sediment overloading and gas hydrate destabilization, that correspond to the indirect effects of regional changes such as sediment delivery or sea-level variations or tectonic uplift or subsidence. Below, we tentatively discuss the possible factors that control turbidity currents offshore eastern Taiwan: tectonic and/or seismic control, and climatic control (i.e turbidity currents generated by floods).

Tectonic and seismic control

In active margin context, earthquakes have been identified as the major factor in turbidites generation (Adams, 1990; Goldfinger et al., 2003; Poudroux et al., 2012). Our analysis suggests that several geological and sedimentological arguments are in good agreement with a tectonic or seismic control of turbidity currents generation. The best example that illustrates this assumption is the site where core KS06 was collected. First of all, from a morphological point of view, this site corresponds to a small isolated intra-slope basin apart from any onland drainage system such as canyon head or turbiditic channels. As previously described, the seismic facies

of this basin shows a gentle surface with stratified reflectors that suggest basin-fill sediment. The core analysis of KS06 concluded that the dominant sedimentary facies is a fine-grained turbidite (turbidite facies *TIIIa*) interbedded with hemipelagite (Facies I) (Fig.3.10, 3.11). The detailed analysis of the coarse fraction contents of turbidite layers shows that these layers are essentially biogenic (Fig.3.12). This biogenic fraction contains mostly planktonic foraminifers, sponge spicules and relatively scarce benthic foraminifera. We suspect that the material was stored on the adjacent slope before it was destabilized, transported and deposited downslope after slope failure event. Moreover, among the element showing sequence changes, Ca and Fe are the most common. Fe and Ca are often used in marine core analysis as detrital and biogenic calcareous proxies respectively (Gràcia et al., 2010). As previously described, the turbidite facies *TIIb*, that mainly characterizes core KS06, shows strong positive anomalies in Ca (relative to the background signal, see Fig.3.12) and a relative depletion in Fe. These two signals are perfectly anticorrelated (Fig.3.12). This geochemical signature corroborates the biogenic calcareous content observed in the turbidite and thus suggests a negligible input from terrigenous material. Finally, we have shown that in the vicinity of site KS06 intense mass wasting occurred (Fig.3.3, 3.4, 3.5, 3.6). This suggests important slope instabilities due to tectonic oversteepening and earthquake shaking since this area is extremely active and dissected by reverse faults (Malavieille et al., 2002). We assume that turbidites recorded in core KS06 are likely under tectonic and/or seismic control.

Following the same approach, we can consider that the intense seismic activity in the Ryukyu margin may generate mass wasting evolving into turbidity currents. Our morphology analysis showed that the slope of the Ryukyu Arc is affected by slope failures. Cores KS08 and KS09 are characterized by fine-grained turbidites (Facies *TI* and *TIIIa* respectively) and located on sedimentary levees (channel-levees system and canyon levee respectively). These two facies (*TI* and *TIIIa*) are characterized by a similar lithogenic composition but express a relative difference in term of grain size signature that suggests different flow dynamics. The chemical signature of these two facies is not as clear as the signature of facies *TIIb* although slight positive anomalies in Fe and depletion in Ca is observed in facies *TI* (Fig.3.11) suggesting that there, the terrigenous input might be significant. We thus conclude that both tectonic and climatic effects might be responsible of turbidity currents generation and deposition in the vicinity of the Ryukyu Arc.

Climatic control

Flood-induced turbidity currents is often recognized to result from hyperpycnal flow generation

in which the density of the river charge is more important than the surrounding seawater (Mulder et al., 2003). In Taiwan, the rivers draining the orogen commonly discharge suspended sediment to the ocean at hyperpycnal conditions (Dadson et al., 2005) especially during typhoon-induced floods. In eastern Taiwan, the Taitung Canyon and the Hualien canyon are the only two canyons that have received important river sediment fluxes at hyperpycnal concentrations (Dadson et al., 2005). As previously described, the SLT is a proximal basin where major rivers deliver sediment discharges during extreme floods and typhoon events (Fig.3.3A). Moreover, we previously showed that the seafloor of the SLT is characterized by a well-developed turbiditic system suggesting a major impact of climatic activity. However, in the SLT no deposits indicate any hyperpycnal conditions. Indeed, hyperpycnites are characterized by a coarsening upward at their base (Mulder et al., 2003), whereas turbidites described in core KC03A are not. Facies *TIII*, representative of most turbidites of SLT, shows classical turbidite deposition (i.e fining-upward sequence) with sandy basal unit. Facies *TIII* is generally interbedded with very thin Facies I (Fig.3.10) and shows that KC03A is characterized by stacked turbidites. Stacked turbidites may suggest high events frequency that could correspond to flood that occur during the Asian monsoon season and typhoon activity that struck the east coast of Taiwan periodically. To conclude, according to, the climatic context with intense flooding, the morphology with major rivers directly connected to the oceanic basin and Facies III characteristics associated to core KC03A, we deduce that the SLT is mainly control by flood-induced turbidites.

In summary, the combined geophysical and sedimentological approaches used in this study have allowed us to observe that the offshore eastern Taiwan is characterized by a variety of sedimentary facies and erosional sedimentary processes from slided masses to turbidity currents. We have shown that turbidity current is the dominating sedimentary facies (covering nearly 60% of the study area) in such active margin. In addition, according to the submarine morphological context, turbidity currents are generated by distinct controlling factors such tectonic and climatic activity. This enable us to define at least two end-members relative to turbidity currents initiation:

- Turbidity currents preconditioned by tectonic activity (oversteepening) and triggered by earthquakes shaking that initiate slope instabilities and likely deposited into isolated intra slope basin
- Turbidity currents likely driven by climatic activity such as extreme flood during typhoon, generated in close basin context directly connected with onland rivers

Finally, we highlight the fact that our results indicate, that offshore eastern Taiwan offers a great potential in investigating the records of (paleo)extreme events at margin-scale.

3.7 Acknowledgments

We would like to thank Ching-Hui Tsai (NCU, Taiwan) Tei-Qei Lee (IES, Taiwan), Yinson Huang (IES, Taiwan), Shun-Wen Yu (NCU, Taiwan), Mo-Tsi Tsai (NCU, Taiwan), Don Su (NTU, Taiwan), Kuo-Yen Wei and his students (NTU, Taiwan), TORI workers, Stephane Dominguez (Montpellier Univ., France), Lucas Messales (UPMC, France), Slawek Giletycz (NCU, Taiwan), Irene Castro and many others who offered their help, advices, technical and expertise support. We are also grateful to the Captain and crew of the R/V Ocean Researcher I for their efficiency during the ORI-1013 and ORI-1048 surveys.

List of figures

- Figure1: A: Geodynamic context of Taiwan and plate boundaries, the box represents a zoom on the study area shown in B. CCM= Chinese Continental Margin, HR= Hsuechan Range, DF= Deformation Front, LF= Lishan Fault, LVF= Longitudinal Valley Fault, CP= Coastal Plain, CR= Central Range, HP= Hengchun Peninsula, SCS= South China Sea, MT= Manila Trench, CoR= Coastal Range; B: Recent sedimentary systems offshore eastern Taiwan showing the main active canyons and the actual drainage system. In yellow boxes are represented the river discharge in Mt/yr after (Liu et al., 2008). HB=Hoping Basin, NB=Nanao Basin, SLT= Southern Longitudinal Trough.
- Figure2: Location of seismic, CHIRP profiles and sedimentary cores.
- Figure3: A. Backscatter imagery of the southern sector. The circles represent the sedimentary cores. Boxes indicate zoom on high resolution DEM; B: Morphosedimentary mapping based on backscatter imagery, seismic and CHIRP data and high resolution DEM. The annotated circles represent the east coast rivers: 1. Xuhai river, 2. Daren river, 3. Dawu river, 4. Nangxi river, 5. Jinlun river, 6. Taimali river, 7. Zhiben river, 8. Taiping river, 9. Beinan river, 10. Donghe river; C: CHIRP profile across the SLT, showing acoustic facies of sedimentary levee; D: high resolution DEM across the SLT showing the well-developed channel-levee system.

- Figure4:A: Zoom on high resolution DEM showing submarine landslides affecting the Taitung Canyon (L4), the slope of the Luzon Arc (L3, L2) and the Huatung Ridge (L1); B: Seismic reflection profil across the Taitung Canyon (S2), showing the slope affected landslides on the Luzon Arc and the Huatung ridge. The levees of the Taitung Canyon are also well observable.
- Figure5:A: Backscatter imagery of the central sector; B: Mapping of the central sector, using backscatter imagery, seismic data and bathymetry data. Annotated circles represent all the rivers identified in that sector. 9. Beinan river, 10. Donghe river, 11. Sanxiantan river, 12. Wushibi river, 13. Baxiandong river, 14. Xiukuluan river, 15. Hualien river, 16. Liwu river.
- Figure6:A: High resolution DEM showing area affected by landslides on the deforming Luzon arc; B: Seismic reflection profiles and CHIRP profile displaying seismic facies of landslide and stratified units of the basin-fill sediment respectively.
- Figure7:A: High resolution DEM showing the Chimei turbiditic system with landslide affecting the northern flank of the deep sea fan and bathymetric highs; B: CHIRP profiles imaging the bathymetric high.
- Figure8:A: Backscatter imagery of the northern sector; B: Mapping of the northern sector using backscatter imagery, seismic profiles and high resolution DEM. Annotated circles represent east coast rivers identified. 16. Liwu river, 17. Hoping river, 18. Nanao river.
- Figure9: High resolution DEM on the Ryukyu arc area showing landslides affecting the slope of the arc. B: CHIRP profiles displaying sedimentary levees.
- Figure10: Sedimentological description of cores.
- Figure11: Characterization of sedimentary facies using grain size distribution, X-Rays and chemical analysis.
- Figure12: Photography and relative composition (%) of the different turbidite facies identified corresponding to the coarser beds of turbidite sequences (fraction $>150\mu\text{m}$).

List of tables

- Table1: List of available seismic lines in the study area. 1:(Schnürle et al., 1998b); 2:(Mcintosh and Nakamura, 1998); 3:(Wang and Chiang, 1998); 4:(Font et al., 2001); 5:(Hetland and Wu, 2001); 6:(Wang et al., 2004); 7:(McIntosh et al., 2005); 8:(Font and Lallemand, 2009); 9:(Lallemand et al., 1997b); 10:(Lallemand et al., 1999); 11:(Malavieille et al., 2002); 12:(Ramsey et al., 2006); 13:(Lallemand et al., 2013)
- Table2: List of the sedimentary cores used in this study; 1:(Bentahila et al., 2008), 2:(Huang et al., 1992), 3: (Huh et al., 2004)

Table 3.1: List of available seismic lines in the study area. 1:(Schnürle et al., 1998b); 2:(Mcintosh and Nakamura, 1998); 3:(Wang and Chiang, 1998); 4:(Font et al., 2001); 5:(Hetland and Wu, 2001); 6:(Wang et al., 2004); 7:(McIntosh et al., 2005); 8:(Font and Lallemand, 2009); 9:(Lallemand et al., 1997b); 10:(Lallemand et al., 1999); 11:(Malavieille et al., 2002); 12:(Ramsey et al., 2006); 13:(Lallemand et al., 2013).

Vessel	Year	Survey	References
Ocean Researcher1	1993	OR1-376	9
Ocean Researcher1	1996	OR1-446	4, 8
L'Atalante	1996	ACT96	10, 11, 12
Maurice Ewing	1995	EW-9509	1, 2, 3, 4, 5, 6, 7, 8
Ocean Researcher1	2009	OR1-886	<i>This study</i>
Ocean Researcher1	2009	OR1-914	<i>Unpublished</i>
Ocean Researcher1	2010	OR1-960	<i>This study</i>
Marcus Langseth	2009	MGL-0905	13
Ocean Researcher1	2012	OR1-1013	<i>This study</i>

Table 3.2: List of the sedimentary cores used in this study; 1:(Bentahila et al., 2008), 2:(Huang et al., 1992), 3: (Huh et al., 2004)

Vessel	Year	Survey	References
Vema	1976	VM-33	1
Ocean Researcher1	1989	OR1-231/232	2
Ocean Researcher1	1996	OR1-687	3
Ocean Researcher1	2009	OR1-960	<i>Unpublished</i>
Ocean Researcher1	2012	OR1-1013	<i>This study</i>
Ocean Researcher1	2013	OR1-1048	<i>This study</i>

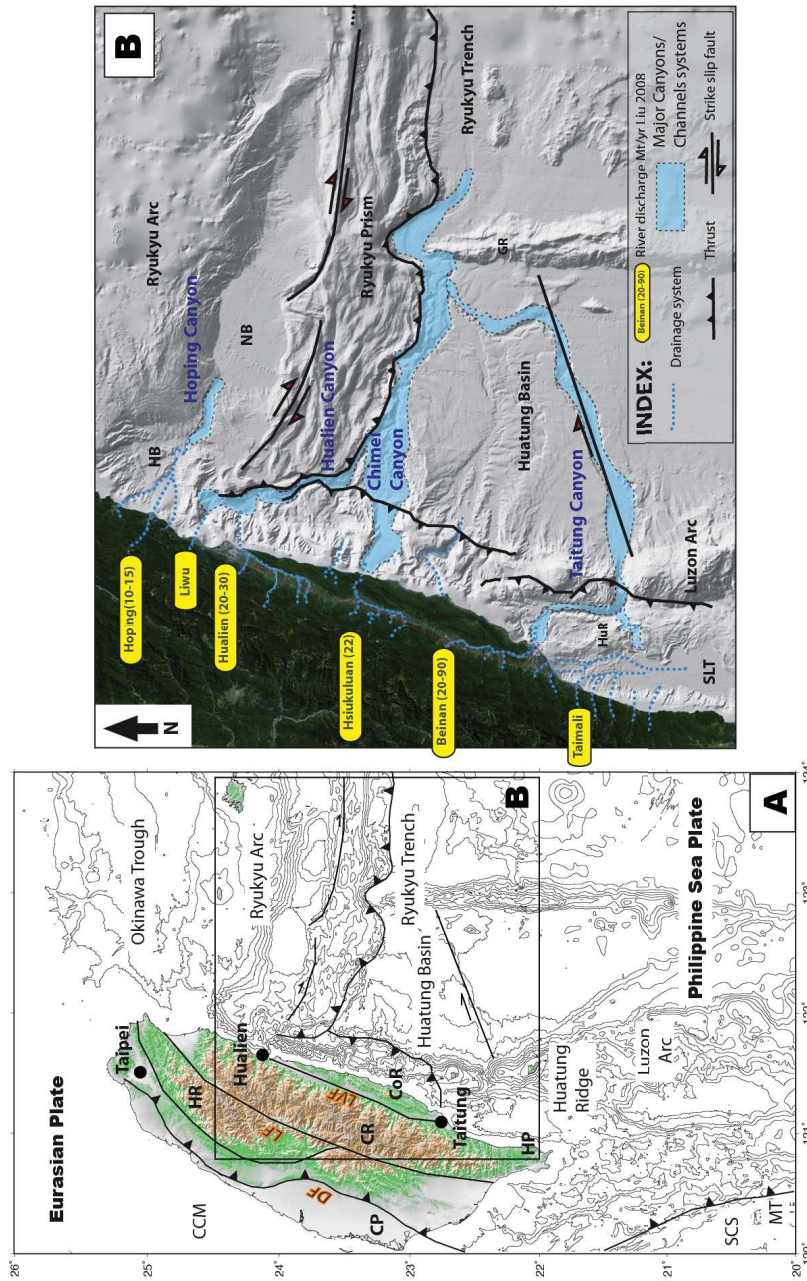


Figure 1.

Figure 3.1: A: Geodynamic context of Taiwan and plate boundaries, the box represents a zoom on the study area shown in B. CCM= Chinese Continental Margin, HR= Hsuechan Range, DF= Deformation Front, LF= Lishan Fault, LVF= Longitudinal Valley Fault, CP= Coastal Plain, CR= Central Range, HP= Hengchun Peninsula, SCS= South China Sea, MT= Manila Trench, CoR= Coastal Range; B: Recent sedimentary systems offshore eastern Taiwan showing the main active canyons and the actual drainage system. In yellow boxes are represented the river discharge in Mt/yr (after Liu et al., 2008). HB=Hoping Basin, HR=Hoping Rise, NB=Nanao Basin, NR= Nanao Rise, ENB=East Nanao Basin, HpC=Hoping Canyon, HC=Hualien Canyon, CC=Chimei Canyon, SLT= Southern Longitudinal Trough, TC=Taitung Canyon.

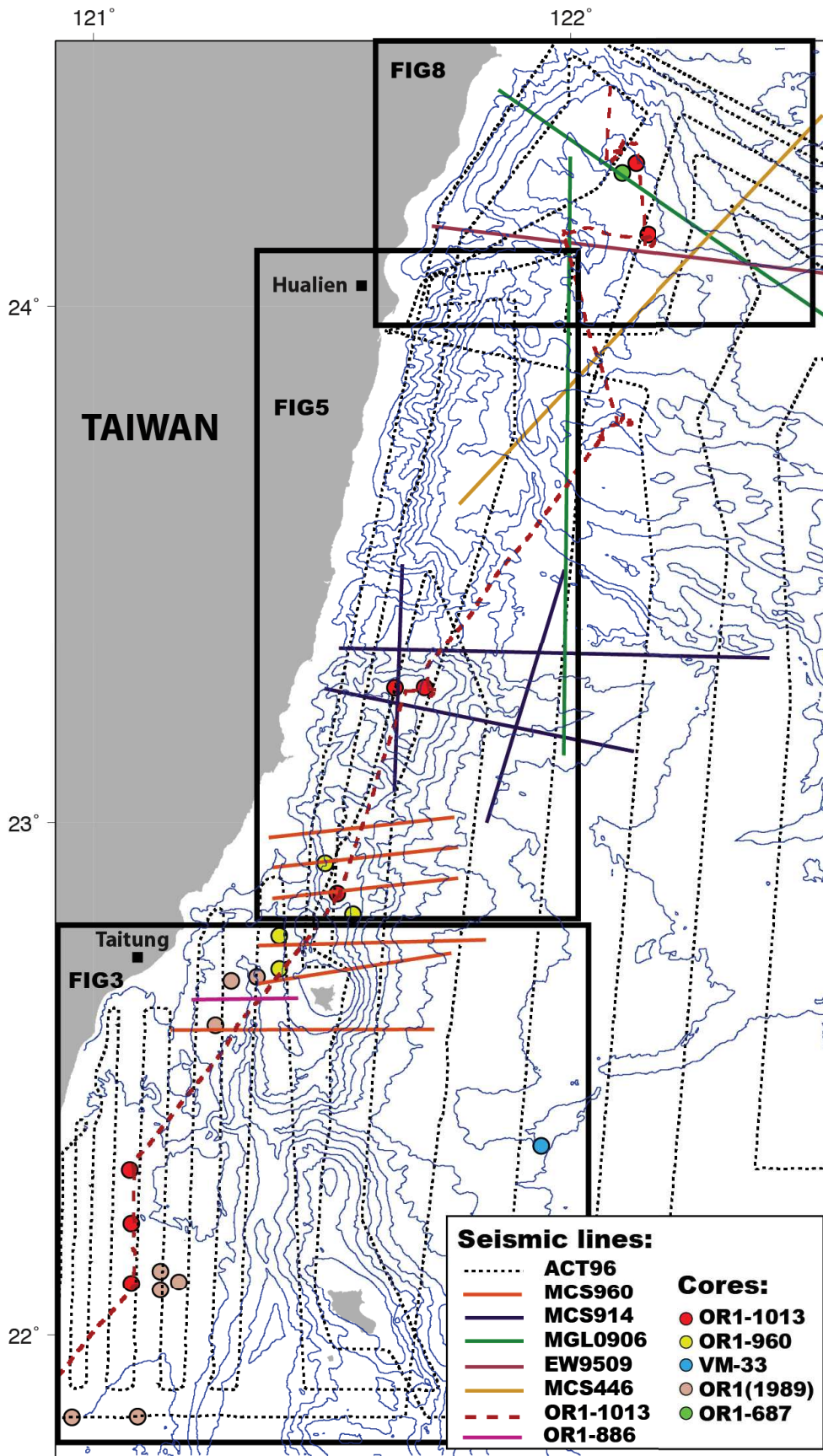


Figure 2.

Figure 3.2: Location of seismic, CHIRP profiles and cores materials.

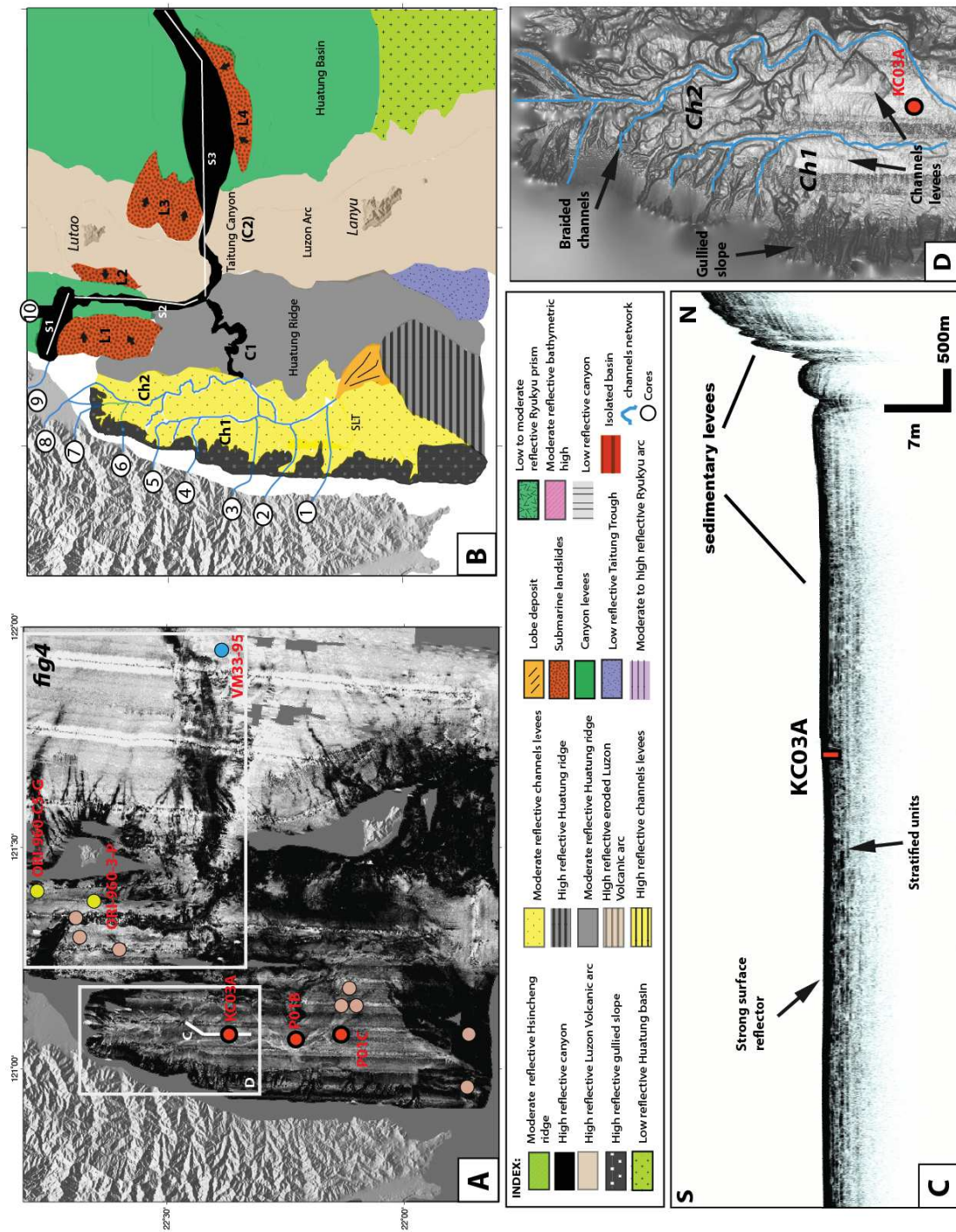


Figure 3.

Figure 3.3: A. Backscatter imagery of the southern sector. The circles represent the sedimentary cores. Boxes indicate zoom on high resolution DEM; B: Morphosedimentary mapping based on backscatter imagery, seismic and CHIRP data and high resolution DEM. The annotated circles represent the east coast rivers: 1. Xuhai river, 2. Daren river, 3. Dawu river, 4. Nangxi river, 5. Jinlun river, 6. Taimali river, 7. Zhiben river, 8. Taiping river, 9. Beinan river, 10. Donghe river; C: CHIRP profile across the SLT, showing acoustic facies of sedimentary levee; D: high resolution DEM across the SLT showing the well-developed channel-levee system.

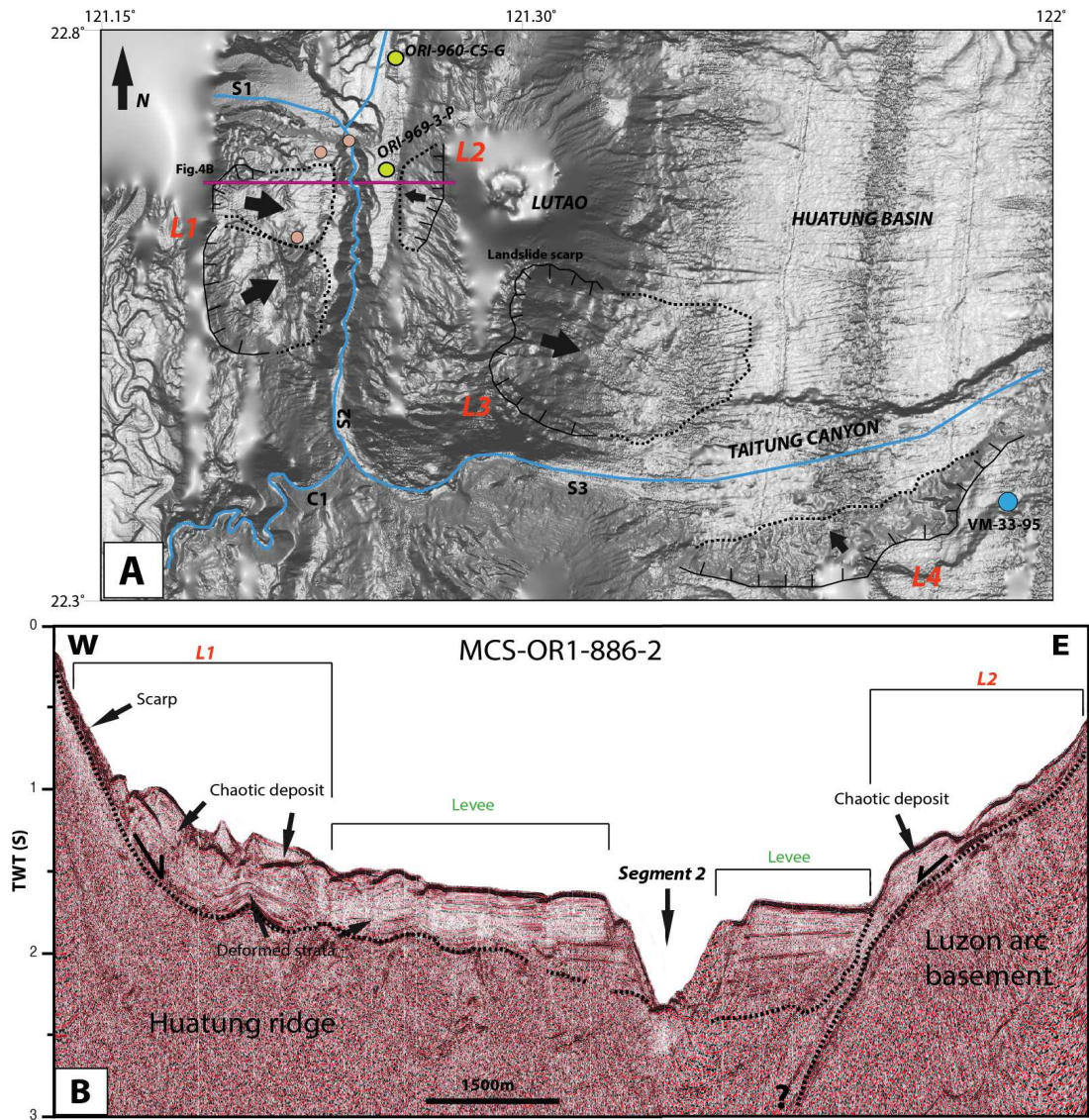


Figure 4.

Figure 3.4: A: Zoom on high resolution DEM showing submarine landslides affecting the Taitung Canyon (L4), the slope of the Luzon Arc (L3, L2) and the Huatung Ridge (L1); B: Seismic reflection profile across the Taitung Canyon (S2), showing the slope affected landslide on the Luzon Arc and the Huatung ridge. The levee of the Taitung Canyon are also well observable.

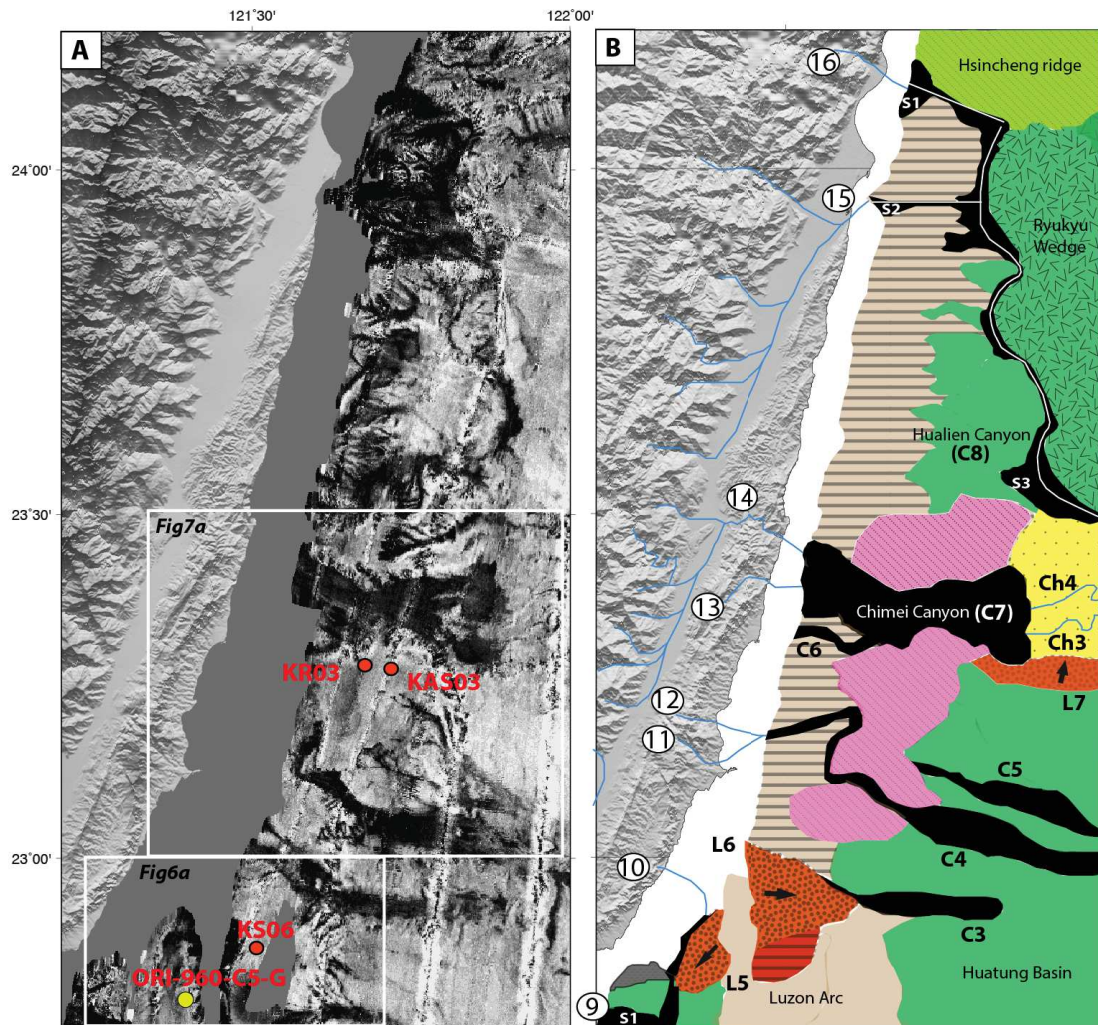


Figure 3.5.

Figure 3.5: A: Backscatter imagery of the central sector; B: Mapping of the central sector, using backscatter imagery, seismic data and bathymetry data. Annotated circles represent all the rivers identified in that sector. 9. Beinan river, 10. Donghe river, 11. Sanxiantan river, 12. Wushibi river, 13. Baxiandong river, 14. Xiukuluan river, 15. Hualien river, 16. Liwu river.

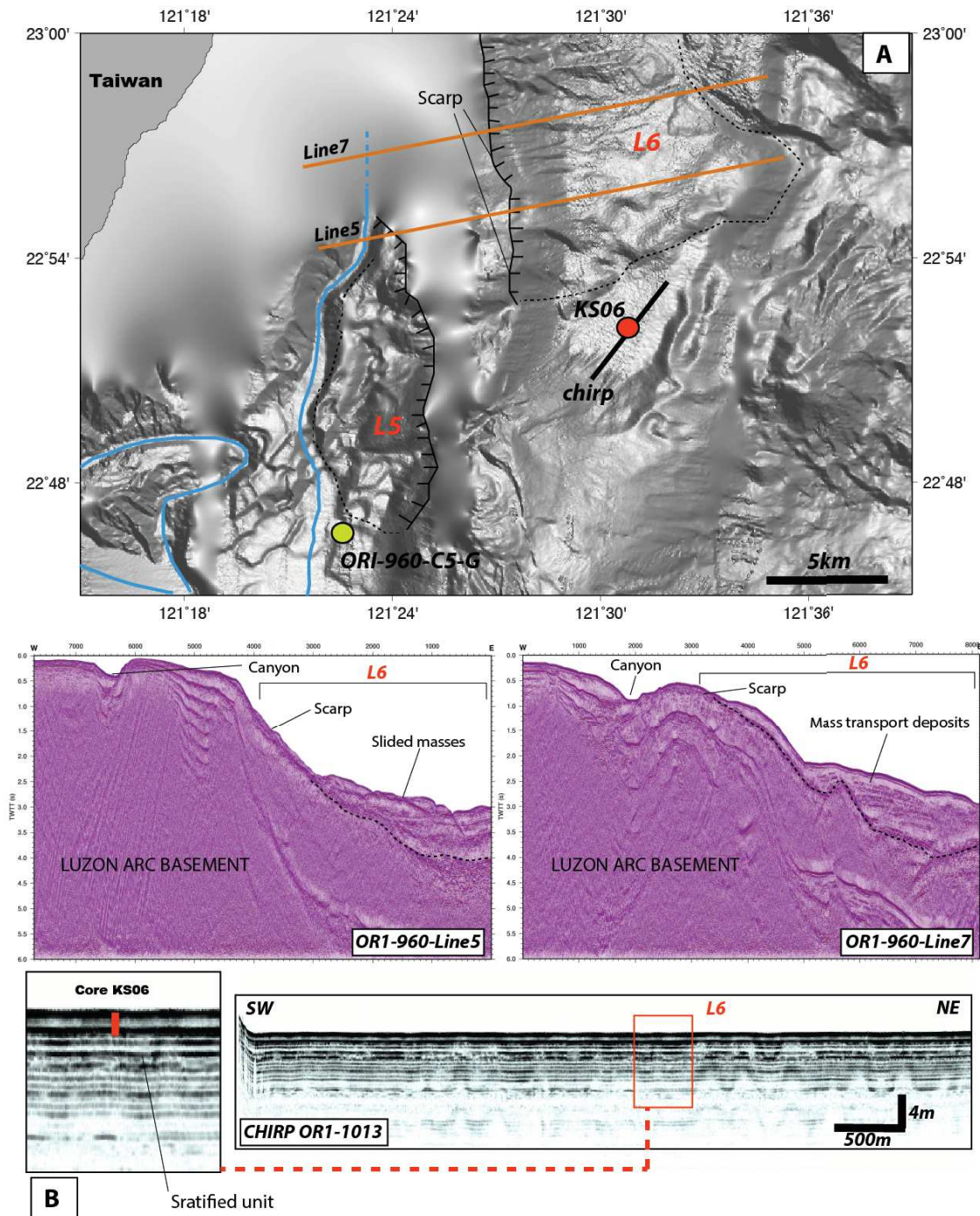


Figure 6.

Figure 3.6: A: High resolution DEM showing area affected by landslides on the deforming Luzon arc; B: Seismic reflection profiles and CHIRP profile displaying seismic facies of landslide and stratified units of the basin-fill sediment respectively.

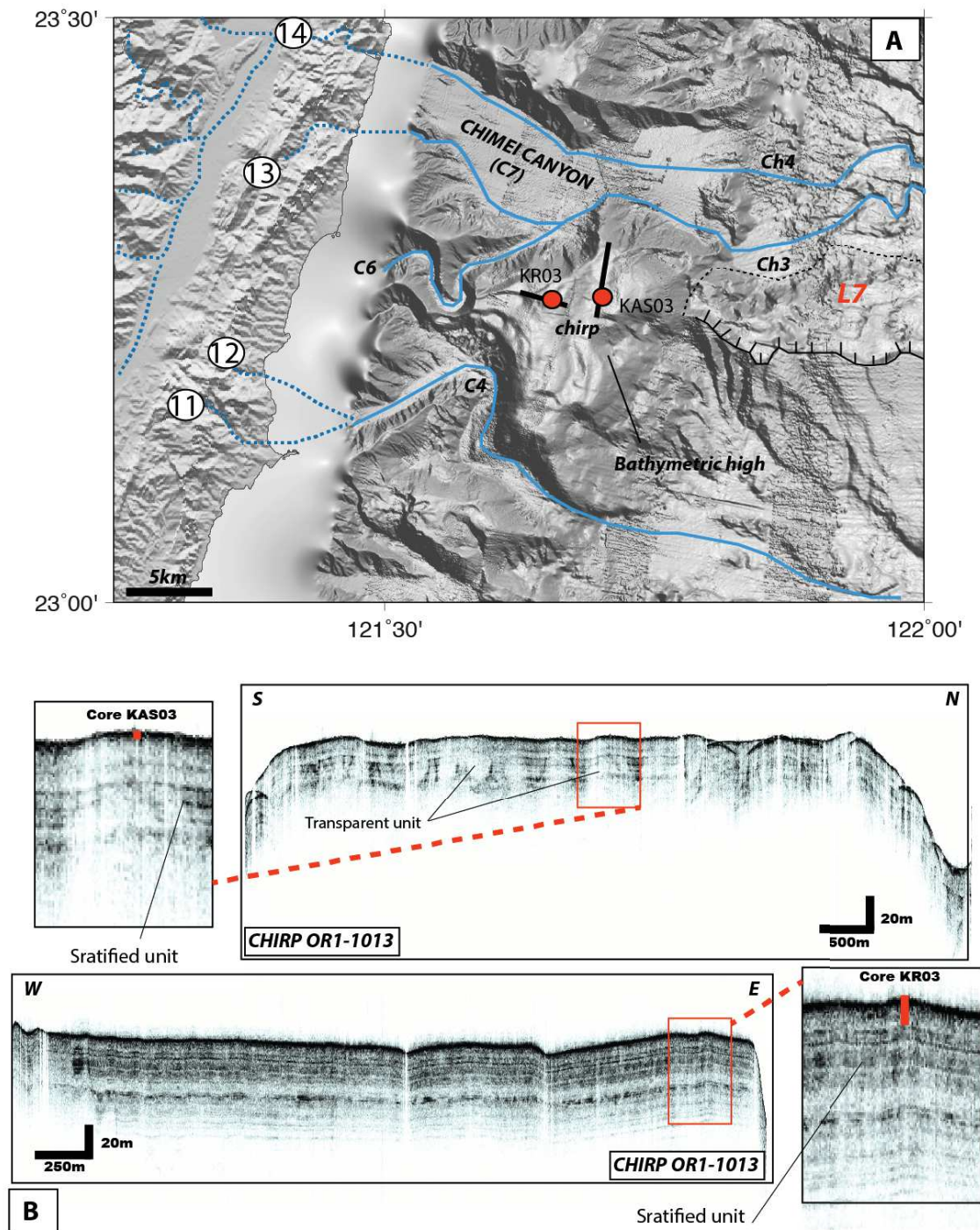


Figure 7.

Figure 3.7: A: High resolution DEM showing the Chimei turbiditic system with landslides affecting the northern flank of the deep sea fan and bathymetric highs; B: CHIRP profiles imaging the bathymetric high.

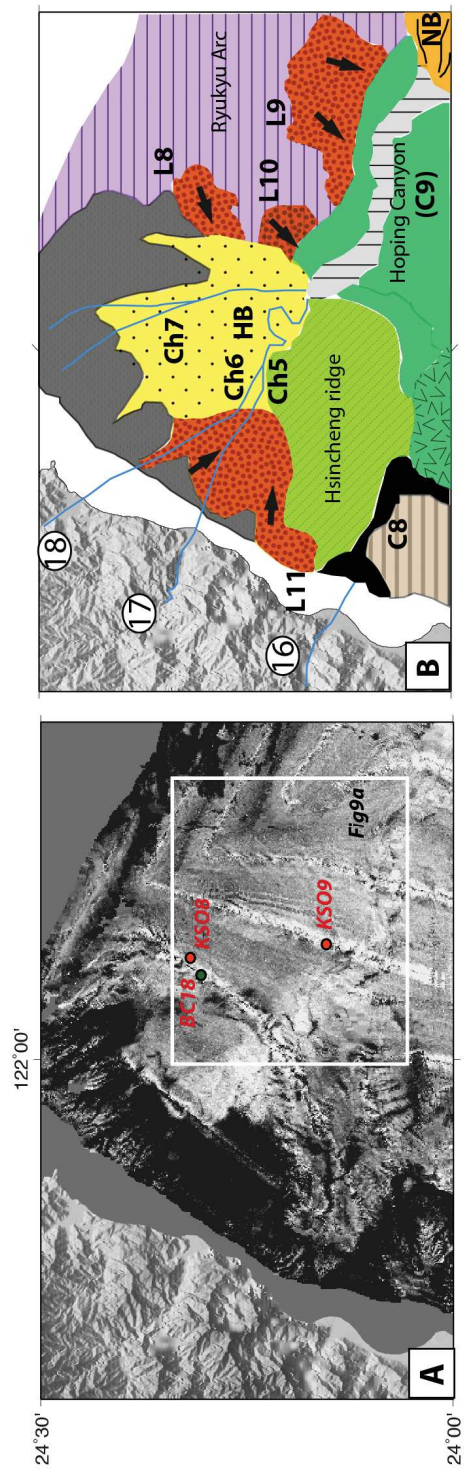


Figure 8.

Figure 3.8: A: Backscatter imagery of the northern sector; B: Mapping of the northern sector using backscatter imagery, seismic profiles and high resolution DEM. Annotated circles represent east coast rivers identified. 16.Liwu river, 17. Hoping river, 18. Nanao river.

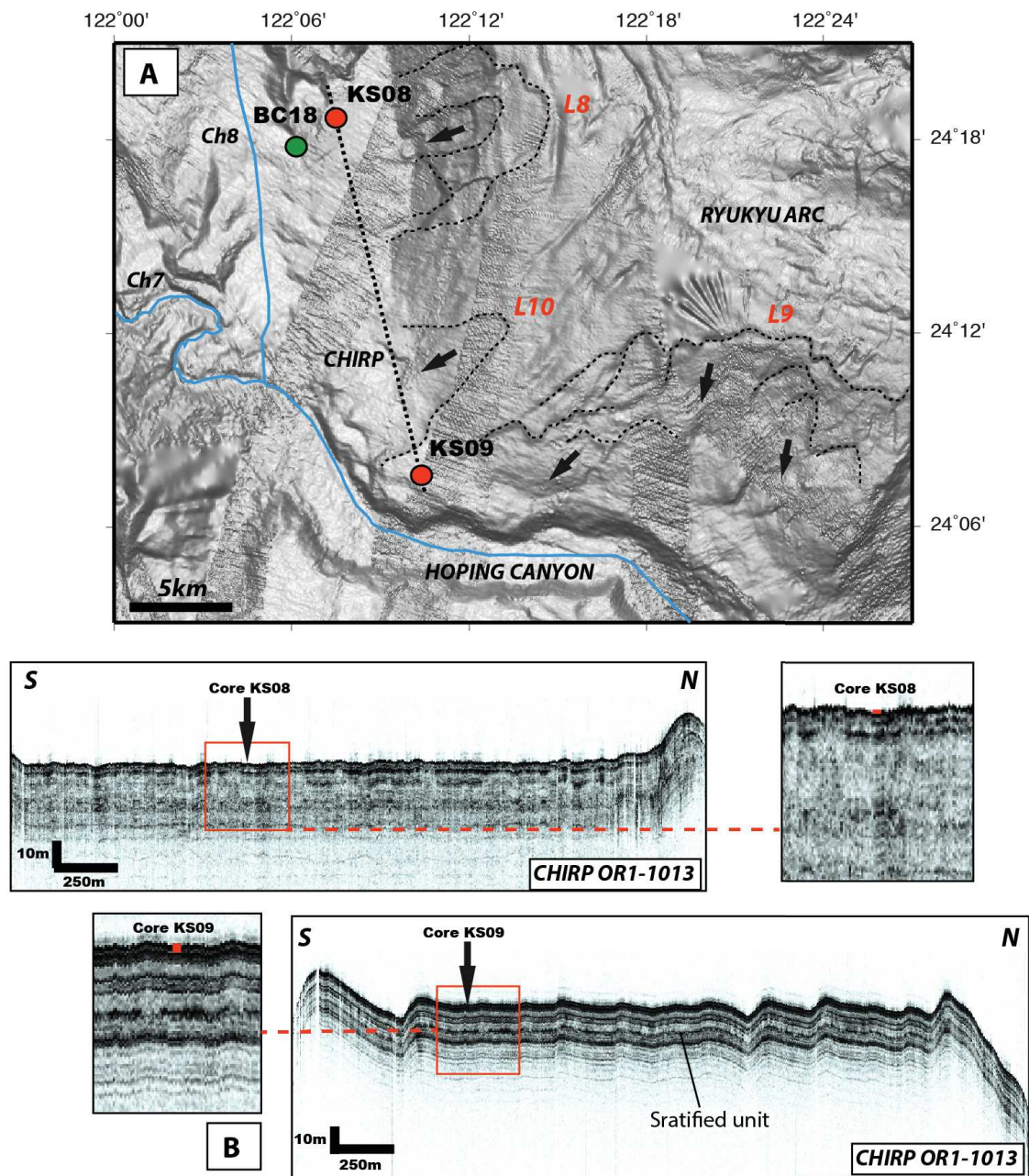


Figure9.

Figure 3.9: High resolution DEM on the Ryukyu arc area showing landslides affecting the slope of the arc. B: CHIRP profiles displaying sedimentary levees.

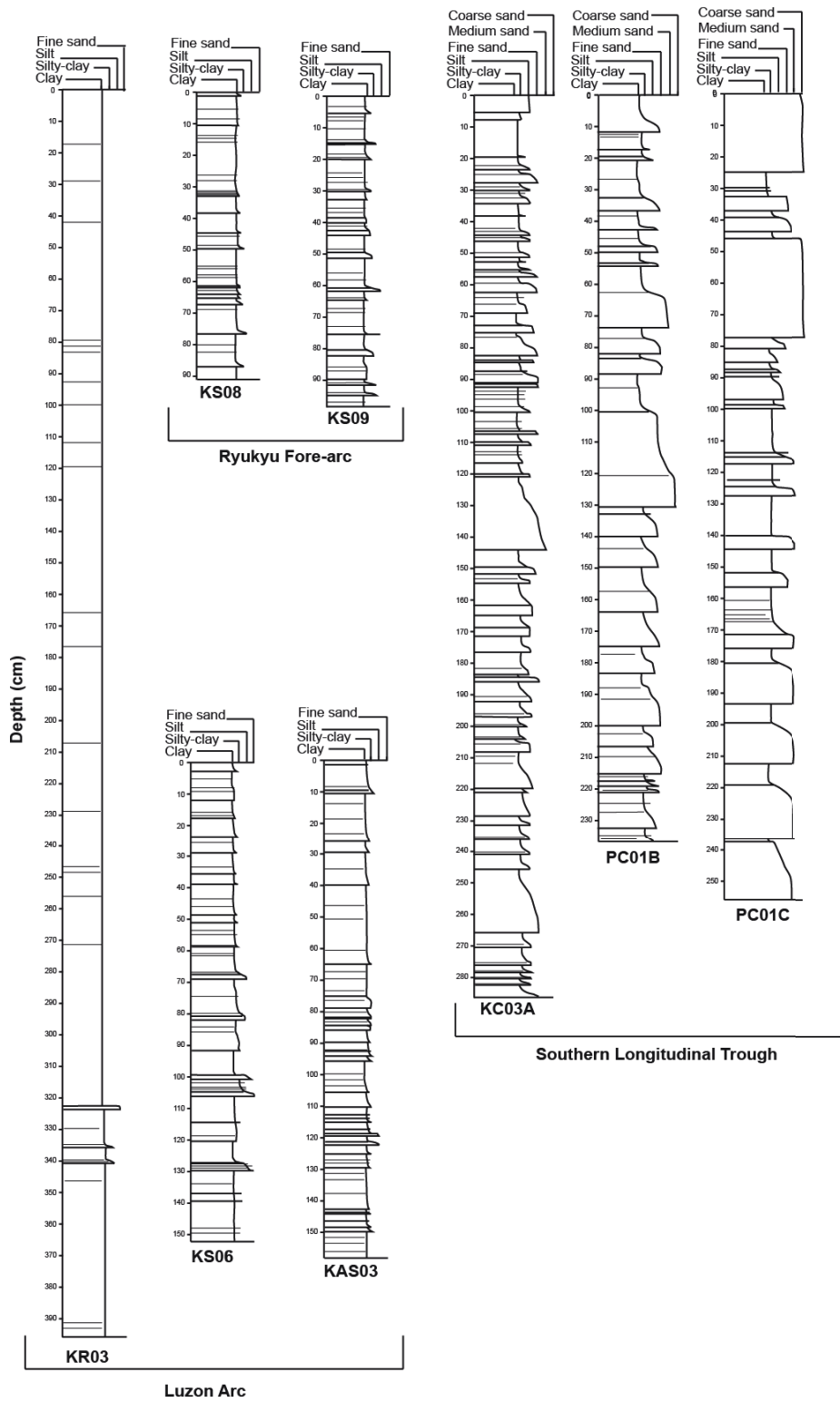


Figure10.

Figure 3.10: Sedimentological description of cores.

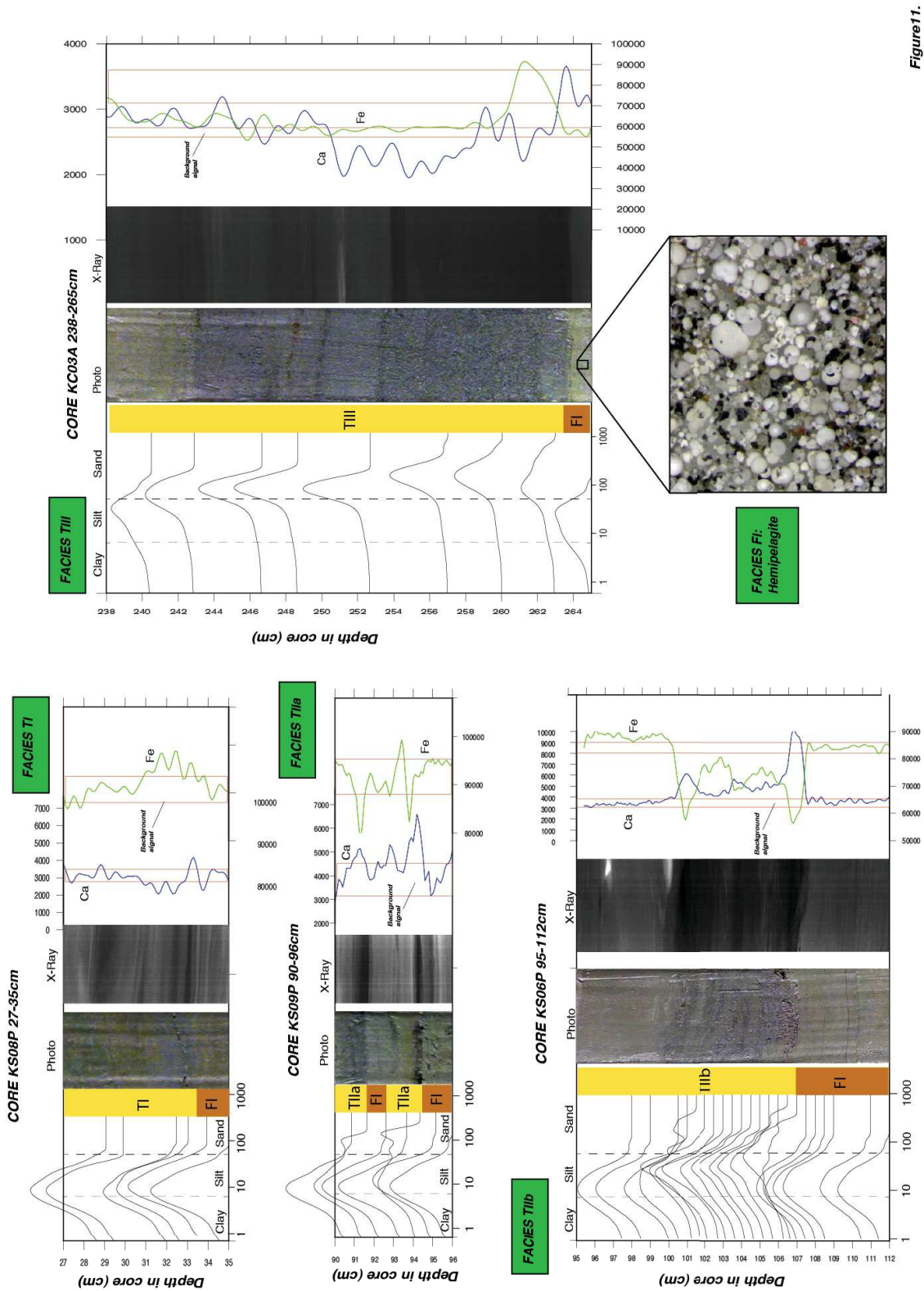


Figure 11.

Figure 3.11: Characterization of sedimentary facies using grain size distribution, X-Rays and chemical analysis.

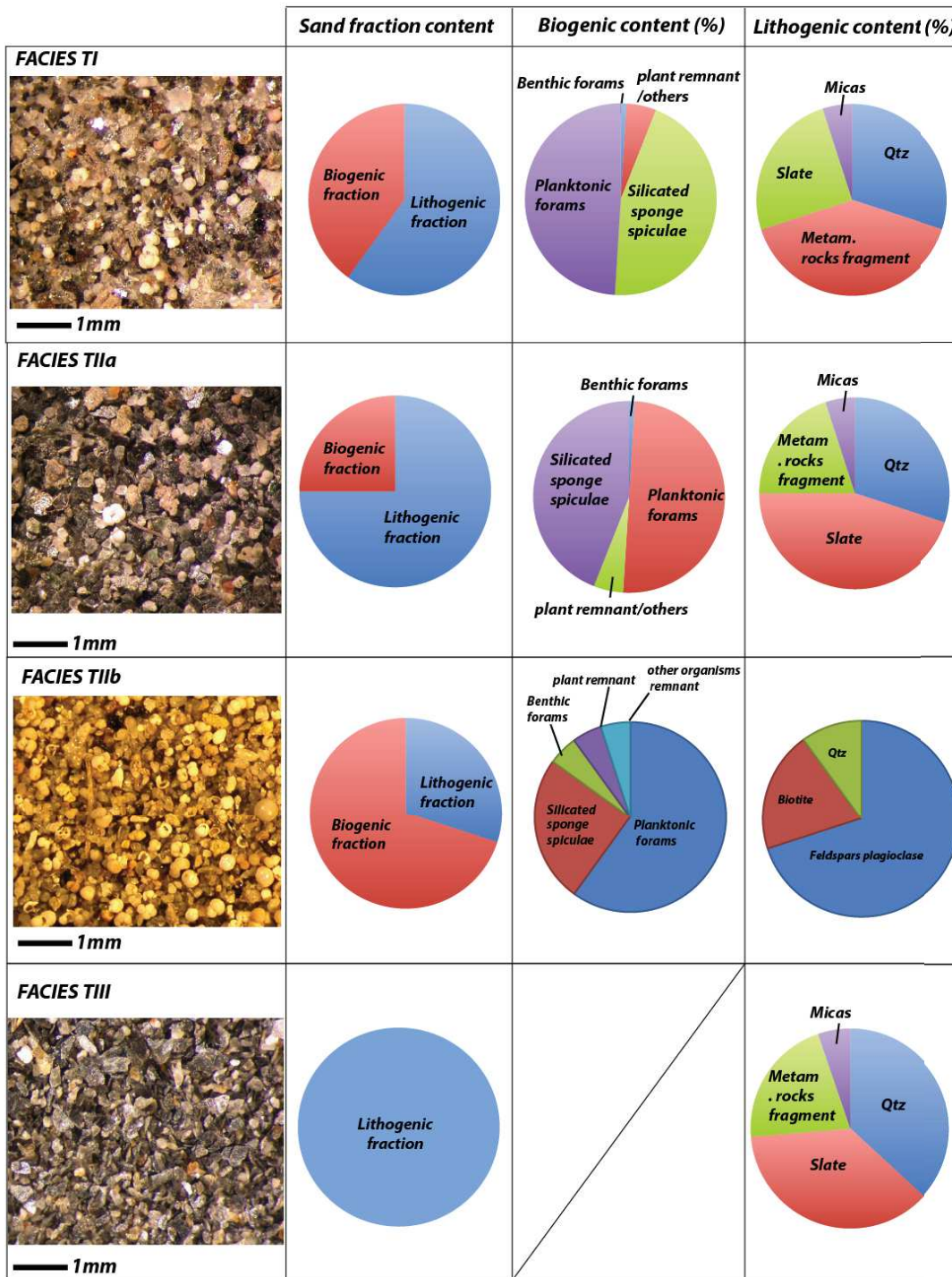


Figure 12.

Figure 3.12: Photography and relative composition (%) of the different turbidites facies identified corresponding to the coarser beds of turbidites sequences (fraction >150 μm).

Part II

Testing a paleoseismological approach offshore eastern Taiwan

Background

Contents

4.1	Turbidites deposits as a marker of paleoseismicity	93
4.2	Datings proxies	96

4.1 Turbidites deposits as a marker of paleoseismicity

As described previously in the **Part I** of this thesis, mass movements are often triggered by earthquakes. Once the deposits are preserved, they may constitute excellent markers of paleoseismicity. Among them, the coseismic turbidites provide the best paleoseismic proxy. This method consists on the identification and dating of the turbidites triggered by an earthquake (Goldfinger et al., 2003, 2007; Gràcia et al., 2010; Polonia et al., 2013). This method is relatively recent since it has been developed on turbidites deposits of the Cascadia margin, western USA during the nineties (Adams, 1990). However, to link the triggering mechanism of turbidity currents to an earthquake and find good discriminant criteria still remains problematic. Since the last decades, several studies have proposed criteria in order to distinguish "seismoturbidites" from "normal" turbidites.

Nakajima and Kanai (2000) and Shiki et al. (2000) established sedimentological criteria. Once they could correlate their turbidites record with instrumental earthquakes (e.g, eastern margin of the Japan Sea in 1983, M_w 7.9), they noticed that the organization of these turbidites differed from the Bouma sequence (Fig.4.1). These seismoturbidites are characterized by amalgamated beds, irregular structure sequences, grain-size breaks or fluctuation, abrupt changes in composition within bed, and variable composition among beds. From these features, these authors inferred that deposition resulted from a series of turbidity currents associated with multiple sources, for example multiple slides that were regionally initiated by the same earthquake.

	"Normal" turbidites	"Seismoturbidites"
Sedimentary structures	Single bed, Bouma sequence	Amalgamated beds, irregular or incomplete sequence
Grain size variation	Normal grading	Normal grading, inverse grading, grain size break, fluctuation
Compositional variation	Uniform composition between beds, continuous change within bed	Variable composition between beds \pm abrupt change within bed
Source	Single source	Multiple or line sources
Inferred depositional process	Deposition from single waning turbidity current	Deposition from a series of surge-type or sustained turbidity currents from the same or different sources

Figure 4.1: Characteristic features of seismoturbidites and comparison with "normal turbidites" (after Nakajima and Kanai, 2000).

Gorsline et al. (2000), proposed that seismoturbidites characterized in Santa Monica Basin, California and in Alfonso Basin, western Gulf of California may involve a higher volume of sediment than those from other triggering mechanisms. The flood-generated turbidites are typically a fifth or less of the volume of the earthquake-generated turbidites (Fig.4.2).

Identification	Age	Area (km ²)	Thickness (cm) ^a	Volume (km ³) ^b	Type
A	1969	460	2.0	0.010	Flood
B1	1880s	350	4.0	0.015	Flood
B2	1860s	350	4.0	0.015	Flood
C	1812	1200	5.0	0.055	Seismic
D	1700	1170	5.5	0.058	Seismic
E	1500s	1400+	5.0	0.075	Seismic
F	1400s	1400+	6.5	0.105	Seismic

^a Thickness is average of basin-wide range of thicknesses.

^b Here 1 m³ is approximately 1 ton of sediment at typical bulk density of uncompacted sediment.

Figure 4.2: Data for turbidites in Santa Monica basin cores, showing the difference of volume between earthquake-generated turbidites and "normal turbidites" (after [Gorsline et al., 2000](#)).

[Goldfinger et al. \(2003\)](#), proposed a new concept to distinguish the seismically-triggered turbidites in the Cascadia margin. They showed that for a large portion of the margin, the **synchronicity** of turbidites deposits in independant sedimentary systems, is a relevant marker of a seismic trigger (Fig.4.3). Since that, several authors used this argument to confirm that synchronous turbidites correspond to an earthquake signature ([Gràcia et al., 2010](#); [Pouderoux et al., 2012](#); [Polonia et al., 2013](#)).

Other criteria exist as defined by [Noda et al. \(2008\)](#) and [Beck \(2009\)](#), suggesting a typical composition of seismoturbidites (typical fauna assemblage for example). This argument allow to determine the source area of turbidites and to link them to an unique mechanism triggering (i.e earthquake).

These observations described above show the relative complexity to find robust criteria for the recognition between flood-generated turbidites and earthquake-generated turbidites. It seems that existing criteria reflect the intrinsic character of the studied environment and that consequently a "universal criteria" applicable in all systems does not exist. The actual criterion that appear to be the most robust and widely used is the **synchronicity** criterion developed by [Goldfinger et al. \(2003\)](#). Moreover it also shows that the coring strategy (i.e, turbiditic system vs confined or perched basin) in that approach is a crucial parameter and that the choice of sampling sites may exclude the non-seismic trigger.

In the following chapters, we will show that the criterion of synchronicity may be applied offshore eastern Taiwan, while the other existing criteria are not fulfilled.

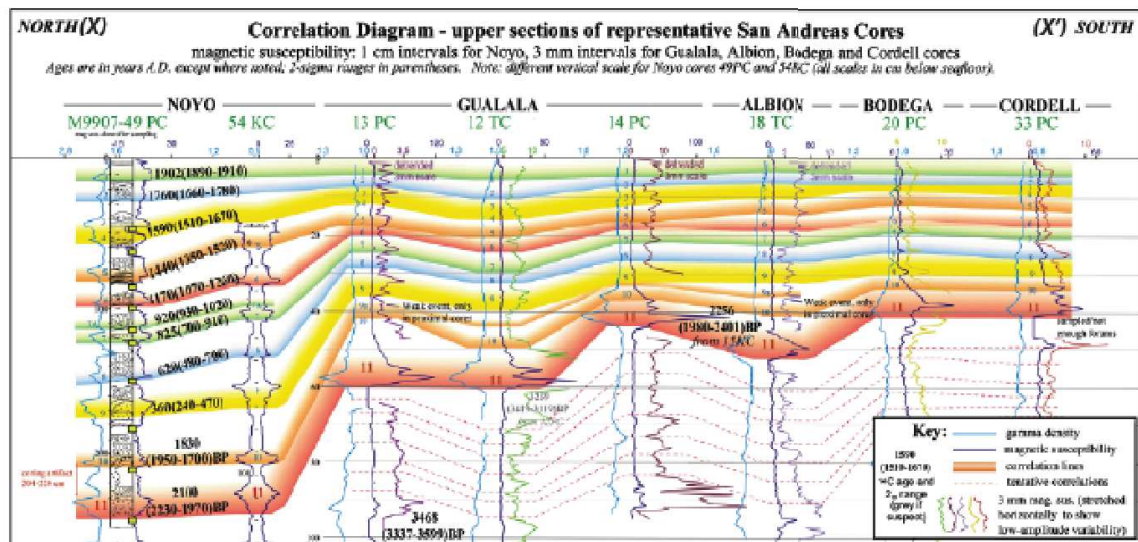
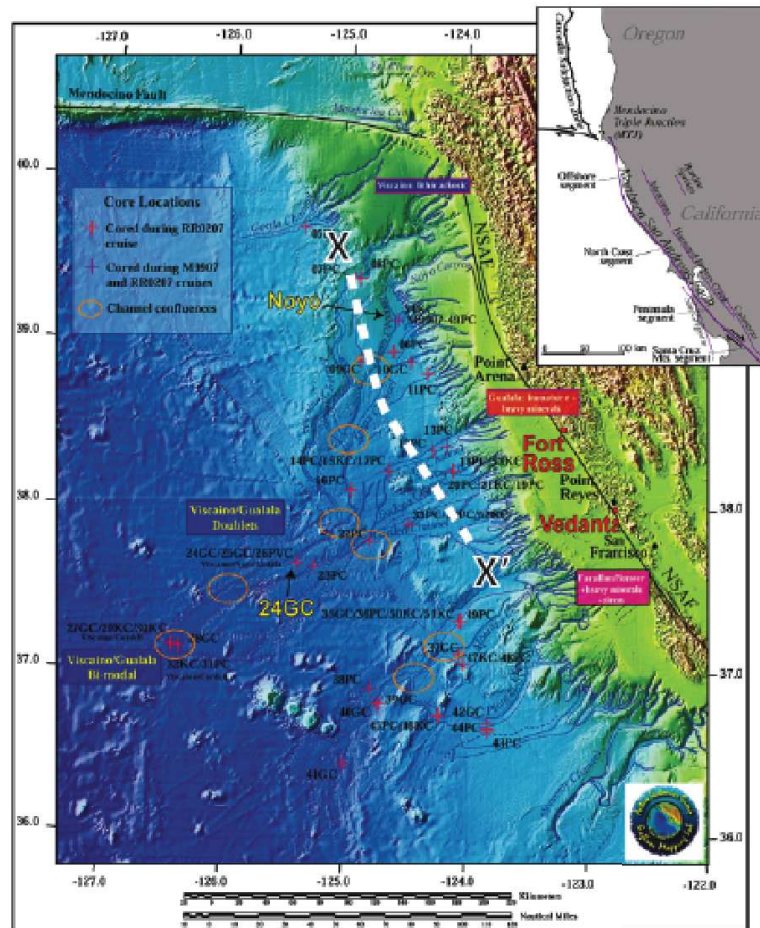


Figure 4.3: Example the synchronicity of turbidite deposits (modified after Goldfinger et al., 2007). The map show the location of cores in different turbiditic systems. In the bottom is showed the correlation (on the latitudinal axis on the map) of turbidites on 5 different turbiditic systems, one color represents one correlated event, a paleo-earthquake.

4.2 Datings proxies

4.2.1 The last century sedimentation: ^{210}Pb and ^{137}Cs proxies

^{210}Pb dating is based on the U/Th series disequilibrium method (Fig.4.4). It uses the fact that the noble gas ^{222}Rn ($T_{1/2}=3.8$ days) escapes from sediments to the atmosphere and then decays to ^{210}Pb ($T_{1/2}=22.3$ years). The particle-reactive ^{210}Pb attached to the aerosols, is deposited, and can be used to date sediments during the last century (~ 100 years). Atmospheric natural fallout of ^{210}Pb is not the only source of ^{210}Pb in sediment. Since most sediments contain U and ^{226}Ra ($T_{1/2}=1600$ years), ^{210}Pb is also naturally produced *in situ* ("supported" ^{210}Pb). Using γ -spectrometry, this part can be determined from ^{214}Pb . The difference between total ^{210}Pb and ^{214}Pb gives the "unsupported" ^{210}Pb further called the ^{210}Pb in excess ($^{210}\text{Pb}_{ex}$) and used for dating. Dating range in natural systems can vary from less than 50 years up to 150 years. Based on the models that predict the distribution of ^{210}Pb with depth, it is possible to date the different sedimentary layers within a sedimentary core and then estimate the sedimentation rate. ^{210}Pb activities are determined using a CAMBERRA γ -spectrometry (see chapter 5 for the description of the method). Several models exist (Appleby and Oldfield, 1992) that allow to calculate sedimentation rate from the ^{210}Pb profiles. The distribution of ^{210}Pb with depth depends on the equilibrium between atmospheric and aqueous transfers, the sedimentation rhythm and bioturbation. The simplest model in the calculation of the sedimentation rate is the CF:CS (Constant Flux, Constant Sedimentation Rate) that supposes a constant ^{210}Pb and accumulation rate, meaning that the initial activity is constant (Goldberg, 1963; Krishnaswamy et al., 1971a). The ^{210}Pb rate P and sedimentation rate W are expressed in $\text{mBq.cm}^{-2}.\text{yr}^{-1}$ and $\text{g.cm}^{-2}.\text{yr}^{-1}$ respectively. The activity A (mBq.g^{-1}) is expressed by $A = P/W$. The ^{210}Pb with depth (z) is given by:

$$(^{210}\text{Pb}_{ex}^z) = (^{210}\text{Pb}_{ex}^0) \times e^{-\lambda t_z} \text{ with } (^{210}\text{Pb}_{ex}) = (^{210}\text{Pb}_{meas}) - (^{226}\text{Ra}_{meas}) \quad (1)$$

Where λ is the radioactive decay constant of the ^{210}Pb : $\lambda = \ln(2)/22.3 \text{ yr.}^{-1}$, $^{210}\text{Pb}_{ex}^z$ is the activity in mBq.g^{-1} at the depth z and $^{210}\text{Pb}_{ex}^0$ is the activity at the surface expressed as P/W . The time t , is the dry sedimentary mass M_z accumulated by cm^2 from the surface to the depth z divided by W , which is the sedimentation rate. If we suppose that the Pb and Ra are immobile in the samples, then we can write from (1):

$$\ln(^{210}\text{Pb}_{ex}^z) = \ln(^{210}\text{Pb}_{ex}^0) - \left(\frac{\lambda^{210}}{W}\right) \times M_z, \text{ with } t_z = \frac{M_z}{W} \quad (2)$$

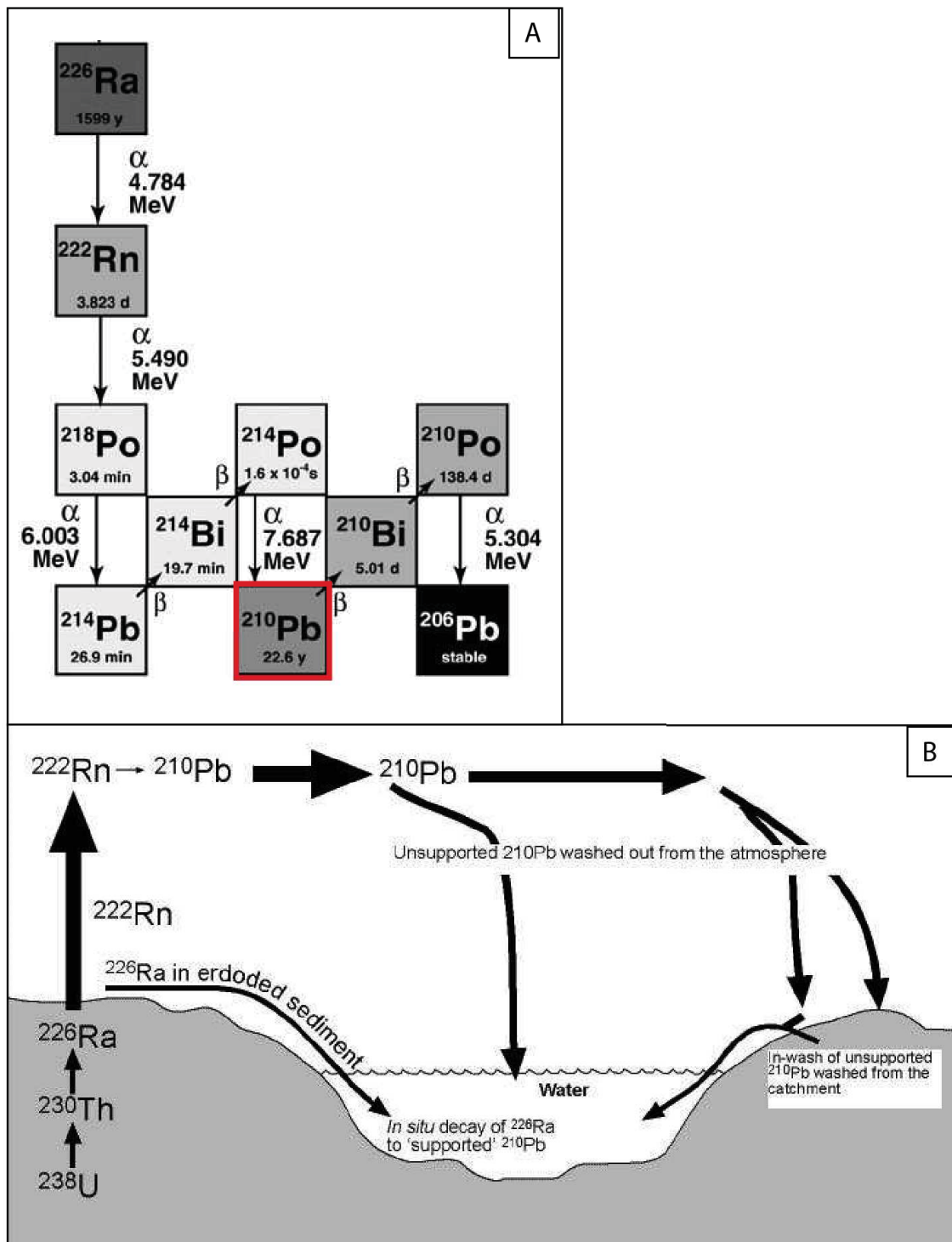


Figure 4.4: A: Disintegration chain of the ^{226}Ra after Bourdon (2003); B: Pathways by which ^{210}Pb reaches aquatic sediments (after Oldfield and Appleby, 1984).

When reporting the measurements in a diagram $\ln(^{210}\text{Pb}_{ex}^z)$ vs M_z they define a line where the slope is given by $-\lambda/W$, that allows to calculate the sedimentation rate (Fig.4.5). It is then

possible once the sedimentation calculated, to estimate the age for each layers of the sedimentary record.

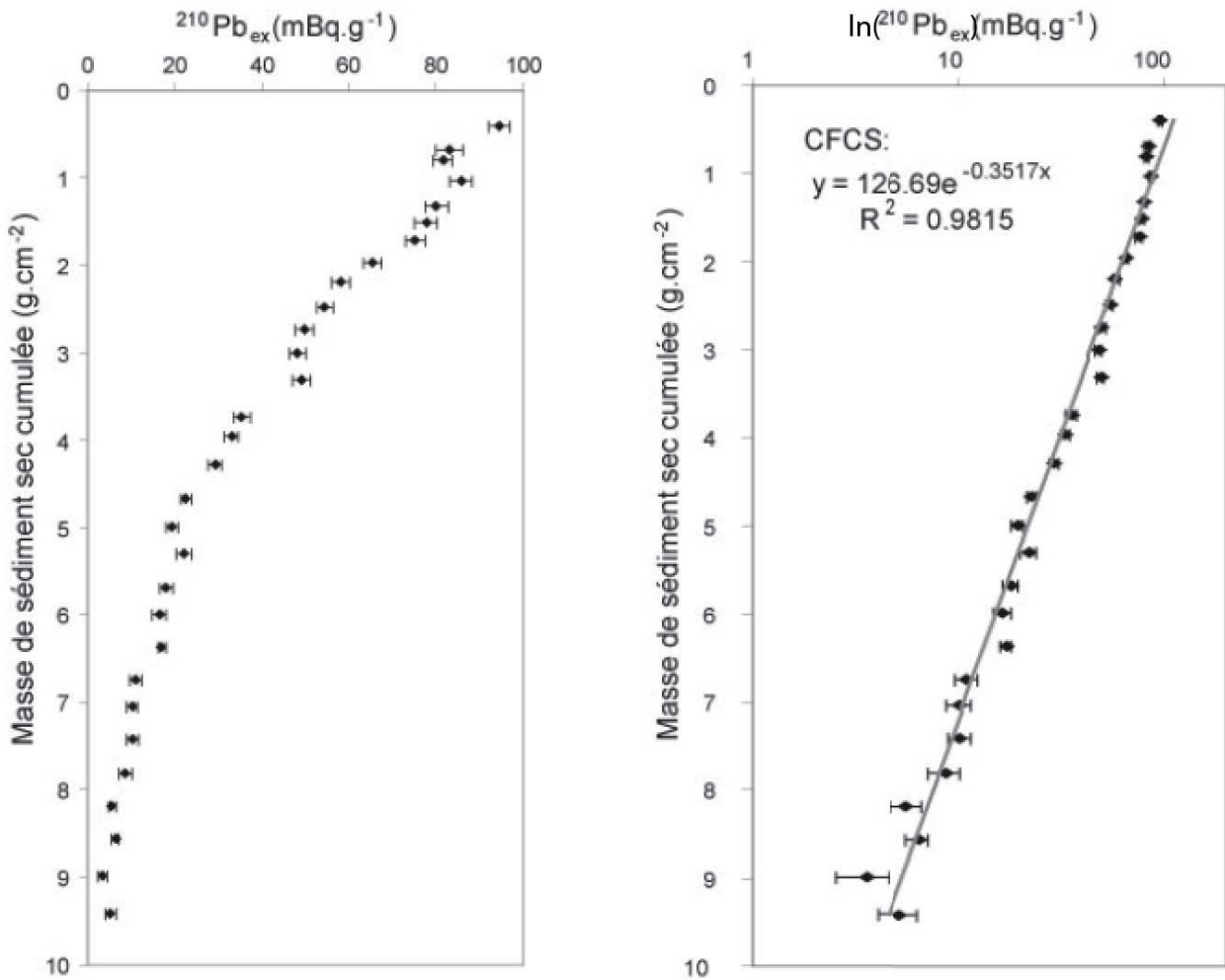


Figure 4.5: On the left : decay curve of $^{210}\text{Pb}_{ex}$ function of the accumulated sedimentary mass. On the right the CF:CS applied to the whole profile (after [Sabatier, 2009](#)).

Another independent time-marker is the artificial radionuclide ^{137}Cs , introduced in the atmosphere by nuclear bomb-test or nuclear accidents (Chernobyl, 1986). The onset ^{137}Cs is circa 1950 and it decays following a half-life of 30 years. The most usual dating method based on ^{137}Cs data ([Robbins and Edgington, 1975](#)) assumes that the depth of the maximum ^{137}Cs activity in the sediment corresponds to the maximum atmospheric production in 1963. On the other hand the 1986 Chernobyl fallout is also used to date most recent part of cores for the area affected by the ^{137}Cs atmospheric pollution (i.e, Europe)([Appleby et al., 1991](#)). One of the Cs properties is its high mobility in marine sediments, with a preferential downward diffusive transport in pore-water ([Radakovitch et al., 1999](#)). Despite the potential Cs mobility by diffusive transport leading to the spreading of the Cs peak, we can see on the Fig.4.6 that the ^{137}Cs profile shows

a clear maximum corresponding to 1963.

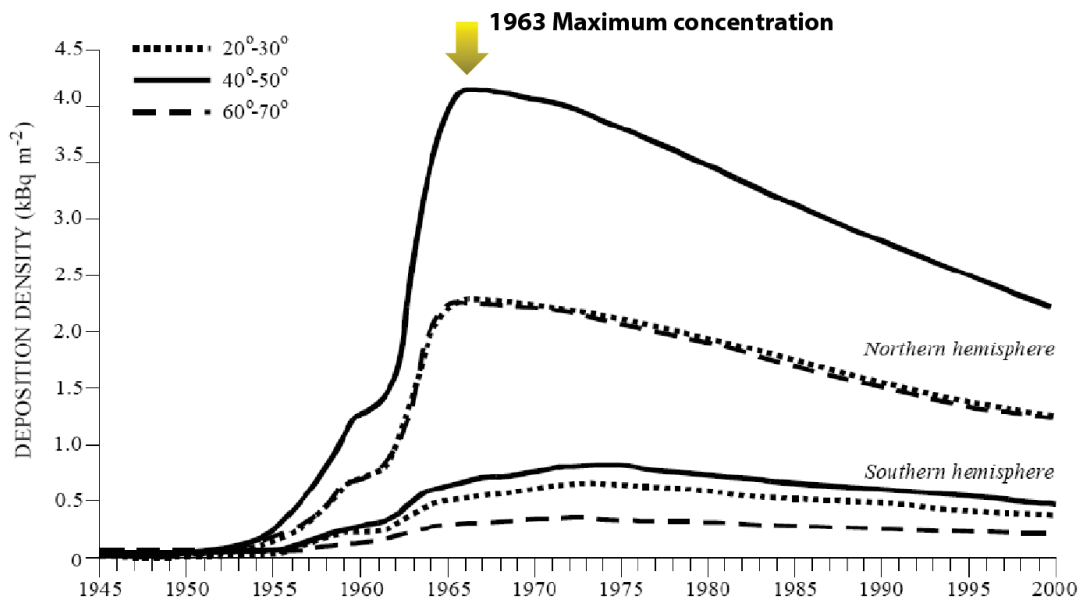


Figure 4.6: ^{137}Cs deposition density in the northern and southern hemispheres calculated from fission production amounts with the atmospheric model.

4.2.2 Radiocarbon ^{14}C : Dating, age calibration and reservoir age

Radiocarbon is widely used for dating geological and archaeological materials. It provides wide possibilities in the studies of present and past environments. The radioactive isotope of the Carbon, ^{14}C is set on the living organisms (e.g, plants, wood, shells, foraminifera). Due to the assimilation from the atmosphere, the concentration of this isotope remains constant on the living organisms (R_o). After the death of the organism, the ^{14}C is no longer counterbalanced by assimilation due to the radioactive decay. The amount of ^{14}C starts to decrease following a half-life of 5730 years. Comparison of $^{14}\text{C}/^{12}\text{C}$ ratio in a sample of dead organic matter (R_m) with that in the atmosphere enables determination of radiocarbon age. This age means the time, which passed between the death of organism and the moment of measure (Fig.4.7). Conventional radiocarbon age is determined after comparison of $^{14}\text{C}/^{12}\text{C}$ in the sample and in the standard of modern biosphere. The dating is thus based on the activity of the ^{14}C . The analysis is reliable over 5 half-lives, in other terms $< 50,000$ years. Radiocarbon age is determined assuming that the initial concentration of ^{14}C at the time of the death of an organism is the same as the concentration in the atmosphere. However during the last 50,000 years, the concentration of ^{14}C was usually higher than the actual standard. There is thus a necessity to carefully calibrate the radiocarbon time-scale (Fig.4.7). High-precision ^{14}C dating of samples of known calendar

age (mostly tree-rings, annual increments of marine and lacustrine sediments and corals) led to the building of the ^{14}C calibration curve. This calibration curve enables reading of calendar age if radiocarbon date is known (calibration curve *IntCal13* available from Reimer et al., 2013). The calendar age is expressed in "cal BP", "cal BC" or "cal AD" (see end of the section for explanations) (Fig.4.7B).

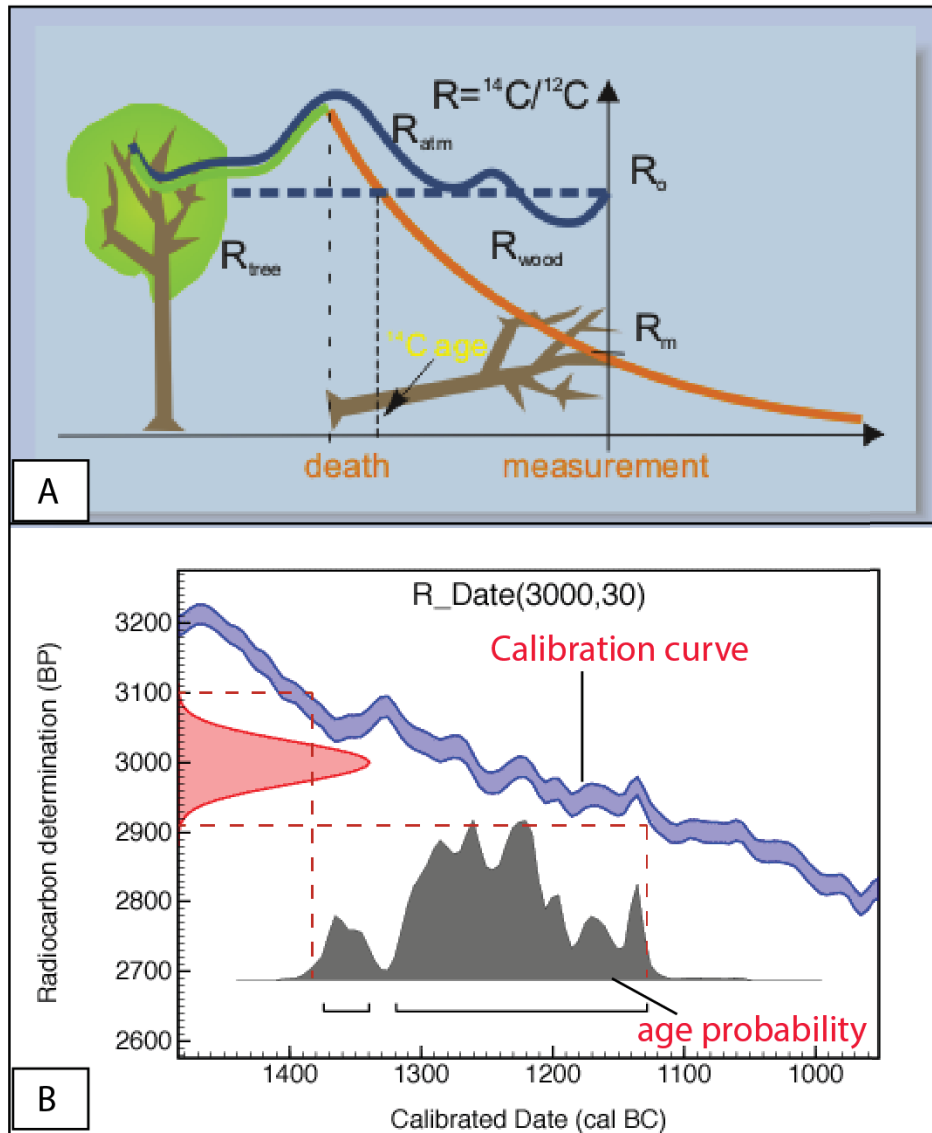


Figure 4.7: A: Principle of radiocarbon measurement on terrestrial organisms (source [www.http://radiocarbon.pl/](http://radiocarbon.pl/)); B: Example of calibration of ^{14}C age. Because of uncertainty of ^{14}C age, calendar age (cal. AD) are expressed only in terms of probability distribution.

The concept previously described is applicable for the terrestrial realm. Radiocarbon age is most easily determined for terrestrial organisms since during their life the carbon derived from the atmosphere. Organisms deriving carbon from aquatic environments usually have lower

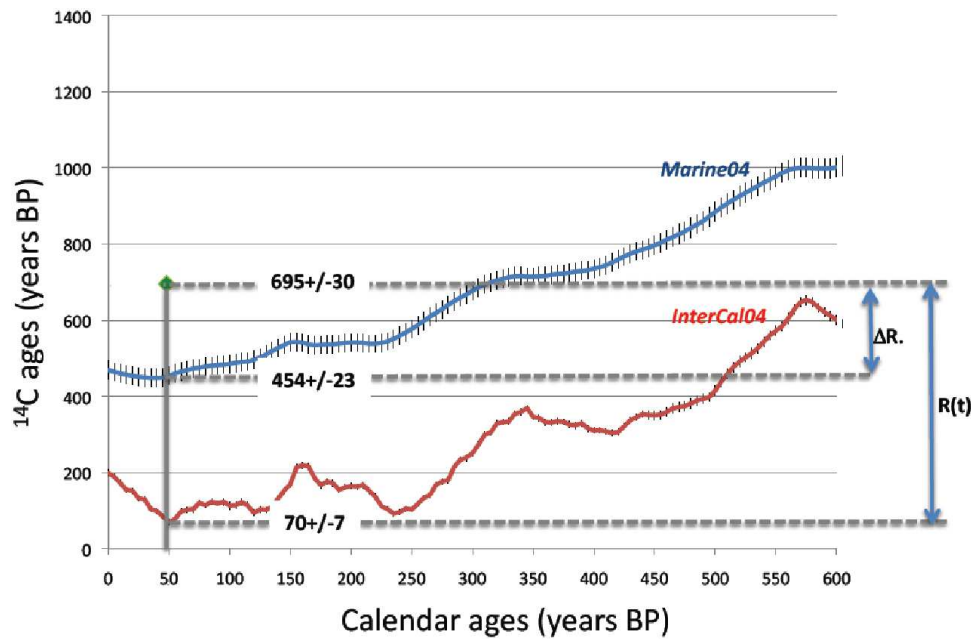


Figure 4.8: Sea surface reservoir ^{14}C ages $R(t)$ for modern sample on core KS06B (see chapter 5 for details on the results) calculated by subtracting the atmospheric ^{14}C estimated for the ^{210}Pb from the measured apparent ^{14}C ages of foraminifera. This gives a $R(t)$ value. The deviance from the global mean reservoir age (ΔR) is then obtained by subtracting the marine model value from the measured apparent ^{14}C age of the foraminifera (see chapter 5 for details on the results and discussion).

$^{14}\text{C}/^{12}\text{C}$ ratio than those living in aerial environment. It is induced by the significant lapse of time required for CO_2 exchange between the atmosphere and the ocean (i.e, to the long residence time of C in the ocean, compared with the ^{14}C half-life) (Stuiver and Reimer, 1986; Stuiver and Braziunas, 1993). This is the so called "reservoir effect". Radiocarbon age of such marine organisms is usually older than the terrestrial calibration curve and should be corrected by subtraction of the "reservoir age" (see for principle Fig.4.8, *N.B: this parameter will also be discussed in the chapter 5*). The world global reservoir age of surface water of seas and oceans has been estimated at circa 400 years. Several studies proposed that it is possible, according to the marine environment and the oceanographic conditions (e.g, upwelling zones, fresh water mixing), to find significant deviations in the regional marine reservoir signature from this average value (Kennett et al., 1997; Goodfriend and Flessa, 1997; Siani et al., 2001; Reimer and McCormac, 2002; Southon et al., 2002; Fontugne et al., 2004; Sabatier et al., 2010).

In the western Pacific area (i.e, Japan, northeast Taiwan and the Okinawa islands), Yoneda et al. (2007) show, based on the ^{14}C dating on molluscan shells that significant deviations of the reservoir age exist depending on the different oceanographic context (i.e, different currents) affecting this area (Fig.4.9).

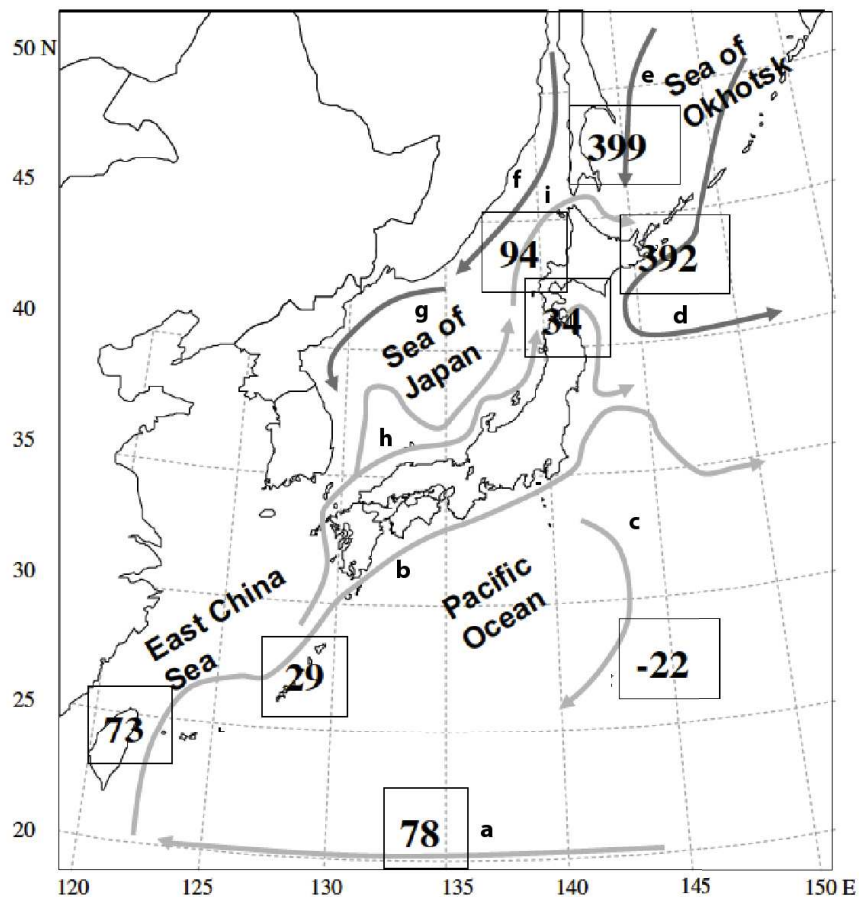


Figure 4.9: The mean ΔR value in the western Pacific. Arrows represent the current: a) North Equatorial current, b) Kuroshio current, c) Kuroshio countercurrent, d) Oyashio current, e) East Sakhalin current, f) Liman current, g) North Korea Cold current, h) Tsushima Warm current, i) Soya Warm current (modified after Yoneda et al., 2007).

To properly calibrate radiocarbon age, the calibration curve for marine samples *Marine013* is used and was established by Reimer et al. (2013). Same as for ^{210}Pb proxy, it is possible once radiocarbon dating calibrated (with the *Marine013* curve and reservoir age correction) to build depositional model to estimate sedimentation rate and also the age of each layers of the sedimentary cores. To do that, specific software are available like *OxCal 4.2* and have been used in this work in order to build depositional model.

Note:

Before Present (BP) years is a time scale used starting from 1 January 1950 as commencement date of the age scale, when ^{14}C dating became practicable in the 1950s; **Anno Domini (AD or A.D.)** and **Before Christ (BC or B.C.)** are designations used to label or number years used with the Julian and Gregorian calendars. There is no year zero in this scheme, so the year AD 1 immediately follows the year 1 BC.

Historical reconstruction of
paleo-earthquakes using ^{210}Pb , ^{137}Cs and
 ^{241}Am turbidite chronology and
radiocarbon reservoir age estimation off
East Taiwan

Contents

5.1	Introduction	107
5.2	Setting and analytical methods	108
5.3	Results and discussion	109
5.4	Conclusion	113
5.5	Aknowledgment	114

Historical reconstruction of paleo-earthquakes using ^{210}Pb , ^{137}Cs and ^{241}Am turbidite chronology and radiocarbon reservoir age estimation off East Taiwan

Paper submitted to Radiocarbon

LAURENT DEZILEAU (1,3), REMI LEHU (1,2), SERGE LALLEMAND (1,3), SHU-KUN HSU (2,3), NATHALIE BABONNEAU (3,4), GUEORGUI RATZOV (3,5), ANDREW T.LIN (2,3), STEPHANE DOMINGUEZ (1,3)

1. *Géosciences Montpellier, Montpellier, France*
2. *Department of Earth Sciences, National Central University, Zhongli, Taiwan (R.O.C)*
3. *LIA ADEPT, MOST, CNRS, Taiwan - France*
4. *Domaines Océaniques Laboratory, Bretagne Occidentale University, IUEM, France*
5. *GéoAzur Laboratory, Nice Sophia-Antipolis University, France*

[*Corresponding author:laurent.dezileau@gm.univ-montp2.fr](mailto:laurent.dezileau@gm.univ-montp2.fr)

Abstract

Taiwan is a young and active mountain belt, where a series of strong earthquakes ($M_w > 7$) have occurred over the past hundred years. Identifying historic earthquakes around Taiwan is key to better understanding of plate movements in this geodynamically active region. Sedimentological and geochemical analyses of surface sediments from one station offshore East Taiwan revealed the presence of coarse-grained layers corresponding to turbidites. The age of these coarse-grained layers have been determined by ^{210}Pb , ^{137}Cs and ^{241}Am chronology. Dating of the three most recent turbidites provides ages of 2001 ± 3 AD, 1950 ± 5 AD and 1928 ± 10 AD. The results show striking temporal correspondence of turbidite layers to large ($M_w > 6.8$) submarine earthquakes recorded in the region since the 20th century. Chronologies of the sediment layers leads us to believe that turbidites respectively result from the 2003 Chengkong (M_w 6.8), the 1951 Taitung Earthquake (M_w 7.1) and the 1935 Lutao Earthquake (M_w 7.0), respectively. Such a good correlation between turbidites and high-magnitude ($M_w > 6.8$) historical and instrumental seismic events suggests that turbidite paleoseismology constitutes a valuable tool for earthquake assessment in the Eastern Taiwan Margin. Moreover, the modern reservoir ^{14}C age was estimated by comparing AMS ^{14}C ages with ages derived from corrected ^{210}Pb profiles and historical accounts of identifiable seismic events. The calculated mean modern $R(t)$ value of 517 ± 54 ^{14}C yr is about 234 yr higher than the global mean sea surface reservoir age. This high value can be explained by the presence of local upwelling cells and turbulence in the Kuroshio Current North of the Green Island. These upwelling cells probably bring more ^{14}C depleted water to the surface, resulting in an increase of modern $R(t)$ value in the Kuroshio Current.

Keywords: Off east Taiwan, Turbidites, ^{210}Pb , ^{137}Cs and ^{241}Am chronology, Instrumental earthquakes, reservoir age fluctuation, Kuroshio current.

5.1 Introduction

The Taiwan mountain belt is known as young and active mountain belt resulting of the rapid collision of the Luzon arc, carried by the Philippine Sea Plate, and the Chinese Continental margin (Fig.5.1) (Biq, 1972; Suppe, 1984). In this region, the convergence is extremely high, about 80 mm/yr (Seno et al., 1993). There, the seismicity rate is significant with more than 20 earthquakes $M > 7$ recorded for the last 100 years, the biggest never recorded in 1920 with revisited magnitude of M_w 7.7 (Theunissen et al., 2010). Submarine landslides and resulting mass transport deposits or turbidites deposits have been recognized in seismic and coring data (Lehu et al., 2014a, submitted to Marine Geology). Interpretation of sedimentary deposits on the eastern Taiwan submarine slope suggests a direct link between submarine gravity processes (submarine landslides and turbidity currents) and occurrence of large earthquakes. In order to investigate modern sedimentation (<150 years) associated with recent seismic events in the Eastern Taiwan Margin, one sediment core was collected by boxcorer for radiometric (^{14}C , ^{210}Pb , ^{137}Cs and ^{241}Am) and sedimentological analyses. ^{210}Pb ($T_{1/2} = 22.3$ yr) is a widely used radiotracer in the study of sedimentary environments on a temporal scale of 100-150 years (e.g. Robbins and Edgington, 1975; Nittrouer et al., 1979). This naturally occurring radionuclide is present in sediments after formation by decay of ^{222}Rn ($T_{1/2} = 3.8$ d) in the atmosphere and the water column (^{210}Pb excess) and in situ decay of ^{226}Ra ($T_{1/2} = 1600$ yr). Age models based on ^{210}Pb activity profiles in sediment cores can be confirmed by independent time-stratigraphic markers, such as artificial radionuclides (e.g., ^{137}Cs , ^{241}Am), which allows us to discriminate the influence of postdepositional processes such as mixing. The onset of ^{137}Cs presence in sediments corresponds to the beginning of the atmospheric nuclear tests in the 1950s, and the highest concentrations correspond to maximum atmospheric activities due to nuclear tests (1963). A non-disturbed sediment profile is characterized by an exponential decrease in ^{210}Pb activity with depth. However, the presence of rapid/instantaneous sedimentation deposits in slow sedimentation deposits induces irregularities in ^{210}Pb profiles. As this kind of deposit is of potential interest in paleoseismic studies, where turbidity flows can transport sediment from the margin slope, solving the problem of dating sediment records with nonlinear ^{210}Pb profiles is of wide interest (Arnaud et al., 2002; Huh et al., 2004, 2006; Garcia-Orellana et al., 2006). The first aims of this paper are to date surface sediments from one station offshore East Taiwan which revealed the presence of coarse-grained layers corresponding to turbidites by using the ^{210}Pb CFCS model (Constant Flux, Constant Sedimentation) constrained by ^{137}Cs and ^{241}Am chronologies; and to

determine whether these turbidite intervals correspond to instrumental and historical earthquakes generated in the eastern Taiwan Margin. To determine the Holocene timescale, absolute chronology is usually based on radiocarbon measurements of carbonaceous samples, allowing accurate paleoenvironmental interpretations. However, when the ^{14}C method is applied to date samples equilibrated in marine water, it requires a correction, called the reservoir age correction. The pre-industrial global reservoir age is estimated as 405 ± 22 ^{14}C yr and a time dependent correction is available by using the Marine04 calibration curve (Hughen et al., 2004). Several studies have suggested the possibility of significant deviations in regional marine reservoir signature from this average value (Goodfriend and Flessa, 1997; Ingram and Southon, 1997; Siani et al., 2001; Reimer and McCormac, 2002; Southon et al., 2002; Fontugne et al., 2004). The second aims of this paper will be to estimate the modern reservoir ^{14}C age by comparing AMS ^{14}C ages with ages derived from corrected ^{210}Pb profiles and historical accounts of identifiable seismic events.

5.2 Setting and analytical methods

To study the recent sedimentary record, we sampled targeted box-core during the OR1-1013 survey (Fig.5.1). Box-core KS06-B (37cm long) was collected in 1947 m of water depth in a small-perched basin on the slope of Luzon Arc, north of Green Island off Taiwan (Lehu et al., 2014a, submitted to Marine Geology). Multidisciplinary analyses were performed, with a particular attention to grain size distribution variation and turbidite/hemipelagite differentiation. Sediment core were sampled at 1 cm interval for grain size analyses using a Coulter laser microgranulometer LS13 320 (size range from $0.4\mu\text{m}$ to 2 mm). Chemical composition and X-ray images were acquired using ITRAX –core scanner at 2mm interval. ^{14}C datings were performed on 10 mg of handpicked planktonic foraminifera (*Globigerinae* species). ^{14}C analyses were conducted at the Laboratoire de Mesure ^{14}C (LMC14) on the ARTEMIS accelerator mass spectrometer in the CEA Institute at Saclay (Atomic Energy Commission). These radiocarbon analyses were done with the standard procedures described by Tisnérat-Laborde et al. (2001). ^{14}C ages were converted to calendar years using the CALIB 5.0.2 calibration program (Stuiver and Braziunas, 1993; Reimer and Reimer, 2001). Dating of sedimentary layers was carried out using ^{210}Pb , ^{137}Cs and ^{241}Am methods on a centennial timescale. Both nuclides together with U, Th, and ^{226}Ra were determined by gamma spectrometry at the Géosciences Montpellier Laboratory. The 1 cm-thick sediment layers were finely crushed after drying, and transferred

into small gas-tight PETP (polyethylene terephthalate) tubes (internal height and diameter of 38 and 14 mm, respectively), and stored for more than three weeks to ensure equilibrium between ^{226}Ra and ^{222}Rn . The activities of the nuclides of interest were determined using a Canberra Ge well detector and compared with the known activities of an in-house standard. Activities of ^{210}Pb were determined by integrating the area of the 46.5-keV photo-peak. The ^{226}Ra activities were determined from the average of values derived from the 186.2-keV peak of ^{226}Ra and the peaks of its progeny in secular equilibrium with ^{214}Pb (295 and 352 keV) and ^{214}Bi (609 keV). In each sample, the ^{210}Pb excess activities ($^{210}\text{Pb}_{ex}$) were calculated by subtracting the (^{226}Ra supported) activity from the total (^{210}Pb) activity.

5.3 Results and discussion

5.3.1 Identifying and dating turbidite layers in core

Turbidites layers identification

As described above core KS06-B is located in an intra-slope basin northward from the Lutao volcanic island (Fig.5.1). The whole core is composed by an alternation of hemipelagic sedimentation and fine-grained turbidites facies. The Hemipelagite facies (HP hereafter) is characterized by homogeneous clay with low content of lithic fragment (<20%). HP contains diluted foraminifera and slight traces of bioturbations. In core KS06-B, this facies also is usually represented by grain size typically < 10 μm (Fig.5.2). Turbiditic facies is recognizable by their coarser grain size and a typical fining upward sequence (Fig.5.2) as defined by the Bouma sequence (Bouma, 1962). The coarser grain size usually indicates an “energetic” event in the sequence, relative to the background sedimentation (i.e Hemipelagite facies). Turbidites facies also are characterized by geochemical anomalies relative to the background signal. Figure 5.2 shows two proxies, Fe and Ca respectively, that are the most representative of both terrestrial and biogenic calcareous environment. In KS06-B, we identified three events named hereafter: T1, T2 and T3 (from top to bottom). Event T1 corresponds to a fine-grained turbidite composed of 8.5 cm thick of silty-clay sediment on the top of a coarser silty basal layer (grain size $\sim 35 \mu\text{m}$). Geochemical proxies show a clear Ca positive anomaly that anticorrelate Fe anomaly (Fig.5.2). Analysis of the coarser sand fraction revealed a high content of biogenic content mainly composed by planktonic foraminifera, sponges spicules and benthic foraminifera (Lehu et al., 2014a, submitted to Marine Geology). T2 is also interpreted as fine-grained turbidite composed of 4

cm thick of silty-clay sediment with a fine-silty basal layer (grain size $\sim 20 \mu\text{m}$). Geochemical composition indicates positive Ca anomalies that anticorrelate Fe anomalies. The sand fraction composition is characterized by high biogenic material content that reaches nearly 80% (Lehu et al., 2014a, submitted to Marine Geology). T3 also is probably a fine-grained turbidite. It is composed of 5 cm thick fining upward silty-clay sequence (grain size $\sim 15 \mu\text{m}$) with a sharp basal contact (Fig.5.2). Geochemical analysis reveals very slight positive Ca anomaly that anticorrelate Fe anomaly (Fig2). Same as T1 and T2, the coarser fraction of T3 is composed by a high biogenic content.

Radiochemical measurements and ^{210}Pb data processing age-depth relation

$^{210}\text{Pb}_{ex}$, ^{137}Cs and ^{241}Am activity profiles of core KS06 are shown in Fig.5.3. The maximum $^{210}\text{Pb}_{ex}$ activity is observed at the top of the core (51,9 dpm/g) and decreases down to 35 cm depth (3,3 dpm/g). The ^{210}Pb activity vs. depth curve is nonlinear (Fig.5.3A) and thus cannot be interpreted to have resulted from radioactive decay alone. The activity of turbidite layers is particularly low compared with hemipelagic layers and seems to be linked to grain-size variations (Arnaud et al., 2002; Huh et al., 2004, 2006; Garcia-Orellana et al., 2006). This pattern is particularly evident in the sequences located between 2 – 10, 20 – 26 and 29 – 33 cm depth (Fig.5.3A). ^{137}Cs and ^{241}Am activity profiles present sharp peaks at 19.5 cm (5,8 mBq/g and 3.6 mBq/g) and are near to zero below 23 cm (Fig.5.3A). In order to understand and establish an age-depth relationship in the core KS06-B, we used the same approach than Arnaud et al. (2002) and, assumed that hemipelagic sediments have been deposited by constant accumulation rate and that turbidite layers represent instantaneous events. A synthetic sedimentary record is then built composed only of the hemipelagic levels by removing the 3 turbidite events (T1, T2 and T3) from the original sedimentary record (Fig.5.3B). This corrected $^{210}\text{Pb}_{ex}$ profile can be considered as a nearly exponential curve (determination coefficients is 0.97) with the slope of the activity vs. depth equal to 0.18 cm.yr^{-1} . In such a case, the CFCS model (Goldberg, 1963; Krishnaswamy et al., 1971b) can be used and provides an accumulation rate (A.R.) of $1.8 \pm 0.2 \text{ mm.yr}^{-1}$ to all of the hemipelagic levels (Fig.5.3B). In order to determine the age of event T1 (2-9 cm), an A.R. of $1.8 \pm 0.2 \text{ mm.yr}^{-1}$ was used for the corrected depth 2-3 cm (without T1). Therefore, the T1 event would have occurred in $2001 \pm 3 \text{ AD}$. Using the same approach, event T2 (20-24 cm) corresponds to $1950 \pm 5 \text{ AD}$. Event T3 (28-33 cm) is near the limit of the ^{210}Pb method ($1928 \pm 10 \text{ AD}$). The most common dating method based on ^{137}Cs and ^{241}Am data (Robbins and Edgington, 1975) assumes that the depth of maximum ^{137}Cs and

^{241}Am activities in the sediment corresponds to the maximum atmospheric production by nuclear bomb testing in 1962-1964. A property of Cs is its high mobility in marine sediments, with a preferential downward diffusive transport in porewater (Radakovitch et al., 1999). Despite the potential Cs mobility by diffusive transport, leading to the spreading of the Cs peak, we can see in Fig.5.3 that the ^{137}Cs profile shows a clear maximum (21 cm which is equivalent to 10 cm in the corrected profile) corresponding to 1963. The ^{137}Cs and ^{241}Am activity depth profiles thus give accumulation rates of 1.84 mm.yr^{-1} . These accumulation rates are in good agreement with ^{210}Pb data ($1.8 \pm 0.2 \text{ mm.yr}^{-1}$) and confirm the age-depth relationship.

5.3.2 Linking turbidites and earthquakes events

At site KS06 (Fig.5.1 and Fig.5.4), earthquakes are the most likely explanation for triggering turbidity currents, as discussed by Lehu et al. (2014b, in prep.). The coring site is an isolated basin, without any sediment feeding from the continent. Hyperpycnal flows generated by typhoons can not have an impact on this basin. Turbidite deposits are only the results of local submarine instabilities of hemipelagic deposits and must be generated by earthquakes (Lehu et al., 2014b, in prep.). Moreover, in a previous study offshore northeastern Taiwan, Huh et al. (2004) have shown that turbidite can be used as a paleoseismicity marker. As regards the turbidite layers identified in core KS06-B, the ^{210}Pb age of the near-surface event T1 corresponds to 2001 ± 3 yr. An examination of the catalog of large earthquakes east Taiwan Margin shows that there is a good temporal correlation with the 2003 Chengkong earthquake of M_w 6.8. The epicenter of this earthquake was located offshore, on the slope of the Coastal Range (Fig.5.4), about 22 km north of the location where core KS06-B was collected. Although the effect of the earthquakes that occurred in the western foothills in 1999 (Chi-Chi earthquake, M_w 7.6) and 2002 (M_w 7) (see Fig.5.1 for locations) could be found in T1, the epicenters were too far away from the sampling site to alter the sediment record. Indeed, if we use empirical relationships established by (Chung, 2013) we found that the ground motion caused by a M_w 7 earthquake is insufficient to trigger slope failures at distance greater than 50 km (Lehu et al., 2014b, in prep.). The age of event T2 corresponds to 1950 ± 5 yr, which fits reasonably well with the 1951 Taitung earthquake of M_w 7.1. The epicenter of this earthquake was located on the emerged part of the Coastal Range, about 45 km north of the KS06 site. Finally, T3 corresponds to 1928 ± 10 yr and indicates a temporal correlation with the 1935 earthquake of M_w 7. The epicenter is located on the slope of the Luzon arc southward Lutaio island and about 45 km from the coring site (Fig.5.4). Note

that it is remarkable that the only three $M_w \geq 6.8$ earthquakes that occurred within less than 50 km from the core site all coincide with three turbidites identified in KS06-B.

5.3.3 Modern reservoir age estimation

Species living in ocean surface waters show depleted radiocarbon ages with respect to those living contemporaneously under atmospheric conditions. This difference, or marine ^{14}C apparent age, is due to 1/ oceanic circulation processes that tend to advect intermediate and deep ^{14}C depleted water masses to the surface, 2/ atmospheric ^{14}C changes, 3/ air-sea CO_2 exchanges processes, and 4/ hardwater effect due to the discharge of coastal rivers. Here we present measurements of the reservoir ages of surficial waters in the Kuroshio current (KC), which is still poorly known. Compared to the average modern ^{14}C marine reservoir age ($R(t) = 405 \pm 22$ ^{14}C yr), the Kuroshio Current (KC) ^{14}C reservoir age close to Taiwan displays higher $R(t)$ values, with a deviance from the global mean sea surface reservoir age (ΔR) of 86 ± 40 ^{14}C yr (Yoneda et al., 2007; Yu et al., 2010). The ^{14}C depletion of KC has been explained by the water from Pacific Equatorial Divergence with lower ^{14}C contents (Yoneda et al., 2007; Yu et al., 2010). Here, we estimate the modern sea surface reservoir ^{14}C age in KS06-B by comparing ^{14}C values of planktonic foraminifera (*Globigerinae* species) with ^{210}Pb chronology. As a reminder, KS06-B was extracted in the east of Taiwan and surface hydrographic conditions in that area are controlled largely by the KC. The first age on KS06-B at 25 cm depth is 690 ± 30 ^{14}C yr. This age corresponds to a date of 1950 ± 5 yr AD, derived from the ^{210}Pb CFCS model (average sedimentation rate of 1.8 ± 0.2 mm/yr). The second age on KS06-B at 33 cm depth is 695 ± 30 ^{14}C yr. This age corresponds to a date of 1928 ± 10 yr AD, also derived from the ^{210}Pb chronology. Sea surface reservoir ^{14}C age $R(t)$ at 25 cm in KS06-B was calculated by subtracting the atmospheric ^{14}C value estimated for the date of 1950 AD (199 ± 9 ^{14}C yr Reimer et al., 2004) from the measured apparent ^{14}C ages of the depth at 25 cm (690 ± 30 ^{14}C yr, Table 6.1). This gives a $R(t)$ value of 491 yr. The deviance from the global mean reservoir age (ΔR) is then obtained by subtracting the marine model age value estimated for 1950 AD (464 ± 23 ^{14}C yr, (Hughen et al., 2004) from the measured apparent ^{14}C age at depth of 25 cm (690 ± 30 ^{14}C yr, Table 6.1). The ΔR value is thus estimated as 226 ± 53 yr (Table 6.1). By adopting a similar approach for the depth at 33 cm on core KS06-B dated to 1928 AD by ^{210}Pb chronology, we obtain $R(t) = 543$ ^{14}C yr ($\Delta R = 241$ yr ± 53 , Fig.5.5). These 2 dated depths suggest that in the study area, the average reservoir age $R(t)$ is 517 ± 54 ^{14}C yr and $\Delta R = 234 \pm 75$ yr. This study gives

a mean ΔR around 234 ± 75 ^{14}C yr ($n=2$), which is substantially different from the previous estimation by using collections of pre-bomb shells, 86 ± 40 ^{14}C yr ($n=9$) (Yoneda et al., 2007; Yu et al., 2010). Our high ΔR value cannot be considered as a typical ΔR values for water belonging to KC off Taiwan. On local scale, different processes may increase ΔR values, such as hardwater effect or local upwellings. On regional scale, hardwater effect due to the discharge of coastal rivers was found to increase ^{14}C ages by 600 years in the Pierre Blanche lagoon in France (Sabatier et al., 2010). However, we consider that high ΔR value in our study area could not be due to hardwater effect for the following reasons: (1) There are no limestone outcrops in the the Taitung watershed, the most proximal watershed in the study area; (2) hardwater effect due to the discharge of coastal rivers is impossible because of the great distance of the KS06 from the nearest land of Taiwan (40 Km away), in fact, hard water effect was usually found in terrestrial lakes, lagoons or coastal area and has never been reported for open marine environment, as mixing with open seawater will quickly dilute any such effect. Particularly here where KC is very strong and deviate strongly the discharge of coastal rivers along the Taiwan coast. Variations in regional oceanic activities, such as local upwelling is the most probably the cause of our high ΔR values. In our study area, an upwelling area in the KC has been identified north of Green Island off Taiwan, exactly in our study area. Vertical profiling with shipboard lowered acoustic Doppler current profiler and conductivity temperature depth profiler revealed sizable anomalies in flow and water characteristics in the lee of Green Island (Chang et al., 2013). The presence of the Green Island induces upwelling and turbulence in the KC (Fig.5.6B). In these zones, the water is colder and higher in chlorophyll-a concentration (Chang et al., 2013). These upwelling cells probably bring more ^{14}C depleted water to the surface, resulting in a more positive ΔR value in our zone.

In summary, the high ΔR value in our study area may mainly be controlled by upwelling activities than by hardwater effect. Moreover, as these upwelling cells are local, our high ΔR value (around 233 ± 30 ^{14}C yr) cannot be considered as a typical ΔR values for water belonging to the KC off Taiwan. We suggest to considered 86 ± 40 ^{14}C yr as a typical ΔR value for the KC (Yoneda et al., 2007).

5.4 Conclusion

Based on $^{210}\text{Pb}_{ex}$, ^{137}Cs and ^{241}Am activity profiles in one box core collected East of Taiwan, three turbidite events dated circa 2001 ± 3 AD, 1950 ± 5 AD and 1928 ± 10 AD have been identified.

These ages correspond to the three $M_w \geq 6.8$ earthquakes that occurred in the region ($d < 50$ km from core site): the 2003 Chengkong Earthquake (M_w 6.8), the 1951 Taitung Earthquake (M_w 7.1) and the 1935 Lutao Earthquake (M_w 7.0). The good agreement between our estimated deposition time of the turbidites and the history of major local earthquakes suggests that the record of mass transport deposits can be used as a paleoseismic indicator in this high-convergence area. The modern reservoir ^{14}C age was estimated by comparing AMS ^{14}C ages with ages derived from a corrected ^{210}Pb profile. The calculated mean modern $R(t)$ value of 517 ± 54 ^{14}C yr is about 234 yr higher than the global mean sea surface reservoir age and 148 yr higher than the Kuroshio Current ^{14}C reservoir age close to Taiwan as proposed by [Yoneda et al. \(2007\)](#). This high value may rather be controlled by upwelling activities than by hardwater effect. Local upwelling cells in the KC North of the Green Island probably bring more ^{14}C depleted water to the surface, resulting in a more positive ΔR value in that area.

5.5 Acknowledgment

This project has benefited from the following financial supports: National Central University (NCU) for ship time and analytical laboratory equipments, Institut National des Sciences de l'Univers (INSU-CNRS) in the frame of "Aléas" program in 2013 and 2014 and Joint Research Projects between MOST and CNRS, LIA-Adept, Bureau de Représentation de Taipei (BRT) in France and France-Taiwan Fundation, and the French Institute in Taipei. We thank the Laboratoire de Mesure ^{14}C (LMC14) ARTEMIS in the CEA Institute at Saclay (French Atomic Energy Commission) for the ^{14}C analyses.

Sample	^{210}Pb age (AD)	^{14}C age (BP)	Tree-ring		Model age Marine04	ΔR (yr)
			^{14}C BP IntCal04	R(t) (yr)		
KS06-B-25	1950 ± 5	690 ± 30	199 ± 9	491 ± 39	464 ± 23	226 ± 53
KS06-B-33	1928 ± 10	695 ± 30	152 ± 7	543 ± 37	454 ± 23	241 ± 53

Table 5.1: ^{14}C dates of modern prep-bomb foraminifera samples in KS06-B and their reservoir ages.

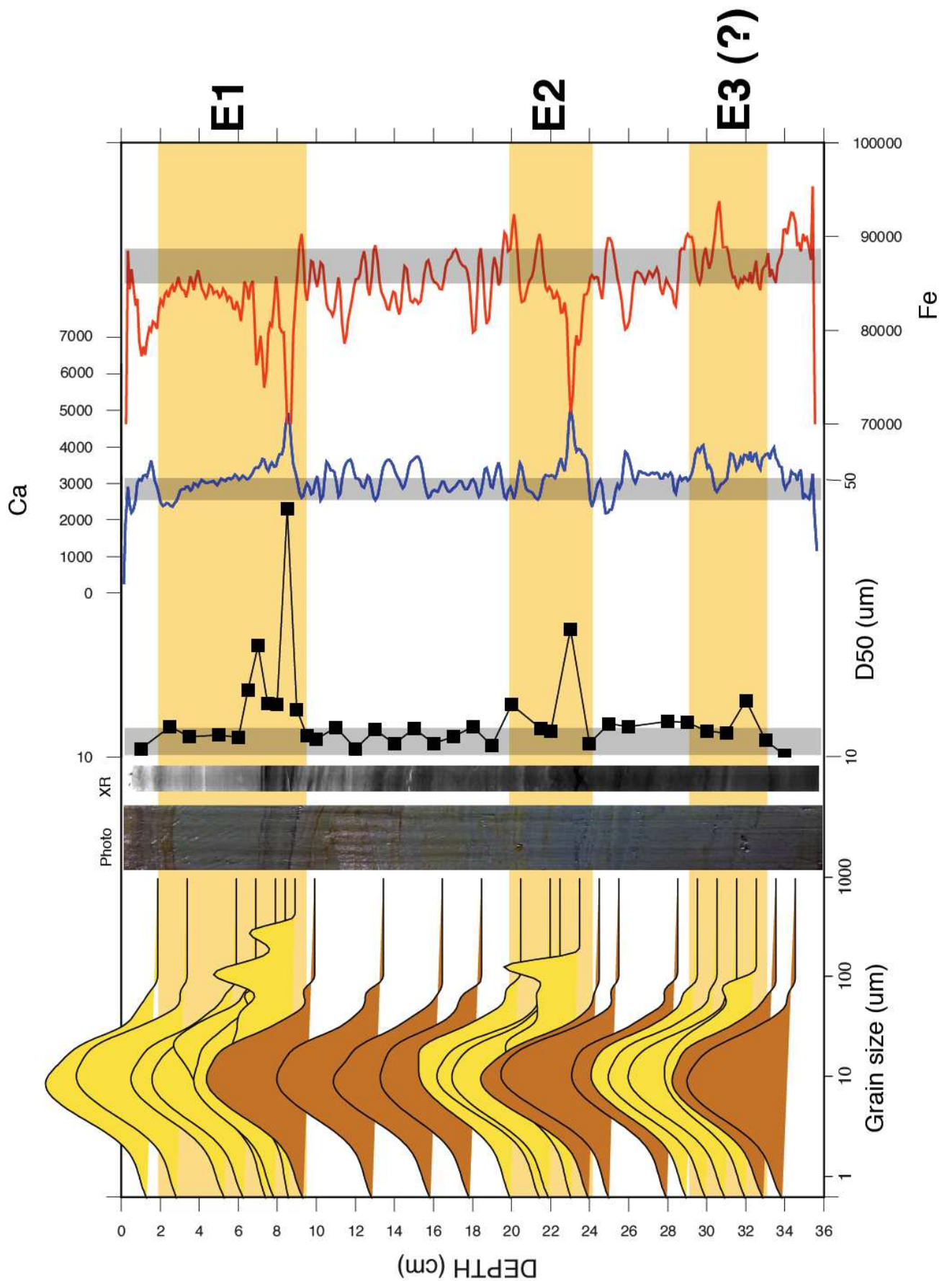


Figure 5.2: Sedimentological analysis of KS06-B and turbidites events identification, using grain size distribution, photo, X-rays, median grain size and geochemical elements (Ca and Fe).

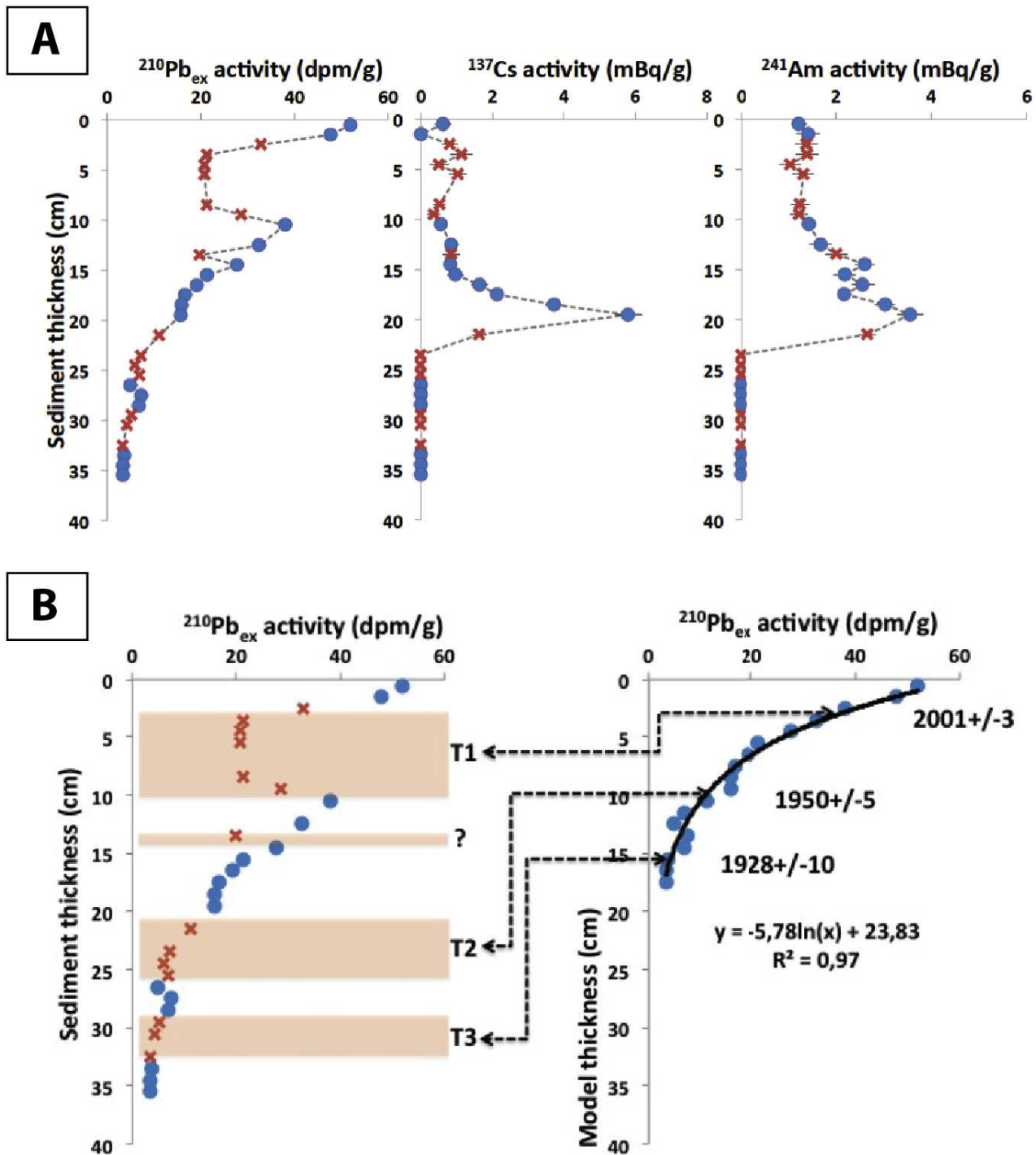


Figure 5.3: A: ^{210}Pb , ^{137}Cs and ^{241}Am activity profiles. Blue dots represent sample from continuous sedimentation (hemipelagite) whereas red crosses represent samples from instantaneous sedimentation (i.e. turbidite event). B: Methodology used to reconstruct depositional model to estimate sedimentation rate and turbidites layers age.

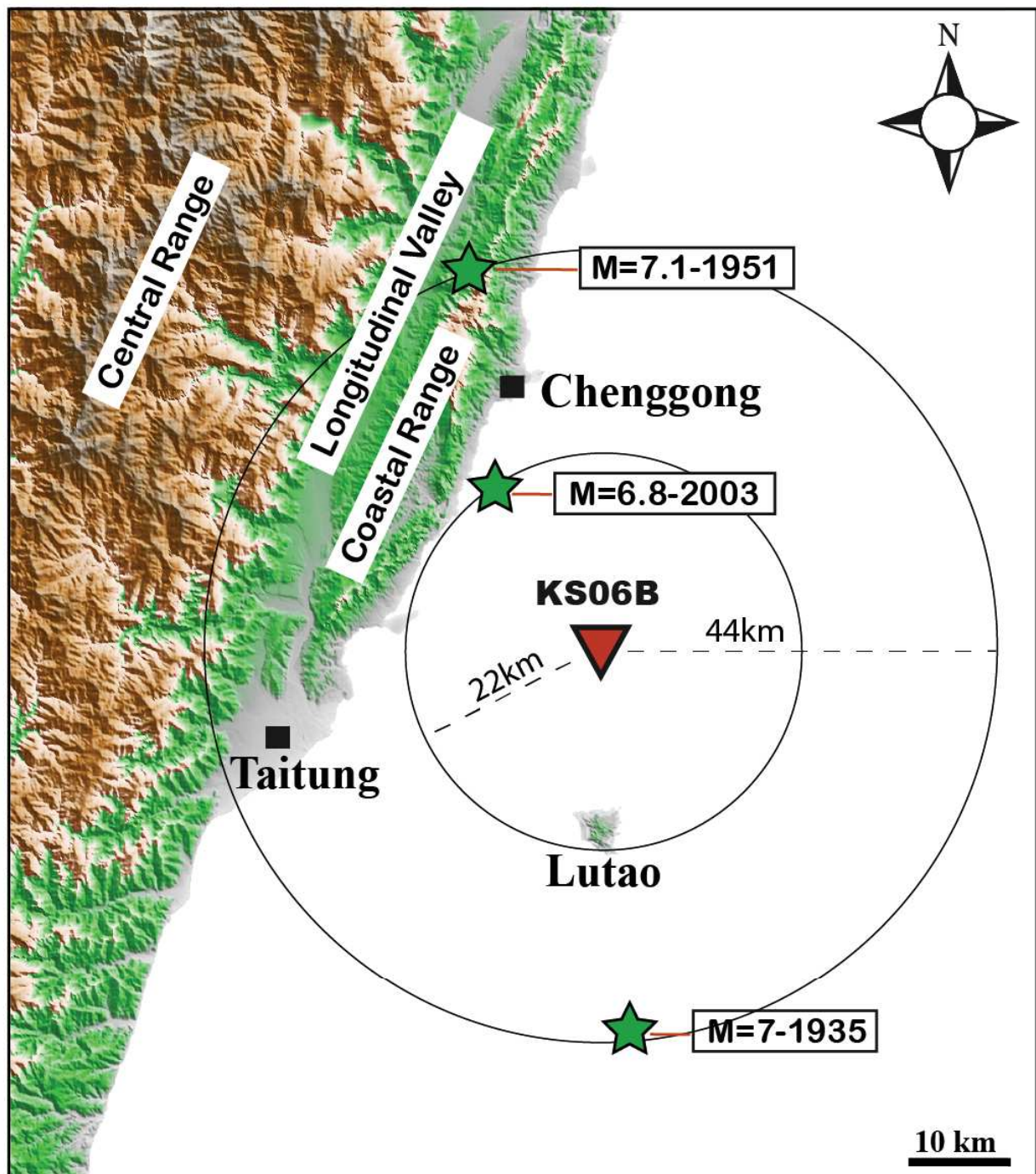


Figure 5.4: Distance from earthquakes correlated with turbidites events to site KS06.

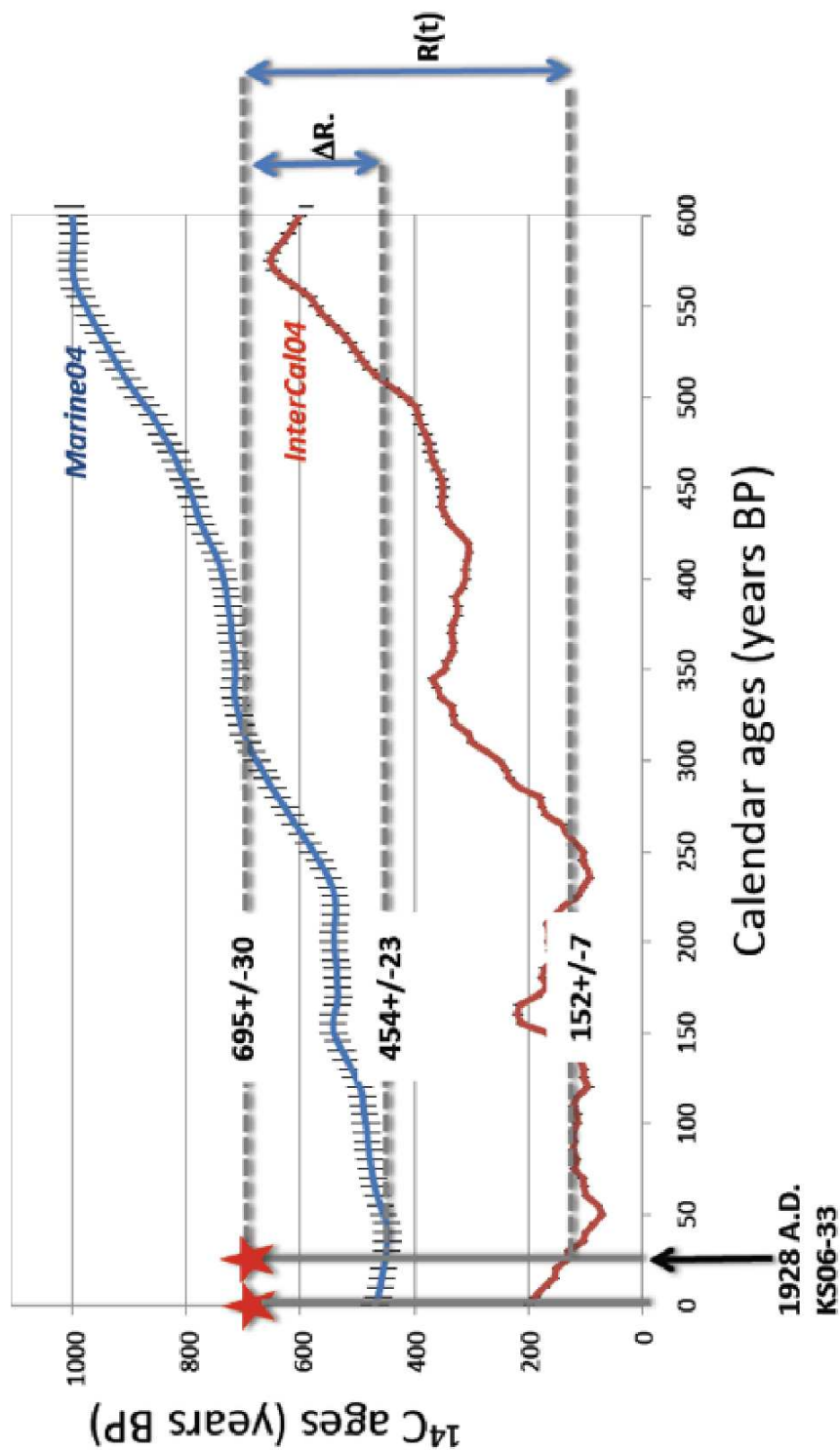


Figure 5.5: Sea surface reservoir ^{14}C ages $R(t)$ for modern sample on core KS06-B calculated by subtracting the atmospheric ^{14}C estimated for the ^{210}Pb from the measured apparent ^{14}C ages of foraminifera. This gives a $R(t)$ value. The deviance from the global mean reservoir age (ΔR) is then obtained by subtracting the marine model value from the measured apparent ^{14}C age of the foraminifera.

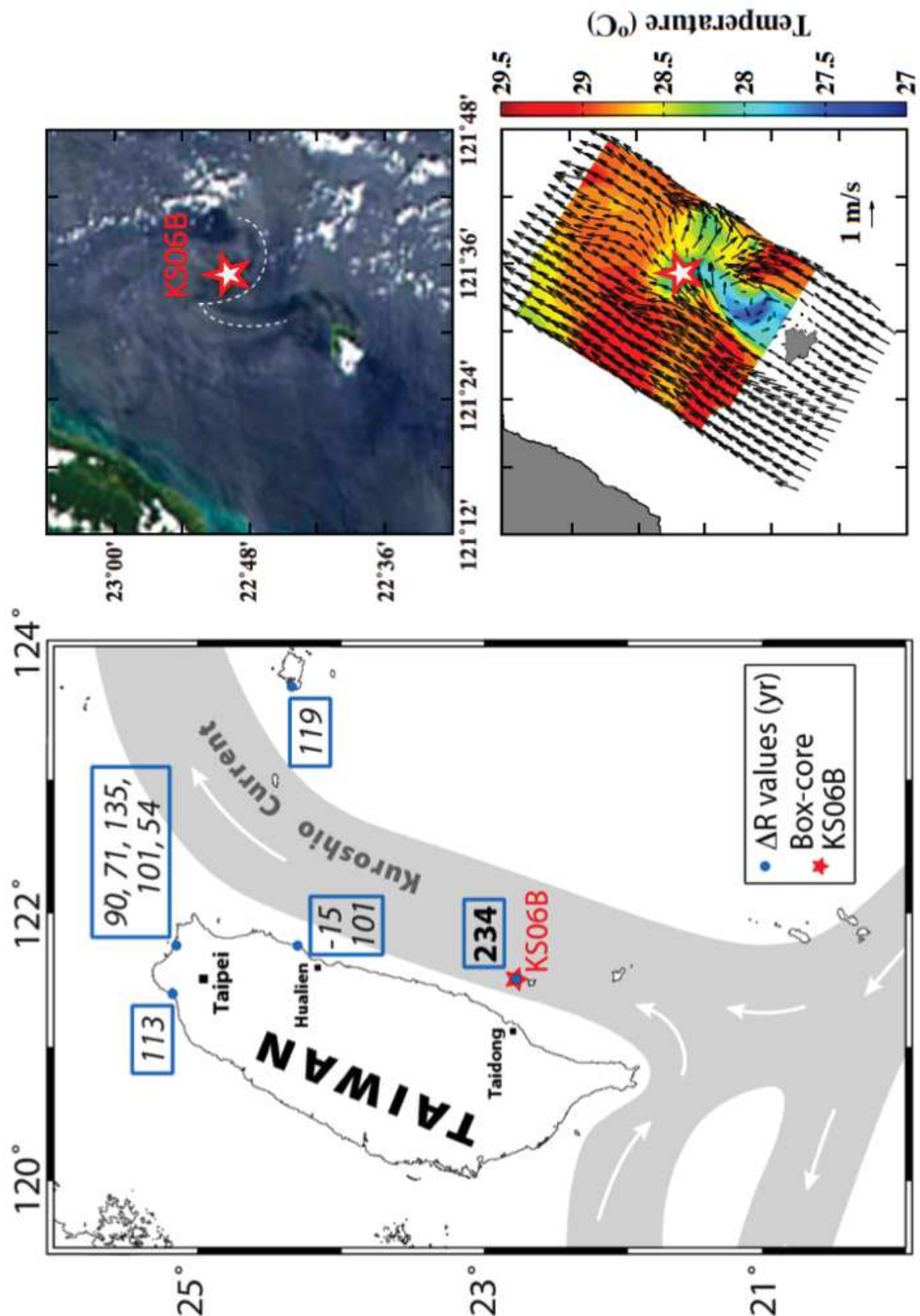


Figure 5.6: A: General map of Taiwan showing the ΔR values around the Taiwan area (this study and Yoneda et al., 2007). In light grey: the mean path of the Kuroshio current (after Hsin et al., 2008). The red star shows the core location; B: Upwelling zone northward Lutao island evidenced by satellite image and sea-water temperature (after Chang et al., 2013)

2,700 years of seismicity recorded offshore eastern Taiwan by turbidites deposits

Contents

6.1	Introduction	127
6.2	Regional settings	129
6.3	Materials and methods	130
6.4	Turbidites identification	133
6.5	Chronostratigraphy	135
6.6	Discussion	136
6.7	Conclusion	143
6.8	Acknowledgments	144

Reconstructing 2,700 years paleo-earthquakes history using deep-sea turbidites offshore eastern Taiwan

Paper in preparation to be submitted to Tectonophysics

REMI LEHU (1,2), SERGE LALLEMAND (1,3), SHU-KUN HSU (2,3), GUEORGUI RATZOV (3,4), NATHALIE BABONNEAU (3,5), ANDREW T.LIN (2,3), LAURENT DEZILEAU (1,3)

1. *Géosciences Montpellier, Montpellier, France*
2. *Department of Earth Sciences, National Central University, Zhongli, Taiwan (R.O.C)*
3. *LIA ADEPT, MOST, CNRS, Taiwan - France*
4. *GéoAzur Laboratory, Nice Sophia-Antipolis University, France*
5. *Domaines Océaniques Laboratory, Bretagne Occidentale University, IUEM, France*

*Corresponding author: lehu@gm.univ-montp2.fr

Abstract

The Taiwan area, where the Philippine Sea Plate collides with the Eurasian, is one of the most seismically active areas in the world and has been consequently struck repeatedly by destructive earthquakes. To better constrain the occurrence of large earthquakes, we have conducted two cruises in 2012 and 2013 from which piston cores and box-cores were retrieved in strategic areas. Turbidite beds in the cores have been interpreted with facies varying from silty clay to coarse sand. We modeled each turbidite layer using the sedimentation rate deduced from radiocarbon age measurements performed on planktonic foraminifera. Precise dating based on ^{210}Pb - ^{137}Cs chronology provided ages for the most recent turbidite beds. A test of synchronicity reveals that sixteen events are synchronous along the entire margin between ~ 50 BC and ~ 2003 AD. Also seven events are synchronous at a local scale, emplaced between ~ 700 AD and ~ 1850 AD. Coring sites locations, biotic association within turbidite beds and seismic calibration based on the instrumental period, suggest that earthquakes are the most likely triggering mechanisms over the last 2,700 years. We used empirical relationships that combine peak ground acceleration, magnitude and distance, to estimate the earthquake magnitude-distance threshold able to destabilize the submarine slopes and thus calibrate the seismic sources. Based on our results, we could identify candidates instrumental earthquakes of M_w that fit ages of the most recent turbidite events. We also could argue that turbidite correlations formerly interpreted as margin-wide were not plausible according to the seismic calibration. We extended this approach over the Holocene turbidites. Results show that the fourteen wide-margin events would correspond to earthquake $M_w \geq 8$ having occurred between circa 50 BC and 1750 AD which is unlikely. Instead we focused on local correlations and estimated return times for earthquakes $M_w \geq 6.8$ off east Taiwan. Despite the fact that turbidite correlations should be cautiously applied, our results suggest that turbidite record may be considered as a valuable proxy for paleoseismicity investigation offshore east Taiwan.

Keywords: Active margin, Offshore eastern Taiwan, turbidite deposits, submarine paleoseismology, synchronous turbidites, earthquakes, peak ground acceleration.

6.1 Introduction

Since the last decade, the Earth has been the theater of unexpected natural disasters such as the December 2004 Sumatra-Andaman earthquake (M_w 9.1), the March 2011 Tohoku-Oki earthquake (M_w 9.0) and their associated destructive tsunamis. This fact dramatically highlighted the gaps that still exist in the understanding of large earthquakes and associated hazards that occur along the subduction zones. Several questions still remain about the seismic potential of subduction zones and the frequency of such large events. A possible alternative to better assess the occurrence of destructive earthquakes is based on the record of paleo-earthquakes. Submarine paleoseismology based on sediment archives provides reliable constraints on the recurrence intervals and spatial distribution of large coastal and submarine earthquakes. Strong seismic ground shaking is one of the triggers for submarine slope failures (Locat and lee 2002) that can evolve downslope into turbidity currents (Mulder and Cochonot, 1996). Other processes than earthquakes could also be responsible of turbidity current generation and the discrimination between different triggering mechanisms still remain ambiguous despite detailed sedimentological characterization (Gorsline et al., 2000; Nakajima and Kanai, 2000; Shiki et al., 2000). However, synchronous turbidites deposited in independent sedimentary systems over a large area require a regional trigger, most likely a large earthquake (Goldfinger et al., 2003, 2007; Gràcia et al., 2010; Pouderoux et al., 2012, 2014). When available, the correlations with historical and instrumental records of seismic events likely corroborate the interpretation of the coseismic trigger of turbidity currents. Numerous settings have shown their suitability for the turbidite paleoseismology approach. This method has been successfully tested in active margins (Adams, 1990; Goldfinger et al., 2003, 2007; Goldfinger, 2011; Goldfinger et al., 2012; Huh et al., 2004; Noda et al., 2008; Gràcia et al., 2010; McHugh et al., 2011; Pouderoux et al., 2012, 2014; Polonia et al., 2013; Barnes et al., 2013), in lakes (Strasser et al., 2006; Beck, 2009; Moernaut et al., 2014), and in intraplate domains (St-Onge et al., 2004b). The offshore eastern part of the Taiwan mountain belt is characterized by a high sediment supply (Liu et al., 2008), and intense tectonic and seismic activity (Malavieille et al., 2002; Wu et al., 2010; Lallemand et al., 2013) that makes it a suitable location for marine turbidite paleoseismology investigations. This area concentrates gravity flow sedimentary processes and records successions of turbidites in different sedimentary systems (Lehu et al., 2014a, submitted to Marine Geology). In the northern part offshore eastern Taiwan, Huh et al. (2004) demonstrated that some major instrumental earthquakes may be correlated with turbidites events. This unique local submarine, paleoseismology

study, based on correlation with known events, shows the suitability of the approach, but lacks a margin-scale investigation essential to infer regional triggers and earthquakes beyond historical seismicity. In fact, the assessment of seismic hazard in the offshore east Taiwan is largely based on the relatively short period of instrumental earthquakes catalog (~ 100 years). Therefore, a submarine paleoseismic approach may allow us to determine past seismic activity and investigate the occurrence for great magnitude earthquakes over the Holocene.

In the present paper, we aim (1) to establish the first 2,700-years-long earthquake record of eastern Taiwan, and (2) to estimate the recurrence and magnitude of earthquakes responsible for turbidites deposition. To reach these objectives, we use morphological and sedimentological observations, chronological correlation and hypothesis on peak ground acceleration threshold able to destabilize the submarine slopes.

6.2 Regional settings

6.2.1 Geological and seismic context

Taiwan is located at the transfer zone between two opposite verging subductions (Tsai et al., 1977; Wu, 1978). South of the island, the Eurasian Plate (EP) is subducting eastwards under the Philippine Sea Plate (PSP), whereas east of Taiwan, the PSP is subducting northwards under the EP along the Ryukyu Trench (Fig.6.1). Considering the EP fixed, the PSP converges northwestwards at a rate of 8.1 cm yr^{-1} (Yu et al., 1997). Taiwan results from the collision between the passive continental margin of the South China Sea and the Luzon Volcanic Arc associated with the Manila Subduction (Biq, 1972; Chai, 1972; Malavieille et al., 2002) (Fig.6.1). The subsequent deformation is characterized by a very high rate of seismicity onland, but also offshore east Taiwan (Kao et al., 1998). More than 20 $M_w \geq 7$ earthquakes struck this island during the last 100 years but no historical $M_w 8$ earthquakes was recorded by the local seismic network (Theunissen et al., 2010). Seismicity concentrates in some very active areas such as the Foothills in the western part of the orogen delimited by the western deformation front (DF on Fig.6.1) (e.g., 1999 $M_w 7.6$ Chichi Earthquake), the Coastal Range which is an extinct segment of the LVA colliding with the orogen (e.g., 1951 $M_w 7$ earthquakes triplet, see Fig.6.1B and Table 6.1), the coastal region north of the Coastal Range is also extremely seismic as well as the E-W-trending South Okinawa Trough (Fig.6.1B).

6.2.2 Sedimentology

The offshore east Taiwan is characterized by a complex morphology. The slope displays steep slope gradients (15 to 20°). It is deeply incised by systems of gullies and canyons (Fig.6.1B). The submarine slope also exhibits seafloor escarpments associated to tectonic structures such as thrusts and folds (Malavieille et al., 2002). The drainage systems involve three major submarine canyons offshore eastern Taiwan collecting the sedimentary discharge from the Central Range and the Coastal Range (Fig.6.1B). This area is characterized by a variety of sedimentary facies and erosional sedimentary processes from submarine landslides to turbidity currents (Lehu et al., 2014a, submitted to Marine Geology). The sedimentation is characterised by interlayering of turbidites and hemipelagites infilling slope and deep-sea basins. The ubiquitous turbidite depositions of the offshore east Taiwan range from fine turbidites deposited on mid-slope basins to massive turbidites deposited in turbiditic systems. As such, according to the

morpho-sedimentary systems and the sedimentological signatures of the turbidite sequences, the controlling factors of recent sedimentation are both related to tectonic and climatic forcing (Lehu et al., 2014a, submitted to Marine Geology).

6.3 Materials and methods

6.3.1 Core site location

This study is based on four piston and gravity cores, and one box-core acquired during the OR1-1013 (September 2012) and the OR1-1048 (August 2013) surveys onboard the Taiwanese research vessel R/V Ocean Researcher I (see Table 6.2). The cores have been strategically selected to characterize the sedimentary depositional areas, where the seismic activity is generated. To record earthquake-triggered deposits and avoid climatically-driven signal (storms, floods...), we favored sites such as isolated terraces and perched basins sheltered from the continental sedimentary paths (Fig.6.1B, 6.2 and 6.3). We defined two zones off east Taiwan where the cores were retrieved: the Ryukyu forearc basin (hereafter RF) and the Luzon volcanic arc zone (hereafter LA) (Fig.6.2 and 6.3). The cores are termed from north to south: KS09-P and KS08-P (P for piston core) (refer to table 2 for cores characteristics), KAS03-P, KS06-B and KS06-G (B for box-core and G for gravity core respectively). In the RF zone, KS08-P and KS09-P have been collected respectively at 2800 and 2900 m below the sea level. They are both located on isolated terraces in the Hopping basin (HB in Fig.6.1B) at the bottom of the northern slope ($\sim 11^\circ$) of the Ryukyu arc (Fig.6.2). About 100 km southward, in the LA zone, KAS03-P was collected at 1700 m below the sea-level on an isolated terrace at mid-slope of a topographic high (Fig.6.3). KS06-B and G have been collected at the same site located at 50 km southward site KAS03, at 1947 m below the sea-level. KS06 site is located in an isolated perched basin in the eastern slope ($\sim 15^\circ$) of the Luzon arc northward from the Lutao volcanic island (Fig.6.3).

6.3.2 Cores analysis

The methodology used to study the cores includes visual description, X-ray imaging and geochemical measurements on half core sections. Sediment composition, grain-size analyses and radiocarbon dating were carried out on selected samples. After core splitting, pictures were taken for all the cores and detailed core description has been performed based on changes in color, lithology, texture and structure of the sediments. X-ray radiography and geochemical

composition was measured on archive sections using the non-destructive X-Ray Fluorescence (XRF) ITRAX scanner from the National Taiwan University (Taipei). Major chemical elements were measured, at 2 mm interval for all the cores. The data obtained correspond to the values of element intensity in counts per second (cps), providing information on the relative element concentration. In the present study we selected elements Sr, Ca and Fe that better characterize the relationship between detrital and biogenic sedimentation. These data help us to characterize different types of turbidites as well as to define the hemipelagic intervals that are essential to compute the age models. Grain-size analyses were systematically carried out every 0.5 cm to 2 cm. We adapted the sampling interval according to the visual facies changes. We used the Coulter LS13-320 from the laboratory of sedimentology at the National Central University (Taiwan), which provides the grain-size data as a volume percentage for all the textural distribution (<4 μm to 2 mm). Sand fraction (>63 μm) was identified using a binocular microscope. Relative mineral abundance was estimated by counting a minimum of 200 grains per sample.

6.3.3 Criteria for turbidites events identification and delimitation

A fundamental step in the core analysis was to establish criteria to correctly identify the turbidites sequences as well as to accurately bound them, in order to build the most robust age model. We systematically used grain size variation and geochemical signatures (i.e, Sr, Ca and Fe). As the background sedimentation shows a median grain-size of value of 10 μm (fine silt facies), we consider values higher than 12 μm as outlining "high energy" events. Positive or negative anomalies of major chemical elements relative to hemipelagites help discriminating the base and top of turbidites (Fig.6.4 and 6.5). For the last century, anomalies in the $^{210}\text{Pb}_{ex}$ decay were also good proxies for the precise identification of turbiditic deposits (Fig.6.6).

6.3.4 Radiometric datings and age model

Radiocarbon dating was performed on 25 samples of hemipelagic sediment bracketing turbidites sequences. For AMS ^{14}C dating, we handpicked between 5 and 11 mg of foraminifera which diameter was larger than 250 μm . *Orbulina universa* was used because it was the most common species. We also selected *Globigerinoides ruber*, *Globigerinoides bulloides*, *Globigerinoides sacculifer*, and *Globigerinoides conglobatus*. Foraminifera were prepared and dated at the Laboratoire de Mesure ^{14}C (LMC14) on the ARTEMIS accelerator mass spectrometer at the CEA (Atomic Energy Commission) Institute in Saclay (Table 6.3). To obtain an accurate turbidite

event chronology, the first step was to calibrate the radiocarbon ages using the Marine13 curve (Reimer et al., 2013) used in the OxCal 4.2 software. To this end, it is necessary to know the value of ΔR : the site-specific offset from the global ocean reservoir. Offshore eastern Taiwan, based on marine shells, a wide range of reservoir ages have been estimated by Yoneda et al. (2007) et Yu et al. (2010), suggesting fluctuations in the intensity of coastal upwelling and of the oceanographic context (Dezileau et al., 2014, submitted to Radiocarbon). We thus considered in our study the weighted mean value of the ΔR available offshore eastern Taiwan, i.e., 86 ± 40 years. The next step consisted to determine accurately the age of each single turbidite. Since the collected samples of hemipelagic sediment are located a few cm below or above turbidites, it was necessary to interpolate or extrapolate the ages from sample's depth to turbidite's depth. For this purpose we used the P_Sequence, a Bayesian model of deposition implemented in the computer program OxCal 4.2 (Ramsey, 2008) (Fig.6.7). Given that the hemipelagic sedimentation rate cannot be regarded as perfectly constant, the P_Sequence depositional model takes into account the uncertainties in the variation of the hemipelagic sedimentation rate by considering sedimentation as an inherently random process. The resulting age model, referring to the calibrated age scale, reflects the increasing uncertainties with distance from the calibrated sample ages (Fig.6.7). To compute the P_Sequence model, beside the ΔR value, several input parameters are needed and follow the procedure described in Fig.6.7. First, we virtually removed all turbidites (instantaneous deposits) and consider a continuous hemipelagic section. The uncalibrated ^{14}C ages and their corresponding hemipelagic depths are provided as the main dataset. Second, the uncalibrated ages of the top and bottom boundaries of each core are estimated. These are determined with ample margins, only constrained by the age of the seafloor at the time of sampling and by the age of the shallowest and deepest samples for top and bottom boundaries. Finally, the regularity of the sedimentation process is determined by a factor k , with the higher values of k reflecting smaller variations in sedimentation rate (Ramsey, 2008). For each core, we chose the highest possible values of k , on condition that the modelled age fitted each individual calibrated age with all agreements $\geq 68.2\%$ in P_Sequence model output. The parameter k have been also chosen assuming the fact that we cannot take into account the basal erosion at the base of each turbidites sequences. Applying these criteria we used $k=1$ for all cores, satisfying the most our models. For each core, we obtained the 68% and 95% probability ranges which are plotted in the calibrated age vs hemipelagic depth model (Fig.6.7, 6.8). Based on the hemipelagic depth of every single turbidite, the age models yield the calibrated ages of each events which are reported as maximum probability values at 1σ range in Table 6.4. In the

following sections, turbidite calibrated ages are reported with 1σ ranges based on the most likely turbidite correlations that characterize the occurrence of events.

Dating of the most recent sedimentary layers were performed using ^{210}Pb , ^{137}Cs and ^{241}Am methods on the centennial timescale (Fig.6.6 and Table 6.3). Both nuclides together with U, Th, and ^{226}Ra were determined by gamma spectrometry at the Geosciences Montpellier Laboratory (Montpellier, France). We sampled box-core KS06-B (36 cm long) each centimeter and the activities of $^{210}\text{Pb}_{ex}$ were determined. This allows to accurately calculate the sedimentation rate and estimate the age of each turbidite events over the last century (Fig.6.6) (Dezileau *et al.*, 2014, submitted for method).

6.3.5 Event's terminology

In our study, a single depositional event, called a turbidite event (T_x , from $x=1$ the youngest event) refers to a single well-dated depositional episode under- and overlain by hemipelagite. We called "local events", events that represent synchronous turbidites events recorded within two cores in a single zone. As such, "local events" in the Ryukyu forearc are labeled R_x (from $x=1$ the youngest event) and in the Luzon volcanic arc zone, events are labeled L_x (from $x=1$ the youngest). Regional-scale event labeled M_x are recorded in at least two cores through the two zones offshore eastern Taiwan. The age of the correlative events is determined by the intersection of the age at 1σ range shared by the synchronous events. Non-correlative events are called "uncorrelated events".

6.4 Turbidites identification

We analyze the cores looking for "high-energy" events in the hemipelagic sedimentation. As such, using the aforementioned criteria we aim to identify, characterize and bound turbidites events. Two main sedimentary facies, recognized by Lehu *et al.* (2014a), were distinguished in the cores: 1) hemipelagites and 2) turbiditic facies. Hemipelagite facies was described as homogeneous dark gray-olive clay (with a median grain size usually $\leq 10\mu\text{m}$) with sometimes traces of bioturbation. It is also characterized by a low content of lithic grains ($< 20\%$). The hemipelagite facies vary in thickness from 1 cm to 30 cm and represents about 45% of the total sedimentary record. Turbiditic facies was characterized as a fining upward sequence with a sharp erosive basal surface interbedded with the hemipelagite facies. We distinguished in our record

two kind of turbiditic deposits: a) fine-grained to medium-grained turbidites characterized by a fining upward sequence with coarse basal layer $> 17 \mu\text{m}$ median grain size, and a turbidite tail (around $10\mu\text{m}$); b) turbidites surges, characterized by a fining upward sequence with fine-grained basal layer from 12 to $17\mu\text{m}$ median grain size, and a tail around $10\mu\text{m}$.

Core KS08-P is 0.91 m-long and composed of clay and silty-clay sediments showing numerous laminations (Fig.6.4). They are interpreted as turbidites surges. We distinguished nine events with thickness from 1 to 13.5 cm. Their base shows a 12 to $16 \mu\text{m}$ median grain size, whereas their tails fines upward around $10 \mu\text{m}$. XRF data exhibit Sr and Ca slightly negative anomalies that anticorrelate Fe anomalies (Fig.6.4). Analysis of the coarser fraction of the basal layers show that they contains $\sim 35\%$ of biogenic content, mostly containing planktonic foraminifera and sponge spicules (Lehu et al., 2014a, submitted to Marine Geology). KS09-P is 0.98 m long, located at the bottom of the northern slope of the Ryukyu arc (Fig.6.2). The whole core is composed of clay and silty-clay hemipelagites alternating with fine-grained turbidites. We recognized thirteen events; among these, six belong to facies fine- to medium-grained turbidite and are 2 to 10 cm-thick. They are fining upwards constituted by a sharp basal coarse layer (from 17 to $70 \mu\text{m}$ median grain size) and a silty-clay tail ($\sim 10 \mu\text{m}$ median grain size). The seven others events have been interpreted as turbidites surges. They are characterized by normal grading sequences, with very fine-grained basal layer ($\sim 12 \mu\text{m}$ median grain size) and clay tail ($\sim 10 \mu\text{m}$ median grain size). The XRF analysis show slightly positive Sr and Ca anomalies that anticorrelate slight Fe anomalies (relative to the background sedimentation) (Fig.6.4). The coarser fraction of the basal layers reveal a composition of $\sim 30\%$ of biogenic content, mostly containing planktonic foraminifera and sponge spicules (Lehu et al., 2014a, submitted to Marine Geology).

KAS03-P core is 1.57 m long and is composed of an alternation of clay and silty-clay sediments that shows numerous sequences and laminations that differ from the hemipelagic sedimentation (Fig.6.5). We identified eleven turbidites events interbedded within the hemipelagites. Among them, one 8 cm-thick event (at 118 cm depth below the seafloor) is interpreted as a fine-grained turbidite. It characterized by a sharp basal silty layer (median grain size $17 \mu\text{m}$) and a fining upward tail (median grain size at top $\sim 10\mu\text{m}$). The ten other events have been interpreted as turbidites surges. They are characterized by thin fining upward sequences (from 2 to 7 cm) with very fine-grained basal layers (ranging from 12 to $16 \mu\text{m}$ median grain size) and clay tail (median grain-size $\sim 11 \mu\text{m}$). The eleven events of KAS03-P are characterized by slight positive Sr and Ca anomalies that are anticorrelated with Fe anomalies (negative relative to the background

sedimentation) (Fig.6.5). The sand composition has been analyzed and corresponds to nearly 30% of biogenic content containing mainly planktonic foraminifera and sponge spicules (Lehu et al., 2014a, submitted to Marine Geology). Gravity core KS06-G is 2.12 m long. The whole core is composed of clay and silty-clay hemipelagites alternating with fine-grained to coarse-grained turbidites. We identified fine- to coarse-grained turbidites with thicknesses ranging from 2 to 10 cm. The fining upward sequences are characterized by a sharp erosive base with a grain size fluctuating from 17 to 200 μm median grain size (from medium silt to fine sand respectively) and a tail characterized by a median grain size of about 10 μm . XRF data show clear Sr and Ca positive anomalies, common to all events, that anticorrelate with Fe anomalies (Fig.6.5). Box-core KS06-B constitutes the uppermost part of the sedimentary record at that site. It is 36 cm-long and contains three events interbedded with hemipelagites. The two uppermost events correspond to medium-grained turbidites with a thickness ranging from 4 to 8 cm and characterized by base with a median grain size ranging from 20 to 35 μm . The third event is likely attributed to turbidite surge facies, is 4 cm thick, and has a base with a median grain size of 13 μm . Like KS06-G, Ca and Sr signals in KS06-B display clear positive anomalies that anticorrelate Fe anomalies for the two uppermost events, whereas less marked anomalies in Ca and Fe are observed in the third event, except the Sr signal that exhibits a clear positive anomaly (Fig.6.5). The biogenic fraction of the coarser fraction represents nearly 80% is composed mainly by planktonic and benthic foraminifera, and sponge spicules (Lehu et al., 2014a, submitted to Marine Geology). The abundance of the benthic foraminifera represents about 5% of the biotic fraction. The following species have been identified (Bassetti, personal communication): *Bolivinita quadrilatera*, *Bulimina aculeata*, *Bulimina costata*, *Bolivinita quadrilatera*, *Bulimina aculeata*, *Cassidulina carinata*, *Cibicidoides pachyderma*, *Gyroidina sp*, *Trifarina angulosa*, *Uvigerina proboscidea*. All the species identified are characteristics to a bathyal and abyssal environments.

6.5 Chronostratigraphy

Cores KS08-P and KS09-P allow to trace turbidite events deposited in the Ryukyu Forearc (RF) over the last ~ 2100 years. The two cores exhibit a ~ 1150 years overlap from ~ 350 AD to ~ 1500 AD. The northernmost site KS08 contains turbidites T1 to T9 deposited respectively around 1625-1785 AD, 1490-1635 AD, 945-1110 AD, 915-1045 AD, 820-950 AD, 790-915 AD, 720-840 AD, 625-745 AD, 605-720 AD, and 245-480 AD (Fig.6.8 and Table 6.4). Note that no turbidites

were deposited between ~ 1100 and ~ 1500 . Site KS09, located more distally records thirteen turbidites events (T'1 to T'13), deposited more homogeneously during the collected time span. Turbidites deposited respectively around 1155-1260 AD, 1100-1200 AD, 910-1020 AD, 860-980 AD, 850-965 AD, 785-900 AD, 690-800 AD, 450-580 AD, 410-555 AD, 205-345 AD, 130-255 AD, 65 BC- 80 AD, and 90 BC - 55 AD (Fig.6.8 and Table 6.4). The mean hemipelagic sedimentation rate for cores KS08 and KS09 are 0.35 ± 0.02 mm/yr and 0.37 ± 0.01 mm/yr.

Cores KAS03-P, KS06-G and box-core KS06-B show turbidite deposition in the Luzon Arc (LA) over the last $\sim 2,700$ years. The two cores overlap from ~ 570 AD to ~ 1900 AD. The slope basin with core KAS03 collected eleven turbidites (T''1 to T''12) deposited around 1730-1810 AD, 625-735 AD, 505-625 AD, 475-595 AD, 410-530 AD, 300-410 AD, 180-300 AD, 100-230 AD, 15-145 AD, 30 BC-100 AD, and 525-365 BC respectively. The mean hemipelagic sedimentation rate is 0.46 ± 0.02 mm/yr. The southern slope basin containing core KS06-G and box-core KS06-B shows a composite stratigraphic section of fourteen turbidite events (T'''1 to T'''14) deposited respectively around age 1998-2004 AD (with the $^{210}\text{Pb}_{ex}$ dating and ^{137}Cs on Fig.6.6), 1950-1980 AD (vs 1947-1953 given by ^{210}Pb and ^{137}Cs), 1922-1938 AD (given by the $^{210}\text{Pb}_{ex}$, on Fig.6.6), 1850-1900 AD, 1795-1845 AD, 1700-1745 AD, 1439-1510 AD, 1380-1445 AD, 1360-1425 AD, 1280-1345 AD, 1120-1195 AD, 1075-1155 AD, 990-1080 AD, 780-870 AD, and 520-625 AD (Fig.6.8 and Table 6.4). Surprisingly, most of the turbidites at site KS06 deposited during a gap without turbidites at site KAS03, between ~ 800 AD and ~ 1650 AD. $^{210}\text{Pb}_{ex}$ and ^{137}Cs measured in the box-core KS06-B reveal a 2.1 mm/yr sedimentation rate over the last century, whereas radiocarbon age modeling in core KS06-G outline 1.05 ± 0.05 mm/yr over the last 1500 years (Fig.6.8).

6.6 Discussion

6.6.1 Turbidites correlation

The characterization and dating of deep-sea turbiditic deposits in multiple cores (Fig.6.4, 6.5) allow us to apply a synchronicity test at two scales: (A) in the Ryukyu forearc and the Luzon volcanic arc zones respectively, and (B) at a regional scale, margin-wide (e.g. between the two areas). We consider that the turbidites correlation are established on the basis that at least 2 turbidites are synchronous when they share the best age overlap at 1σ range (Fig.6.9). We also compared our results with the age results of box-core BC-18 from the study of Huh et al. (2004)

(from the RF area) .

A: Correlations at local scale

In the RF zone, the turbidites events correlate from core KS08-P and KS09-P (Fig.6.9, 6.10). In this area turbidites events are recorded between ~ 100 BC to ~ 1800 AD. Despite the important age overlap between turbidites deposition emplacements, we correlate and recognize only six "local events" deposited between ~ 700 to ~ 1100 AD (R1 to R6 on Fig.6.9, Table 6.4). Interestingly, after 1100 AD there is no correlation between the two cores since no events are recorded in KS08-P during ~ 400 years. This ~ 400 years gap occurred right after a cluster of seven events (T3 to T9) and could result from a flush of the slope sediment buffer, thus preventing the trigger of slope failure during this time span. Moreover, the lack of correlation may be explained by the temporal overlap between the two cores, thus discarding events T1 and T2 of core KS08, and T'8 to T'13 of core KS09. Therefore, only the period between ~ 500 to ~ 1500 AD has to be considered for the correlation at local scale in the RF area. In the LA area, KAS03-P and KS06-G turbidites cover from 765 AD to 2004 AD constituting the most longest time record offshore eastern Taiwan. However, given the temporal overlap of the cores, only the time span between 600 AD and 1900 AD is suitable for correlation between the cores and only a single "local event" (L1) (~ 1780 -1840 AD) is correlated across sites in this area. Indeed, core KAS03-P displays a ~ 1000 years-long gap of events. This gap occurred right after a cluster of nine events (T''2 to T''10) suggesting that as in the RF zone, the slope could have been flushed and lacked sediment prone to failure. It is also interesting to note that most events recorded in KS06-G (T'''6 to T'''14) were deposited during that time.

B: Correlations at regional scale

We define a "regional event" (or widespread event) when turbidites events can be correlated on, at least, two cores across two zones (RF+LA) (Fig.6.9, 6.10). The most recent turbidites are identified in both KS06-B and G in the LA zone and BC-18 in the RF zone. In the LA area, we identified three events T'''1, T'''2 and T'''3 in the box-core KS06-B (Fig.6.9), whereas only T'''2 may be correlated in the associated gravity core KS06-G. In the RF, boxcore BC-18 displays four turbidites events 1, 2, 3 and 4 (1 being the youngest) that have been interpreted and dated by Huh et al. (2004). Based on the age results on both box-cores and the time overlap between turbiditic events, two events can be correlated (Fig.6.9B). The first named M1 is deduced from the correlation of events 1 (boxcore BC-18 in the RF zone) and T'''1 (boxcore KS06-B in the

LA), circa 2002 AD and 2001 ± 3 AD respectively. The second, M2, corresponds to events 4 (RF) and T''3 (LA), circa 1922 AD and 1928 ± 10 AD respectively. Sixteen "regional events" fulfill the criterion of synchronicity in the four long cores (Fig.6.9A, 6.10); they occurred between 50 BC and 1750 AD. Twelve events are found in two cores (M1, M2, M3, M4, M5, M10, M11, M12, M13, M14, M15, M16), and four are recorded in three cores (M6, M7, M8, M9). According to different time spans recorded by the sedimentary cores, the regional event correlation is only possible between 150 BC and 1930 AD (Fig.6.9).

To summarize, twenty-three Holocene turbidites are observed on at least two cores over the last 2150 years offshore eastern Taiwan (Fig.6.10). Among them, seven are recognized as "local events" (R1 to R6 and L1 for the RF and the LA zones respectively), two events are widespread (i.e., detected in at least two cores within the two zones) during the 20th century (M1 and M2) and fourteen are widespread and emplaced between 50 BC and 1750 AD (M3 to M16). The remaining six turbidites events were only identified in one sediment core and have been qualified as "uncorrelated events" (Fig.6.10).

6.6.2 From turbidites to earthquakes

Large earthquakes are one of the main driving mechanisms for turbidity current generation resulting from the evolution of a slope failure (Piper et al., 1999). Turbidity currents have been used as proxy for paleoearthquakes since the 1929 Grand Banks Earthquake and associated turbidity current (Heezen and Ewing, 1952). However, this study shows the difficulties to link gravity flow with the 1929 Earthquake because turbidity currents may also be triggered by other processes. Adams (1990), proposed that turbidite generation may be triggered following four mechanisms a) sediment loading, b) wave-induced slumping, c) tsunamis and d) large earthquakes. This list was further extended by Goldfinger et al. (2003) that added e) crustal earthquakes, f) slab earthquakes, g) aseismic accretionary slip wedge, h) hyperpycnal flows, and i) gas hydrate dissociation. Postglacial isostatic rebound (Blumberg et al., 2008) has also been regarded as a possible turbidite triggering mechanism. Most of these mechanisms are related to local processes. However, only large earthquakes, storm and hyperpycnal flows can trigger widespread events in a given region (Goldfinger et al., 2003; Gràcia et al., 2010; Poudoux et al., 2012, 2014).

Synchronicity criterion

In the turbidite paleoseismology approach, the criteria of synchronicity is the most accepted and

robust criteria to suggest that a turbidity currents is triggered by slope failure consecutive to a seismic ground shaking.

The criterion of "synchronicity of turbidites events", defined by Adams (1990), Nelson et al. (1996) and Goldfinger et al. (2003, 2007), is in first approximation, based on the "confluence channel test", meaning that the same number of turbidites should be detected upstream and downstream between tributaries, slope channels and the deep-sea channels. Offshore eastern Taiwan, canyon heads are very closely located to river mouths; to avoid the record of turbidites triggered by major floods related to frequent typhoons, we chose to locate the core sites away from submarine canyons and deep-sea channels.. Instead of applying the "confluence channel test", the synchronicity test in this work is established on the existence of coeval turbiditic events deposited in separated areas (perched basins and isolated terraces) (Fig.6.2, 6.3, 6.9, 6.10). Therefore, the twenty-three synchronous events observed in our cores suggest that they may be related to slope failures triggered by seismic shaking that occurred between ~50 BC and ~2003 AD.

Sediment sources

To support the assumption that our sites mainly record seismic events, another argument is discussed such as the biogenic composition of the coarse fraction of the turbiditic beds, to deduce the origin of sediments mobilized and transported by turbidity currents (Pouderoux et al., 2012; Gràcia et al., 2010). For cores KS08-P, KS09-P and KAS03-P, the sand fraction of the basal layer reaches ~30% and is composed of planktonic foraminifera and sponge spicules suggesting a slope origin of sediments prior they were reworked during slope failures. This is more striking at core site KS06 where the sand fraction reaches 80%. Turbidites are composed of large amount planktonic foraminifera, sponge spicules and also benthic foraminifera (Lehu et al., 2014a, submitted to Marine Geology). As previously described, Benthic foraminifera assemblage contained in the turbidites beds suggests a slope origin comprises between ~200-1000 m below sea level (Bassetti, personal communication). This clearly suggests a slope origin of the materials reworked after slope instabilities related to seismic ground shaking. Moreover, it has been observed that sedimentary cores retrieved and analyzed from the Southern Longitudinal Trough a proximal basin directly fed by major rivers (SLT on Fig.6.1B), display a different coarser fraction composition. There, thick and massive sandy turbidites are only composed by lithogenic materials suggesting a direct terrestrial supply from onland rivers to the deep-sea basin during large storm or flood events (Lehu et al., 2014a, submitted to Marine Geology).

Correlation with instrumental seismicity

Numerous seismic events have been instrumentally recorded in the area since the 20th century, the largest being the 1920 M_w 7.7 earthquake that occurred offshore east Taiwan (Fig.6.1A, Table 6.1) (Theunissen et al., 2010). In the RF area, Huh et al. (2004) have demonstrated that turbidite can be used as a paleoseismicity marker. In their box-core located nearby KS08 site (BC-18 on Fig.6.2) four turbidites 1, 2, 3 and 4 (Fig.6.9) have been interpreted and dated using $^{210}\text{Pb}_{ex}$ at circa 2002, 1986, 1966 and 1922 respectively (Fig.6.9). Among the possible earthquakes candidates shown in Table 6.1 and Fig.6.1, they attributed turbiditic events 1, 2, 3 and 4 to the 2002 M_w '7 earthquake (where M_w ' is the equivalent moment magnitude defined by Theunissen et al., 2010), the earthquake M_w '7.3 1986, the 1966 M_w '7.5 earthquake and the 1922 M_w '7 earthquake respectively.

In order to associate possible earthquakes to the three most recent turbidites identified in KS06-B (LA area), we aim to calibrate the seismic source responsible for slope instabilities and turbidity currents generation. To do so, we use empirical relationships established by Chung (2013) that link peak ground acceleration, magnitude and epicentral distance to estimate the impact of high-magnitude earthquakes on slope failures. We choose 0.1 g as critical peak ground acceleration from which a slope starts to be destabilized (Dan et al., 2009; Pouderoux et al., 2014). Considering soft sediments conditions, the distance required for a M_w 7 and M_w 8 earthquake to trigger mass failures has been calculated. We found that 0.1 g is reached at 50 km epicentral distance for an earthquake M_w 7 and at 100 km epicentral distance for an earthquake M_w 8. This allows us to draw 50 km and 100 km circles respectively centered on the turbidites source areas of both sites KS06 and BC-18 (Fig.6.11).

After an examination of the catalog of earthquakes along the east Taiwan (see Table 6.1) we identified the candidates earthquakes within the source area of KS06 site (Fig.6.11). The uppermost turbidite layer T1'' corresponds to 2001 ± 3 AD (Dezileau et al., 2014, submitted to Radiocarbon) and shows a good temporal correlation with the 2003 M_w 6.8 Chengkong earthquake. The epicenter of this earthquake was located on the offshore slope of the Coastal Range (Fig.6.1), about 22 km north from the KS06 site, which suggests a relatively close source and consequently a good candidate for T''1. T''2 corresponds to 1950 ± 5 AD (Dezileau et al., 2014, submitted to Radiocarbon) and shows a good temporal correlation with the 1951 M_w 7.1 Taitung earthquake. The epicenter of this earthquake was located on the emerged part of the Coastal Range, about 45 km north of the KS06 site. Finally, T3'' has been estimated at 1928 ± 10 AD (Dezileau et al., 2014, submitted to Radiocarbon) and may be correlated with the 1935

M_w 7 earthquake. The epicenter is located on the slope of the Luzon arc southward Lutaos island and about 45 km from the coring site (Fig.6.11). These results thus show that both KS06 and BC-18 can record M_w 7 within 50 km radius. It also shows that neither the circles of magnitude M_w 7 and M_w 8 of the two source areas overlap (Fig.6.11), indicating that regional scale correlation between BC-18 and KS06-B sites are not possible, unless if an earthquake $M_w > 8$ would occur. Given that such large events have never been recorded during the last century, the two widespread correlation M1 and M2 are not plausible. Furthermore, the earthquakes $M_w \geq 6.8$ instrumentally recorded during the last century, occurred in a very short lapse of time which is comprised in the error bars of the turbidites ages, making these two "margin-wide" correlations M1 and M2 fortuitous.

6.6.3 Estimation of earthquake sources and magnitudes, and recurrence intervals

Applying the same approach as for the instrumental period, we extend these results to the fourteen other potentially regional events (M3 to M16) and the seven potentially local events. Fig.6.12A shows the possible overlap domains for a M_w 8 earthquake (red zones) of the source areas from both the RF and LA zones. In other words, the two red zones represent the regions off Hualien where if a M_w 8 earthquake should occur, it may trigger synchronous turbidites at a regional scale based on three cores (see Fig.6.9 and 6.10 for turbidites correlations). In the very restricted red area, synchronous turbidites are possible between cores KS06-G, KAS03-P and KS09-P. In the second red surface, synchronous turbidites are possible between cores KAS03-P, KS09-P and KS08-P. However, no overlap exists between KS06 and KS08 sites showing that no synchronous turbidites are possible for earthquake M_w 8. As such, the black zones indicate the overlap regarding the source areas on a single zone. We thus estimate that the fourteen events recognized as regional events could potentially correspond to M_w 8 earthquakes having occurred in the red zones. The seven local events may correspond to $M_w \geq 7$ earthquakes as shown in Fig.6.12B.

If we consider that the fourteen at regional scale are reliable, it means that we mostly recorded $M_w \geq 8$ earthquakes in restricted areas between 50 BC and 1750 AD, which is less probable (Fig.6.12). Furthermore, no such big events were instrumentally recorded offshore eastern Taiwan. Moreover, we also demonstrated that over the last century events M1 and M2 were not widespread as assumed by the synchronicity criterion (Fig.6.9B). Consequently synchronous tur-

bidites at margin scale should be cautiously regarded. We thus decide to not consider the correlations at regional scale. Instead, we regard cores individually and correlations at local scale (Fig.6.9 and 6.10).

In the RF, we have considered that we mainly recorded seismic related turbidites between 100 BC and 1800 AD. Furthermore, the study of Huh et al. (2004) revealed that only earthquakes $7 \leq M_w \leq 7.5$ were responsible of turbidites deposition over the last century. This suggests that most of turbidites record within KS08 and KS09 are likely to be considered as related to earthquakes $M_w < 8$, even if we cannot not completely ruled out the occurrence of $M_w \geq 8$ within the sedimentary archives. Moreover, between 688 AD and 1109 AD we have a relatively good events correlation between cores KS08-P and KS09-P based on the six synchronous events (at local scale) previously discussed (R1 to R6, Fig.6.9 and 6.10). We can thus estimate an approximate return time of 70 years for the period between 688 AD and 1109 AD in the RF area for earthquakes $M_w \geq 7$.

In the LA area, we also suggested that turbidites deposition is mainly related to seismic activity between 500 BC to 1900 AD. The results obtained on the instrumental period have shown that earthquakes $6.8 \leq M_w \leq 7.1$ are likely recorded in box-core KS06-B. However, only one event was correlated (L1) at a local scale in that area since no events are recorded in KAS03-P right after T² and since the stratigraphy of KS06-G does not share a common span of time able to correlate with the events of KAS03-P (Fig.6.9). It appears thus not possible to establish a recurrence time based on events correlation between the two cores. Also, because of the lack of correlations between KS06-G and KAS03-P, it appears difficult to consider KAS03-P individually since the turbidites does not display distinct sedimentological and chemical signatures (Fig.6.5).

In contrast, KS06-G displays continuous turbidites record with clear chemical, grain-size and biotic signatures. Furthermore, the three turbidites layers, recorded in its sister KS06-B, display similar facies and have been correlated to three instrumental earthquakes. It is thus possible to determine a mean return time only based on turbidites of KS06-G between 779 AD and 1897 AD. We estimate an approximate mean return time of 80 years for earthquakes $M_w \geq 6.8$.

The return times of earthquakes $M_w \geq 6.8$ estimated in both areas, indicate that they are higher than the return time of the earthquakes $M_w \geq 6.8$ that occurred during the instrumental period. Indeed, for the RF area, if we consider the six earthquakes that occurred within the black area as drawn on Fig.6.12B, we estimate a return time of $M_w \geq 6.8$ of 16 years. As such, in the RF area we estimate a return time of $M_w \geq 6.8$ of 34 years based on the three instrumental earthquakes that occurred within the black zone (Fig.6.12B). These higher values obtained for

the instrumental period clearly indicate that turbidites do not record all earthquakes events.

6.7 Conclusion

This work presents a first chronological correlation of deep-sea turbiditic deposits along the offshore eastern Taiwan based on the detailed description and dating of sedimentary cores collected in the Ryukyu forearc basin and the Luzon volcanic arc. Age modeling provide an estimate of each turbiditic layers deposited during the last 2,700 years. The age of turbidites ranges from 500 BC to 2003 AD. Over the instrumental period (20th century), seven turbiditic events occurred and correspond to seven instrumental $\geq M6.8$ earthquakes offshore eastern Taiwan. For the last 2,700 years, we recognized seven local scale events between 700 AD and 1840 AD deposited in the RF and LA area. Sixteen regional scale correlations are possible based on age correlation. Also twenty turbiditic events are interpreted as uncorrelated. According to the sites locations and the biotic composition of turbidites beds, we suggest that earthquakes are the most likely triggering mechanisms of turbidites record off east Taiwan. The use of empirical relationships evaluating the upper slope stability allows us to estimate the distance required for an $M_w 8$ and $M_w 7$ earthquakes to trigger slope failures. The constraints provided by the instrumental period point out that: 1) earthquake calibration using peak ground acceleration and magnitude allowed us to identify three candidate earthquakes that may be attributed to the three most recent turbidites layers; 2) all the turbidites in cores BC-18 and KS06-B (RF and LA areas respectively) are correlated with historical earthquakes, confirming that earthquakes are the main triggering mechanisms of slope failures in both RF and LA areas. We also argue the fact that two events former interpreted as widespread (M1 and M2) are not plausible for the following reasons: 1) because the seismic calibration clearly shows that a $M_w > 8$ earthquake is required to trigger synchronous turbidites between the two sites However no such events occurred during the last century; 2) because the frequency $M_w \geq 6.8$ during the instrumental period is comprised in the errors bars of the turbidites ages, making these two regional correlations fortuitous.

Once calibrated, we extend our findings over longer span of time. We then considered correlations at local scale (or cores individually) and that turbidites records mainly correspond to $M_w \geq 6.8$. Return times of 70 years for the period between 688 AD and 1109 AD and 80 years for the period 779 AD to 1897 AD were estimated for the RF and LA areas respectively for earthquakes $M_w \geq 6.8$. Finally, return times for $M_w \geq 6.8$ estimated over the last 2,700 years are higher than those estimated over the instrumental period indicating that, not all the seismic

events cannot be recorded by turbidites and that it may severely affect the return time estimation over longer period. We thus suggest that turbidite correlations approach must be cautiously undertaken and that more sedimentary cores are needed to strengthen our results.

6.8 Acknowledgments

We thank: Maria-Angela Bassetti (CEFREM, Perpignan) for benthic forams identification and interesting discussions, Kuo-Yen Wei (NTU) for XRF analyses, Lee Teh-Quei (IES) for MSCL measurements, TORI for core management, Shun-Wen Yu (NCU, Taiwan), Mo-Tsi Tsai (NCU, Taiwan), Don Su (NTU, Taiwan), Jean-Pascal Dumoulin for ^{14}C dating (ARTEMIS program), also all others people who offered their help, advice, technical support. We are also highly grateful to our supports: FIT, BRT, CNRS-INSU, the National Central University, the MOST and the LIA-ADEPT.

Eq. number	Date (yy/mm/dd)	Lon.(°)	Lat. (°)	Depth (km)	M_w '(*)	Loc. origin references
1	1915/2/28	123.50	23.60	0	7.5	1
2	1919/12/20	122.50	22.50	35	6.9	1
3	1920/6/5	122.22	24.29	35	7.7	2
4	1921/4/2	123.00	23.00	35	7.1	1
5	1922/9/1	122.04	24.50	35	7.3	1
6	1922/9/14	122.64	24.370	35	7	1
7	1935/9/4	121.55	22.50	20	7	3
8	1935/4/20	120.82	24.35	5	6.9	3
9	1947/9/26	123.00	24.75	110	7.3	1
10	1951/10/21	121.72	23.87	4	7.1	4
11	1951/11/24	121.35	23.27	36	7.1	4
12	1951/10/22	121.72	24.07	1	6.9	4
13	1951/10/22	121.95	23.82	18	6.9	4
14	1957/2/23	121.80	23.80	30	7.1	3
15	1959/4/26	122.79	24.68	126	7.5	1
16	1963/2/13	122.06	24.35	35	7.1	1
17	1966/3/12	122.69	24.30	28	7.5	1
18	1972/1/25	122.32	22.54	10	7.3	1
19	1978/7/23	121.32	22.35	6	7.2	3
20	1986/11/14	121.83	23.99	15	7.3	3
21	1999/9/20	120.80	23.85	6	7.6	5
22	2002/3/31	122.16	24.16	16	7	5
23	2003/12/10	121.38	23.07	21	6.8	5

Table 6.1: $M_w \geq 6.8$ earthquakes recorded over the instrumental period (20th century) in the studied area. References for the location origin: 1. Engdahl and Villaseñor (2002); 2; Theunissen et al. (2010); 3. Cheng and Yeh (1989); 4. Chen and Tsai (2008); Cheng et al. (1996); 5. Wu et al. (2008). (*) M_w : equivalent moment magnitude determined by Theunissen et al. (2010).

Core	Longitude	Latitude	Depth (mbsl)	Length (cm)	Sample depth (cm)	¹⁴ C age (yr BP)	Calibrated age (*) (BC/AD)
KS08-P	122°08'	24°19'	2800	91	10-11	940± 30	1446-1551
					34-36	1540± 30	962-1127
					52-54	1675± 30	775-900
					69-71	1530± 30	711-834
					82-84	1540± 30	582-692
KS09-P	122°11'	24°08'	2900	98	0-2	970± 30	1435-1505
					12-13	1415± 30	1142-1237
					21-23	1470± 30	1006-1097
					45-47	1650± 30	728-848
					52-54	1845± 30	644-736
					63-64	286± 30	412-557
					83-85	2305 ± 30	100-220
96-98	2550± 30	(BC)158-(BC)19					
KAS03-P	121°42'	23°15'	1700	157	10-12	565± 30	1714-1786
					30-32	1310± 30	1205-1270
					45-47	1405± 30	1010-1078
					59-61	1690± 30	715-800
					93-95	2130± 30	263-363
126-128	2475± 30	(BC)135-(BC)29					

					152-154	2885± 30	(BC)669-(BCB)514
KS06-G	121°30'	22°51'	1947	212	26-28	575± 30	1829-1877
					56-58	585± 30	1696-1738
					103-105	1045± 30	1319- 1371
					129-131	1365± 30	1110- 1185
					199-201	1800± 30	645-716
KS06-B	121°30'	22°51'	1947	36			

Table 6.2: Location of the studied cores, AMS radiocarbon data and sample age calibrations based on the Marine13 curve. (*) Corrected ages with the local reservoir correction of $\Delta R = 86 \pm 40$ based on [Yoneda et al. \(2007\)](#).

Core depth (cm)	$^{210}\text{Pb}_{ex}$ (dpm/g)	^{137}Cs (mBq/g)
0.5	51.962	0.621
1.5	47.722	0.000
2.5	32.861	0.804
3.5	21.359	1.125
4.5	20.695	0.514
5.5	20.732	1.030
8.5	21.355	0.522
9.5	28.598	0.359
10.5	37.976	0.567
12.5	32.507	0.852
13.5	19.771	0.852
14.5	27.764	0.822
15.5	21.306	0.964
16.5	19.148	1.629
17.5	16.723	2.123
18.5	15.869	3.718
19.5	15.746	5.793
21.5	11.085	1.624
23.5	7.126	0.000
24.5	5.968	0.000
25.5	6.916	0.000
26.5	4.967	0.000
27.5	7.371	0.000
28.5	6.734	0.000
29.5	5.130	0.000
30.5	4.197	0.000
32.5	3.346	0.000
33.5	3.618	0.000
34.5	3.429	0.000
35.5	3.375	0.000

Table 6.3: Activity-depth profiles of $^{210}\text{Pb}_{ex}$ and ^{137}Cs in KS06-B core.

Core	Name	Age min (1σ)	Age max (1σ)	Turbidite event
KS08-P	Top	1930	1931	-
	T1	1625	1784	M3
	T2	1491	1634	M4
	T3	943	1109	M6, R1
	T4	917	1046	M7, R2
	T5	820	949	R3
	T6	788	915	R4
	T7	720	841	M8, R5
	T8	627	747	M9, R6
	T9	604	719	M10
	Bottom	243	481	-
KS09-P	Top	1451	1535	-
	T'1	1155	1260	M5
	T'2	1102	1201	M6, R1
	T'3	909	1020	M7, R2
	T'4	862	978	R3
	T'5	851	967	R4
	T'6	785	897	M8, R5
	T'7	688	797	M9, R6
	T'8	450	578	M11
	T'9	412	555	M12
	T'10	206	345	M13
	T'11	130	256	M14
	T'12	(BC)65	80	M15
	T'13	(BC)90	53	M16
Bottom	(BC)185	(BC)36	-	
KAS03-P	Top	1900	1901	-
	T'1	1734	1811	L1

T''2	626	734	M9	
T''3	505	626	M10	
T''4	474	596	M11	
T''5	410	532	M12	
T''6	300	410	-	
T''7	176	296	M13	
T''8	100	230	M14	
T''9	16	147	M15	
T''10	(BC)30	100	M16	
T''11	(BC)524	(BC)365	-	
Bottom	(BC)765	(BC)585	-	
<hr/>				
KS06-G/B	Top	2011	2012	-
	T''1	(**)1998	(**)2004	M1
	T''2	1950	1980	-
	T''3	(**)1922	(**)1938	M2
	T''4	1850	1897	-
	T''5	1794	1844	L1
	T''6	1702	1746	M3
	T''7	1439	1510	M4
	T''8	1378	1443	-
	T''9	1360	1423	-
	T''10	1282	1346	-
	T''11	1122	1196	M5
	T''12	1077	1156	M6
	T''13	995	1080	M7
	T''14	779	870	M8
	Bottom	520	624	-

Table 6.4: Calibrated ages of the turbidite events. Calibration is based on Marine13 included in OxCal 4.2 calibration software. Turbidite ages are modeled using the P_Sequence model of deposition implemented in OxCal 4.2 (Ramsey, 2008). (**) Ages obtained with $^{210}\text{Pb}_{ex}$ and ^{137}Cs dating.

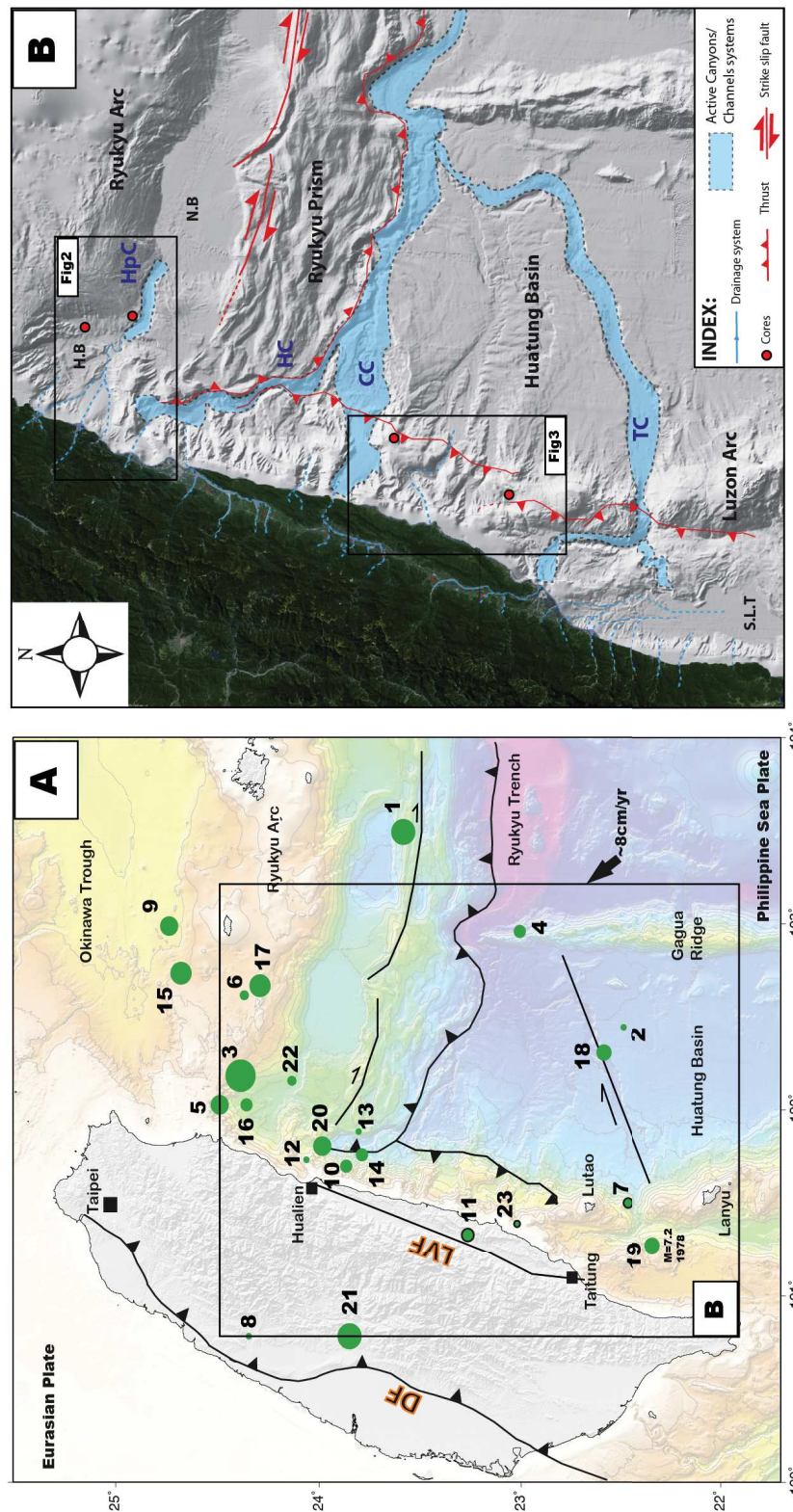


Figure 6.1: A: General geodynamic setting of Taiwan. Onland are represented the two major fault zones are DF: Deformation Front and LVF: Longitudinal Valley Fault. The black arrow shows the plate convergence component. Green dots represent the instrumental seismicity over the 20th century with corresponding numbers listed in Table 6.1; B: morpho-tectonic map of the study area. Blue dashed-lines represent drainage systems from rivers to offshore channels. In blue are represented the major submarine canyon east Taiwan. Red dots represent the studied cores locations. SLT= Southern Longitudinal Trough; TC= Taitung Canyon; CC=Chimei Canyon; HC=Hualien Canyon; HpC=Hoping Canyon; N.B= Nanao Basin; H.B= Hoping Basin.

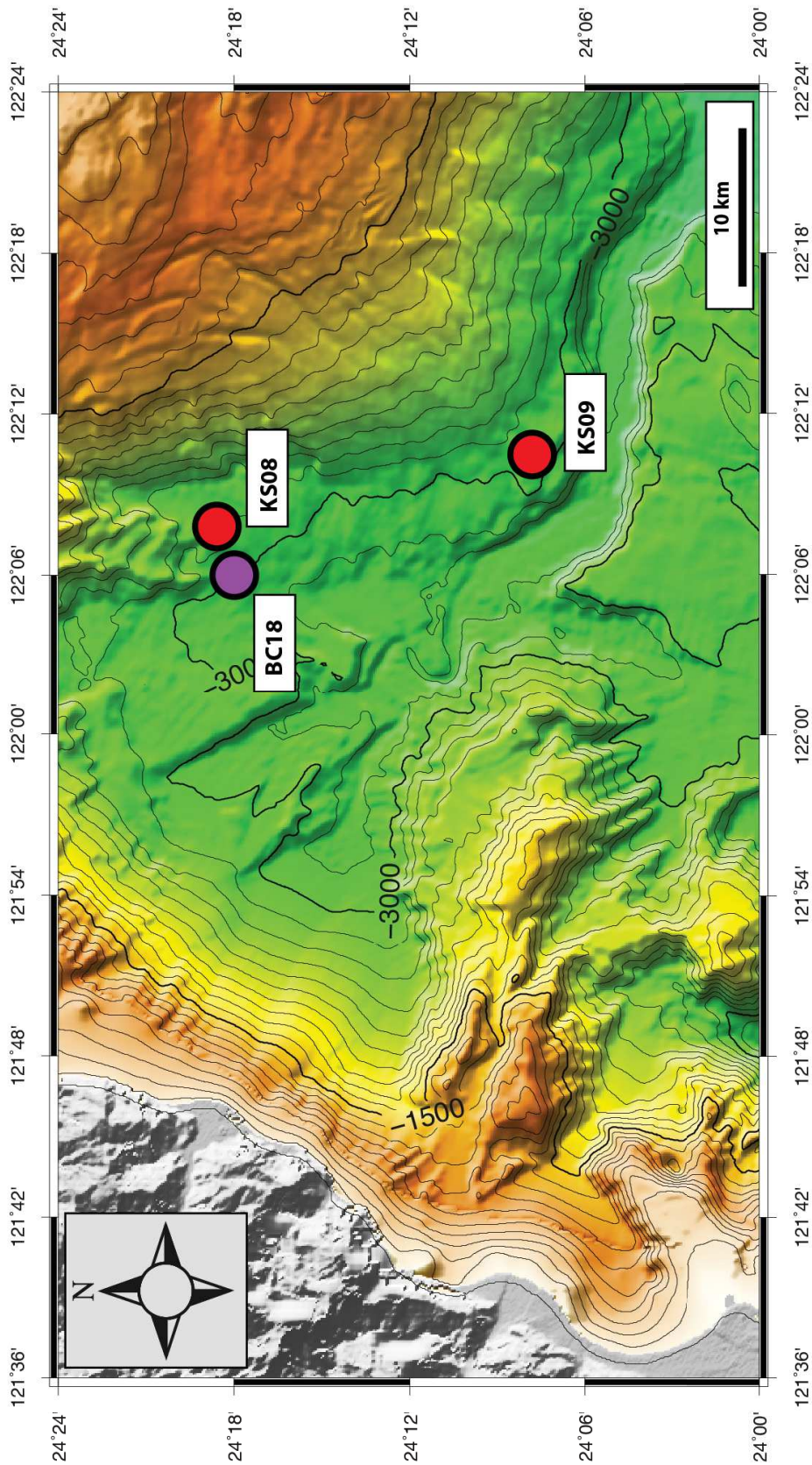


Figure 6.2: Close bathymetric view of the Ryukyu forearc zone. Red dots are cores from the present study. Purple dot represents the core location of the study of [Huh et al. \(2004\)](#).

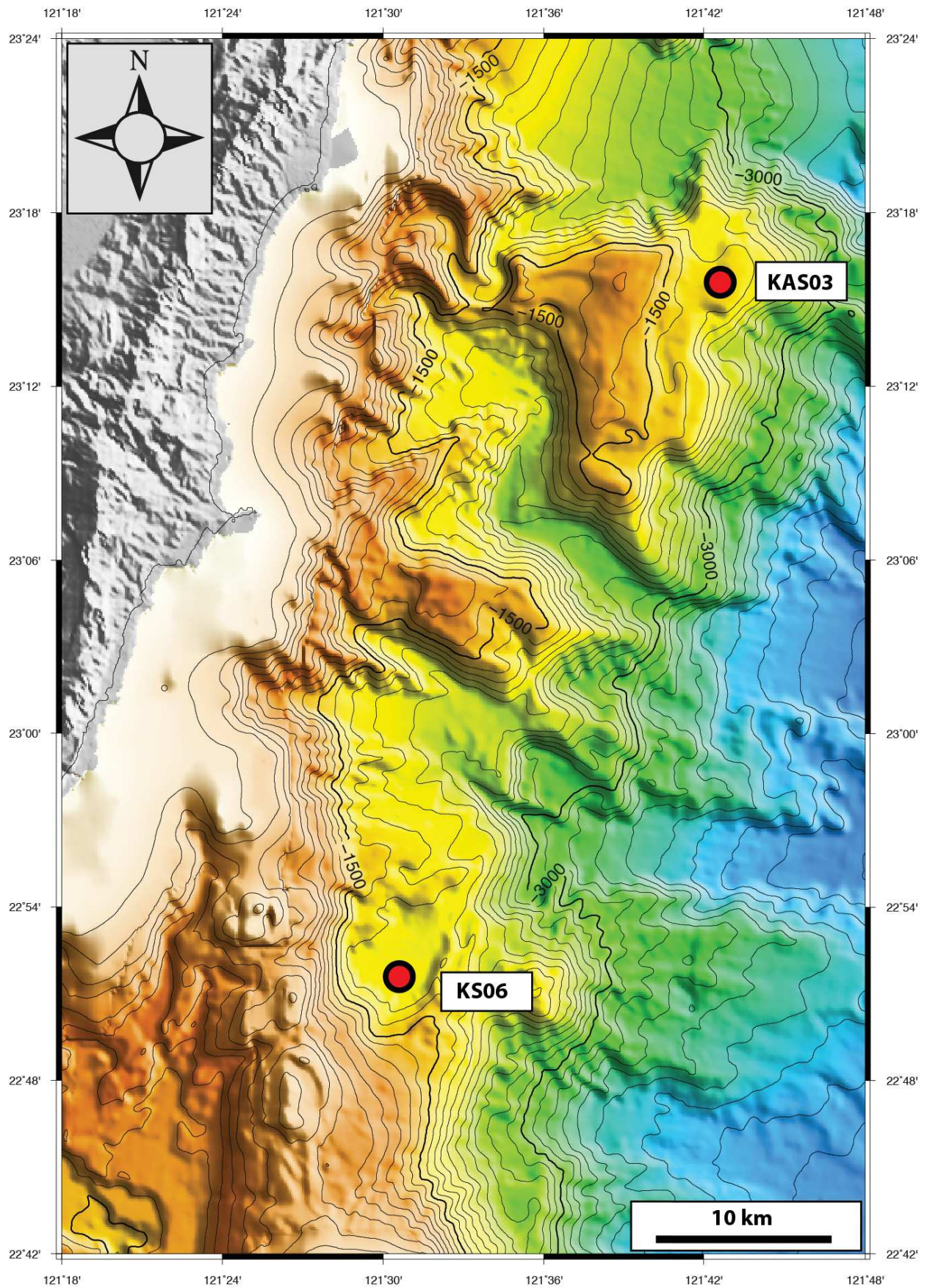


Figure 6.3: Bathymetric map representing a zoom on the Luzon volcanic arc zone. Red dots are the cores studied in the present paper.

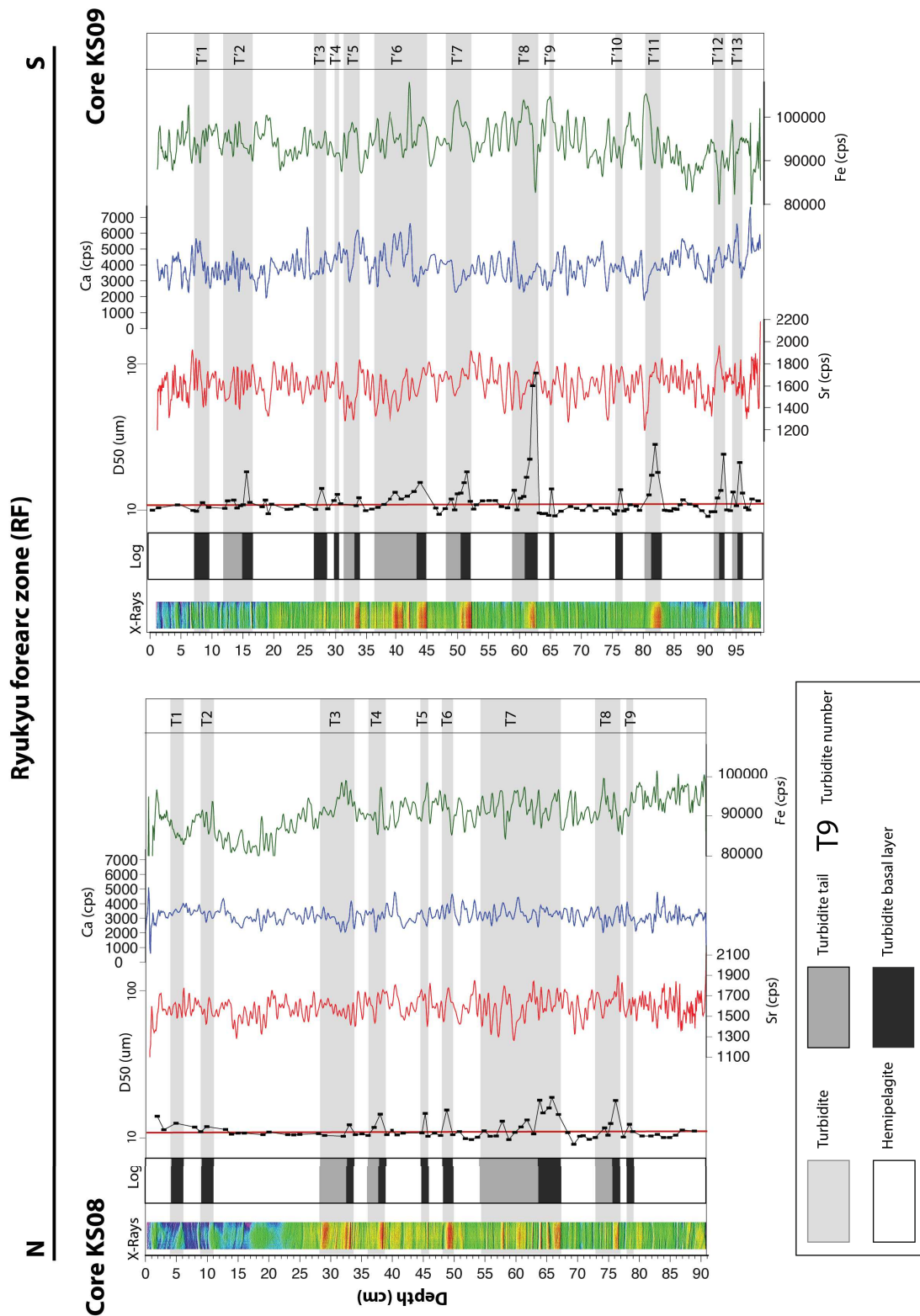


Figure 6.4: X-rays imagery (given with equivalent colors of gray tones), lithological description, median grain size, geochemical composition (Sr, Ca and Fe) of the studied sections of the OR1-1013 and OR1-1048 cores from the Ryukyu forearc zone. Turbidite numbers are depicted for each core. Red line marks the $12\mu\text{m}$ threshold in the grain size.

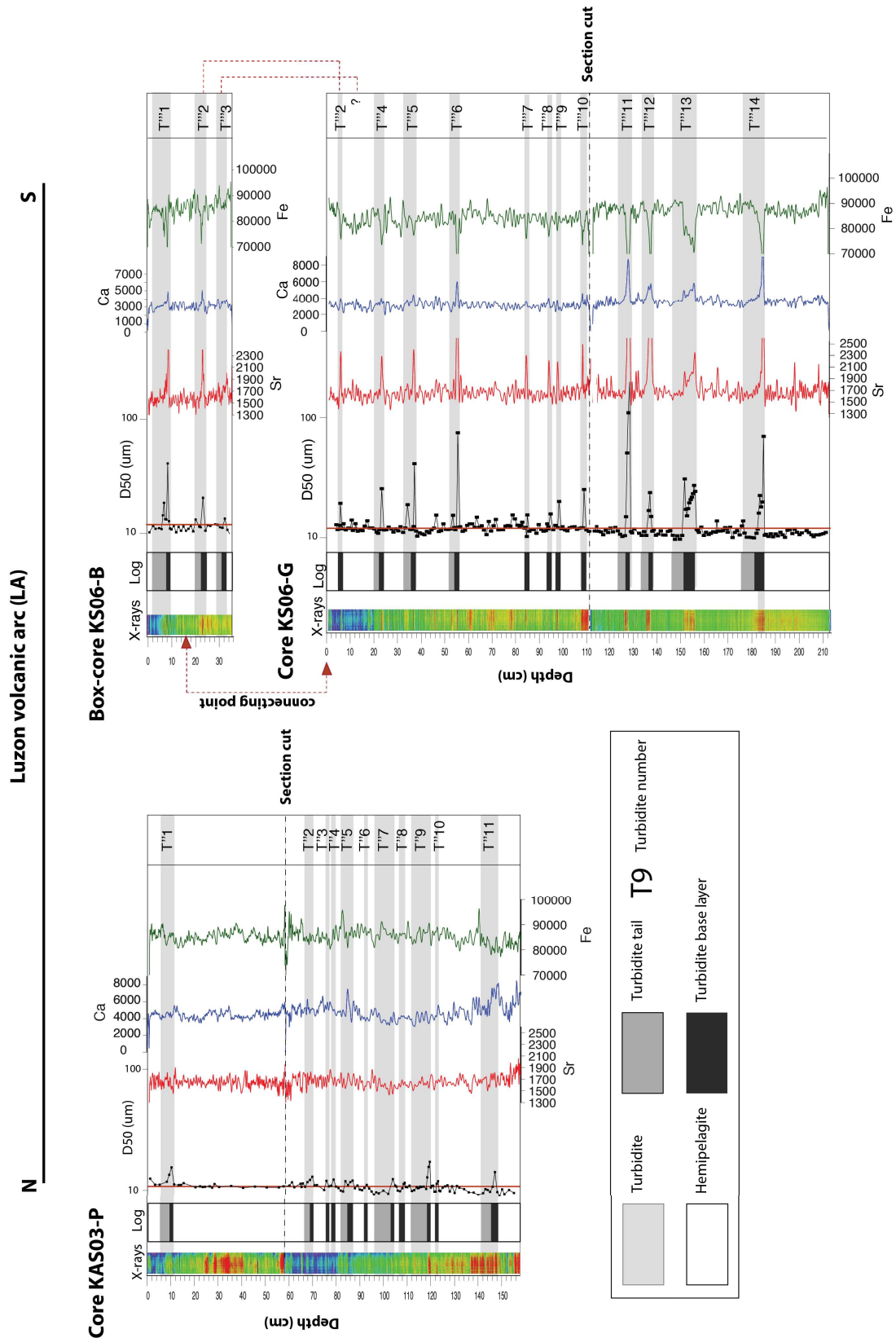


Figure 6.5: X-rays imagery (given with equivalent colors of gray tones), lithological description, median grain size, geochemical composition (Sr, Ca and Fe) of the studied sections of the OR1-1013 and OR1-1048 cores from the Luzon volcanic arc zone. Turbidite numbers are depicted for each core. Red line marks the 12 μ m threshold in the grain size.

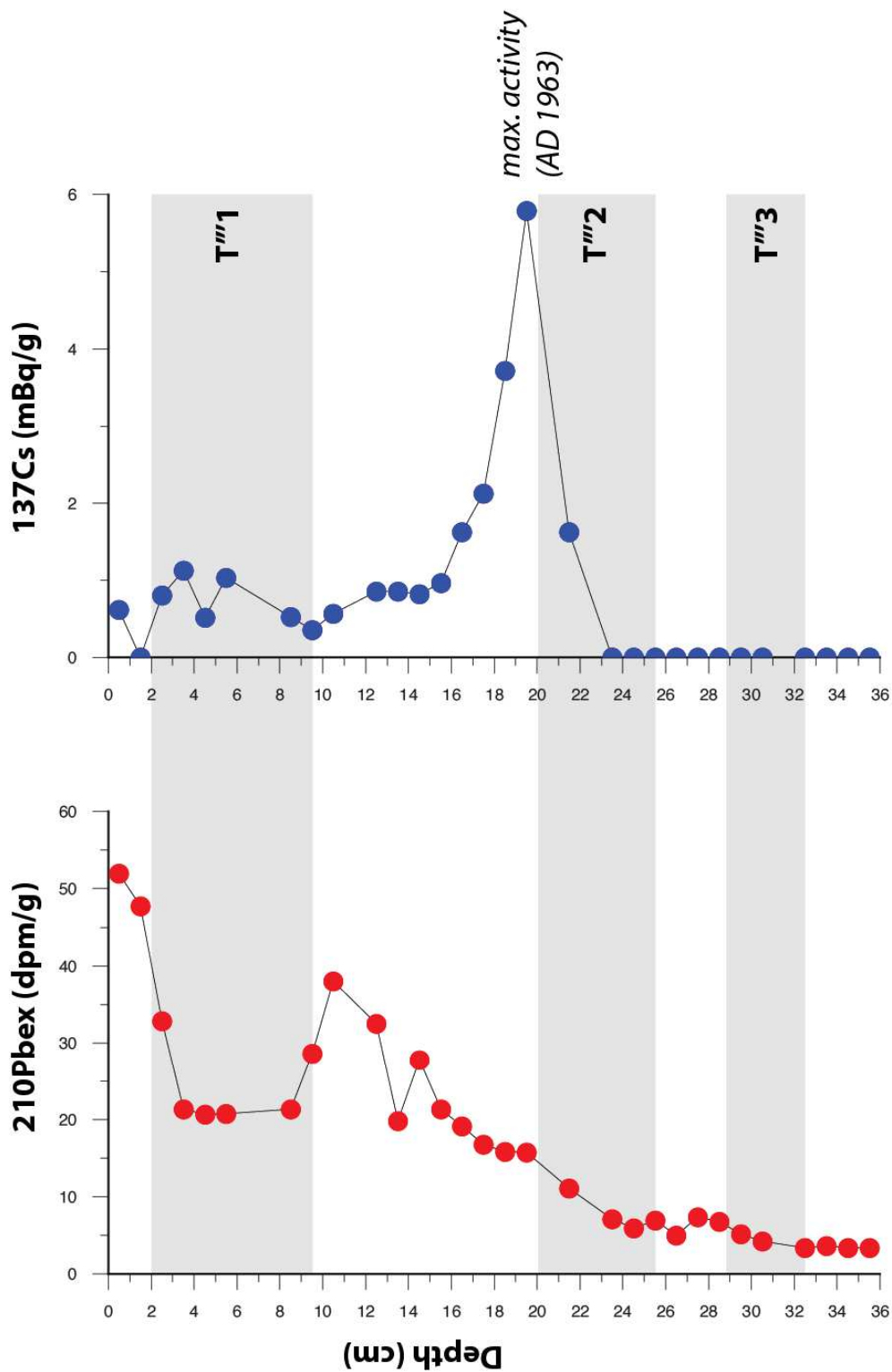


Figure 6.6: Activity-depth profiles of $^{210}\text{Pb}_{ex}$ and ^{137}Cs in boxcore KS06-B

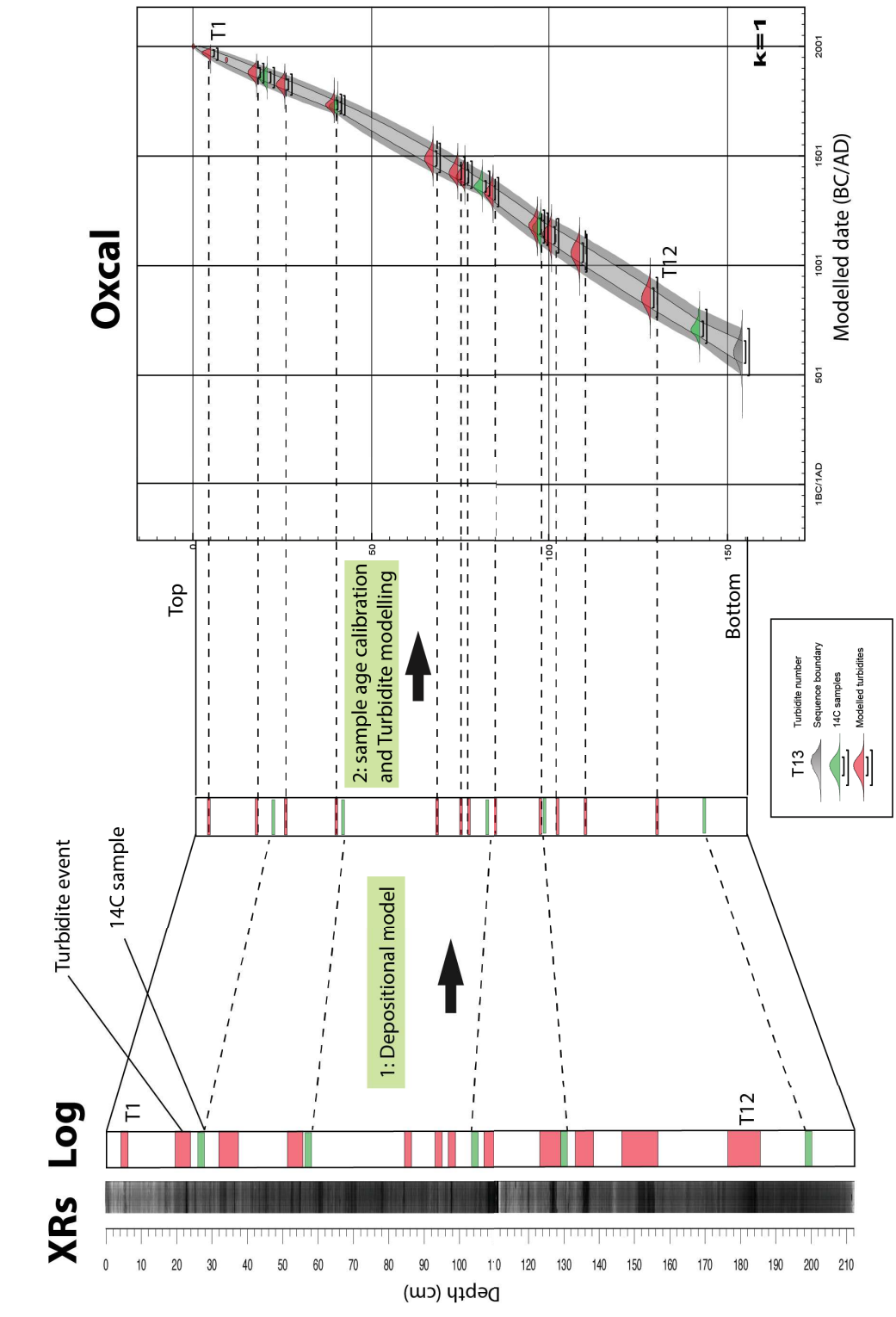


Figure 6.7: Methodology used for ^{14}C age modeling, using the P_sequence in OxCal program: 1. All turbidites sequences are virtually removed to build hemipelagite model; 2. ^{14}C date are calibrated. Input parameters to generate the age model are the uncalibrated ^{14}C ages and respective ΔR correction with their corresponding corrected depths. Age model are built using the P_Sequence (a Bayesian model of deposition) implemented in the computer program OxCal 4.2 that assimilates sedimentation as a random process (Ramsey, 2008). The regularity of sedimentation is determined by the k parameter (see text for details). Sequence boundary indicates the boundary of the depositional model. Each turbidites layers are then inserted in the age model and their ages modeled.

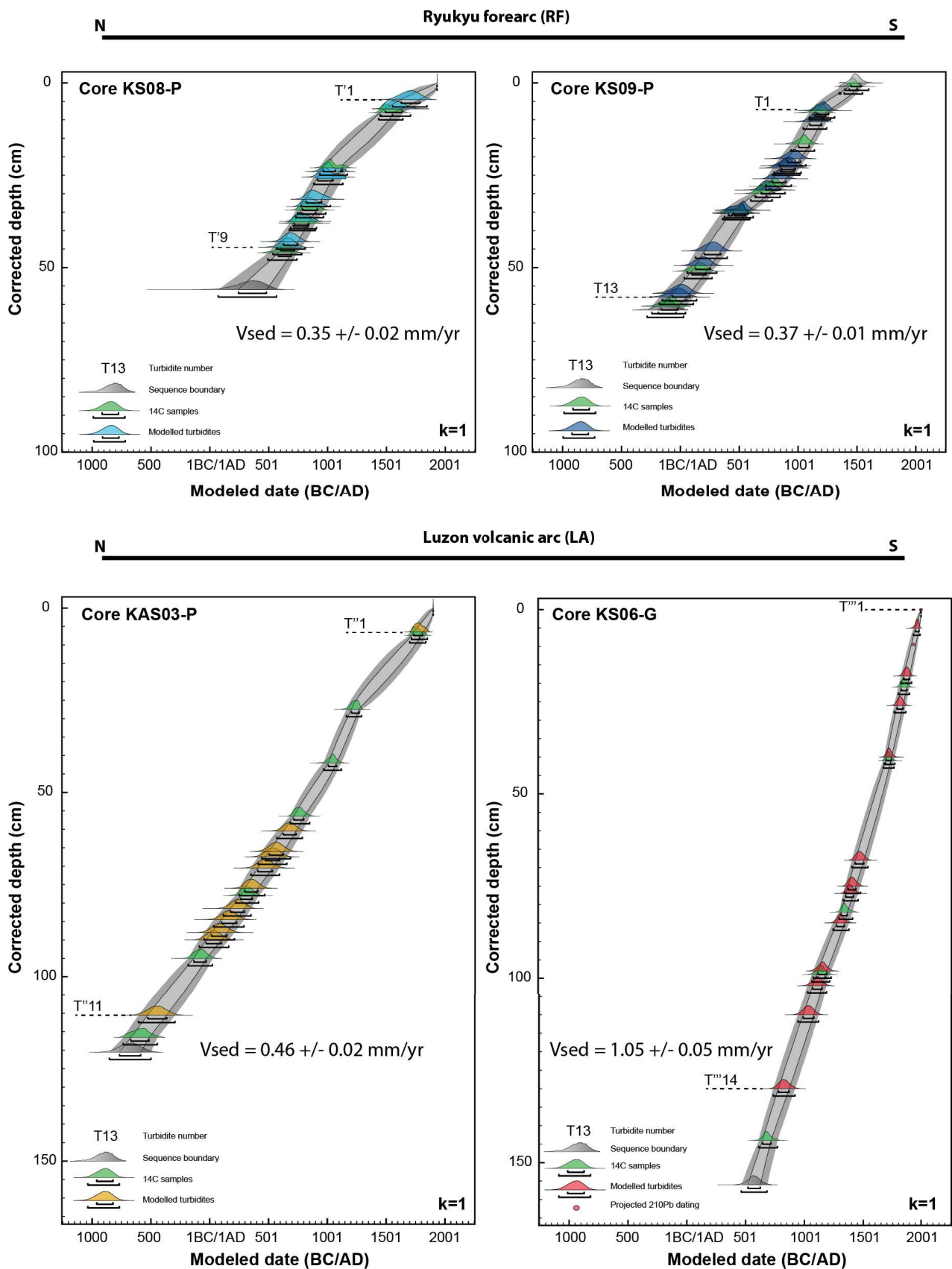


Figure 6.8: Oxcal age models from the four studied cores, showing the sedimentation rate of hemipelagite through time and turbidites ages modeled. The k parameter is used to define the regularity of the sedimentation rate along the core. Since hemipelagite is assumed roughly constant rate, the highest k parameter was chosen for each core. All ages are plotted with their 1 and 2σ age range.

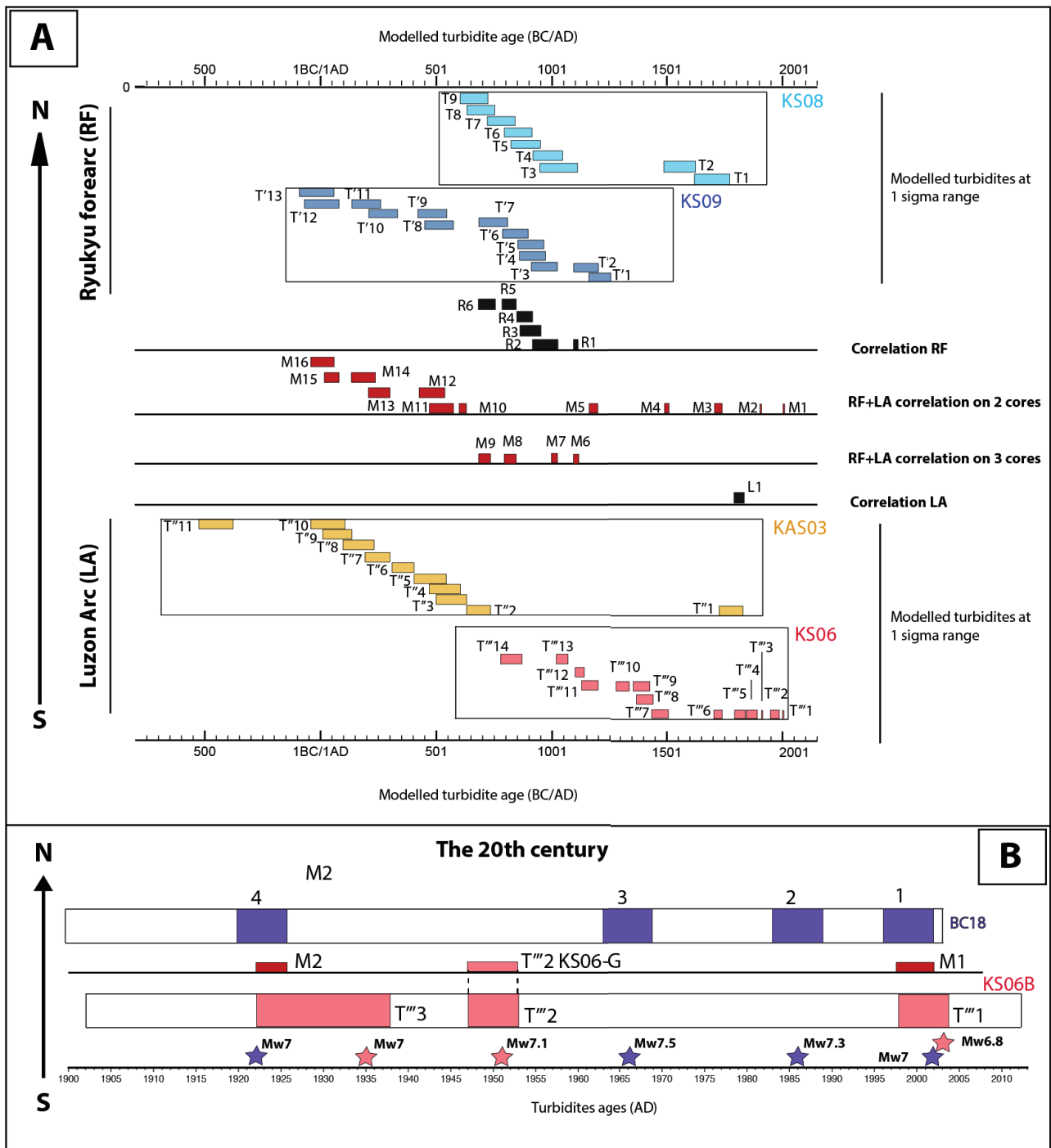


Figure 6.9: A. Age correlation of turbidites from the RF cores and LA cores. Colored rectangles represent turbidites modeled ages at 1σ projected on time axis. Two types of correlation are proposed: zone scale correlation (black rectangle) considering synchronous turbidites between two cores within one zone and margin scale correlation i.e., synchronous turbidites between at least two cores within the two zones (RF+LA); B. Age correlation over the 20th based on ^{210}Pb and ^{137}Cs between box-core BC-18 and KS06-B. Rectangles represent events with their uncertainties projected on time axis. Stars represent candidates earthquakes that correlate the turbidites events.

OFFSHORE EASTERN TAIWAN

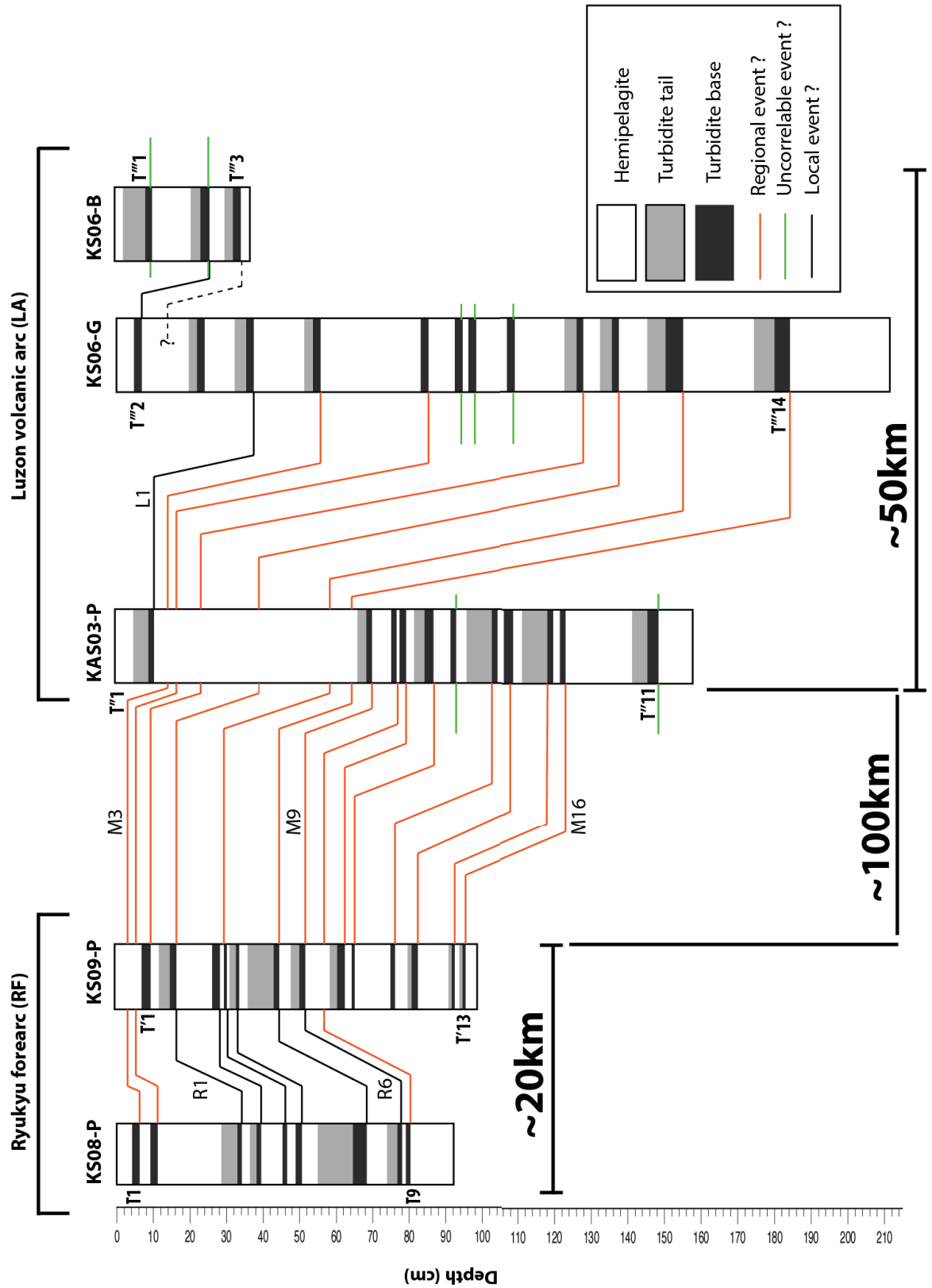


Figure 6.10: Chronostratigraphic event correlation from all the studied cores offshore eastern Taiwan showing local events labeled Rx and Lx, and regional events labeled Mx.

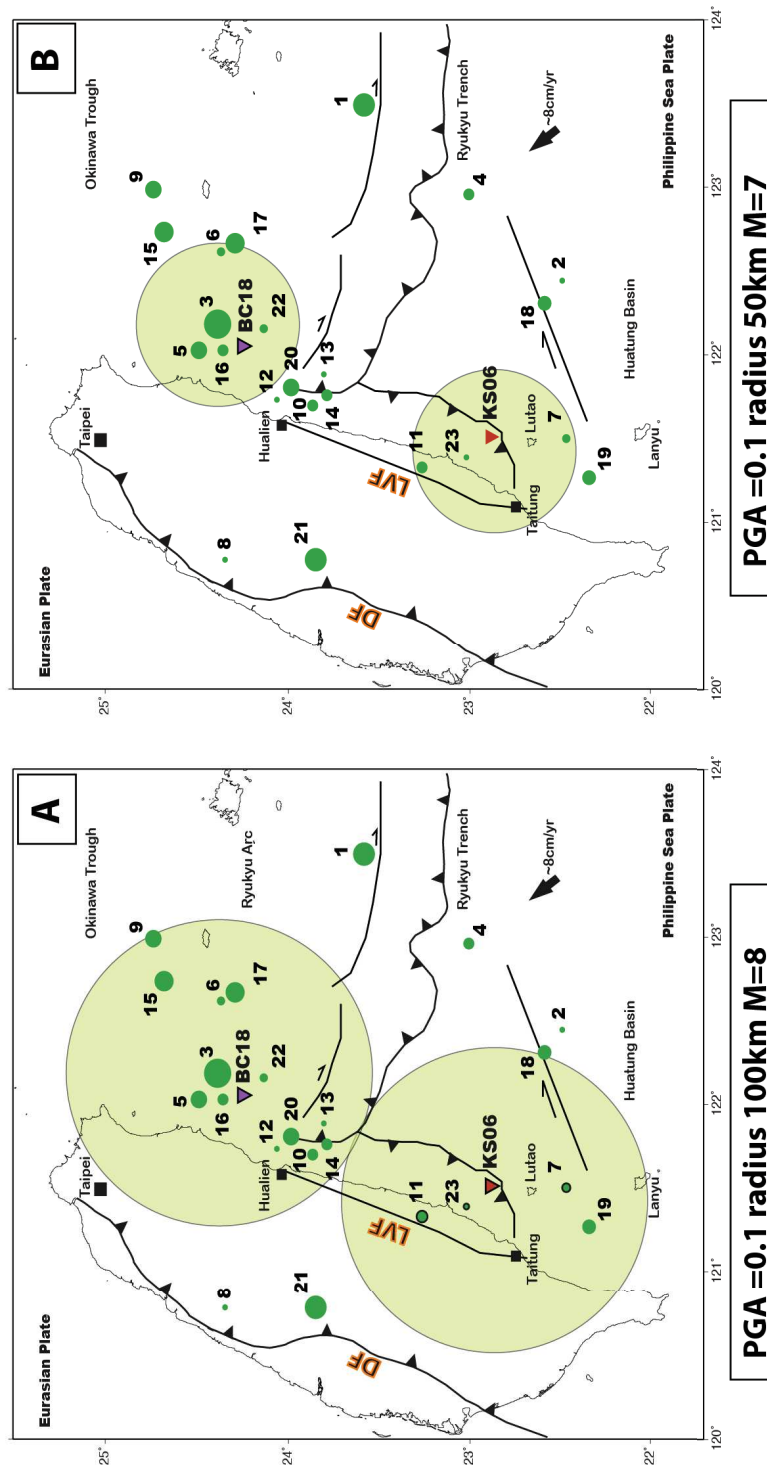


Figure 6.11: A. Map showing radius in which an M_w 8 earthquake will trigger slope failures. Circles have been centered on the turbidite source areas. At 100 km radius peak ground acceleration 0.1g is reached for such earthquakes. The 0.1 g corresponds to the threshold for slope failures generation. Note that no overlap is possible between the two sites, suggesting that an earthquake M_w 8 cannot be recorded in both KS06-B and BC-18 cores; B. Same as A for M_w 7 earthquake. The value of 0.1 g is reached at 50 km radius. Note that there is no overlap between the two circles, suggesting that it is not possible to record the same M_w 7 events in both coring sites BC-18 and KS06-B. Reversed triangles represents coring sites. Green dots are the seismic event recorded over the instrument period and listed in Table1.

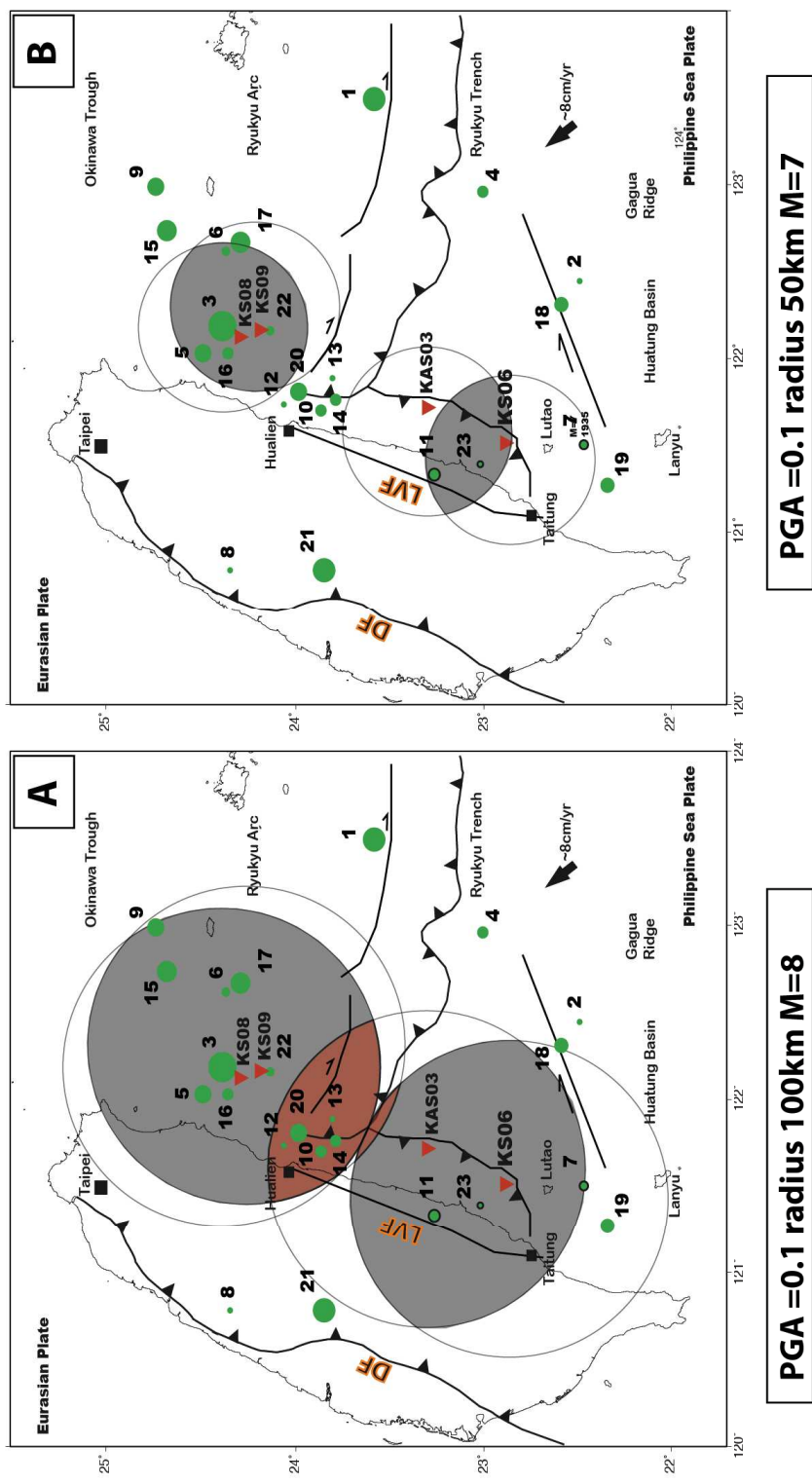


Figure 6.12: A. As shown in figure 7, the circles represent the impact of a $M_w 8$ earthquake on slope instabilities. The circles have been drawn around the turbidite source areas. The black areas correspond to the possible local scale events correlations showing the relative areas in which a $M_w 8$ earthquake should occurred to trigger synchronous turbidites within a single zone. Red areas corresponds to the overlap of three cores and suggests that to record synchronous turbidites between three cores within the two zones, a $M_w 8$ earthquake should occur within this area; B. Idem as A but for a $M_w 7$ earthquake. We note that regional event cannot be recorded for a $M_w 7$ earthquake.

A $\sim 3,000$ years-old super-event revealed
by marine deposits east of Taiwan: paleo-
landslide, earthquake, tsunami or typhoon
?

Contents

7.1	Introduction	167
7.2	Geological, oceanic and atmospheric setting	167
7.3	Core sampling strategy, data and results	171
7.4	Discussion	175
7.5	Conclusion	180
7.6	Acknowledgments	181
	Appendices	182

A $\sim 3,000$ years-old super-event revealed by marine deposits east of Taiwan: paleo- landslide, earthquake, tsunami or typhoon ?

Paper submitted to Earth and Planetary Science Letters

SERGE LALLEMAND (1,2), REMI LEHU (1,3), FABIEN RETIF (1), SHU-KUN HSU (2,3), NATHALIE BABONNEAU (2,4), GUEORGUI RATZOV (5), MARIA-ANGELA BASSETTI (6), LAURENT DEZILEAU (1,2), STEPHANE DOMINGUEZ (1,2)

1. *Géosciences Montpellier, Montpellier, France*
2. *LIA ADEPT, MOST, CNRS, Taiwan - France*
3. *Department of Earth Sciences, National Central University, Zhongli, Taiwan (R.O.C)*
4. *Domaines Océaniques Laboratory, Bretagne Occidentale University, IUEM, France*
5. *GéoAzur Laboratory, Nice Sophia-Antipolis University, France*
6. *CEFREM, Perpignan University, France*

*Corresponding author: lallem@gm.univ-montp2.fr

Abstract

Coastal areas in geodynamically active tropical regions such as Taiwan are vulnerable to extreme events originating offshore such as submarine landslides, earthquakes, tsunamis or typhoons. Some of these extreme events have recurrence intervals much larger than human memory so that populations are not prepared for such catastrophes. We have discovered in a marine core located 20 km east of the coastal range of Taiwan, at a depth of 1,200 meters at the top of a submarine high sheltered from rivers discharges from the nearby island and gravitational flows, a 22 cm-thick anomalous sequence topped with broken bivalves and wood fragments that we interpret as the record of several local submarine landslides followed by a major tsunami or typhoon. Submarine landslides were likely triggered by clustered earthquakes that are common in this tectonically active area. Based on radiocarbon dating, we constrain this event to about 3,000 years ago. Despite the high level of climatic and tectonic recent activity, no comparable event occurred there since that time, so that we have evidenced a pluri-millenia "super-event". Hydrodynamical modeling stimulated with a set of submarine landslide-triggered tsunami sources and combined with the global oceanic circulation, including the Kuroshio Current, allow us to better constrain the transport paths of the suspended material, the expected run-up at the coast, and ultimately the trigger that best fits our observations. Either a shallow submarine landslide, a large tsunami or a giant typhoon may explain both the run-up observed at the coast and the removal of nearshore material but the Kuroshio Current appears as a strong constraint that prevents cross-shore transport of suspended material even during a major tsunami. We discuss the various scenarii but further investigations, such as additional coring or high-resolution nearshore imagery, are needed to better constrain the main cause of this "super-event" as well as its return period.

Keywords: marine deposits, extreme events, submarine landslides, tsunami, typhoon, Taiwan.

7.1 Introduction

During the last decade, several major disasters were caused by, human-perceived overscaled, natural hazards. Among them, the 2004 Sumatra $M_w 9.2$ mega-earthquake and consecutive tsunami with a death toll of nearly 250,000 people. At that occasion, many people noticed that Indonesian population living along the shoreline had forgotten the memory of major past disasters such as the $M_w \geq 8.5$ earthquakes which occurred in 1797 and 1833 (Natawidjaja et al., 2006). More recently, the occurrence of the 2011 Japan $M_w 9.0$ earthquake and tsunami, that killed some 20,000 people, surprised both the population and the geophysicists themselves around the world, because almost nobody remembered the previous $M_w \geq 8.3$ earthquake that struck the same region in AD 869, i.e., more than a millennium earlier (Lay and Kanamori, 2011). These recent reminders have motivated the geologists and geographers to go deeper into the available archives either sedimentological through excavations or coring, written or often oral for the last centuries or millennia.

Assessing natural hazards in tectonically active tropical regions like Taiwan needs to better estimate the occurrence of "super-events" such as giant earthquakes, tsunamis, landslides or typhoons. A catalog of palaeo-"super-events" has started since a few decades in Japan, Canada or USA for example but is still infant in Taiwan where most of the population lives either close to the shore or back inland but in low-altitudes coastal plains that can be submerged by a large tsunami. The average elevation of the low-land areas in the Taipei Basin is about four meters above sea-level. Most of the Taipei urban area, i.e., the capital, counting nearly 7 millions of people, is then susceptible to be flooded if the sea-level rises by a few meters. The Taipei basin communicates with the open ocean through the Tanshui river which is rimed by levees along the banks with a 200-year return period protection level (Lai et al., 2010). These considerations push us to better explore the past catastrophic events by all available means. In this study, we use sedimentological archives preserved offshore east Taiwan supported by hydrodynamic modeling to suggest that a "super-event" occurred there about 3,000 years BP.

7.2 Geological, oceanic and atmospheric setting

Geology, morphology and geodynamics of the studied area

Taiwan is an active -only a few m.y. old- mountain belt riding over two opposite-verging subduc-

tion zones (Fig.7.1). One of them extends eastward along the Ryukyu Arc up to Honshu Island in Japan. In spite of a high subduction rate ranging from north to south from 47 to 104 mm/yr (Lallemand et al., 2005), the Ryukyu subduction zone is known to have not produced any large ($M_w \geq 8$) earthquake during the last century except in its northernmost Nankai segment (e.g. Ando, 1975).

The submarine slope east of the Coastal Range belongs to the Taiwan orogen, involved in crustal shortening (Malavieille et al., 2002; Lallemand et al., 2013), and shaped by erosional processes (Ramsey et al., 2006) (Fig.7.2). By extrapolation from the onshore, the bedrock should include volcanic and volcanoclastic series representative of the colliding northernmost Luzon volcanic arc. The slope is relatively steep and incised by canyons and gullies (Fig.7.2). V-shaped canyons meander across the slope suggesting either that they are structurally controlled by dissecting faults, or that they formed when the slope was shallower and then steepened. Some of them are headless indicating rapid changes in the morphology of the coastal area. One is straight from the mouth of the Hsiukuluan river (H.R. on Fig.7.2) down to the Huatung Basin. In fact, rather than a typical canyon, the slope there is marked by a flat-floored valley (hereafter called Chimei Valley) about 10 km wide with a regular 6 to 7° slope marked by two knickpoints at 3 and 4 km depth (K1 and K2 on Fig.7.2). The Chimei Valley is bounded by the steep southern flank of the Takangkou High (T.H. on Fig.7.2) to the north and the steep northern flank of the Changping High (C.H. on Fig.7.2) to the south. Both bathymetric highs overhang the valley by more than one km (see section AA' on Fig.7.2). They consist of thick well stratified sub-horizontal sedimentary layers lying on a deformed basement, probably of volcanoclastic origin, that outcrops in the valley especially near the scarps K1 and K2 (see Fig.7.2) underlining active eastward vergent thrusts (Malavieille et al., 2002; Ramsey et al., 2006, Yu-Huan Hsieh, personal communication). As shown on Fig.7.2, hyperpycnal flow originating from the Hsiukuluan River follows the foot of the Takangkou High southern flank straight down to the deep Huatung Basin. The Hsiukuluan River drains a significant part of the Central Range discharging 22 Mt/yr of terrigenous material according to Liu et al. (2008). About 10 kilometers southward, a small river flows into a short canyon and then follows the southern side of the flat Chimei Valley at the foot of the Changping High. The geomorphic configuration of this unusual wide 6 to 7° dipping flat valley might suggest a cumulative gravitational origin (S61 and S62 on Fig.7.2).

Historical earthquakes and tsunamis in Taiwan

The largest instrumental earthquake recorded nearby Taiwan was the June 5, 1920 M_w 7.7 event

supposed to have ruptured the southernmost Ryukyu subduction interface off Hualien (Theunissen et al., 2010). Nevertheless, more than twenty $M_w \geq 7$ earthquakes struck the island and its surroundings during the last century. Most earthquakes occurred east of Taiwan where we focus our study. Moreover, a huge tsunami has been reported in the southernmost segment close to Taiwan in 1771. It is known as the Meiwa tsunami of April 24, 1771 which caused more than 12,000 casualties (Goto et al., 2010) but, surprisingly, was never reported along the east coast of Taiwan. Its origin is still debated but an interplate subduction earthquake or a splay fault branched on the plate interface appear to be the most plausible triggers (Nakamura, 2006, 2009; Hsu et al., 2013). Furthermore, coastal boulders, supposed to attest for the occurrence of paleotsunamis, are reported in the southern portion of Ryukyu islands which led Goto et al. (2013) speculate that tsunamigenic earthquakes preferentially occur there. Based on radiocarbon datings of massive coral boulders scattered along the shorelines of the Yaeyama Islands (Fig.7.1) - from Ishigaki to Miyako - paleotsunamis have been described with a recurrence interval of 150~400 yrs (Araoka et al., 2013).

The second subduction zone extends south of Taiwan up to Luzon Island in the Philippines, giving its name to the Manila Trench. Again, no $M \geq 8$ earthquakes have been reported along the Manila subduction zone during the last century and none either since the Spanish colonization in the 1560s (Repetti, 1946) in spite of a subduction rate reaching 103 mm/yr in its central portion (Lallemant et al., 2005). However, moderate tsunamis occurred either along the west coast of Luzon island (1677, 1852, 1872, 1915, 1924, 1934) or mainland China coast near Hong-Kong (1076, 1918) (Megawati et al., 2009; Okal et al., 2011). The probable sources for most of these tsunamis are plate interface earthquakes along the Manila trench.

Since Taiwan is located at the termination of both subduction zones, the island can potentially undergo the action of giant waves on both sides. Because no significant tsunamis struck the island during the last century, the population is generally not aware of such danger. Ma and Lee (1997) first simulated tsunami occurrence along Taiwan coast based on some reports of past damages and potential sources. Among the tsunamis that were suspected to have occurred in Taiwan, most of them are of small intensity with waves less than 1 meter high. The oldest one for which authors have confirmed its validity hit the northern coast of the island near Keelung in 1867 (Zhou and Adams, 1985; Lau et al., 2010). It might have caused the death of more than a hundred persons with a maximum height of the wave estimated at 7.5 meters (Lau et al., 2010). Two older major events, located along the southwestern coast of Taiwan, appear in written records in 1781 and 1782 with dramatic (and inconsistent) death tolls up to 50,000 and

40,000 respectively. If the last one is generally considered as having a storm origin, the first one (in 1781) might have a tsunami origin (Lau et al., 2010). Wave heights overpassed 30 meters for the 1781 event and 10 meters for those of 1782. Another big event possibly occurred only 10 years later in 1792 with a wave more than 10 meters high near Tainan (southwest Taiwan Lau et al., 2010). During the last century, a series of moderate tsunamis were observed (1917, 1922, 1951, 1960, 1963, 1964, 1966, 1972, 1978, 1986, 1993, 1996, 1998, 1999, 2001, 2002), most of them triggered by earthquakes (Ma and Lee, 1997; Lau et al., 2010). Surprisingly, they were all reported along the eastern or eventually northern coast of Taiwan. Six of them were caused by distant earthquakes with sources located in Chile (1922, 1960), Alaska (1964), Guam (1993), Indonesia (1996) or Vanuatu (1999) showing that the eastern and northern coasts of Taiwan are vulnerable to distant earthquakes in terms of tsunami risk, even if wave heights never reached 1 meter. In terms of human lives loss, 7 casualties were reported after March 13, 1966 event and 15 after February 13, 1963 that occurred offshore Suao (northeast coast of Taiwan).

Abe (1938) and then Ando et al. (2013) mentioned a legend transmitted orally within the aboriginal Ami tribe living on the east coast of Taiwan. The first settlement of the Amis occurred in Chengkong area (Fig.7.2) between the middle of the 18th and the middle of the 19th centuries. In their folklore, they named a place located 400 m inland and 18 m in altitude on an Holocene terrace "Malaulau", which means "withered". The legend tells that *"a big sea wave struck the area, then plants and trees all perished, and afterwards the place was named as Malaulau"* (Abe, 1938). Several scenarii were tested regarding the origin of an eventual tsunami there, none of which being reliable within the required time window (Ando et al., 2013). Matta et al. (2014) identified three probable tsunami deposits during the past 3,000 years from soil excavations done at Malaulau site. Paleo-marine invasions are reasonably preserved in some of the cores done on the aerial terrace but the method fails in precise dating of the events.

Oceanic setting, Kuroshio current

Figure 7.1 shows the areas under the influence of the Kuroshio Current. It originates from the North Equatorial Current in the western equatorial Pacific Ocean, fringes the Philippine islands and then diverts south of Taiwan between two branches making a loop southwest of Taiwan in the South China Sea. The fastest northward directed branch is located east of Taiwan with currents reaching a depth of 1000 m at some latitudes. There, the mean Kuroshio transports are $\sim 30 \pm 5$ Sv ($1 \text{ Sv} = 10^6 \text{ m}^3 \cdot \text{s}^{-1}$) with annual mean surface rates, between 0 and 50 m, reaching up to $1.3 \text{ m} \cdot \text{s}^{-1}$ (~ 2.5 knots) at a distance between 20 and 40 km from the east coast

of Taiwan (Hsin et al., 2008). The main branch then turns east after passing along Taiwan to follow the Okinawa Trough. Kuroshio Current is thought to play a role in the transport of suspended material, as detailed further.

Climate

Taiwan is crossed by the Tropic of the Cancer. This humid subtropical region is under the influence of the monsoon with abundant precipitations especially during summer. Typhoons hit Taiwan every year with a high frequency (3 or 4 per year in average). Taiwan was even surnamed the Typhoon Alley by Liu et al. (2008). As for earthquakes, some of them are giant and cause severe damages such as the Haiyan event in 2013 that caused 8000 victims in the nearby Philippines, or the Morakot typhoon in August 2009. The Morakot typhoon was the deadliest typhoon to impact Taiwan in recorded history. It left 461 people dead and 192 others missing, most of them in the village of Xiaolin that was buried by a landslide. Rainfalls peaked at 2,777 mm during this event (Chen et al., 2012).

7.3 Core sampling strategy, data and results

7.3.1 Sampling strategy

We have conducted a cruise onboard the Taiwanese R/V Ocean Researcher I in late September 2012 (OR1-1013) devoted to collect sedimentary cores offshore east Taiwan for paleoseismology purposes. During that cruise, we have collected nine cores, most of them in perched basins far from channels and canyons in order to avoid hyperpycnal flows triggered by massive floodings (Lehu et al. (2013)). One of the sites was selected to represent a reference site for estimating the hemipelagic sedimentation rate excluding any turbiditic event. This site (KR03 on Fig. 7.1 and 7.2) was located about 20 km offshore the Coastal Range northeast of Chengkong, right at the top of a topographic high sheltered from gravitational flows: the Changping High, culminating at a depth of 1200 meters below the sea-level. The piston core KR03 was the most successful in terms of penetration with a total length of four meters.

7.3.2 Methods

Detailed visual logs were generated and analyses were undertaken to further characterize sedimentary facies within the core KR03. Geotek Multi-Sensor-Core-Logger (MSCL) was used to

provide a continuous measurement of the gamma-density, the P-wave velocity and the magnetic susceptibility over 1 cm sampling rate. Major chemical elements as well as X-ray radiographs of split core were performed at 2 mm sampling scale using the ITRAX core scanner equipment. We also analysed the variation of the grain size of selected samples using a Beckman-Coulter LS13-320 (size range of $0.4\text{-}2000\mu\text{m}$). To complement the petro-physical measurements, composition of the sand fraction ($>63\mu\text{m}$) has been determined, following a semi-quantitative approach on wet sieved 1 cm thick samples. A semi-quantitative study on benthic foraminifera assemblages in the medium sand fraction ($>150\mu\text{m}$) was performed in order to determine the source of sediments. Timing and age were provided by ^{14}C radiocarbon datings using the French mass spectrometer ARTEMIS, on >5 mg handpicked planktonic foraminifera within hemipelagites collected at five locations in the core. The planktonic foraminifera selected for dating belong to different species of the genus of Globigerinoides: *G. sacculifer*, *G. conglobatus*, *G. ruber* as well as to *Globigerina bulloides*, and *Orbulina universa*. Radiocarbon datings, were then calibrated and used to build an age model of the core calculated using the P-sequence of the OxCal software. Radiocarbon datings were also performed on shells and wood fragments. Measurements of ^{210}Pb excess activity and ^{137}Cs were also performed on the sedimentary layers over a centennial timescale in order to calculate the sedimentation rate and deduce the age of the top of the core.

7.3.3 Core description

As expected when selecting the core site, most of the core consists of a monotonous sequence of olive-grey clay hemipelagites characterized by a median grain size (d50) finer than $12\mu\text{m}$ (Fig.7.3). Unexpectedly, we have observed an anomalous sequence between 322 and 345 cm characterized from the base to the top by silts with a median grain size (d50) up to $18\mu\text{m}$ from 344 to 331 cm and then decreasing back to $11\mu\text{m}$ (see Fig.7.5). Four granular peaks, labelled P1 to P4 on Fig.7.5, correspond to silty beds observed both on the median and the mean grain size, alternating with clay hemipelagites. After sorting, a small proportion of sand consists in quartz, feldspar and mica grains which size may reach $200\mu\text{m}$ (see Fig.7.6D). The mean grain size shows an additional peak labeled T at 323 cm which is related to the presence of $\leq 1\text{cm}$ bivalves and wood debris scattered within a deposit interval of about 5 cm (between 322 and 327 cm depth) mixed with hemipelagic clays. XRF analyses on major elements are not discriminating except the Fe content that shows a clear positive anomaly between 325 and 355 cm. Peaks in Fe closely coincide with peaks in grain size. The highest peak in Fe correlates with the

highest peak in magnetic susceptibility (Fig.7.3). We also notice that the last event T does not correlate with a Fe anomaly. Many specimens of undetermined Veneroida, 5 to 10 mm large and often fragmented (Fig.7.6A and B) were found exclusively in the upper section of the anomalous sequence. We have also found pluri-millimetric wood debris (Fig.7.6C identified by Lucie Chabal from CBAE, Montpellier, France, personal communication) in the same interval. Despite their small size, bivalves are not juvenile forms because some characters such as hinge and external ornamentations are well-developed, as observed in the articulated valves or debris (Fig.7.6A and B). This is an indication of high energy transport from their living habitat in shallow water, i.e., 20 ± 10 meters deep (Hua-Wen Chen from Central Geological Survey in Taiwan, personal communication) to 1200 m depth. The thickness of their shells is compatible with carbonate-rich shallow water environment. They probably lived slightly buried in the sediment as suggested by the endobionte character of their hinges.

Few benthic foraminifers are found in this 5cm-thick level where species living at depths deeper than 200 m such as *Lenticulina sp.* or *Bulimina aculeata* co-exist with *Bolivinita quadrilatera* that typically lives at depths greater than 600 m. Very few benthic foraminifers such as *Bulimina marginata* or *Cassidulina carinata* living between 50 and 800 m, or even *Amphistegina sp.* or *Quinqueloculina sp.* living between 10 and 150 m might attest for a shallow source.

7.3.4 Age model

Based on eight measurements of $^{210}Pb_{ex}/^{137}Cs$, and five radiocarbon datings, the core appears chronologically extremely coherent, without indications of reworking or bioturbation, from the seabottom down to the maximum depth of 390 centimeters.

Presence of ^{137}Cs has been detected in the top 8 cm with an apparent maximum of 1.2 mBq/g at 2.5 cm (sample between 2 and 3 cm depth). The peak deposition value of ^{137}Cs marking the year 1963 (culmination of nuclear weapon tests) is comprised between 1.5 and 4.5 cm (Fig.7.4). $^{210}Pb_{ex}$ shows a decay curve from the surface down to 14-16 cm with a local plateau around 10 cm that may show some short-term variations in sedimentation rate. The mean sedimentation rate based on the slope of $\ln(^{210}Pb_{ex})$ vs core's depth in the top 14-16 cm ranges between 1.37 mm/yr (all values) and 1.24 mm/yr (when removing the data at 10 cm depth). Using 1.24 mm/yr as a mean sedimentation rate, calendar year 1963 should be observed at a depth of 6 cm but we estimate the ^{137}Cs peak value between 1.5 and 4.5 cm. This means that about 1.5 to 4.5 cm of the top sediment have been removed during piston core recovery. The age at the top of

the core is thus estimated at A.D. 1992 ± 12 and A.D. ~ 1900 should be reached near 12.5 cm depth.

The mean sedimentation rates for older sediment based on five radiocarbon ages on planktonic foraminifera were estimated to 1.09 ± 0.7 mm/yr in the upper 206 cm of the core and 1.18 ± 0.13 mm/yr between 206 and 316 cm. The rate apparently falls to 0.84 ± 0.27 mm/yr in the basal section of the core between 351 and 389 cm (Fig.7.3). Such rates are indicative since corrected radiocarbon ages have intrinsic errors in the measure itself (typically ± 30 years) and then when correcting with the atmospheric production and lapse-time in shallow water. For the above estimates, we have corrected our radiocarbon ages with a mean reservoir age offset (ΔR) of 86 ± 40 years based on global compilation by Yoneda et al. (2007) and by adjustment of our $^{210}Pb_{ex}$ and ^{14}C ages on a nearby core KS06 (Dezileau et al., 2014, submitted to Radiocarbon).

To estimate the age of the anomalous sequence between 322 and 345 cm, we have used three radiocarbon dates within the hemipelagites: 6 cm above, 6 cm below and within the sequence. The three dates are very coherent meaning that the "silty pulses" (P1 to P4) and the "shells and wood layer" (T in Fig.7.5) were deposited within about one century between B.C. 1139 ± 140 and B.C. 1034 ± 139 , i.e., about 3,000 years ago. To discriminate between a single event with several pulses and several events, we have sampled the anomalous sequence between P3 and P4 because both the color and the granulometry suggested that it were hemipelagites (see Fig.7.3 and 7.5) and obtained an intermediate age with respect to ^{14}C ages above and below the anomalous sequence. Furthermore, we have modeled the ages using OxCal for two extreme scenarii : one single event 22 cm thick versus 5 events separated by hemipelagites. The best fit for the modeled ages within the core is those with 5 separated events (P1 to P4 and T). In that case the age gradient vs depth is linear. If we consider a single 22 cm thick event, there is a break in the sedimentation rate gradient meaning that either material is missing, which is not observed in the core, or the assumption is wrong. Using an age model considering 5 events, we were able to estimate ages for each of them (Fig.7.5). We observe that the wood debris found in event T have the same age than the event, which "validates" the estimated age of the main event, i.e., B.C. 1056 ± 78 for the wood debris vs B.C. 1034 ± 139 for the modeled age of T layer (Fig.7.3 and 7.5). Radiocarbon measured on the shells provided an age of B.C. 2440 ± 149 much older than the surrounding sediment.

7.4 Discussion

On top of the Changping High, at 1,200 m of water depth, 20 km off the east coast of Taiwan, at a location sheltered from turbidity currents, we have discovered a 22 cm thick anomalous sequence of silty material topped with transported fragments of shells and wood interbedded within clay hemipelagites and dated around 1034 ± 140 years BC.

7.4.1 Age of shells vs age of sediment

The shells present in the T-layer appear to be $1,400 \pm 150$ years older than the sedimentary matrix. Such "apparent aging" is quite common especially for species living in the nearshore area. Several explanations can be proposed such as a lagoon origin with continental waters feeding the bivalves (e.g. [Sabatier et al., 2010](#)), removal of old shells into younger sediment, or marine shells feeded by submarine groundwater discharges (e.g. [Swarzenski et al., 2001](#); [Lofi et al., 2013](#)). Since the bivalves are known to live in marine environment, we exclude the first hypothesis. Similarly, even if some shells are broken showing sharp cracks, most of them are entire and well-preserved. We thus hypothesize that they were not removed from older sediment. The last hypothesis is supported by their living habitat, buried within the sediment as attested by their endobionte hinge. As a matter of fact, one may suspect that artesian coastal aquifers seep through the sediment along the shoreline and feed the buried bivalves with groundwater characterized by large reservoir ages, i.e., "old" radiocarbon ages.

7.4.2 Possible origin of the anomalous deposit

This deposit is exceptional in many aspects : (1) it is 22 cm thick and unique within a monotonous clay sequence covering 3750 ± 150 years, attesting that only a rare event may be at the origin of the deposit. We will further called it "super-event". (2) The most reasonable source of silts, according to the morphological context is likely turbidity surges or plumes resulting from a turbulent mass flow allowing the fine component of the mass-transported material to rise up to the top of the high at site KR03, i.e., over more than 1000 meters in vertical. (3) The presence of shallow water shells and wood fragments concentrated in the upper sequence is enigmatic. Since these "exotic" debris originate from the nearshore, we will further discuss three possible scenarii that may explain why they are observed at a large distance from their source, i.e., at least 20 km, and in such position, i.e., at the top of a submarine high supposed to

be sheltered from gravity flows (see Fig.7.2). Submarine landslides in active areas likely result from slope's destabilization during shaking by earthquakes, generally when peak ground acceleration overpass 0.1 g (Pouderoux et al., 2014), whereas tsunami may generally either results from landslides or earthquakes. Tropical storms such as typhoons should also be considered as candidates for submarine material removal.

Scenario 1: the effect of (a) submarine landslide(s)

The presence of a succession of silty layers (P1 to P4 on Fig.7.5) concentrated in a short time range (~ 100 years) within a four meters long core covering 3750 years could be explained by a series of submarine landslides. Indeed, despite the uncertainty on radiocarbon datings that does not allow to discriminate between a single or multiple events, the visual observation of the core and the fact that a sample of hemipelagites situated between P3 and P4 (see Fig.7.5) has been dated right between the two others below and above the anomalous sequence indicates that normal planktonic sedimentation resumed at least between these two events. We thus consider that P1, P2, P3, P4 and T are distinct events separated short periods of regular sedimentation. If we observe such events only at those depths: 333 ± 12 cm below the seafloor, it probably means that they result from a main composite-event such as clustered earthquakes. Detailed bathymetry combined with careful examination of chirp and reflection seismics in the study area led us to suggest candidate sites for mass wasting at distances between 10 and 40 km from the core site (see S1 to S6 in Fig.7.2). Destabilization of shallow sediment on candidate sites S1, S4 or S62 either by typhoon, tsunami, fault activity, or earthquake may be favored by meteoric water discharges at significant depths below sea-level. Deeper candidate sites are suggested for submarine landslides in Fig.7.2 such as S2, S3 or S5. S1 and S5 are described in Lehu et al. (2014a, submitted to Marine Geology). They are well characterized both in the morphology and based on seismic lines analyses. S2 and S3 are more speculative. They may also be interpreted as small submarine slumps based on available seismic lines, especially those acquired during the ACT cruise in 1996 (Lallemand and Tsien, 1997). Since they are proximal with respect to site KR03, they might potentially constitute sources of the silty pulses P1 to P4. If we assume that the last event T also results from a landslide, we must consider that the head of the slumped mass reached the nearshore (water depths less than 20-30 m) in order to incorporate the shallow living shells, benthic forams and wood debris. In this hypothesis, we should find a fresh scar close to the coast in the study area (S4 or S62 in Fig.7.2 for example) and the energy of the slumped mass should be strong enough to transport shells and wood debris downslope over about 15 km

and then 900 m uphill for S4 (see section BB' on Fig.7.2) and even more for S62. The available bathymetry near the shore close to Chengkong is not good enough to decipher whether or not a fresh scar exists there, but one may speculate that such a debris flow or turbidity current will transport as much or even more silty material than shell or wood debris. Since no silt and Fe anomaly has been described in the T layer (see median grain d50 size in Fig.7.5), we disregard this hypothesis.

Finally, several submarine landslides may eventually explain events P1 to P4 but probably fail to explain event T.

Scenario 2: the effect of a tsunami

To explain event T, we now consider the occurrence of a tsunami removing the beach and the nearshore sediment within a turbid plume. A tsunami can be triggered either by an earthquake or a submarine landslide which can, in turn, also be triggered by an earthquake. Submarine processes of tsunami effects are poorly known. However, it has been demonstrated in Japan after the M_w 9 2011 Tohoku earthquake that the subsequent tsunami has triggered turbidity currents that have been monitored on the seafloor (Arai et al., 2013). Numerical simulations by Parker (2006) and Traykovski et al. (2007) led Arai et al. (2013) to show that the turbidity currents probably developed from the downslope motion of sheet-like suspension cloud of seafloor sediment particles stirred up by the tsunami at shallower depths but cannot have been transported by the backwash flow. We have seen in the introduction that the area is frequently struck by $\sim M7$ earthquakes but none of the twenty M7 events occurring in the region during the last century has been recorded in KR03 core. So, if the source for the landslide or the tsunami was an earthquake, it had to be much larger or less distant than those of $\sim M8$ that produced the 1771 Meiwa tsunami (see Fig.7.1), because we have not observed any record of it in KR03 core. One may thus hypothesize that a $M > 8$ earthquake occurred at some distance from our site, far enough to cause a huge tsunami without causing much slope failure in our study area. The subduction interface in the South Ryukyu subduction zone, located at distance of 200 to 500 km off the site, is a good candidate for such mega-earthquake that could theoretically reach a magnitude 9 (Lin et al., 2014). Such tsunami, larger than those that occurred in 1771, has been described in Miyako and Ishigaki islands as the "Okinawa-Sakishima tsunami". It has been dated around 2,000 yrs BP and it is known to have transported many huge coral reef boulders across the shore of these islands (KAWANA and NAKATA, 1994). We do not record it in KR03 core. Unfortunately, the tsunami records from coral boulders do not explore events older than

2,400 yrs BP which is younger than our studied event. As mentioned earlier, excavations through terrace deposits at Chengkong site, close to our site, has revealed three environmental changes from terrestrial to marine conditions (Ota et al., 2011), the oldest being dated at 3,000-2,800 cal. yrs BP, which overlaps our dating range : 3,124-2,844 cal. yrs BP. Considering that a huge tsunami might have occurred at those dates, we can speculate that the shells and benthic forams living in shallow water in the nearshore were suspended in a turbid plume, carried offshore and drifted away by strong currents such as the Kuroshio current (Fig.7.1) which can reach $1,2 \text{ m}\cdot\text{s}^{-1}$ and transport between 15 and $44\cdot 10^6 \text{ m}^3\cdot\text{s}^{-1}$ (Hsin et al., 2008). We will later present hydrodynamic simulations to test this hypothesis and verify if mm shells can be transported at shallow depths over tens of kilometers before sinking.

Scenario 3: the effect of a typhoon

Considering that events P1 to P4 were caused by nearby submarine landslides and subsequent silty plumes, we only focus on event T. Most tsunami effects described above can be applied to a storm or a typhoon. Indeed, waves up to 14 meters at the coast have been recently observed during typhoon Neoguri (July 10, 2014) off Ryukyu islands. Since we have not found such deposit (shells and wood) in the rest of the core KR03. This indicates that only a "super-typhoon" can possibly be a candidate. Discussing with meteorologists (H.-H. Hsu and Y.-C. Hsin from Research Center for Environmental Changes, Academia Sinica, Taiwan, and J.-P. Chen from National Taiwan University, Taipei, Taiwan, personal communications), it is possible that a tornado imbedded in a typhoon suck out the shallow water and sediment with small shells and wood debris, lift them to the top of the typhoon's eye following the outflow in the upper troposphere and drops them into the ocean tens of kilometers away from their source. It can also produce the same effects than the tsunami by suspending shallow sediment and shells and carrying them offshore by the strong shallow currents forced by the wind.

Summary of hypotheses

To summarize the various alternatives, we suggest that events P1 to P4 resulted from nearby submarine landslides (scenario 1) probably triggered by (clustered) earthquakes since they were distant in time by only a few decades. Then a "super" typhoon or tsunami occurred, resulting in the deposition of layer T. The record of a marine invasion at an altitude of 18 m on the nearby Malaulau terrace possibly at the same time (Fig.7.2, Ota et al., 2011) is compatible with both scenarii 2 and 3. Same with the sorting of the material with mainly shells and

wood debris compared with the small silty fraction. The coincidence between the occurrence of silty pulses P1 to P4 and event T within one century is puzzling if we invoke two different causes such earthquakes-triggered landslides and tropical storm. One may thus envisage that a climatic "super-event" occurred during a century with several "super-storms" triggering shallow landslides first and then transporting shells and wood debris in the air in an ultimate event.

7.4.3 Hydro-dynamical tests

To discriminate between the above mentioned scenarii, we have performed numerical simulations to test the impacts on the coast and on the coastal circulation of landslide-triggered tsunamis at the candidate sites (S1 to S6). Our modelling strategy is based on the classical view of tsunamis involving three steps: generation, propagation and run-up computation. The first step was carried out with the Tsunami Open and Progressive Initial Conditions System v1.2 (TOPICS) developed by [Watts \(2002\)](#). TOPICS approximates initial water surface elevations and the wave length at the source according to underwater slide parameters (see Appendix A for further details). For the second step, the free-surface sigma-coordinate SYMPHONIE model ([Marsaleix et al., 2008](#)) was applied to tsunami propagation (see Appendix B for further details) and in the last step, we used an analytical theory of long wave run-up on a planar beach proposed by [Choi et al. \(2011\)](#) to estimate the wave height on the coast (see Appendix C for further details).

Since no detailed bathymetry is available in our study area, especially in shallow waters, we have decided to maximize the volume of candidate submarine landslides based on morphological characteristics of the seafloor and available seismic data. Major earthquakes probably destabilize several candidate sites at the same time but with smaller volumes. Since we ignore what happened, we simply assume that each candidate site has produced a large landslide (labelled S1 to S6 on Fig.7.2 and 7.7) and let just consider that the hydrodynamic perturbation is maximized in our tests but focused on a single site rather than distributed on several sites.

Models show that the Kuroshio Current effect is dominant with respect to any tsunami effect, whatever the landslide source could be. Variations of drifters's paths are not significant from one landslide source to another, when accounting for the Kuroshio. We show in Figure 7.7 the motion of the drifters (D1 to D10) in the case of S4 landslide because it is the only one that was able

to generate a run-up of more than 20 meters at Malaulau terrace near Chengkong, where Ota et al. (2011) found evidences of marine invasions at an altitude of 18 m. We see that S4 tsunami source only (without Kuroshio) is compatible with cross-shore transport of particules (orange lines). Shallow drifter D3 reaches the KR03 site after about 4 days of drift, whereas D5 reaches the KR03 site area within about 3 days. Drifts are estimated for particles of water or floating wood debris but we should consider that the shells very probably sunk soon after they started to drift. Indeed, shallow drifters starting at 15 meters depth slightly deepen during their transit to reach about 100 m depth after 5 days. We thus believe that debris denser than water would rapidly sink. Furthermore, if we add the Kuroshio component to those generated by the tsunami, we observe that all the drifters head northward along the coast (see pink paths on Fig.7.7). The same conclusions are reached for sea bottom drifters (see blue and green dotted lines on Fig.7.7) even if the paths are different. Expected run-ups for the eight candidate landslides are computed at three places along the coast: Malaulau terrace near Chengkong, Changping and Takangkou. We see that even when maximizing the volumes of slided material for each candidate site, only S4 was able to generate a run-up of more than 18 meters at Malaulau terrace (Fig.7.7). We thus conclude that a large shallow submarine landslide sourcing nearby Chengkong (like S4) may be responsible for a marine invasion such as those described by Ota et al. (2011) but unlikely explains the transport of shallow living shells at large distances from the shore, especially if the Kuroshio current is acting.

7.5 Conclusion

The discovery of clustered silty layers topped by a concentration of shallow-living shells and wood debris, all dated around 3,000 years BP within a monotonous core of hemipelagites offshore the east coast of Taiwan has been interpreted as a "super-event" occurring with a return period of the order of few millennia. The nature of this super-event is still a matter of debate but three plausible scenarii can be proposed : (1) Four large earthquakes occurred in the region within less than a century accompanied by significant gravity flows which silty plumes reached the top of the Changping High, then a "giant-typhoon" occurred producing a big wave that invaded the coastal area, lifting in the air shallow water shells and wood debris, and drop them 20 to 30 km away from their source; (2) same as (1) for P1 to P4 but then a major tsunami occurred that washed the nearshore especially in Lutao island located offshore Taitung south of KR03, but we must accept that centimetric shells drifted at shallow depths with the Kuroshio Current over

distances larger than 60 kilometers; (3) About 3,000 years ago, the climate underwent a period during which major typhoons hit the island of Taiwan, the first four large typhoons generated hyperpycnal flows and/or shallow water sediment destabilizations responsible for silty beds even at the top of the Changping High, then a giant typhoon occurred as in the previous scenario. This study clearly indicates that complementary investigations are needed in this region to better constrain the source of this event (or cluster of events) in particular but also to identify and characterize the "super-events" back in time and thus better estimate their return period. A detailed survey off east Taiwan especially close to the shore would greatly help to characterize the submarine landslides hazard and their consequences for the population living in the coastal area.

No other cores reaching those depths have been sampled east of Taiwan, except during ODP Leg 195 but the site was located in the Southern Okinawa Trough far north of our studied area (Wei, 2006). Our observation is thus unique for instance and can not be correlated today with other cores.

7.6 Acknowledgments

We deeply acknowledge several experts with whom we have discussed: hydrodynamics - Frédéric Bouchette (GM, Montpellier), shells provenance - Hua-Wen Chen (CGS, Taipei), fossil wood determination - Lucie Chabral (CBAE, Montpellier), typhoon dynamics - H.-H. Hsu and Y.-C. Hsin (Research Center for Environmental Changes, Academia Sinica) and J.-P. Chen (National Taiwan University), tsunami occurrence - Yoko Ota (NTU, Taipei). We are grateful to colleagues who assisted us in various analyses like XRF - Kuo-Yen Wei (NTU, Taipei), magnetic susceptibility - Lee Teh-Quei and (IES), radiocarbon dating - Jean-Pascal Dumoulin and the ARTEMIS group (LMC14, Gif/Yvette), core preparation and routine analyses-TORI team (Kaoshiung). We finally deeply thank the Captain and crew of the R/V Ocean Researcher 1 during the OR1-1013 cruise.

Appendices

Tsunami generation

The initial free surface elevation and water velocities in TOPICS were derived from multivariate, semiempirical curve fits as a function of nondimensional parameters characterizing the landslide (e.g. density, geometry, etc.) and the local bathymetry (e.g. slope, depth, etc.) (Watts, 2002). The inputs for TOPICS (Table 7.1) are, in descending order, the longitude of the initial slide center x_0 , the latitude of the initial slide center y_0 , the specific density γ , the initial landslide length b , the maximum initial landslide thickness T , the maximum landslide width w , the mean initial landslide depth d , and the mean initial incline angle θ . The outputs from TOPICS (Table 7.1) are the slide initial acceleration a_0 , the theoretical maximum (terminal) slide velocity u_t , the characteristic distance of slide motion s_0 , the characteristic time of slide motion t_0 , the characteristic wavelength γ_0 , and the characteristic tsunami amplitude η_0 from the depression wave at time $t = t_0$.

Propagation model

The 3D coastal circulation model SYMPHONIE developed by the SIROCCO team (Marsaleix et al., 2008) was applied on the studied area with the eight tsunami sources terms given by TOPICS (see outputs in Table 7.1). The components of the current, the temperature and the salinity are computed on a staggered C-grid thanks to a classic finite difference method. A generalized sigma coordinate (Ulses et al., 2008) is used in order to improve resolution near the bottom and the surface with special attention on the pressure gradient (Marsaleix et al., 2009, 2011). To this vertical grid is associated a polar curvilinear horizontal grid which refines resolution near the coast while keeping reasonable computing times (Bentsen et al., 1999). We compute the baroclinic and barotropic velocity components separately following the time stepping method consisting of a Leap Frog scheme combined to a Laplacian filter (Marsaleix et al., 2012). The domain has a varying resolution from 4 km offshore to 100 m nearshore. This polar grid allows to increase the density of the grid points in the area of interests, thus helping to avoid an excessive computational load. The vertical discretisation is 10 sigma levels. The 100 m bathymetry resolution acquired during the ACT cruise in 1996 (Lallemand and Tsien, 1997) was used. The barotropic time step is 0.3 sec, baroclinic is 3.5 sec and the drag coefficient for the bottom boundary is 0.0025. As SYMPHONIE doesn't allow to introduce directly a sea surface

perturbation because of the preservation of the advection schemes, we chose to set the sea surface elevation by setting an anomalous horizontal divergence of barotropic current at the neighboring grid points. The current direction is centred on the perturbation making instantaneously an elevation of the sea level on this point. For each landslide, two kinds of simulations were computed. A first simulation, with the initial conditions of temperature and salinity settled from the daily outputs of the MERCATOR system (Madedec, 2008) and the sea surface perturbation of the tsunami. We simulated the hydrodynamics until 5 days after the slide then we computed the run-up elevation at the shore. This duration allows us to verify the transport of millimetric shells and wood debris represented by ten Lagrangian drifters spread at 15 m depth and at sea bottom along the coast (D1 to D10 on Fig.7.7). We performed a second simulation for checking the influence of the Kuroshio current. Large scale forcing terms (Kuroshio current) are included in radiative conditions applied at the lateral open boundaries (Marsaleix et al., 2006). These terms are also provided by the daily outputs of the MERCATOR system (Madedec, 2008). Here, we assumed that the Kuroshio is still the same than 3,000 years ago. Then to avoid seasonal effects or others effects like typhoons which modify the Kuroshio features, we chose a period during the spring with no typhoon which represents the main trend of the Kuroshio.

Run-up height estimations

The time series that were computed by the numerical simulation of the water elevation on the last sea grid points are converted into the displacement of the water on the shore by the following formula (Choi et al., 2011):

$$\eta(x = 0, t) = \int_0^{t-\tau} \sqrt{(t - \tau)^2 - T^2} [(d^2\eta(x = L, \tau))/d\tau^2] d\tau$$

where $\eta(x=0,t)$ is the run-up oscillations on the shore, $\eta(x,t)$ is water oscillations in the last sea points, T is the travel time of the wave and L is the distance from this point to the shore. According to nonlinear theory, the extreme of $\eta(x=0,t)$ yields the maximal run-up height of the tsunami wave. Note that this 1D analytical theory is not able to describe some local amplification on the coast due to complicated bathymetry, topography and bottom friction effect. More details of this analytical solution can be found in Choi et al. (2011). However, in our modelling, the last sea points are at less than 500 m of the coastline in order to reduce the impacts of non-included effects. The Table 7.2 presents the details of the last grid points used for the run-up computation at the Holocene "Malaulau" terrace, Changping and Takangkou. The

arrival time t_{at} , the maximum elevation at the last grid point $\eta(x=L)_{max}$ and the maximum estimated run-up $\eta(x=0)_{max}$ for each case are presented in Table 7.3.

Quantities	Slide S1	Slide S2	Slide S3 ₁	Slide S3 ₂	Slide S4	Slide S5	Slide S6 ₁	Slide S6 ₂
x_0 (deg)	121.47	121.65	21.70	121.78	121.45	121.83	121.75	121.62
y_0 (deg)	22.88	23.00	23.15	23.20	23.15	23.27	23.37	23.40
γ (kg/m ³)	1850	1850	1850	1850	1850	1850	1850	1850
b (m)	3500	3000	6000	7000	4500	2000	17000	24000
T (m)	1000	1000	500	800	500	500	1000	1000
w (m)	14000	7000	2000	3000	3500	10000	12000	15000
d (m)	1000	2750	3000	3600	500	4200	3500	1800
θ (degrees)	18	18	15	12	18	18	6	7
a_0 (m/s ²)	0.87	0.87	0.73	0.58	0.86	0.87	0.29	0.34
u_t (m/s)	115.82	107.22	138.78	134.35	131.33	87.55	148.46	190.46
s_0 (km)	15.42	13.22	26.43	30.84	19.83	88.11	74.9	10.57
t_0 (s)	133.14	123.27	190.48	229.55	150.87	100.64	504.52	555.2
λ_0 (km)	13.2	20.25	32.68	43.14	10.58	20.43	93.48	73.77
η_0 (m)	79	15.35	2.45	3.65	70.75	4.2	5 11.24	58.66

Table 7.1: Input and output parameters of TOPICS simulations for 8 different submarine landslides sources S1 to S62. Parameters are described in Appendices A and B.

	Malaulau	Changping	Takangkou
Grid point x,y (deg)	121.368, 23.093	121.481, 23.318	121.522, 23.460
Depth (m)	54	247	489
L (m)	440	1700	2000

Table 7.2: Nearest grid points used for the run-up computation at the Holocene "Malaulau" terrace, Changping and Takangkou locations along the coast. L is the distance from the shore in meters.

Quantities	Slide S1	Slide S2	Slide S3 ₁	SlideS3 ₂	Slide S4	Slide S5	Slide S6 ₁	Slide S6 ₂
tat (min)	5:20	12:36	14:56	15:46	4:29	17:38	17:22	9:13
(1) $\eta(x=L)_{max}$ (m)	6.95	1.5	3 0.80	0.67	13.59	0.30	0.41	4.25
$\eta(x=0)_{max}$ (m)	11.84	3.53	1.64	1.44	20.87	0.45	0.69	9.67
tat (min)	6:07	12:58	-	-	3:03	-	-	1:31
(2) $\eta(x=L)_{max}$ (m)	3.47	0.12	-	-	4.07	-	-	10.54
$\eta(x=0)_{max}$ (m)	13.02	1.0	-	-	15.01	-	-	51.27
tat (min)	7:55	-	-	-	5:31	-	-	0:30
(3) $\eta(x=L)_{max}$ (m)	1.89	-	-	-	1.40	-	-	5.54
$\eta(x=0)_{max}$ (m)	8.47	-	-	-	4.23	-	-	17.33

Table 7.3: Run-up computations using the analytical solution of (Choi et al., 2011) at the shore ($x = 0$) extrapolated from the last grid points ($x = L$) accounting for the slope between the shore and the last grid point. t_{at} is the arrival time (hour, minutes) of the wave at the last grid point.-means that the run-up computed is negative. The inaccuracy of grid resolution in these areas and the small amplitude of waves causes a retreat of the sea, following by small waves but the elevation induced by these waves wasn't higher than 0.

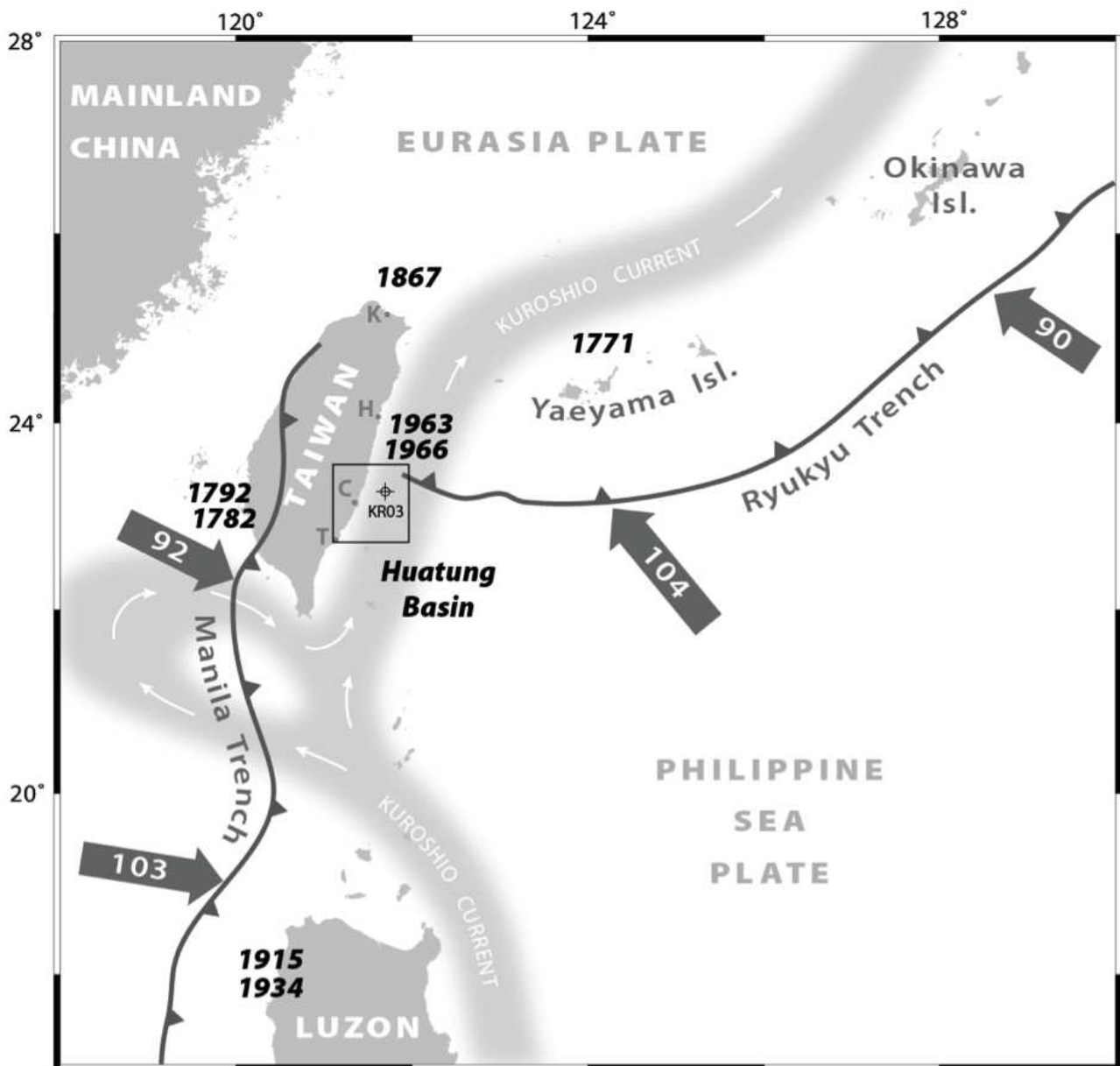


Figure 7.1: General map of the Ryukyu and Luzon subduction zones overlapping in Taiwan. The numbers in the arrows indicate the relative subduction rates in mm/yr. The bold dates are major tsunami events described in the literature (see the text for further details). In light grey : the mean path of the Kuroshio current (after Hsin et al., 2008)

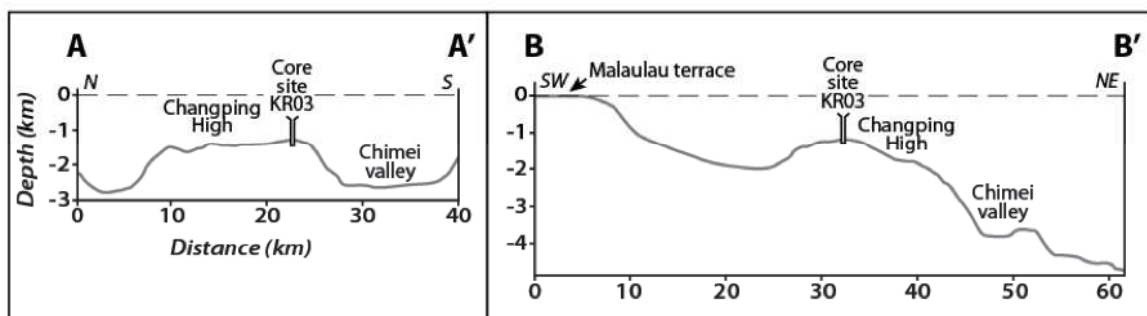
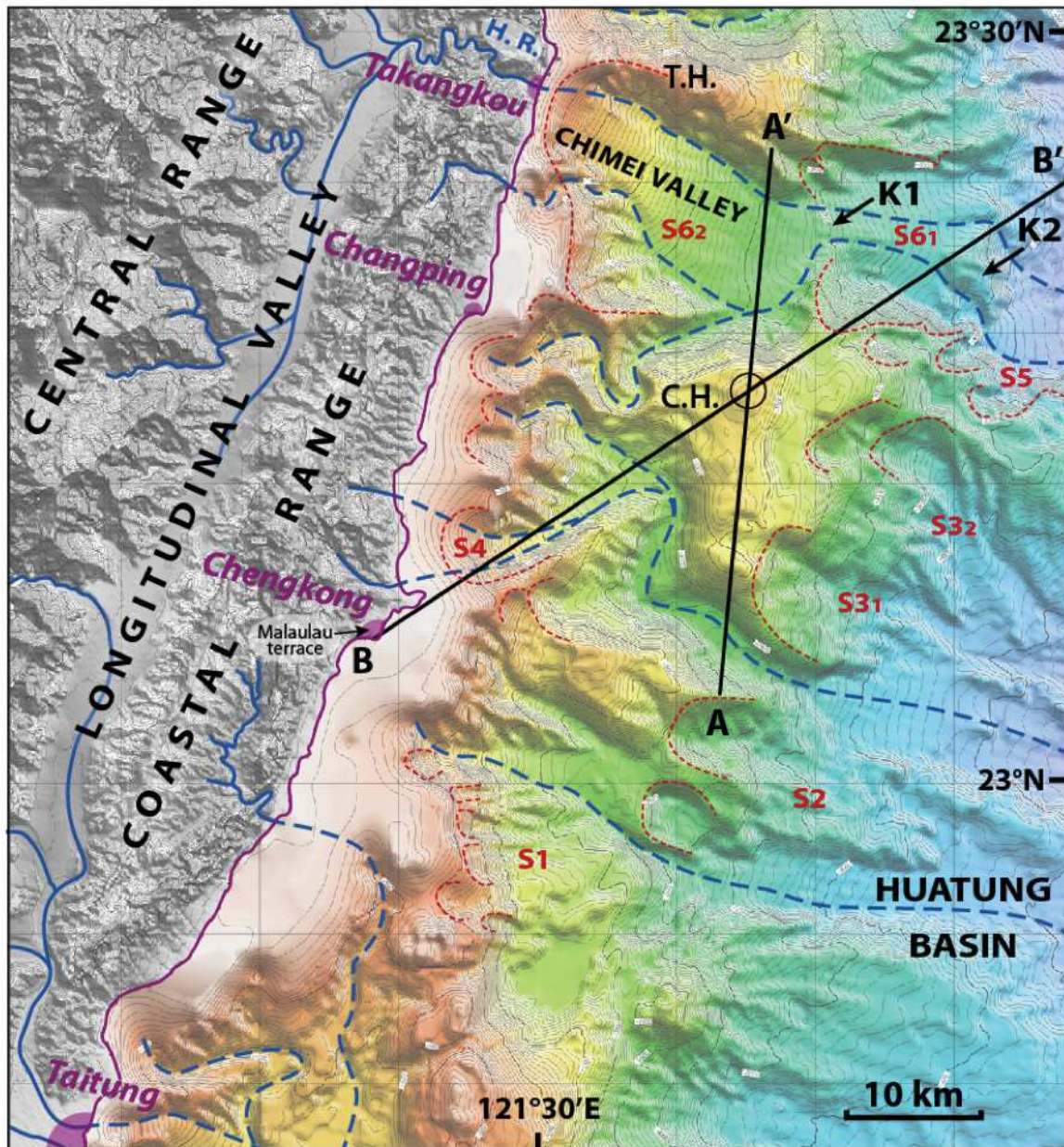


Figure 7.2: Topographic and bathymetric map of the studied area based on ACT swath mapping (Lallemand and Tsien, 1997). Isobaths every 100 m. H.R. = Hsiukiulian River, T.H. = Takangkou High, C.H. = Changping High. S1 to S6 are candidate submarine landslides. Red dotted lines are suspected scars. K1 and K2 are knickpoints of the Chimei Valley.

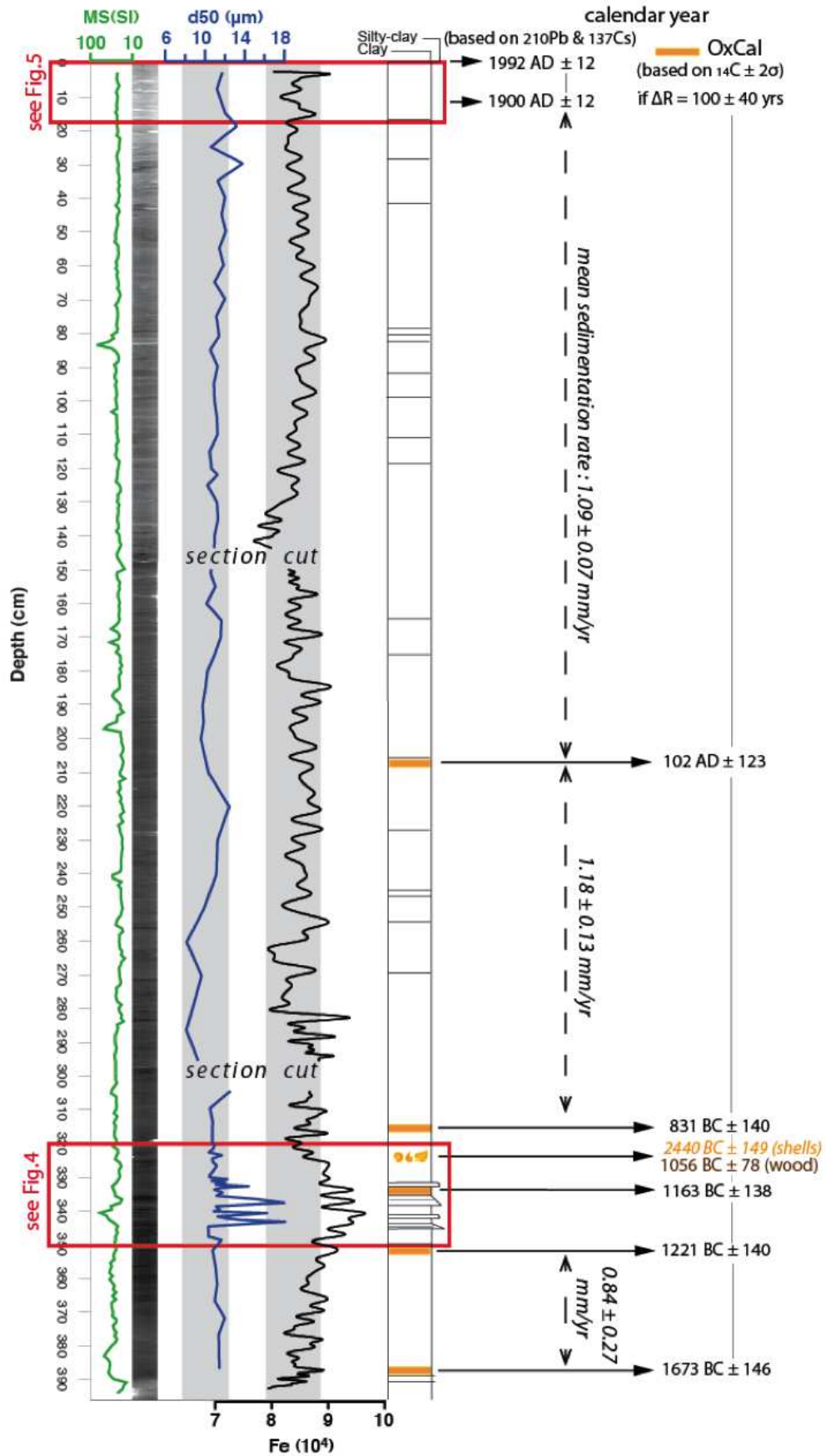


Figure 7.3: KR03 core logs : MS = Magnetic susceptibility, X-ray, d50 median grain size, Fe content, visual description and radiocarbon sampling in orange.

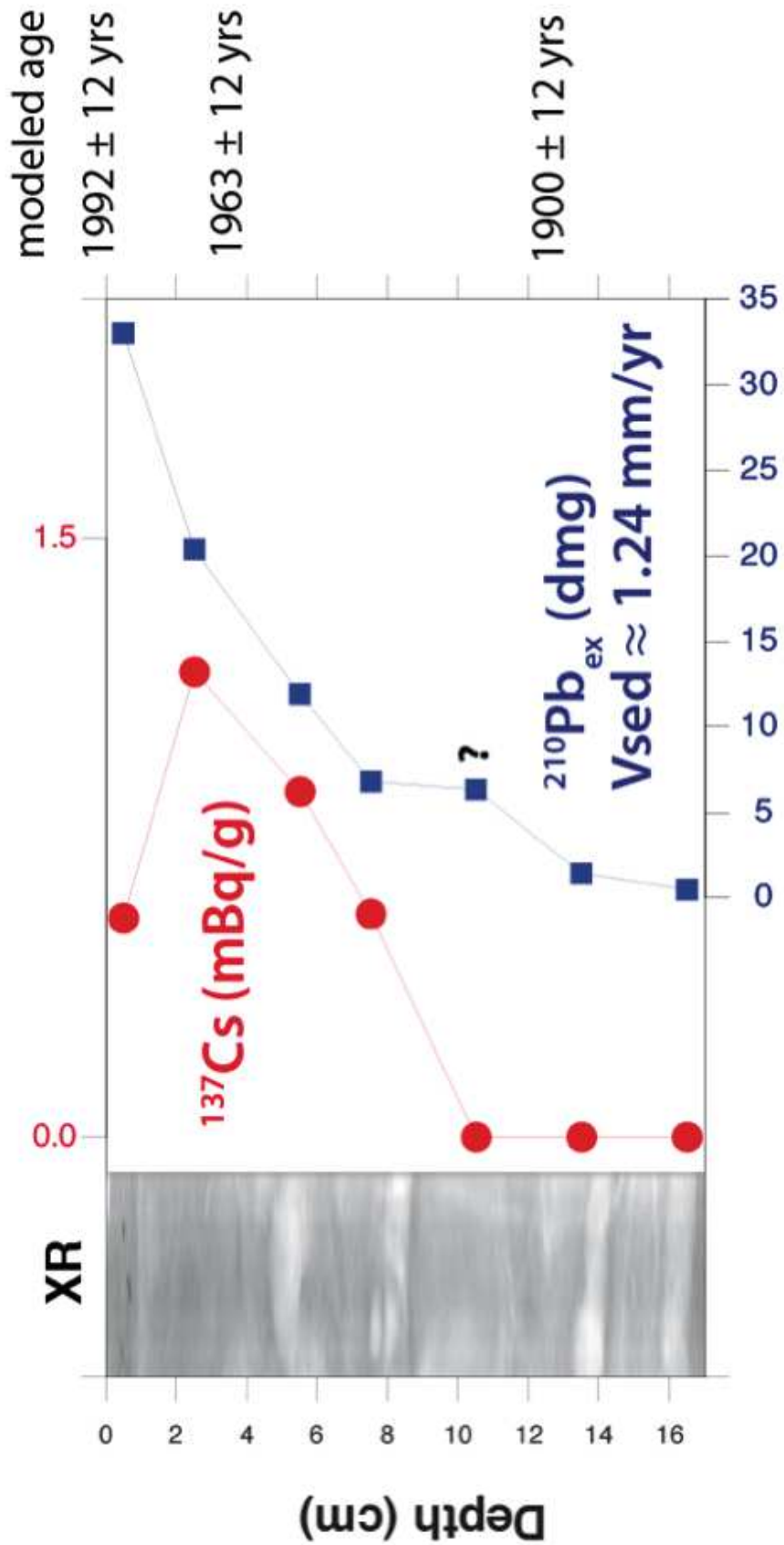


Figure 7.4: Top of core KR03 (upper 17 cm) with ^{137}Cs and $^{210}\text{Pb}_{\text{ex}}$ measurements and modeled ages (see text for further details).

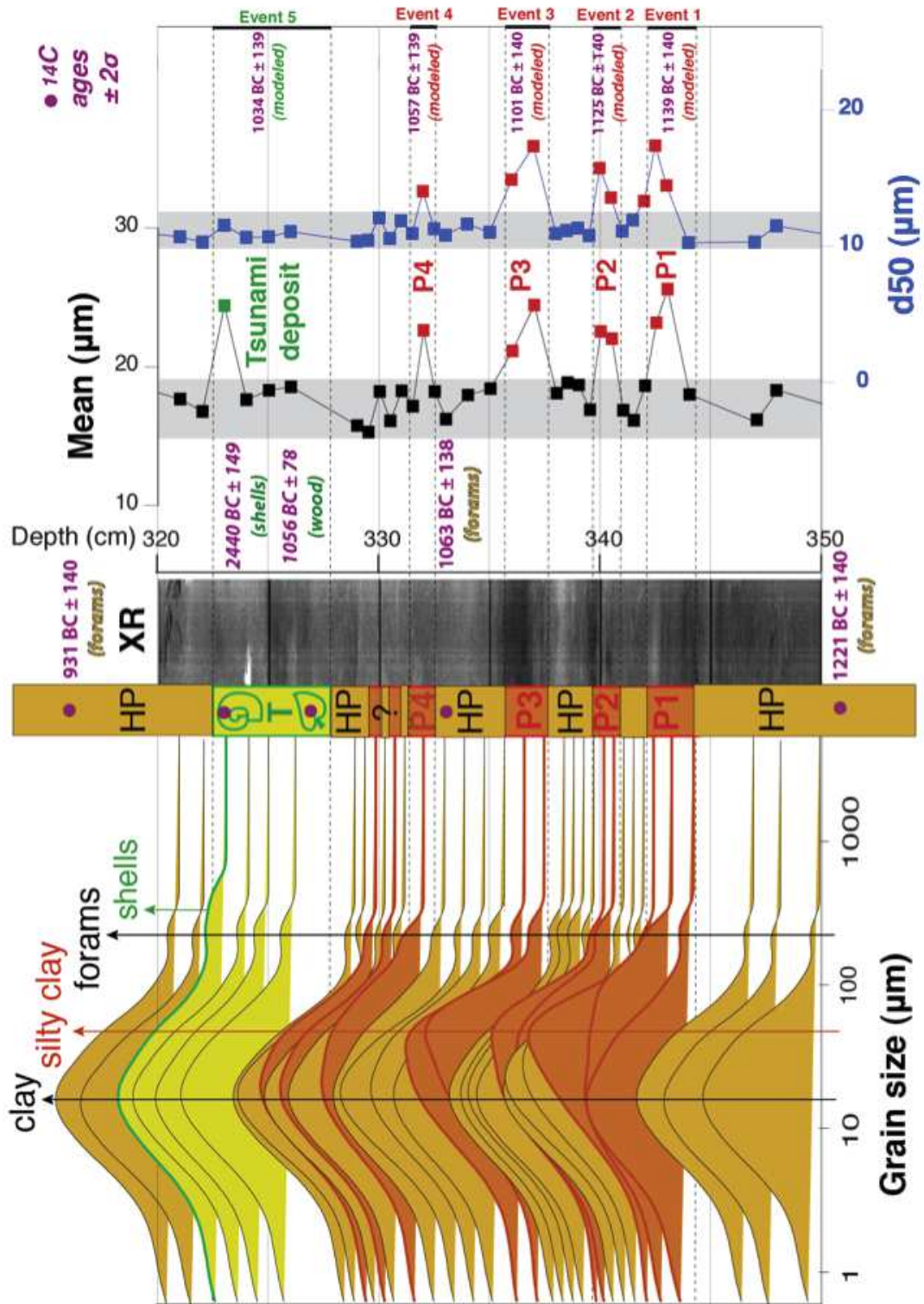


Figure 7.5: Detailed description of anomalous sequence of core KR03. Grain size distribution stacked with depth, core layers interpretation with purple dots marking the radiocarbon samples, HP = hemipelagite, P1 to P4 = silty layers, T = top anomalous layer with shells and wood fragments, XR = X-ray, Mean = mean grain size, d50 = median grain size. Radiocarbon ages are indicated in bold letters. Modeled ages are specified in parentheses as well as the dated material.

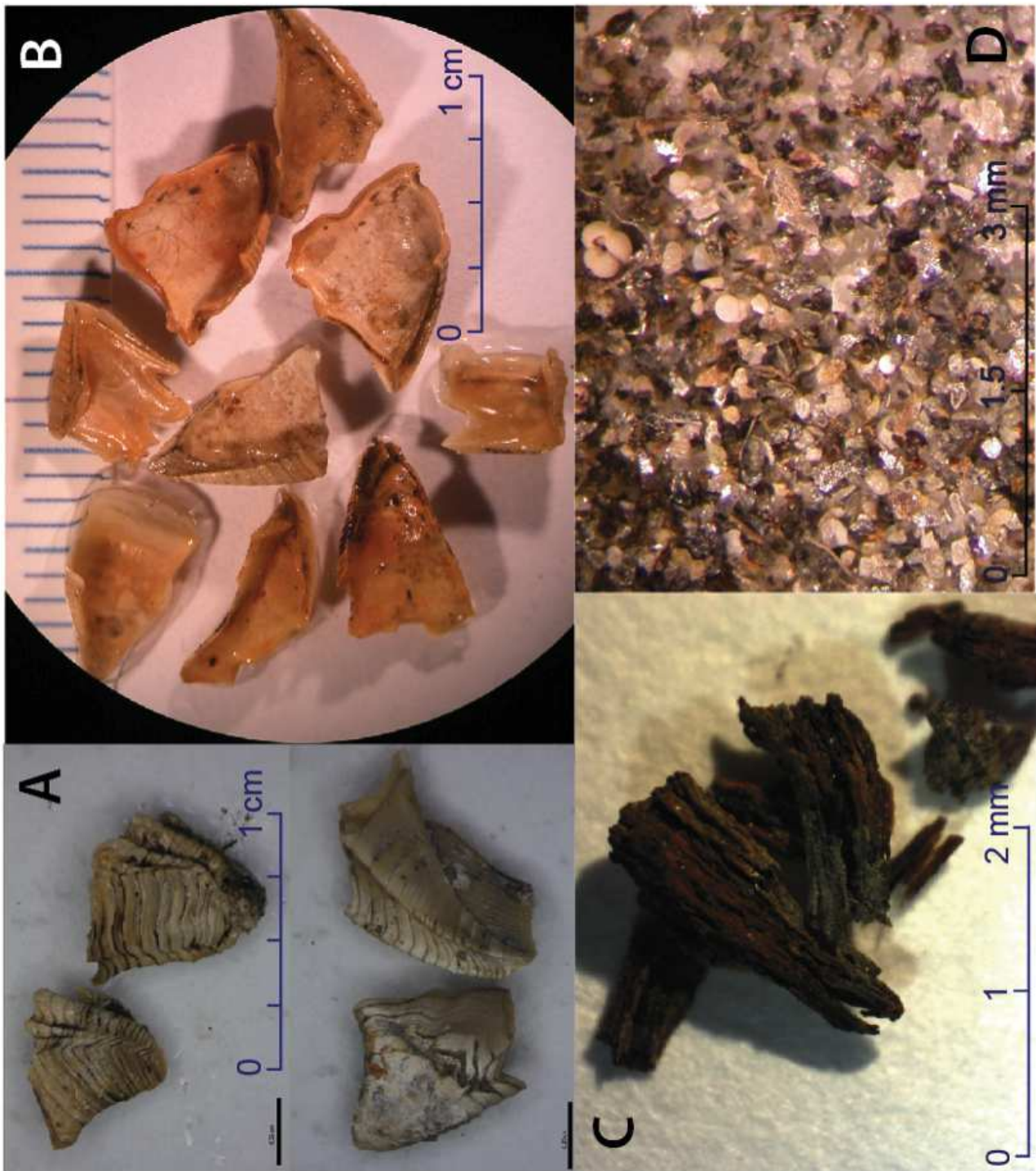


Figure 7.6: A: undetermined Veneroida bivalves external sides, B: bivalves internal sides, C: wood debris, D: silty fraction

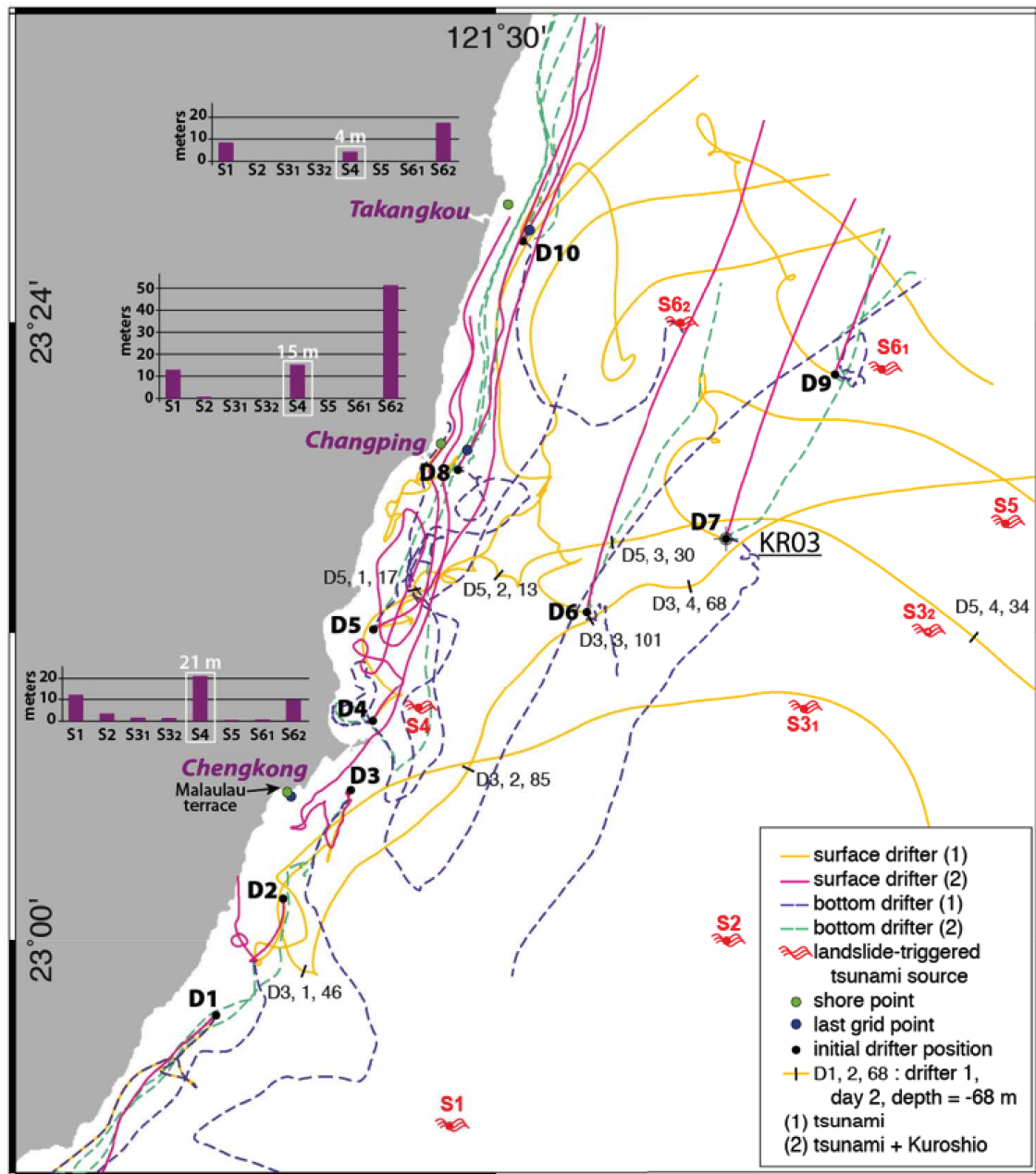


Figure 7.7: Results of hydro-dynamic modeling for S4 submarine landslide source. The paths of drifters D1 to D10 are computed during 5 days after initial input. Two drifters start from each D point, one at 15 m depth and one at sea bottom. The position of other sources S1 to S6 is shown on the map even if the drifters's paths are not indicated for all sources. It helps to locate the sources with respect to the run-ups computed at 3 coastal locations. KR03 located the core site at 1,200 m depth. See the text and Appendices A, B, C for further details.

General conclusions

Contents

8.1	Summary	197
8.2	Concluding remarks	200
8.3	Perspectives	202

8.1 Summary

By using a new set of sedimentary data selected in strategic areas, we reveal for the first time part of the ~3000 years-long history of extreme events that occurred offshore eastern Taiwan. The methodology used in this work was based on submarine paleoseismology, which provides the means to derive reliable information on the spatial distribution and recurrence of paleo-earthquakes in the marine environment from the sedimentary record.

This work has been thus guided following two main axes. The first was to investigate the present sedimentary systems off east Taiwan, essential to understand the morphosedimentary features, sedimentary facies and processes governing the evolution of the submarine slope, and the controlling factors of the recent sedimentation. The second axis was to apply a paleoseismic approach based on turbidites record at two time-scales. First, we tested and validated the method over the instrumental period (i.e, the 20th century). Then once calibrated we extended the time-series back in time.

The main results and conclusions of this work are summarized in the following paragraphs.

Deep-sea sedimentation offshore eastern Taiwan: facies and processes characterization

- A combined approach of geophysical and sedimentological data allowed us to investigate the recent sedimentary facies and processes that shape the offshore slope east Taiwan.
- We mapped morphosedimentary features based on backscatter imagery, detailed bathymetry, chirp and seismic profiles (see **Appendix** section to access the full size map) in order to characterize zones of slope failures, turbiditic systems, erosional features, depositional basins, etc..
- A detailed core analysis has been led in the aim to identify and characterize the different sedimentary facies observed in our sedimentary cores. The main interpreted facies are hemipelagites sedimentation, debrites and turbidites.
- Results showed that the offshore slope east Taiwan is affected by a variety of sedimentary systems and processes, and that turbidity currents appear as the main erosional and depositional processes covering nearly 60% of the sedimentary record.
- Turbidites facies ranges from very thin silty-clay turbidites (also called turbidites surges) to massive coarse grained turbidites. Compositions range from 80% of biotic content to 100% of lithic content.

- Site morphology and sand composition analysis showed that turbidity currents are generated by distinct controlling factors such as tectonic and climatic activity that enabled us to define at least two end-members relative to turbidity currents initiation: Turbidity currents preconditioned by tectonic activity (oversteepening) and triggered by earthquakes shaking that initiate slope instabilities and likely deposited into intra-slope basin and turbidity currents driven by climatic activity such as extreme floods or typhoons, generated in basin directly connected with onland rivers.

Historical reconstruction of paleo-earthquakes using ^{210}Pb , ^{137}Cs and ^{241}Am turbidite chronology and radiocarbon reservoir age estimation off East Taiwan

- A 36cm-long box-core has been collected east Taiwan located in a slope basin of Luzon volcanic arc in which three turbidites events have been identified.
- Based on $^{210}\text{Pb}_{ex}$, ^{137}Cs and ^{241}Am activity profiles these 3 turbidites layers have been dated circa AD 2001 ± 3 , AD 1950 ± 5 and AD 1928 ± 8 .
- The morphology of the coring site as well as the sand composition of the turbidites layers suggest a triggering mechanisms by slope failure after seismic ground shaking
- The turbidites correlate with large earthquakes that occurred in the region: the Chengkong Earthquake 12/10/2003 (Mw 6.8), the 11/24/1951 Taitung Earthquake (Mw 7.1) and the 9/4/1935 Lutao Earthquake (Mw 7.0)
- The good agreement between deposition time of the turbidites and the history of major local submarine earthquakes suggest that the record of turbidites deposits can be used as a paleoseismic indicator in this active tectonic area
- The modern reservoir ^{14}C age was estimated by comparing AMS ^{14}C ages with ages derived from a corrected ^{210}Pb profile: $R(t)$ is 517 ± 25 ^{14}C yr and $\Delta R = 234 \pm 30$ yr. This value is 112 yr higher than the global mean value and 56 yr higher than the value close to Taiwan
- This high value may be explained by upwelling activities than by hardwater effect. Local upwelling cells in the Kuroshio North of the Green Island probably bring more ^{14}C depleted water to the surface, resulting in a more positive ΔR value in that area.

2,700 years of seismicity recorded offshore eastern Taiwan by turbidites deposits

- First kyr-long chronological correlation of deep-sea turbiditic deposits along the offshore eastern Taiwan based on the detailed description and dating of four sedimentary cores

collected in the Ryukyu forearc basin and the Luzon volcanic arc.

- Coring sites have been cautiously selected to avoid climatic-driven turbidity currents, i.e., far away from continental supply paths.
- Datings and age modeling provided age of each turbidites layers since the last 2,700 years.
- We argued that earthquakes are the most plausible triggering mechanisms using 1) the test of synchronicity and 2) the biotic composition of turbidites layers
- The correlation between turbidites and seismic events over the 20th has been established by calibrating earthquakes using empirical relationship linking magnitude, distance attenuation and peak ground acceleration.
- Results indicate that Mw7 may generate slope failures around 50 km radius and Mw8 around 100 km radius.
- We thus attributed three local large instrumental earthquakes to three turbidites deposits at KS06 site within a radius of ~50 km. It also corroborates the results of Huh et al. (2004) that argued that four large earthquakes were recorded in box-core BC-18 within ~50 km radius.
- Results also suggested that synchronous turbidites events at regional scale should be cautiously considered.
- Once calibrated, we extended this approach to older time-series. Results show that the five regional events could correspond to Mw8 earthquakes that occurred in the area off Hualien between BC 50 and AD 600 giving an approximate return period of 130 years for this period.

A ~3000 years-old super-event revealed by marine deposits east of Taiwan :palaeo-landslide, earthquake, tsunami or typhoon ?

- Silty layers underlying a cm-thick concentration of shallow-living shells and wood debris have been identified within a monotonous hemipelagite core offshore east Taiwan.
- Deposits have been dated using ¹⁴C at ~3000 years BP.
- The nature of this super-event is still a matter of debate but two plausible scenarii can be proposed : (1) four large earthquakes occurred in the region within less than a century accompanied by significant gravity flows which silty plumes reached the top of the Changping High, then a "super-typhoon" occurred producing a big wave that invaded the coastal area and lifting in the air shallow water shells and wood debris to drop them 20 to 30 km away from their source. (2) about 3,000 years ago, the climate underwent a

period during which major typhoons hit the island of Taiwan, the first four major events generated hyperpycnal flows and/or shallow water sediment destabilizations responsible for silty beds even at the top of the Changping High, then a giant typhoon occurred as in the previous scenario.

8.2 Concluding remarks

The aforementioned results and conclusions of that work, allow us to raise several critical points that are discussed in the following paragraphs.

Importance of the coring rationale in paleoseismic approach

Findings of this work as well as feedback from numerous investigations in various tectonic and morphological setting (Cascadia, Portugal, Algeria, New Zealand, Sumatra...) indicate that a cautious and appropriate coring sites strategy is a fundamental step prior any paleoseismic studies. This rationale is important for the main following reasons: 1) To obtain a maximized record, 2) to avoid climatically-related turbidites, 3) to preserve a good alternation between hemipelagites and turbidites records and 4) to avoid foraminifera test dissolution for dating.

As such, to reach these objectives, the understanding of flow paths, source zones, and depositional areas of turbidity currents is critical. For example, channelized currents are highly energetic and may travel hundreds of kilometres, whereas unchannelized flows tend to wane and deposit rapidly, close to their sources (Goldfinger et al., 2012, 2014). As a result, core sites associated to submarine canyons or channels should be emplaced relatively away from sediment paths in order to avoid the coarsest deposits that may prevent efficient and long coring and that may erode the underlying deposits.

Also, core sites in isolated slope basins should be close to the surrounding slope in order to record the limited turbidite. For this work, the four cores used for our paleoseismic purpose have been all collected in isolated basin or terrace far away from major flow paths, surrounded by steep slopes and shallow enough to preserve foraminifera test. Additionally, coring sites are located close to the slope bottom in order to avoid possible turbidity current waning (between ~1-2 km away from the slope).

Criteria to discriminate co-seismic turbidites

The interpretation of co-seismic turbidites is usually based on the following three criteria: 1) A greater volume of mobilized material than climatic-related turbidity currents (Blumberg et al., 2008; Gorsline et al., 2000), 2) a synchronous trigger of turbidity currents (Goldfinger et al., 2003; Gràcia et al., 2010; Poudoux et al., 2012, 2014) and 3) a slope failure origin located below the waves action depth (Beck, 2009; Noda et al., 2008).

If turbidites are synchronous in independent basins, or sedimentary systems over tens to hundreds kilometers, then the trigger can reasonably be interpreted as regional and related to an earthquake. Offshore east Taiwan, the synchronicity criteria was established by accurately identifying, characterizing, and dating turbidites in each sedimentary cores collected across the margin. Moreover, a compositional analysis of the mineral and biotic content of turbidites can allowed us in characterizing the sources origin of turbidites and their water depth. Such information gave us insights on the triggering mechanisms. Our findings suggest that turbidites in core collected in proximal basin (e.g. SLT, see Chapter 3) for climatic purposes, display pure lithic composition, suggesting a direct terrestrial supply to the deep basin during storms. Reversely, presence planktonic fauna related to water depths below the influence of storm waves allowed us to discard a climatic trigger. In this work we were also able to validate these criteria by establishing strong time-relationship between turbidites events and instrumental earthquakes. This may represent a powerful way in discriminating and characterizing turbidites-related earthquakes.

Possible biases in the age modeling

The age of each turbidites layers (considered as instantaneous deposits) is estimated from the sedimentation rate of the hemipelagites (continuous deposits).

Identify the limit between hemipelagite and turbidites is thus crucial in the building of accurate model age and consequently primordial for the paleoseismic approach. The differentiation between the top of turbidites sequences (the finest fraction) and hemipelagites is not always trivial and was established by a sedimentological (grain size, composition of the sand fraction) and geochemical characterization (major elements and ^{210}Pb). Thus, a detailed sedimentological analysis allows to accurately differentiate hemipelagites from turbidites tails, fundamental for sedimentation rate calculation and consequently turbidites ages modeling.

When using ^{14}C method in marine environment, an important step is the age calibration and it is this crucial to use an appropriate value of the local ΔR , the site-specific offset from the global

ocean reservoir. In the offshore eastern Taiwan, ^{14}C dating spanning the Holocene yielded a wide range of reservoir ages and their values suggesting fluctuations of the oceanographic context such as local upwelling. Other biases have been also recognized such as basal erosion and sediment compaction. These two parameters may also affect age modeling and their quantification still remains difficult.

In conclusion, applying a paleoseismic approach in the offshore east Taiwan is a challenge because this area displays a complex geodynamical setting, a high seismicity rate and also a strong effect of the climate. However, this pioneer work has shown the great potential of this method and it represents a good starting-point for future investigations to better assess Holocene time series of extreme events.

8.3 Perspectives

From this work, we highlight some points that it would be interesting to develop for future investigations, in order to better constrain the paleoseismic approach and to extend the investigations of extreme events offshore eastern Taiwan:

1. Multibeam data on the studied area especially between the shelf and the upper slope, would help in creating high-resolution bathymetric maps, allowing a more accurate determination of morphometric parameters for sub-recent landslides. Besides, these maps might reveal detailed morphological information that can be used as indicator of recent sediment flow paths.
2. Chirp data would also provide good constraints on the recent sedimentation. We have seen that such data are crucial when selecting cores sites and consequently may help to prevent unsuccessful coring operation.
3. Our interpretations were also limited by a lack of sedimentary core. We propose to collect complementary cores in key areas in order to strengthen our interpretations. It would also be interesting to acquire longer cores in the preexisting site to extend time series, especially at site KS06 since this site appears as the most suitable. A piston core on the Takangkou high would help to better characterize and interpret this 3,000 years old deposits only found in core KR03 collected in the Changping high.

4. We have seen also that the constraint brought by the results obtained over the last century were decisive for further interpretations. So far in the study areas only two box-cores are available (BC-18 and KS06-B). We suggest that it would be of great interest to extend the box-core coverage, especially at sites KAS03, KS09 and KS08 where we failed to recover recent sedimentation.
5. A systematic analysis of clay mineral in both sedimentary cores and river beds should also be conducted in order to better constrain sediment sources (marine versus continental supply). This could help in discriminating between different triggering mechanisms. Also it should provide a complementary constraint in the differentiation between hemipelagite and turbidites tails.
6. We finally suggest that a more extended exploitation of the three cores collected in the SLT, will bring important constraints on the typhoons or large storms-related turbidity currents.

Bibliography

- Abe, Y. (1938). The research of locality names in taiwan. *Sugita Publication, Tokyo, 300 pp.* (*in japanese*), page 300 pp. 170
- Adams, J. (1990). Paleoseismicity of the cascadia subduction zone: Evidence from turbidites off the oregon-washington margin. *Tectonics*, 9(4):569–583. 4, 70, 93, 127, 138, 139
- Ando, M. (1975). Source mechanisms and tectonic significance of historical earthquakes along the nankai trough, japan. *Tectonophysics*, 27(2):119–140. 168
- Ando, M., Nakamura, M., and Lin, C. (2013). Tsunami folklore and possible tsunami source on the eastern coast of taiwan. *terr. Atmos. Ocean.* 170
- Appleby, P. and Oldfield, F. (1992). Applications of lead-210 to sedimentation studies. In *Uranium-series disequilibrium: applications to earth, marine, and environmental sciences.* 2. ed. 96
- Appleby, P., Richardson, N., and Nolan, P. (1991). 241am dating of lake sediments. In *Environmental History and Palaeolimnology*, pages 35–42. Springer. 98
- Arai, K., Naruse, H., Miura, R., Kawamura, K., Hino, R., Ito, Y., Inazu, D., Yokokawa, M., Izumi, N., Murayama, M., et al. (2013). Tsunami-generated turbidity current of the 2011 tohoku-oki earthquake. *Geology*, 41(11):1195–1198. 177
- Araoka, D., Yokoyama, Y., Suzuki, A., Goto, K., Miyagi, K., Miyazawa, K., Matsuzaki, H., and Kawahata, H. (2013). Tsunami recurrence revealed by porites coral boulders in the southern ryukyu islands, japan. *Geology*, 41(8):919–922. 169
- Arnaud, F., Lignier, V., Revel, M., Desmet, M., Beck, C., Pourchet, M., Charlet, F., Trentesaux, A., and Tribouvillard, N. (2002). Flood and earthquake disturbance of 210pb geochronology (lake anterne, nw alps). *Terra Nova*, 14(4):225–232. 107, 110
- Arzola, R. G., Wynn, R. B., Lastras, G., Masson, D. G., and Weaver, P. P. (2008). Sedimentary features and processes in the nazaré and setúbal submarine canyons, west iberian margin. *Marine Geology*, 250(1):64–88. 31

- Babonneau, N., Savoye, B., Cremer, M., and Klein, B. (2002). Morphology and architecture of the present canyon and channel system of the zaire deep-sea fan. *Marine and Petroleum Geology*, 19(4):445–467. 31
- Barnes, P. M., Bostock, H. C., Neil, H. L., Strachan, L. J., and Gosling, M. (2013). A 2300-year paleoearthquake record of the southern alpine fault and fiordland subduction zone, new zealand, based on stacked turbidites. *Bulletin of the Seismological Society of America*, 103(4):2424–2446. 37, 127
- Beck, C. (2009). Late quaternary lacustrine paleo-seismic archives in north-western alps: Examples of earthquake-origin assessment of sedimentary disturbances. *Earth-Science Reviews*, 96(4):327–344. 36, 70, 94, 127, 201
- Beck, C., Mercier de Lépinay, B., Schneider, J.-L., Cremer, M., Çağatay, N., Wendenbaum, E., Boutareaud, S., Ménot, G., Schmidt, S., Weber, O., et al. (2007). Late quaternary co-seismic sedimentation in the sea of marmara's deep basins. *Sedimentary Geology*, 199(1):65–89. 4
- Bentahila, Y., Ben Othman, D., and Luck, J.-M. (2008). Strontium, lead and zinc isotopes in marine cores as tracers of sedimentary provenance: A case study around taiwan orogen. *Chemical Geology*, 248(1):62–82. XXV, 75, 76
- Bentsen, M., Evensen, G., Drange, H., and Jenkins, A. (1999). Coordinate transformation on a sphere using conformal mapping*. *Monthly Weather Review*, 127(12):2733–2740. 182
- Biq, C. (1972). Dual-trench structure in the taiwan-luzon region. *Proc. Geol. Soc. China*, 15:65–75. 5, 55, 107, 129
- Blumberg, S., Lamy, F., Arz, H., Echtler, H., Wiedicke, M., Haug, G., and Oncken, O. (2008). Turbiditic trench deposits at the south-chilean active margin: a pleistocene–holocene record of climate and tectonics. *Earth and Planetary Science Letters*, 268(3):526–539. 4, 138, 201
- Bonnel, C. (2005). *Mise en place des lobes distaux dans les systèmes turbiditiques actuels: analyse comparée des systèmes du Zaïre, Var, et Rhône*. PhD thesis, Bordeaux 1. 32
- Bouma, A. H. (1962). *Sedimentology of some flysch deposits: a graphic approach to facies interpretation*, volume 168. Elsevier Amsterdam. 25, 26, 55, 64, 66, 109
- Bouma, A. H. (2000). Coarse-grained and fine-grained turbidite systems as end member models: applicability and dangers. *Marine and Petroleum Geology*, 17(2):137–143. 33, 34

- Bourdon, B. (2003). Introduction to U-series Geochemistry. *Reviews in Mineralogy and Geochemistry*, 52(1):1–21. XVII, 97
- Carrillo, E., Beck, C., Cousin, M., Jouanne, F., Cano, V., Castilla, R., Melo, L., Villemin, T., et al. (2006). A late pleistocene-holocene natural seismograph along the boconó fault (merida andes, venezuela): the moraine-dammed los zerpa paleo-lake. *Bulletin de la Société Géologique de France*, 177(1):3–17. 4
- Chai, B. H. (1972). Structure and tectonic evolution of taiwan. *American Journal of Science*, 272(5):389–422. 129
- Chang, M.-H., Tang, T. Y., Ho, C.-R., and Chao, S.-Y. (2013). Kuroshio-induced wake in the lee of Green Island off Taiwan. *Journal of Geophysical Research: Oceans*, 118(3):1508–1519. XIX, 113, 121
- Chapron, E., Beck, C., Pourchet, M., and Deconinck, J.-F. (1999). 1822 earthquake-triggered homogenite in lake le bourget (nw alps). *Terra Nova*, 11(2-3):86–92. 4
- Chen, C.-T. A., Liu, J. T., and Tsuang, B.-J. (2004). Island-based catchment—the taiwan example. *Regional Environmental Change*, 4(1):39–48. 10, 56
- Chen, K.-P. and Tsai, Y.-B. (2008). A catalog of taiwan earthquakes (1900–2006) with homogenized mw magnitudes. *Bulletin of the Seismological Society of America*, 98(1):483–489. XXV, 14, 145
- Chen, L.-K., Wu, T.-Y., and Chen, S.-C. (2012). Morakot typhoon : capacity of rainfall to landslide in taiwan. *Conference Proceedings, 12th Congress INTERPRAEVENT 2012, Grenoble, France*, pages 67–76. 171
- Chen, Y.-G. and Liu, T.-K. (2000). Holocene uplift and subsidence along an active tectonic margin southwestern taiwan. *Quaternary Science Reviews*, 19(9):923–930. 9
- Cheng, S. N. and Yeh, Y. T. (1989). *Catalog of the Earthquakes in Taiwan from 1604 to 1988*. Institute of Earth Sciences, Academia Sinica. XXV, 14, 145
- Cheng, S.-N., Yeh, Y.-T., and Yu, M.-S. (1996). The 1951 taitung earthquake in taiwan. *JOURNAL-GEOLOGICAL SOCIETY OF CHINA-TAIWAN-*, 39:267–286. XXV, 14, 145

- Chiu, J.-K. and Liu, C.-S. (2008). Comparison of sedimentary processes on adjacent passive and active continental margins offshore of sw taiwan based on echo character studies. *Basin Research*, 20(4):503–518. 67
- Choi, B., Kaistrenko, V., Kim, K., Min, B., and Pelinovsky, E. (2011). Rapid forecasting of tsunami runup heights from 2-d numerical simulations. *Natural Hazards and Earth System Science*, 11(3):707–714. XXVI, 179, 183, 186
- Chung, J.-K. (2013). Peak ground motion predictions with empirical site factors using taiwan strong motion network recordings. *Earth Planets Space*, 65(9):957–972. 111, 140
- Collot, J.-Y., Lewis, K., Lamarche, G., and Lallemand, S. (2001). The giant Ruatoria debris avalanche on the northern Hikurangi margin, New Zealand: Result of oblique seamount subduction. *Journal of Geophysical Research*, 106(B9):19271–19297. 55
- Dadson, S., Hovius, N., Pegg, S., Dade, W. B., Horng, M. J., and Chen, H. (2005). Hyperpycnal river flows from an active mountain belt. *Journal of Geophysical Research*, 110(F4):F04016. 10, 57, 72
- Dadson, S. J., Hovius, N., Chen, H., Dade, W. B., Hsieh, M.-L., Willett, S. D., Hu, J.-C., Horng, M.-J., Chen, M.-C., Stark, C. P., Lague, D., and Lin, J.-C. (2003). Links between erosion, runoff variability and seismicity in the Taiwan orogen. *Nature*, 426(6967):648–51. 9
- Dadson, S. J., Hovius, N., Chen, H., Dade, W. B., Lin, J.-C., Hsu, M.-L., Lin, C.-W., Horng, M.-J., Chen, T.-C., Milliman, J., and Stark, C. P. (2004). Earthquake-triggered increase in sediment delivery from an active mountain belt. *Geology*, 32(8):733. 10, 56
- Dan, G., Sultan, N., Savoye, B., Deverchere, J., and Yelles, K. (2009). Quantifying the role of sandy–silty sediments in generating slope failures during earthquakes: example from the algerian margin. *International Journal of Earth Sciences*, 98(4):769–789. 37, 140
- Derrioux, F., Siame, L. L., Boulès, D. L., Chen, R.-F., Braucher, R., Léanni, L., Lee, J.-C., Chu, H.-T., and Byrne, T. B. (2014). How fast is the denudation of the taiwan mountain belt? perspectives from in situ cosmogenic^{< sup> 10} be. *Journal of Asian Earth Sciences*, 88:230–245. 9</sup>
- Dezileau, L., Lehu, R., Lallemand, S., Hsu, S.-K., Babonneau, N., Ratzov, G., Lin, A. T., and S., D. (2014). Historical reconstruction of submarine earthquakes using 210pb, 137cs and 241am

- turbidite chronology and radiocarbon reservoir age estimation off east taiwan. *Radiocarbon*, 132, 133, 140, 174
- Einsele, G. (1996). Event deposits: the role of sediment supply and relative sea-level changes-an introduction. *Sedimentary Geology*, 104(1):11–37. 55
- Engdahl, E. R. and Villaseñor, A. (2002). 41 global seismicity: 1900–1999. *International Geophysics*, 81:665–XVI. XXV, 14, 145
- Eschard, R., Albouy, E., Deschamps, R., Euzen, T., and Ayub, A. (2003). Downstream evolution of turbiditic channel complexes in the pab range outcrops (maastrichtian, pakistan). *Marine and Petroleum Geology*, 20(6):691–710. XIV, 34
- Flood, R. D., Manley, P. L., Kowsmann, R. O., Appi, C. J., and Pirmez, C. (1991). Seismic facies and late quaternary growth of amazon submarine fan. In *Seismic facies and sedimentary processes of submarine fans and turbidite systems*, pages 415–433. Springer. 31
- Font, Y. and Lallemand, S. (2009). Subducting oceanic high causes compressional faulting in southernmost Ryukyu forearc as revealed by hypocentral determinations of earthquakes and reflection/refraction seismic data. *Tectonophysics*, 466(3-4):255–267. XXV, 62, 75, 76
- Font, Y., Liu, C.-S., Schnurle, P., and Lallemand, S. (2001). Constraints on backstop geometry of the southwest Ryukyu subduction based on reflection seismic data. *Tectonophysics*, 333(1-2):135–158. XXV, 75, 76
- Fontugne, M., Carre, M., Bentaleb, I., Julien, M., and Lavallee, D. (2004). Radiocarbon reservoir age variations in the south peruvian upwelling during the holocene. *Radiocarbon*, 46(2):531–537. 101, 108
- Forel, F.-A. (1887). *Le ravin sous-lacustre du Rhône dans le lac Léman*. Impr. L. Corbaz. 25
- Galewsky, J., Stark, C. P., Dadson, S., Wu, C.-C., Sobel, a. H., and Horng, M.-J. (2006). Tropical cyclone triggering of sediment discharge in Taiwan. *Journal of Geophysical Research*, 111(F3):F03014. 9, 56
- Galloway, W. E. (1998). Siliciclastic slope and base-of-slope depositional systems: component facies, stratigraphic architecture, and classification. *AAPG bulletin*, 82(4):569–595. 31

- Garcia-Orellana, J., Gràcia, E., Vizcaino, A., Masqué, P., Olid, C., Martínez-Ruiz, F., Piñero, E., Sanchez-Cabeza, J.-A., and Dañobeitia, J. (2006). Identifying instrumental and historical earthquake records in the sw iberian margin using 210pb turbidite chronology. *Geophysical Research Letters*, 33(24). 107, 110
- Gaudin, M. (2006). *Processus et enregistrements sédimentaires dans les canyons sous-marins Bourcart et de Capbreton durant le dernier cycle climatique*. PhD thesis, Bordeaux 1. 31
- Ge, X., Li, T., Zhang, S., and Peng, M. (2010). What causes the extremely heavy rainfall in taiwan during typhoon morakot (2009)? *Atmospheric science letters*, 11(1):46–50. 10, 56
- Genesseeux, M., Mauffret, A., and Pautot, G. (1980). Les glissements sous-marins de la pente continentale niçoise et la rupture de câbles en mer ligure (méditerranée occidentale). *Comptes Rendus de l'Académie des Sciences de Paris*, 290(14):959–962. 21
- Goldberg, E. D. (1963). Geochronology with 210pb. *Radioactive dating*, pages 121–131. 96, 110
- Goldfinger, C. (2011). Submarine paleoseismology based on turbidite records. *Annual review of marine science*, 3:35–66. 4, 127
- Goldfinger, C., Morey, A. E., Nelson, C. H., Gutiérrez-Pastor, J., Johnson, J. E., Karabanov, E., Chaytor, J., and Eriksson, A. (2007). Rupture lengths and temporal history of significant earthquakes on the offshore and north coast segments of the Northern San Andreas Fault based on turbidite stratigraphy. *Earth and Planetary Science Letters*, 254(1-2):9–27. XVII, 93, 95, 127, 139
- Goldfinger, C., Nelson, C. H., and Johnson, J. E. (2003). Holocene earthquake records from the cascadia subduction zone and northern san andreas fault based on precise dating of offshore turbidites. *Annual Review of Earth and Planetary Sciences*, 31(1):555–577. 4, 36, 70, 93, 94, 127, 138, 139, 201
- Goldfinger, C., Nelson, C. H., Morey, A. E., Johnson, J. E., Patton, J., Karabanov, E., Gutierrez-Pastor, J., Eriksson, A. T., Gracia, E., Dunhill, G., et al. (2012). *Turbidite event history: Methods and implications for Holocene paleoseismicity of the Cascadia subduction zone*. US Department of the Interior, US Geological Survey. 127, 200
- Goldfinger, C., Patton, J. R., Van Daele, M., Moernaut, J., Nelson, C. H., de Batist, M., and

- Morey, a. E. (2014). Can turbidites be used to reconstruct a paleoearthquake record for the central Sumatran margin?: COMMENT. *Geology*, 42(9):e344–e344. 200
- Goodfriend, G. A. and Flessa, K. W. (1997). Radiocarbon reservoir ages in the gulf of california: roles of upwelling and flow from the colorado river. *Radiocarbon*, 39(2):139–148. 101, 108
- Gorsline, D., De Diego, T., and Nava-Sanchez, E. (2000). Seismically triggered turbidites in small margin basins: Alfonso Basin, Western Gulf of California and Santa Monica Basin, California Borderland. *Sedimentary Geology*, 135(1-4):21–35. XVII, 93, 94, 127, 201
- Goto, K., Kawana, T., and Imamura, F. (2010). Historical and geological evidence of boulders deposited by tsunamis, southern ryukyu islands, japan. *Earth-Science Reviews*, 102(1):77–99. 169
- Goto, K., Miyagi, K., and Imamura, F. (2013). Localized tsunamigenic earthquakes inferred from preferential distribution of coastal boulders on the ryukyu islands, japan. *Geology*, 41(11):1139–1142. 169
- Gràcia, E., Vizcaino, A., Escutia, C., Asioli, A., Rodés, A., Pallàs, R., Garcia-Orellana, J., Lebreiro, S., and Goldfinger, C. (2010). Holocene earthquake record offshore Portugal (SW Iberia): testing turbidite paleoseismology in a slow-convergence margin. *Quaternary Science Reviews*, 29(9-10):1156–1172. 4, 37, 71, 93, 94, 127, 138, 139, 201
- Hampton, M. A. (1972). The role of subaqueous debris flow in generating turbidity currents. *Journal of Sedimentary Research*, 42(4). 28
- Hampton, M. a., Lee, H. J., and Locat, J. (1996). Submarine landslides. *Reviews of Geophysics*, 34(1):33. 21, 60, 67, 68
- Heezen, B. C. and Ewing, W. M. (1952). Turbidity currents and submarine slumps, and the 1929 grand banks [newfoundland] earthquake. *American Journal of Science*, 250(12):849–873. 138
- Hetland, E. A. and Wu, F. T. (2001). Crustal structure at the intersection of the ryukyu trench with the arc-continent collision in taiwan: Results from an offshore-onshore seismic experiment. *Terrestrial Atmospheric And Oceanic Sciences*, 12(SUPP):231–248. XXV, 62, 75, 76

- Hsieh, M.-L., Liew, P.-M., and Hsu, M.-Y. (2004). Holocene tectonic uplift on the hua-tung coast, eastern taiwan. *Quaternary International*, 115:47–70. 9
- Hsin, Y.-C., Wu, C.-R., and Shaw, P.-T. (2008). Spatial and temporal variations of the kuroshio east of taiwan, 1982–2005: A numerical study. *Journal of Geophysical Research: Oceans (1978–2012)*, 113(4). XIX, XXI, 121, 171, 178, 187
- Hsu, M.-T. (1961). Seismicity of taiwan (formosa). *Bull. earthq. Res. Inst. Tokyo University*, 39:831–847. 7, 56
- Hsu, S.-K., Kuo, J., Lo, C.-L., Tsai, C.-H., Doo, W.-B., Ku, C.-Y., and Sibuet, J.-C. (2008). Turbidity currents, submarine landslides and the 2006. *Terr. Atmos. Ocean. Sci.*, 19(6):762–772. 21, 67
- Hsu, S.-K., Yeh, Y.-C., Sibuet, J.-C., Doo, W.-B., and Tsai, C.-H. (2013). A mega-splay fault system and tsunami hazard in the southern ryukyu subduction zone. *Earth and Planetary Science Letters*, 362:99–107. 169
- Hsu, Y.-J., Yu, S.-B., Simons, M., Kuo, L.-C., and Chen, H.-Y. (2009). Interseismic crustal deformation in the taiwan plate boundary zone revealed by gps observations, seismicity, and earthquake focal mechanisms. *Tectonophysics*, 479(1):4–18. XIII, 7
- Huang, C., Shyu, C., Lin, S., Lee, T., and Sheu, D. (1992). Marine geology in the arc-continent collision zone off southeastern taiwan: Implications for late neogene evolution of the coastal range. *Marine Geology*, 107:183–212. XXV, 58, 64, 66, 75, 76
- Huang, C.-Y., Yuan, P. B., and Tsao, S.-J. (2006). Temporal and spatial records of active arc-continent collision in taiwan: A synthesis. *Geological Society of America Bulletin*, 118(3-4):274–288. XIII, 8
- Hughen, K. A., Baillie, M. G., Bard, E., Beck, J. W., Bertrand, C. J., Blackwell, P. G., Buck, C. E., Burr, G. S., Cutler, K. B., Damon, P. E., et al. (2004). Marine04 marine radiocarbon age calibration, 0–26 cal kyr bp. *Radiocarbon*, 46:1059–1086. 108, 112
- Huh, C.-A., Su, C.-C., Liang, W.-T., and Ling, C.-Y. (2004). Linkages between turbidites in the southern Okinawa Trough and submarine earthquakes. *Geophysical Research Letters*, 31:2–5. XIV, XIX, XXV, 4, 5, 36, 37, 39, 40, 55, 58, 75, 76, 107, 110, 111, 127, 136, 137, 140, 142, 152, 199

- Huh, C.-A., Su, C.-C., Wang, C.-H., Lee, S.-Y., and Lin, I.-T. (2006). Sedimentation in the southern okinawa trough—rates, turbidites and a sediment budget. *Marine geology*, 231(1):129–139. 55, 107, 110
- Ingram, B. and Southon, J. (1997). Reservoir ages in eastern pacific coastal and estuarine waters. radiocarbon. *Radiocarbon*, 38(3):573–582. 108
- Izumi, N. (2004). The formation of submarine gullies by turbidity currents. *Journal of Geophysical Research: Oceans (1978–2012)*, 109(C3). 31
- Kao, H., Shen, S.-s. J., and Ma, K.-F. (1998). Transition from oblique subduction to collision: Earthquakes in the southernmost ryukyu arc-taiwan region. *Journal of Geophysical Research: Solid Earth (1978–2012)*, 103(B4):7211–7229. 129
- Kao, S. and Milliman, J. (2008). Water and sediment discharge from small mountainous rivers, taiwan: The roles of lithology, episodic events, and human activities. *The Journal of Geology*, 116(5):431–448. 10, 57
- KAWANA, T. and NAKATA, T. (1994). Timing of late holocene tsunamis originated around the southern ryukyu islands, japan, deduced from coralline tsunami deposits. *Journal of geography (Chigaku Zasshi), in Japanese*, 103(4):352–376. 177
- Kennett, D. J., Ingram, B. L., Erlandson, J. M., and Walker, P. (1997). Evidence for temporal fluctuations in marine radiocarbon reservoir ages in the santa barbara channel, southern california. *Journal of Archaeological Science*, 24(11):1051–1059. 101
- Krishnaswamy, S., Lal, D., Martin, J., and Meybeck, M. (1971a). Geochronology of lake sediments. *Earth and Planetary Science Letters*, 11(1):407–414. 96
- Krishnaswamy, S., Lal, D., Martin, J., and Meybeck, M. (1971b). Geochronology of lake sediments. *Earth and Planetary Science Letters*, 11(1):407–414. 110
- Kuenen, P. H. and Migliorini, C. (1950). Turbidity currents as a cause of graded bedding. *The Journal of Geology*, pages 91–127. 25
- Lai, J.-S., Chiu, C.-Y., Chang, H.-K., Hu, J.-C., and Tan, Y.-C. (2010). Potential inundation hazards in the taipei basin induced by reactivation of the shanchiao fault in northern taiwan. *Terrestrial, Atmospheric and Oceanic Sciences*, 21(3):529–542. 167

- Lallemand, S., Heuret, A., and Boutelier, D. (2005). On the relationships between slab dip, back-arc stress, upper plate absolute motion, and crustal nature in subduction zones. *Geochemistry, Geophysics, Geosystems*, 6(9). 168, 169
- Lallemand, S., Liu, C.-S., Dominguez, S., Schnürle, P., and Malavieille, J. (1999). The act scientific crew, 1999. trench-parallel stretching and folding of forearc basins and lateral migration of the accretionary wedge in the southern ryukyus: a case of strain partition caused by oblique convergence. *Tectonics*, 18(2):231–247. XXV, 75, 76
- Lallemand, S., Theunissen, T., Schnürle, P., Lee, C.-S., Liu, C.-S., and Font, Y. (2013). Tectonophysics Indentation of the Philippine Sea plate by the Eurasia plate in Taiwan : Details from recent marine seismological experiments. *Tectonophysics*, 594:60–79. XXV, 39, 62, 68, 69, 75, 76, 127, 168
- Lallemand, S. E., Liu, C.-S., and Font, Y. (1997b). A tear fault boundary between the taiwan orogen and the ryukyu subduction zone. *Tectonophysics*, 274(1):171–190. XXV, 75, 76
- Lallemand, S. E. and Tsien, H.-H. (1997). An introduction to active collision in Taiwan. *Tectonophysics*, 274:1–4. XXI, 58, 176, 182, 188
- Lau, A. Y. A., Switzer, A. D., Dominey-Howes, D., Aitchison, J., and Zong, Y. (2010). Written records of historical tsunamis in the northeastern south china sea: challenges associated with developing a new integrated database. *Nat. Hazards Earth Syst. Sci.*, (10):1793–1806. 169, 170
- Lay, T. and Kanamori, H. (2011). Insights from the great 2011 japan earthquake. *Phys. Today*, 64(12):33. 167
- Lee, H., Locat, J., Dartnell, P., Israel, K., and Wong, F. (1999). Regional variability of slope stability: application to the eel margin, california. *Marine Geology*, 154(1):305–321. 37
- Lee, H. J. and Edwards, B. D. (1986). Regional method to assess offshore slope stability. *Journal of Geotechnical Engineering*, 112(5):489–509. 37
- Lee, S. and Pradhan, B. (2007). Landslide hazard mapping at selangor, malaysia using frequency ratio and logistic regression models. *Landslides*, 4(1):33–41. 67

- Lehu, R., Lallemand, S., Hsu, S.-K., Lin, A. T., Ratzov, G., Babonneau, N., and Dezileau, L. (2013). Submarine paleoseismology offshore eastern taiwan: New insights from turbidite records. *Abstract in AGU Fall meeting*. 171
- Lehu, R., Lallemand, S., Hsu, S.-K., Lin, A. T., Ratzov, G., Babonneau, N., and Dezileau, L. (2014a). Deep-sea sedimentation offshore eastern taiwan: facies and processes characterization. *Marine Geology*. 107, 108, 109, 110, 127, 129, 130, 133, 134, 135, 139, 176
- Lehu, R., Lallemand, S., Hsu, S.-K., Ratzov, G., Babonneau, N., Lin, A. T., and Dezileau, L. (2014b). 2,700 years of seismicity recorded offshore eastern taiwan by turbidites deposits. *Tectonophysics*. 111
- Li, Y.-H. (1976). Denudation of taiwan island since the pliocene epoch. *Geology*, 4(2):105–107. 10, 56
- Liew, P., Pirazzoli, P., Hsieh, M., Arnold, M., Barusseau, J., Fontugne, M., and Giresse, P. (1993). Holocene tectonic uplift deduced from elevated shorelines, eastern coastal range of taiwan. *Tectonophysics*, 222(1):55–68. 9
- Lin, J.-Y., Sibuet, J.-C., Hsu, S.-K., and Wu, W.-N. (2014). Could a sumatra-like megathrust earthquake occur in the south ryukyu subduction zone? *Earth, Planets and Space*, 66(1):1–8. 177
- Lin, Y.-L., Ensley, D. B., Chiao, S., and Huang, C.-Y. (2002). Orographic influences on rainfall and track deflection associated with the passage of a tropical cyclone. *Monthly weather review*, 130(12). 9, 56
- Litchfield, N. J. and Berryman, K. R. (2005). Correlation of fluvial terraces within the hiku-rangi margin, new zealand: implications for climate and baselevel controls. *Geomorphology*, 68(3):291–313. 35
- Liu, J., Liu, C., Xu, K., Milliman, J., Chiu, J., Kao, S., and Lin, S. (2008). Flux and fate of small mountainous rivers derived sediments into the Taiwan Strait. *Marine Geology*, 256(1-4):65–76. XVI, 9, 10, 37, 56, 57, 73, 77, 127, 168, 171
- Locat, J. and Lee, H. J. (2002). Submarine landslides: advances and challenges. *Canadian Geotechnical Journal*, 39(1):193–212. 55, 67

- Lofi, J., Inwood, J., Proust, J.-N., Monteverde, D. H., Loggia, D., Basile, C., Otsuka, H., Hayashi, T., Stadler, S., Mottl, M. J., et al. (2013). Fresh-water and salt-water distribution in passive margin sediments: Insights from integrated ocean drilling program expedition 313 on the new jersey margin. *Geosphere*, 9(4):1009–1024. 175
- Lowe, D. R. (1982). Sediment gravity flows: Ii depositional models with special reference to the deposits of high-density turbidity currents. *Journal of Sedimentary Research*, 52(1). XIV, 26
- Ma, K.-F. and Lee, M.-F. (1997). Simulation of historical tsunamis in the taiwan region. *Digui Kexue Jikan= TAO, Terrestrial, Atmospheric and Oceanic Sciences*, 8(1):13–30. 169, 170
- Madec, G. (2008). Nemo ocean engine. 183
- Malavieille, J., Lallemand, S., Dominguez, S., Deschamps, A., Lu, C., Liu, C., Schnürle, P., Hsu, J., Liu, S., Sibuet, J., and Others (2002). Arc-continent collision in taiwan new marine observations and tectonic evolution. *Geological Society of America Special Paper*, pages 189–213. XXV, 7, 8, 39, 48, 57, 59, 61, 62, 63, 68, 71, 75, 76, 127, 129, 168
- Marsaleix, P., Auclair, F., Duhaut, T., Estournel, C., Nguyen, C., and Ulses, C. (2012). Alternatives to the robert–asselin filter. *Ocean Modelling*, 41:53–66. 182
- Marsaleix, P., Auclair, F., and Estournel, C. (2006). Considerations on open boundary conditions for regional and coastal ocean models. *Journal of Atmospheric and Oceanic Technology*, 23(11):1604–1613. 183
- Marsaleix, P., Auclair, F., and Estournel, C. (2009). Low-order pressure gradient schemes in sigma coordinate models: The seamount test revisited. *Ocean Modelling*, 30(2):169–177. 182
- Marsaleix, P., Auclair, F., Estournel, C., Nguyen, C., and Ulses, C. (2011). An accurate implementation of the compressibility terms in the equation of state in a low order pressure gradient scheme for sigma coordinate ocean models. *Ocean Modelling*, 40(1):1–13. 182
- Marsaleix, P., Auclair, F., Floor, J. W., Herrmann, M. J., Estournel, C., Pairaud, I., and Ulses, C. (2008). Energy conservation issues in sigma-coordinate free-surface ocean models. *Ocean Modelling*, 20(1):61–89. 179, 182
- Masson, D. G., Harbitz, C. B., Wynn, R. B., Pedersen, G., and Løvholt, F. (2006). Submarine landslides: processes, triggers and hazard prediction. *Philosophical transactions. Series A, Mathematical, physical, and engineering sciences*, 364(1845):2009–2039. 55, 67

- Matta, N., Ota, Y., Ando, M., Nishikawa, N., Switzer, A., Haraguchi, T., and Lin, C. H. (2014). Possible paleotsunami at chenggong coast, eastern taiwan, as deduced from the excavation of holocene sediments. *Submitted to Journal of Asian Earth Sciences*, page 300 pp. 170
- McAdoo, B. and Watts, P. (2004). Tsunami hazard from submarine landslides on the oregon continental slope. *Marine Geology*, 203(3):235–245. 68
- McHugh, C. M., Seeber, L., Braudy, N., Cormier, M.-H., Davis, M. B., Diebold, J. B., Dieudonne, N., Douilly, R., Gulick, S. P., Hornbach, M. J., et al. (2011). Offshore sedimentary effects of the 12 january 2010 haiti earthquake. *Geology*, 39(8):723–726. 127
- McIntosh, K., Nakamura, Y., Wang, T.-K., Shih, R.-C., Chen, A., and Liu, C.-S. (2005). Crustal-scale seismic profiles across taiwan and the western philippine sea. *Tectonophysics*, 401(1):23–54. XXV, 75, 76
- McIntosh, K. D. and Nakamura, Y. (1998). Crustal structure beneath the nanao forearc basin from taicrust mcs/obs line 14. *Terr. Atmos. Ocean. Sci*, 9(3):345–362. XXV, 75, 76
- Megawati, K., Shaw, F., Sieh, K., Huang, Z., Wu, T.-R., Lin, Y., Tan, S. K., and Pan, T.-C. (2009). Tsunami hazard from the subduction megathrust of the south china sea: Part i. source characterization and the resulting tsunami. *Journal of Asian Earth Sciences*, 36(1):13–20. 169
- Middleton, G. V. and Hampton, M. A. (1973). Part i. sediment gravity flows: mechanics of flow and deposition. *Pacific Section SEPM*, pages 1–38. XIV, 21, 27, 29, 36
- Milliman, J. D. and Syvitski, J. P. (1992). Geomorphic/tectonic control of sediment discharge to the ocean: the importance of small mountainous rivers. *The Journal of Geology*, pages 525–544. 10, 27, 56
- Moernaut, J., Daele, M. V., Heirman, K., Fontijn, K., Strasser, M., Pino, M., Urrutia, R., and De Batist, M. (2014). Lacustrine turbidites as a tool for quantitative earthquake reconstruction: New evidence for a variable rupture mode in south central chile. *Journal of Geophysical Research: Solid Earth*, 119(3):1607–1633. 127
- Mountjoy, J. J., Barnes, P. M., and Pettinga, J. R. (2009). Morphostructure and evolution of submarine canyons across an active margin : Cook Strait sector of the Hikurangi Margin , New Zealand. *Marine Geology*, pages 1–24. XIV, 33, 60

- Mulder, T. and Alexander, J. (2001). The physical character of subaqueous sedimentary density flows and their deposits. *Sedimentology*, 48(2):269–299. 21, 24, 25, 27, 36, 55, 64, 70
- Mulder, T. and Cochonat, P. (1996). Classification of offshore mass movements. *Journal of Sedimentary Research*, 66(1):43–57. XIV, 21, 22, 23, 24, 55, 127
- Mulder, T. and Syvitski, J. P. (1995). Turbidity currents generated at river mouths during exceptional discharges to the world oceans. *The Journal of Geology*, pages 285–299. 27
- Mulder, T., Syvitski, J. P., Migeon, S., Faugeres, J.-C., and Savoye, B. (2003). Marine hyperpycnal flows: initiation, behavior and related deposits. a review. *Marine and Petroleum Geology*, 20(6):861–882. XIV, 27, 28, 35, 70, 72
- Nakajima, T. and Kanai, Y. (2000). Sedimentary features of seismoturbidites triggered by the 1983 and older historical earthquakes in the eastern margin of the japan sea. *Sedimentary Geology*, 135(1):1–19. XVII, 93, 127
- Nakamura, M. (2006). Source fault model of the 1771 yaeyama tsunami, southern ryukyu islands, japan, inferred from numerical simulation. *pure and applied geophysics*, 163(1):41–54. 169
- Nakamura, M. (2009). Fault model of the 1771 yaeyama earthquake along the ryukyu trench estimated from the devastating tsunami. *Geophysical Research Letters*, 36(19). 169
- Natawidjaja, D. H., Sieh, K., Chlieh, M., Galetzka, J., Suwargadi, B. W., Cheng, H., Edwards, R. L., Avouac, J.-P., and Ward, S. N. (2006). Source parameters of the great sumatran megathrust earthquakes of 1797 and 1833 inferred from coral microatolls. *Journal of Geophysical Research: Solid Earth (1978–2012)*, 111(B6). 167
- Nelson, C., Goldfinger, C., Vallier, T., McGann, M., and Kashgarian, M. (1996). North to south variation in cascadia basin turbidite event history: Implications for paleoseismicity. In *Geological Society of America Abstracts with Programs*, volume 28, page 95. 139
- Nittrouer, C., Sternberg, R., Carpenter, R., and Bennett, J. (1979). The use of pb-210 geochronology as a sedimentological tool: application to the washington continental shelf. *Marine Geology*, 31(3):297–316. 107
- Noda, A., TuZino, T., Kanai, Y., Furukawa, R., and Uchida, J.-i. (2008). Paleoseismicity along the southern kuril trench deduced from submarine-fan turbidites. *Marine Geology*, 254(1):73–90. 36, 37, 94, 127, 201

- Normark, W. R. and Carlson, P. R. (2003). Giant submarine canyons: Is size any clue to their importance in the rock record? *Special Papers-Geological Society of America*, pages 175–190. 31
- Normark, W. R., Piper, D. J., Posamentier, H., Pirmez, C., and Migeon, S. (2002). Variability in form and growth of sediment waves on turbidite channel levees. *Marine Geology*, 192(1):23–58. 32
- Okal, E. A., Synolakis, C. E., and Kalligeris, N. (2011). Tsunami simulations for regional sources in the south china and adjoining seas. *Pure and applied geophysics*, 168(6-7):1153–1173. 169
- Oldfield, F. and Appleby, P. (1984). Empirical testing of ²¹⁰Pb-dating models for lake sediments. In *Lake sediments and environmental history*. XVII, 97
- Ota, Y., Matta, N., Ando, M., Haraguti, T., Nishikawa, Y., , and Switzer, A. (2011). Geological data for possible paleotsunami at the eastern coast of taiwan. *abstract in Quaternary Sciences - the view from the mountains, Bern, Switzerland, July 21-27*. 178, 180
- Parker, G. (2006). Theory for a clinof orm of permanent form on a continental margin emplaced by weak, dilute muddy turbidity currents. In *Proceedings of the 4th IAHR Symposium on River, Coastal and Estuarine Morphodynamics, RCEM 2005, 4-7 October 2005*, pages 553–561. 177
- Peng, T.-H., Li, Y.-H., and Wu, F. T. (1977). Tectonic uplift rates of the taiwan island since the early holocene. *Mem. Geol. Soc. China*, 2:57–69. 9
- Piper, D. J. and Normark, W. R. (2009). Processes that initiate turbidity currents and their influence on turbidites: a marine geology perspective. *Journal of Sedimentary Research*, 79(6):347–362. 31, 55
- Piper, D. J. W., Cochonat, P., and Morrison, M. L. (1999). The sequence of events around the epicentre of the 1929 Grand Banks earthquake: initiation of debris flows and turbidity current inferred from sidescan sonar. *Sedimentology*, 46(1):79–97. 27, 36, 138
- Polonia, a., Panieri, G., Gasperini, L., Gasparotto, G., Bellucci, L. G., and Torelli, L. (2013). Turbidite paleoseismology in the Calabrian Arc Subduction Complex (Ionian Sea). *Geochemistry, Geophysics, Geosystems*, 14(1):112–140. 4, 37, 93, 94, 127

- Popescu, I., Lericolais, G., Panin, N., Normand, A., Dinu, C., and Le Drezen, E. (2004). The danube submarine canyon (black sea): morphology and sedimentary processes. *Marine Geology*, 206(1):249–265. XIV, 32
- Postma, G. (1986). Classification for sediment gravity-flow deposits based on flow conditions during sedimentation. *Geology*, 14(4):291–294. 24
- Pouderoux, H. (2011). *Sédimentation gravitaire et paléosismicité d'une marge active: exemple de la marge en subduction Hikurangi en Nouvelle-Zélande*. PhD thesis, Université Rennes 1. XIV, 36
- Pouderoux, H., Lamarche, G., and Proust, J.-N. (2012). Building an 18 000-year-long paleo-earthquake record from detailed deep-sea turbidite characterisation in Poverty Bay, New Zealand. *Natural Hazards and Earth System Science*, 12(6):2077–2101. 4, 37, 70, 94, 127, 138, 139, 201
- Pouderoux, H., Proust, J.-N., and Lamarche, G. (2014). Submarine paleoseismology of the northern hikurangi subduction margin of new zealand as deduced from turbidite record since 16 ka. *Quaternary Science Reviews*, 84:116–131. 127, 138, 140, 176, 201
- Puig, P., Ogston, A., Mullenbach, B., Nittrouer, C., Parsons, J., and Sternberg, R. (2004). Storm-induced sediment gravity flows at the head of the eel submarine canyon, northern california margin. *Journal of Geophysical Research: Oceans (1978–2012)*, 109(C3). 70
- Radakovitch, O., Charmasson, S., Arnaud, M., and Bouisset, P. (1999). ²¹⁰Pb and caesium accumulation in the rhône delta sediments. *Estuarine, Coastal and Shelf Science*, 48(1):77–92. 98, 111
- Ramsey, C. B. (2008). Deposition models for chronological records. *Quaternary Science Reviews*, 27(1):42–60. XX, XXV, 132, 150, 157
- Ramsey, L. a., Hovius, N., Lague, D., and Liu, C.-S. (2006). Topographic characteristics of the submarine Taiwan orogen. *Journal of Geophysical Research*, 111(F2):1–21. XXV, 9, 57, 62, 67, 75, 76, 168
- Ratzov, G., Collot, J.-Y., Sosson, M., and Migeon, S. (2010). Mass-transport deposits in the northern ecuador subduction trench: Result of frontal erosion over multiple seismic cycles. *Earth and Planetary Science Letters*, 296(1):89–102. 4

- Reading, H. G. and Richards, M. (1994). Turbidite systems in deep-water basin margins classified by grain size and feeder system. *AAPG bulletin*, 78(5):792–822. 30
- Reimer, P. and McCormac, F. (2002). Marine radiocarbon reservoir corrections for the mediterranean and aegean seas. *Radiocarbon*, 44(1):159–166. 101, 108
- Reimer, P. J., Baillie, M. G., Bard, E., Bayliss, A., Beck, J. W., Bertrand, C. J., Blackwell, P. G., Buck, C. E., Burr, G. S., Cutler, K. B., et al. (2004). Intcal04 terrestrial radiocarbon age calibration, 0–26 cal kyr bp. *Radiocarbon*, 46:1029–1058. 112
- Reimer, P. J., Bard, E., Bayliss, A., Beck, J. W., Blackwell, P. G., Ramsey, C. B., Buck, C. E., Cheng, H., Edwards, R. L., Friedrich, M., et al. (2013). Intcal13 and marine13 radiocarbon age calibration curves 0–50,000 years cal bp. *Radiocarbon*, 55(4):1869–1887. 100, 102, 132
- Reimer, P. J. and Reimer, R. W. (2001). A marine reservoir correction database and on-line interface. *Radiocarbon*, 43(2; PART A):461–464. 108
- Repetti, W. C. (1946). Catalogue of philippine earthquakes, 1589–1899. *Bulletin of the Seismological Society of America*, 36(3):133–322. 169
- Robbins, J. A. and Edgington, D. N. (1975). Determination of recent sedimentation rates in lake michigan using pb-210 and cs-137. *Geochimica et Cosmochimica Acta*, 39(3):285–304. 98, 107, 110
- Rodine, J. D. and Johnson, A. M. (1976). The ability of debris, heavily freighted with coarse clastic materials, to flow on gentle slopes. *Sedimentology*, 23(2):213–234. 24
- Sabatier, P. (2009). *Reconstitution des évènements climatiques extrêmes (crues et tempêtes) au cours de l'Holocène dans le Golfe d'Aigues-Mortes (Sud de la France)*. PhD thesis, Université de Montpellier 2. XVII, 98
- Sabatier, P., Dezileau, L., Blanchemanche, P., Siant, G., Condomines, M., Bentaleb, I., and Piquès, G. (2010). Holocene variations of radiocarbon reservoir ages in a mediterranean lagoonal system. *Radiocarbon*, 52(1):91. 101, 113, 175
- Schneider, J.-L., Le Ruyet, A., Chanier, F., Buret, C., Ferrière, J., Proust, J.-N., and Rosseel, J.-B. (2001). Primary or secondary distal volcanoclastic turbidites: how to make the distinction? an example from the miocene of new zealand (mahia peninsula, north island). *Sedimentary Geology*, 145(1):1–22. 70

- Schnurle, P., Liu, C.-S., Lallemand, S., and Reed, D. (1998). Structural controls of the taitung canyon in the huatung basin east of taiwan. *Terr. Atmos. Oceanic Sci*, 9:453–473. 59, 68
- Schnürle, P., Liu, C.-S., Lallemand, S. E., and Reed, D. L. (1998b). Structural insight into the south ryukyu margin: Effects of the subducting gagua ridge. *Tectonophysics*, 288(1):237–250. XXV, 75, 76
- Seno, T., Stein, S., and Gripp, A. E. (1993). A model for the motion of the philippine sea plate consistent with nuvel-1 and geological data. *Journal of Geophysical Research: Solid Earth (1978–2012)*, 98(B10):17941–17948. XIII, 6, 7, 55, 107
- Shanmugam, G. (2000). 50 years of the turbidite paradigm (1950s—1990s): deep-water processes and facies models—a critical perspective. *Marine and Petroleum Geology*, 17(2):285–342. XIV, 30
- Shanmugam, G. (2003). Deep-marine tidal bottom currents and their reworked sands in modern and ancient submarine canyons. *Marine and Petroleum Geology*, 20(5):471–491. XIV, 22
- Shanmugam, G. (2006). The tsunamite problem. *Journal of Sedimentary Research*, 76(5):718–730. 70
- Shanmugam, G., Lehtonen, L. R., Straume, T., Syvertsen, S. E., Hodgkinson, R. J., and Skibeli, M. (1994). Slump and debris-flow dominated upper slope facies in the cretaceous of the norwegian and northern north seas (61-67 n): implications for sand distribution. *AAPG bulletin*, 78(6):910–937. XIV, 27, 29
- Shepard, F. P. and Dill, R. F. (1966). Submarine canyons and other sea valleys. 70
- Shiki, T., Kumon, F., Inouchi, Y., Kontani, Y., Sakamoto, T., Tateishi, M., Matsubara, H., and Fukuyama, K. (2000). Sedimentary features of the seismo-turbidites, lake biwa, japan. *Sedimentary Geology*, 135(1):37–50. 93, 127
- Siame, L., Angelier, J., Chen, R.-F., Godard, V., Derrieux, F., Bourlès, D., Braucher, R., Chang, K.-J., Chu, H.-T., and Lee, J.-C. (2011). Erosion rates in an active orogen (ne-taiwan): A confrontation of cosmogenic measurements with river suspended loads. *Quaternary Geochronology*, 6(2):246–260. 9

- Siani, G., Paterne, M., Michel, E., Sulpizio, R., Sbrana, A., Arnold, M., and Haddad, G. (2001). Mediterranean sea surface radiocarbon reservoir age changes since the last glacial maximum. *Science*, 294(5548):1917–1920. 101, 108
- Sibuet, J.-C., Hsu, S.-K., and Normand, A. (2004). Tectonic significance of the taitung canyon, huatung basin, east of taiwan. *Marine Geophysical Researches*, 25(1-2):95–107. 68
- Southon, J., Kashgarian, M., Fontugne, M., Metivier, B., and Yim, W. W. (2002). Marine reservoir corrections for the indian ocean and southeast asia. *Radiocarbon*, 44(1):167–180. 101, 108
- St-Onge, G., Mulder, T., Piper, D. J., Hillaire-Marcel, C., and Stoner, J. S. (2004a). Earthquake and flood-induced turbidites in the saguenay fjord (québec): a holocene paleoseismicity record. *Quaternary Science Reviews*, 23(3):283–294. 70
- St-Onge, G., Mulder, T., Piper, D. J., Hillaire-Marcel, C., and Stoner, J. S. (2004b). Earthquake and flood-induced turbidites in the saguenay fjord (québec): a holocene paleoseismicity record. *Quaternary Science Reviews*, 23(3):283–294. 127
- Stow, D., Reading, H., and Collinson, J. (1996). Deep seas. *Sedimentary environments: processes, facies and stratigraphy*, 3:395–453. XIV, 21, 23
- Stow, D. A., Howell, D. G., and Nelson, C. H. (1985). Sedimentary, tectonic, and sea-level controls. In *Submarine fans and related turbidite systems*, pages 15–22. Springer. 33
- Stow, D. A. and Shanmugam, G. (1980). Sequence of structures in fine-grained turbidites: comparison of recent deep-sea and ancient flysch sediments. *Sedimentary Geology*, 25(1):23–42. XIV, 26, 64, 65
- Strasser, M., Anselmetti, F. S., Fäh, D., Giardini, D., and Schnellmann, M. (2006). Magnitudes and source areas of large prehistoric northern alpine earthquakes revealed by slope failures in lakes. *Geology*, 34(12):1005–1008. 127
- Strasser, M., Moore, G. F., Kimura, G., Kopf, A. J., Underwood, M. B., Guo, J., and Screatton, E. J. (2011). Slumping and mass transport deposition in the nankai fore arc: Evidence from iodp drilling and 3-d reflection seismic data. *Geochemistry, Geophysics, Geosystems*, 12(5):1–24. 67

- Strasser, M., Stegmann, S., Bussmann, F., Anselmetti, F. S., Rick, B., and Kopf, A. (2007). Quantifying subaqueous slope stability during seismic shaking: Lake lucerne as model for ocean margins. *Marine Geology*, 240(1):77–97. 37
- Stuiver, M. and Braziunas, T. F. (1993). Modeling atmospheric ^{14}C influences and ^{14}C ages of marine samples to 10,000 bc. *Radiocarbon*, 35:137–137. 101, 108
- Stuiver, M. and Reimer, P. J. (1986). A computer program for radiocarbon age calibration. *Radiocarbon*, 28(2B):1022–1030. 101
- Suppe, J. (1984). Kinematics of arc-continent collision, flipping of subduction, and back-arc spreading near taiwan. *Mem. Geol. Soc. China*, 6:21–33. 5, 55, 107
- Swarzenski, P., Reich, C., Spechler, R., Kindinger, J., and Moore, W. (2001). Using multiple geochemical tracers to characterize the hydrogeology of the submarine spring off crescent beach, florida. *Chemical Geology*, 179(1):187–202. 175
- Theunissen, T., Font, Y., Lallemand, S., and Liang, W.-T. (2010). The largest instrumentally recorded earthquake in Taiwan: revised location and magnitude, and tectonic significance of the 1920 event. *Geophysical Journal International*, 183(3):1119–1133. XXV, 11, 14, 39, 57, 62, 107, 129, 140, 145, 169
- Tisnérat-Laborde, N., Poupeau, J., Tannau, J., and Paterne, M. (2001). Development of a semi-automated system for routine preparation of carbonate samples. *Radiocarbon*, 43(2; PART A):299–304. 108
- Traykovski, P., Wiberg, P. L., and Geyer, W. R. (2007). Observations and modeling of wave-supported sediment gravity flows on the po prodelta and comparison to prior observations from the eel shelf. *Continental Shelf Research*, 27(3):375–399. 177
- Tsai, Y., Teng, T., Chiu, J., and Liu, H. (1977). Tectonic implications of the seismicity in the taiwan region. *Mem. Geol. Soc. China*, 2:13–41. 129
- Tsou, C.-Y., Feng, Z.-Y., and Chigira, M. (2011). Catastrophic landslide induced by typhoon morakot, shiaolin, taiwan. *Geomorphology*, 127(3):166–178. 10, 56
- Ulses, C., Estournel, C., Puig, P., Durrieu de Madron, X., and Marsaleix, P. (2008). Dense shelf water cascading in the northwestern mediterranean during the cold winter 2005: Quantifi-

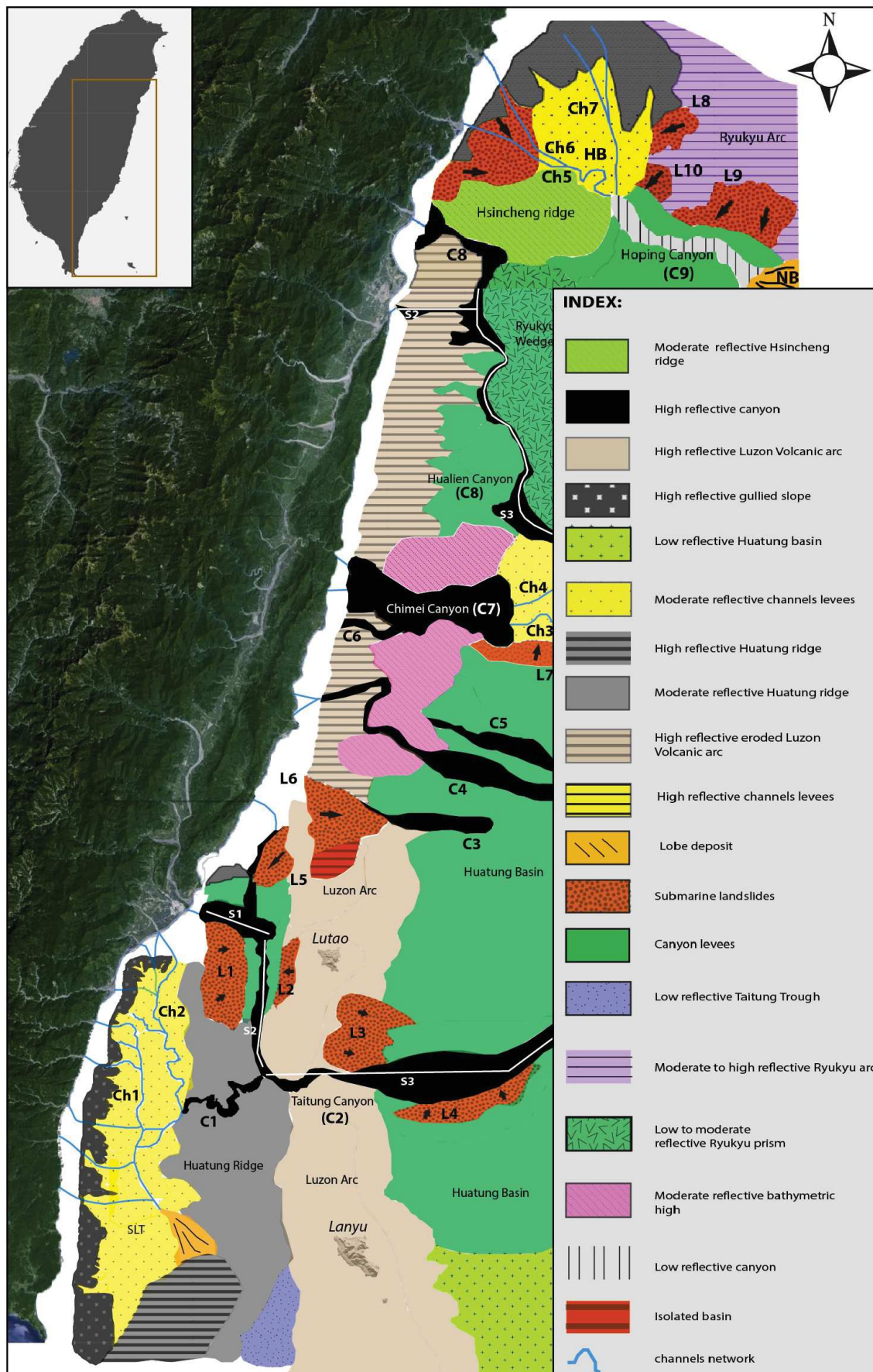
- cation of the export through the gulf of lion and the catalan margin. *Geophysical Research Letters*, 35(7). 182
- Wang, C.-H. and Burnett, W. C. (1990). Holocene mean uplift rates across an active plate-collision boundary in taiwan. *Science*, 248(4952):204–206. 9
- Wang, T. K. and Chiang, C.-H. (1998). Imaging of arc-arc collision in the ryukyu forearc region offshore hualien from taicrust obs line 16. *Terr. Atmos. Ocean. Sci*, 9(3):329–344. XXV, 75, 76
- Wang, T. K., Lin, S.-F., Liu, C.-S., and Wang, C.-S. (2004). Crustal structure of the southernmost ryukyu subduction zone: Obs, mcs and gravity modelling. *Geophysical Journal International*, 157(1):147–163. XXV, 75, 76
- Watts, P. (2002). Topics v1.2, (a component of geowave). *courtesy of Applied Fluids*. 179
- Wei, K.-Y. (2006). Leg 195 synthesis: Site 1202ólate quaternary sedimentation and paleoceanography in the southern okinawa trough. In *Proceedings of the Ocean Drilling Program, Scientific Results*, volume 195, pages 1–31. 181
- Wu, C.-C., Kuo, Y.-H., et al. (1999). Typhoons affecting taiwan: Current understanding and future challenges. *Bull. Am. Meteorol. Soc*, 80(1):67–80. 9, 56
- Wu, C.-H., Chen, S.-C., and Chou, H.-T. (2011). Geomorphologic characteristics of catastrophic landslides during typhoon morakot in the kaoping watershed, taiwan. *Engineering Geology*, 123(1–2):13 – 21. 10, 56
- Wu, F. T. (1978). Recent tectonics of taiwan. *Journal of Physics of the Earth*, 26(Supplement):S265–S299. 129
- Wu, F. T., Liang, W.-T., Lee, J.-C., Benz, H., and Villasenor, A. (2009). A model for the termination of the ryukyu subduction zone against taiwan: A junction of collision, subduction/separation, and subduction boundaries. *Journal of Geophysical Research: Solid Earth (1978–2012)*, 114(B7). 62
- Wu, W.-N., Kao, H., Hsu, S.-K., Lo, C.-L., and Chen, H.-W. (2010). Spatial variation of the crustal stress field along the ryukyu-taiwan-luzon convergent boundary. *Journal of Geophysical Research: Solid Earth (1978–2012)*, 115(B11). 127

- Wu, Y.-M., Chang, C.-H., Zhao, L., Teng, T.-L., and Nakamura, M. (2008). A comprehensive relocation of earthquakes in taiwan from 1991 to 2005. *Bulletin of the Seismological Society of America*, 98(3):1471–1481. XXV, 14, 145
- Yoneda, M., Uno, H., Shibata, Y., Suzuki, R., Kumamoto, Y., Yoshida, K., Sasaki, T., Suzuki, A., and Kawahata, H. (2007). Radiocarbon marine reservoir ages in the western pacific estimated by pre-bomb molluscan shells. *Nuclear Instruments and Methods in Physics Research Section B: Beam Interactions with Materials and Atoms*, 259(1):432–437. XVIII, XIX, XXV, 101, 102, 112, 113, 114, 121, 132, 147, 174
- Yu, K., Hua, Q., Zhao, J.-x., Hodge, E., Fink, D., and Barbetti, M. (2010). Holocene marine 14c reservoir age variability: Evidence from 230th-dated corals in the south china sea. *Paleoceanography*, 25(3). 112, 113, 132
- Yu, S.-B., Chen, H.-Y., and Kuo, L.-C. (1997). Velocity field of gps stations in the taiwan area. *Tectonophysics*, 274(1):41–59. 129
- Zhou, Q. and Adams, W. (1985). Tsunamigenic earthquakes in china 1831 b.c. - 1980 a.d. *Extended abstract in International Tsunami Symposium, Victoria, BC, Canada*, pages 543–550. 169

Appendices

Morphosedimentary facies map offshore
east Taiwan

Figure A.1: Morphosedimentary facies map offshore eastern Taiwan based on imagery, bathymetry and seismic data



APPENDIX B

Technical sheets

Technical sheet I

-The Box-corer



Cable

Box full of sediment

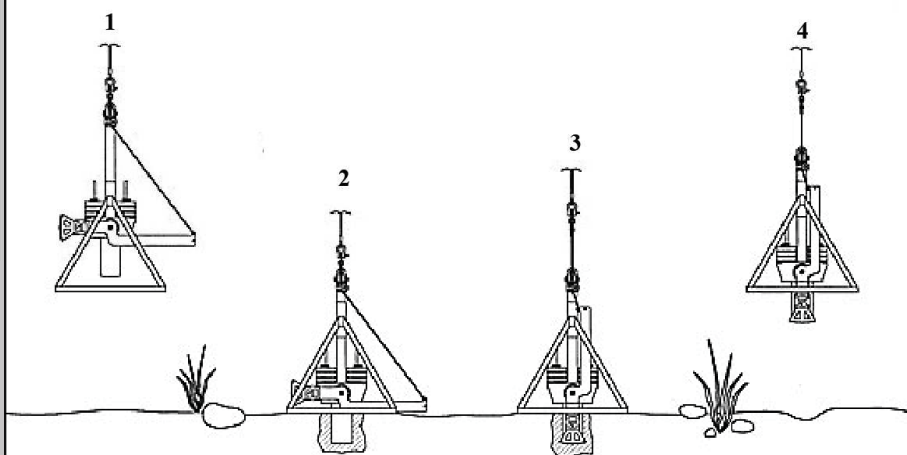
Metallic support frame

A box-corer can provide the best quality samples from among the various sampling devices, but it tends to have very little penetration, resulting in relatively limited length samples. Instead of using a tube with a circular cross-section, the sampler consists of a square or rectangular cross-section, and the samplers are available in many sizes. A support frame guides the box to the seafloor where it is hydraulically pushed locally. For retrieval, a pulley system may be used to help bring the sample above the water's surface. Covers at the top and a blade at the bottom prevent the contents from spilling during the recovery.



Pictures from the Box-corer and box-cores collected at site KS06 during the OR1-1013 survey. Photos from R. Lehu

Principle of the Box-corer:



1. The box-corer is lowered toward the sea-floor
2. At the sea-floor the box penetrates into the sediment
3. The main cable is redrawn and the closing grab goes into position beneath the box
4. The box-corer is on its way up to the ship with the secured sample inside the box

Figure B.1: Principle of the Box-Corer

-The Kullenberg corer: Gravity and piston corer

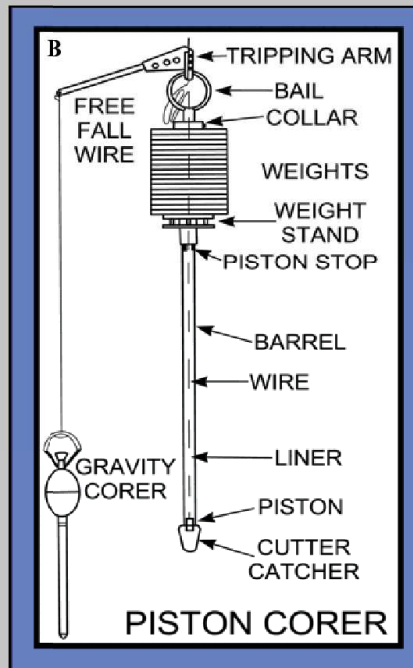
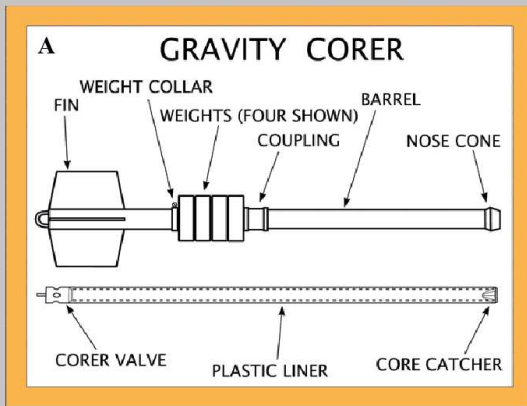


A gravity corer (A) is the most basic of all the sediment core samplers because it is merely a tube that is weighted at the top. Due to the simple design, the gravity corer can sample nearly any depth of water. Gravity corer is used through the free fall to penetrate the soil. The weight provides assistance to the plummet, helping the tube to penetrate deeper. Unfortunately, recovered samples tend to be shorter due to the restricted penetration depth. Also, since the sampler penetrates under gravity alone (i.e., without mechanical push assistance), the layers of sediment may be disturbed from the frictional compression of the tube and water may be able to escape

Pictures from the Kullenberg during the OR1-1013 survey. Photos from R. Lehu



Orange peel closing system prevents the sample from exit.

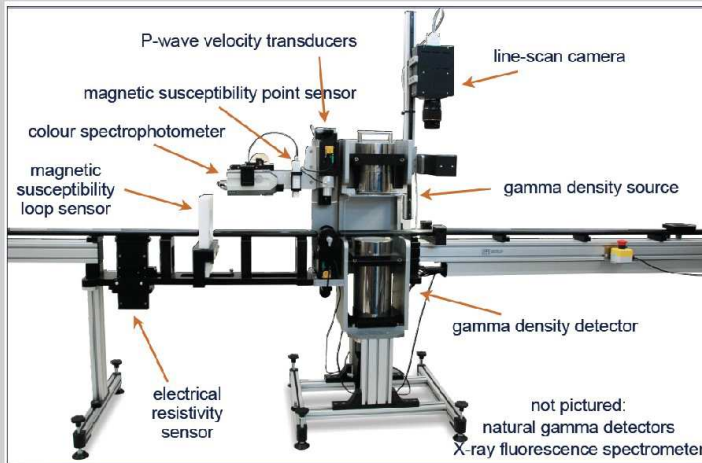


For better penetration depth, the piston corer is used (B). Composed of a tube with an internal piston, the sampler is pressed onto the seabed, either manually or hydraulically. The tube penetrates the sediment while the piston remains on top of the seabed. During sample retrieval, the piston, along with a cable, helps pull the core from the sediment and back to the surface. The sample is usually of good quality because there isn't as much frictional compression as in the gravity corer; however, the top layer of soil can be damaged due to the force the piston applies to the seabed surface during extraction.

Figure B.2: Principle of the Piston and Gravity-Corer

Technical sheet II

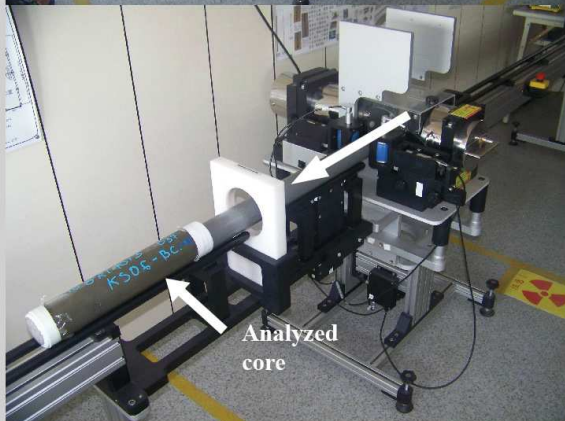
-The Multi Sensor Core Logger (Geotek)



The Multi Sensor Core Logger (MSCL) is an non-destructive analysis. Measurements on sedimentary and rock cores provide a large panel of high-resolution petrophysical parameters (e.g. gamma density, P-wave, velocity, magnetic susceptibility etc.). Measurements are used for the values within the sediments or as a proxies for changes in sedimentary facies, lithology or formation environment. The MSCL accepts a wide range of cores sizes, and is usable on both split whole cores. Once system correctly set up according to the core type and calibrated, user interaction with the machine consists of placing individual core sections on one end of the track and by removing them from the other.



-MCSL in split core configuration-



-MCSL in whole core configuration-



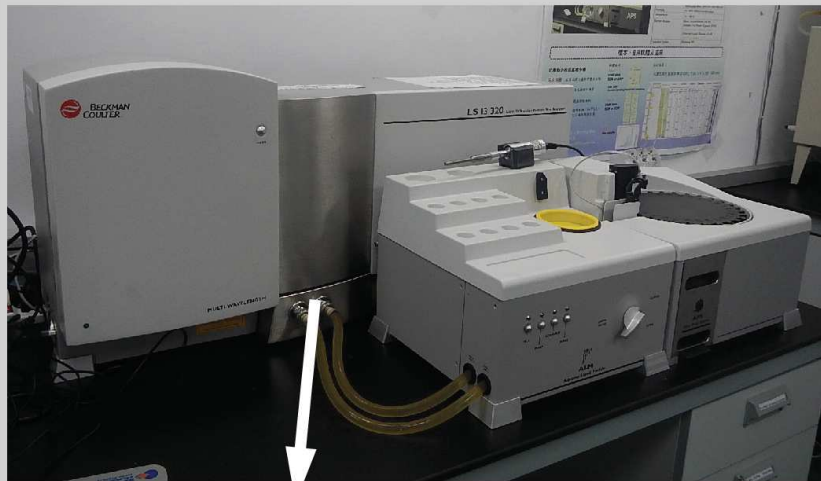
Magnetic susceptibility point sensor (on split core)

Pictures from the Geotek MSCL used for this study. Photos taken in Changwa bore-hole site, Taiwan (Photos from R. Lehu)

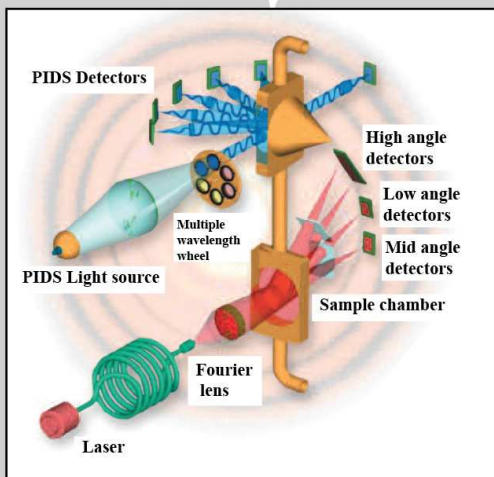
Figure B.3: Principle of the Geotek Multi Sensor Core Logger

Technical sheet III

- Grain size analyzer (Beckman-Coulter LS13-320)



The Laser Diffraction Particle Analyzers measure particle size using the theory of the light scattering. The analyzer provides size distribution in volume, number and surface area in one measurement. The sizes of measured particle range from 17 nanometers to 2000 micrometers. Sediments are transported by the water from the ALM (Aqueous Liquid Module) to the analysis cells.

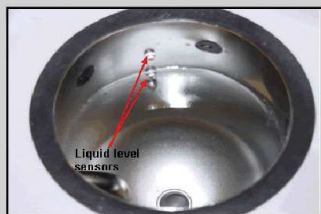


The scattering of light is one of the most widely used techniques for measuring the size distribution of particles. The basis of the method is simple: a laser light source is used to illuminate particulates, usually contained within a suitable sample cell. The light scatter by the particles is then detected by silicon photo-detectors. The intensity of light on each detector measured as a function of angle, is then subjected to mathematical analysis using a complex inversion matrix algorithm. The result is a particle size distribution displayed as volume % in discrete size classes.

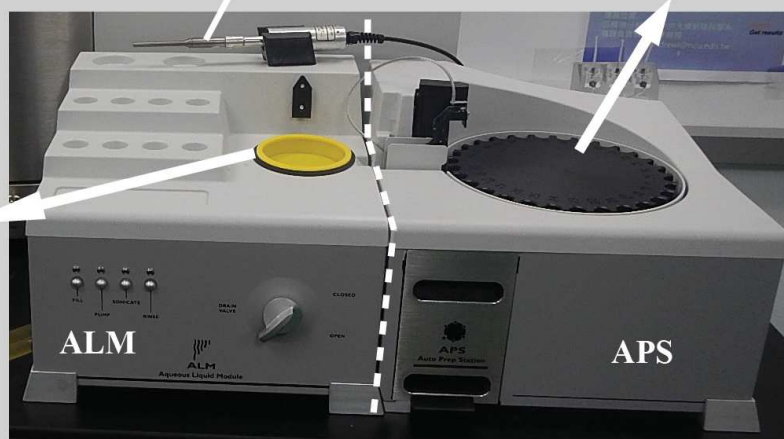
-Light scattering technique-

The sonicator is a tool use in the ALM to aid the dispersion of the sample in the water tank

The APS (Auto Preparation Station), is a module that permit to add a total of 30 samples.



-Water tank where sediments are dropped-



Pictures from the particle analyzer used for this study. Photos taken in Sedimentary Lab, NCU, Taiwan (Photos from R. Lehu)

Figure B.4: Principle of the Coulter LS13-320

Technical sheet IV

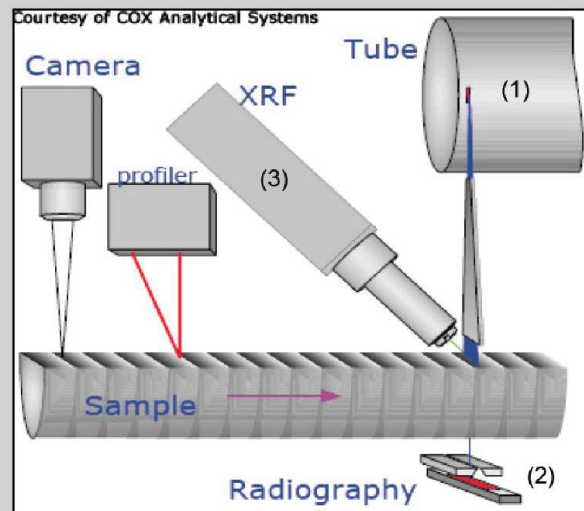
- ITRAX Core scanner



The ITRAX Core scanner, is a non destructive tool for the radiography and chemical analysis by microfluorescence X at high resolution of rocks and sediments.

The principle is based on the simultaneous acquisition of micro-variations of the density and the chemical composition of the sample using distinct X radiance systems. The analysis is undertaken without contact with the surface sediment and thus totally non destructive.

The maximum length of measurable sediment cores reaches 1.8 meters.



1) X-ray source: An intense source of X-rays is provided using a Molybdenum X-ray tube anode (maximum power load is 3 kW at 60 mA). These X-rays are squeezed through a flat-beam capillary optic that generates a beam with a rectangular cross-section of nominally 22 mm x 100 microns.

2) Microradiography: The transmitted X-rays are recorded with an array of 1024 diodes, each 25 microns wide. Successive radiographic lines are acquired strictly perpendicular to the core as the sample moves through the beam, therefore minimizing the blur and distortion that usually occur at the edges of classic radiography.

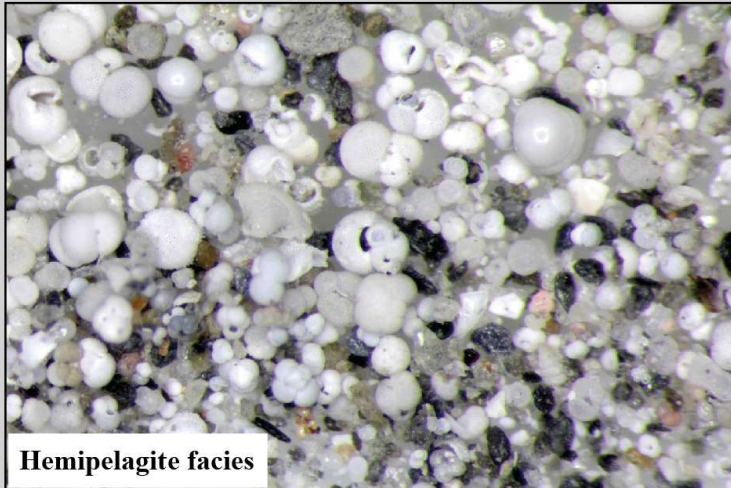
3) Chemical profiles along sediment samples are recorded for a broad range of elements. The concentrations of elements (from Si to U, for the Molybdenum tube) can be determined simultaneously, based on X-ray fluorescence. Most of these elements can be determined in concentrations down to 20 ppm depending on the element, analysis time and matrix composition.

Pictures from the ITRAX Core scanner used for this study. Photos taken in Sedimentary Lab, NTU, Taiwan (Photos from R. Lehu)

Figure B.5: Principle of the ITRAX Core scanner

Technical sheet V

-Foraminifera picking

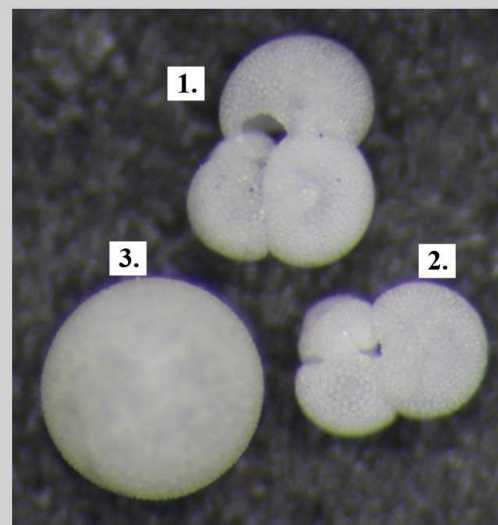
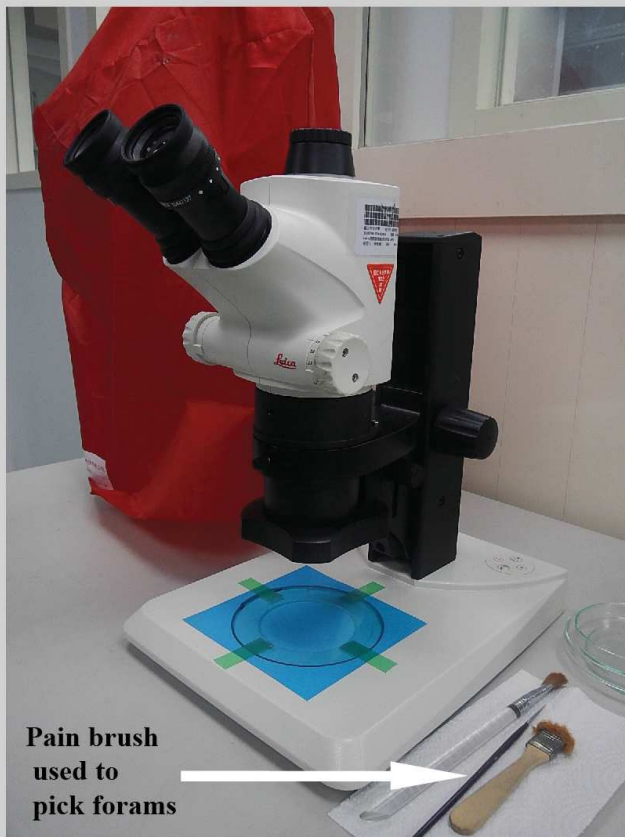


¹⁴C is based on the dating of carbaceous organisms. In the deep marine realm, the most common organism used for the dating are the planktonic foraminifera. They usually live near the oceans surface between 0 and 100m.

The samplings have been performed on hemipelagite layers on wet sieved 1-2cm thick samples.

The sample is then sieved on the 62 um fraction. Foraminifera are then isolated and handpicked using a binocular and fine brush (c.f picture). To avoid dating problem, it is recommended to pick foraminifera that belong to the same specy (e.g. Globigerinae) living at the same depth.

Between 400 and 600 specimens must be collected to reach the ~6-8mg required for the ¹⁴C dating.



Example of picked foraminifera:

- 1. Globigerina Ruber**
- 2. Globigerina Saculifer**
- 3. Universa Orbulina**

Pictures from taken in Sedimentary Lab, NCU, Taiwan (Photos from R. Lehu)

Figure B.6: Principle of the foraminifera picking

Coring site KS06: Morphology and core analysis

-SITE KS06- Luzon Volcanic Arc-

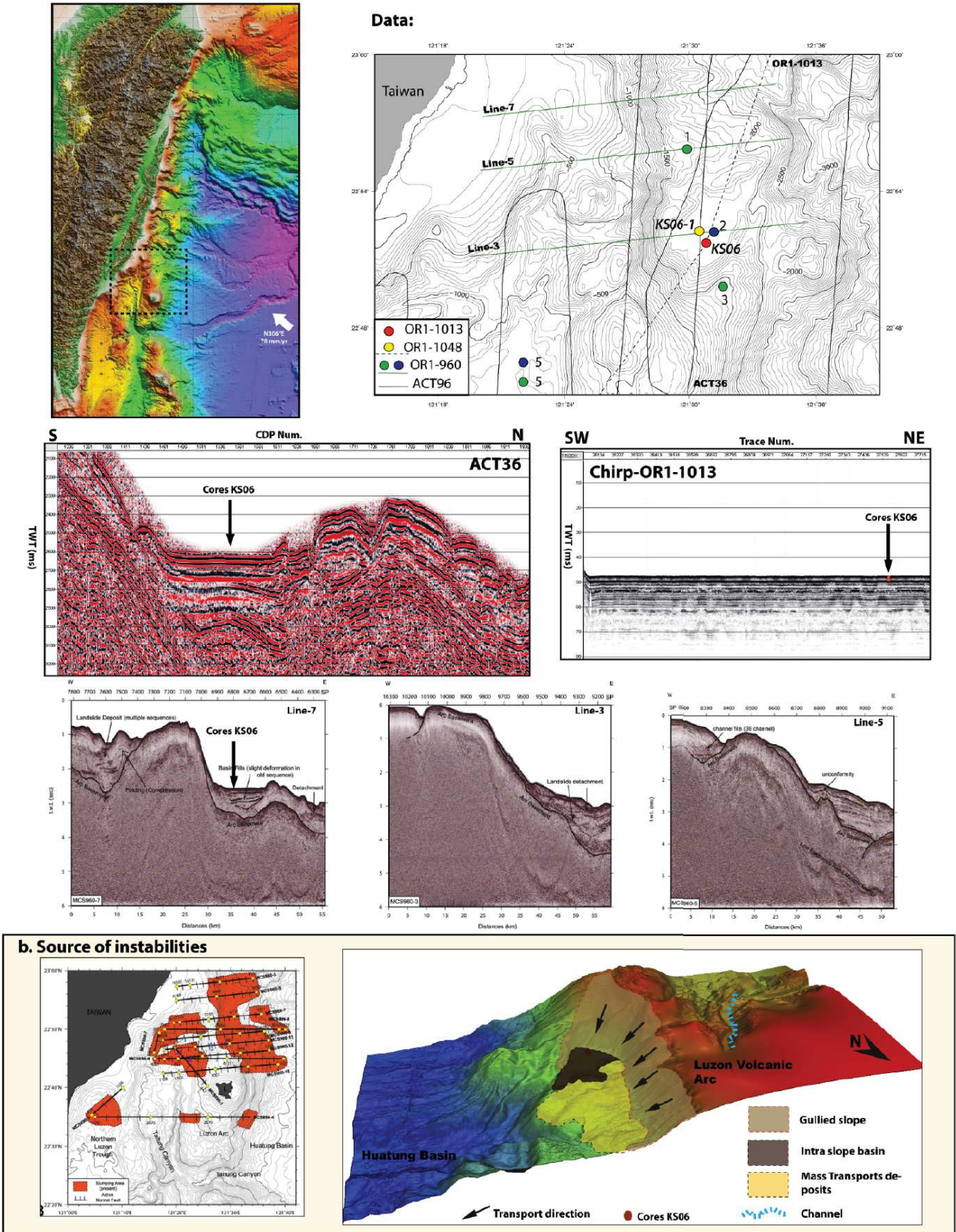
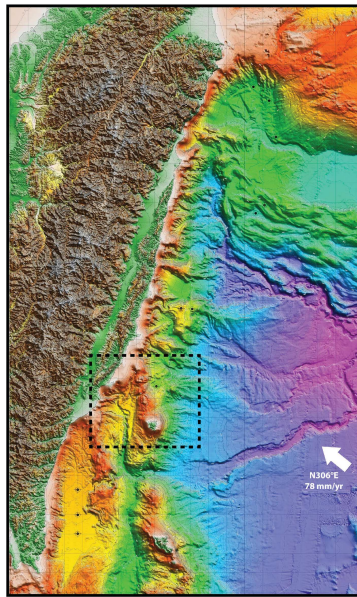
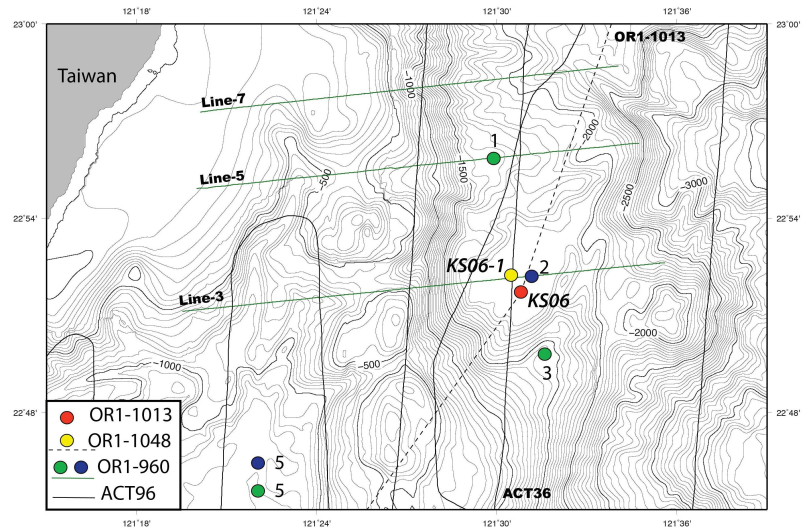


Figure C.1: Seismic, chirp profiles and source of instabilities.

-SITE KS06- Luzon Volcanic Arc-



Available data:



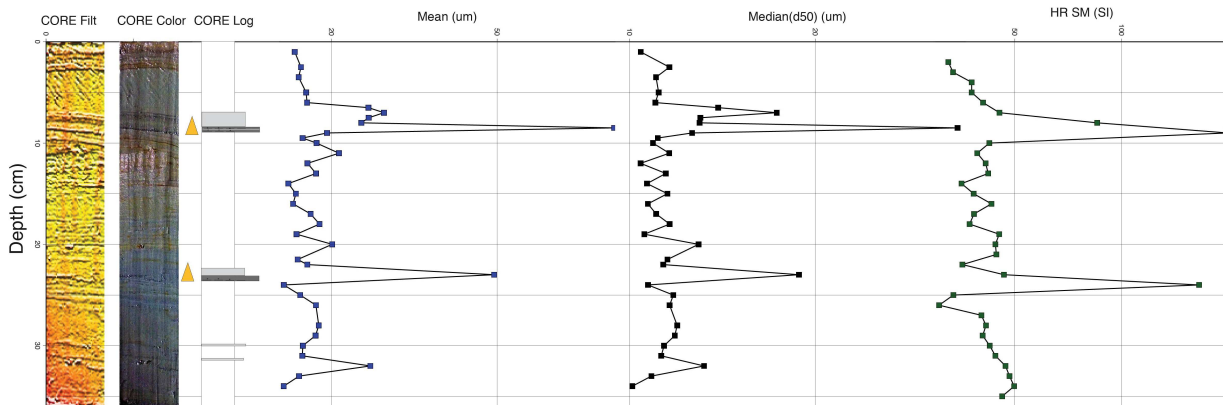
c. Cores Analysis

c.1. Characteristics

Core ID	Core Type	Area type	Longitude	Latitude	Depth (m)	Length (cm)
KS06P	Piston Core	Slope basin	121°30.6'	22°51.57'	1947	152
KS06B	Box-Core	Slope basin	121°30.6'	22°51.57'	1947	36
KS06G-1	Gravity Core	Slope basin	121°30.6'	22°51.57'	1947	212

c.2-Description-Log-GrainSize-MS.

-KS06B-



Observations:

- 0-8: Oxydated laminae
- 7-8cm: silty laminae, fine turbidite
- 8.5 to 22.5: homogeneous clay
- 22.5-23cm: silty laminae, not continuous Bioturbation?
- 23-36: Silty clay with 2 laminae more silty and not continue.
- 210Pb sampling each 1cm over the core

KEY:

- 210Pb Samples
- Erosive base
- Bioturbation
- Shell
- Shell fragment
- Vegetal fragment
- Foraminifers
- Turbidites

Figure C.2: Grain size analysis of KS06-B

Figure C.3: Grain size analysis of KS06-P

-SITE KS06- Luzon Volcanic Arc-

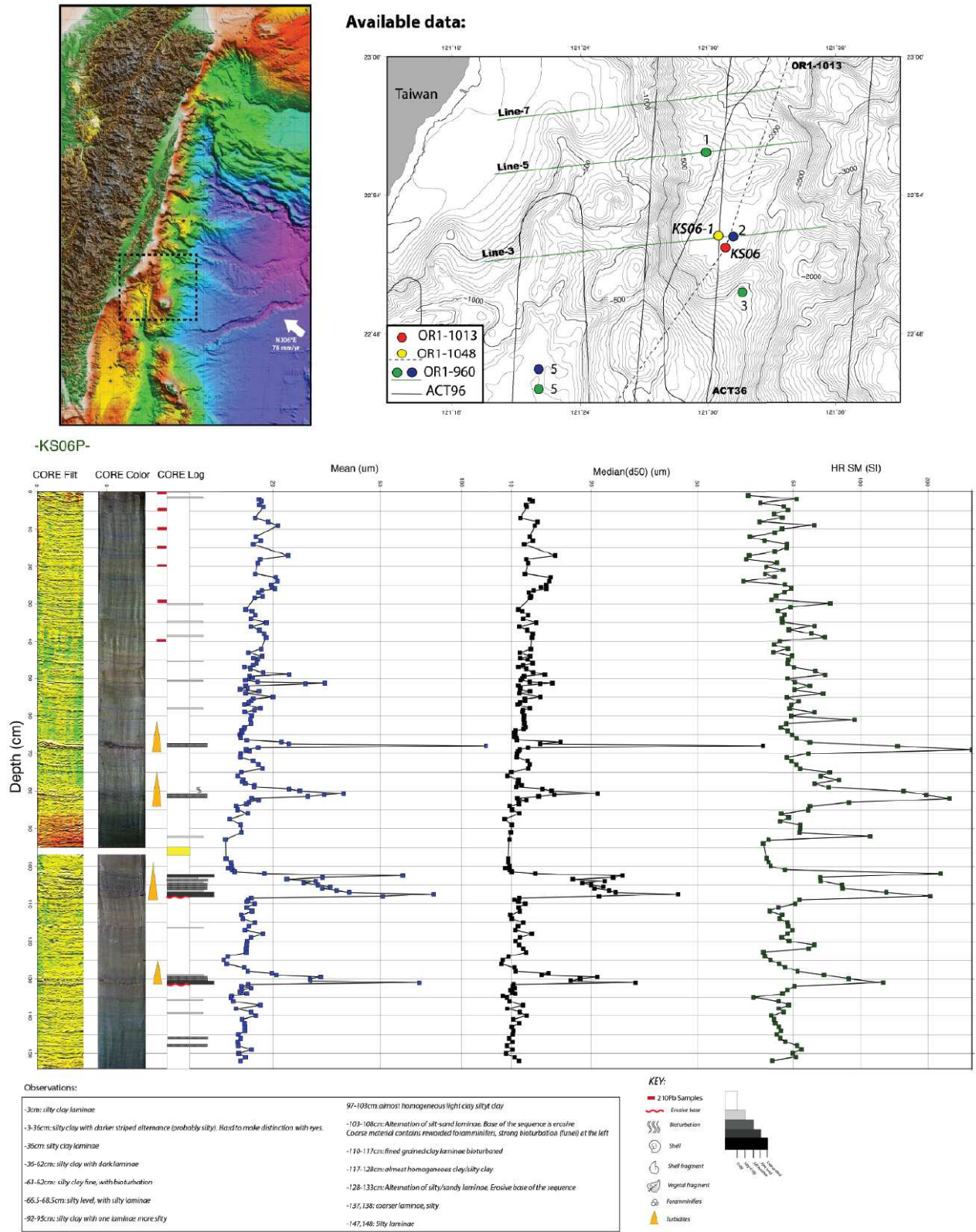
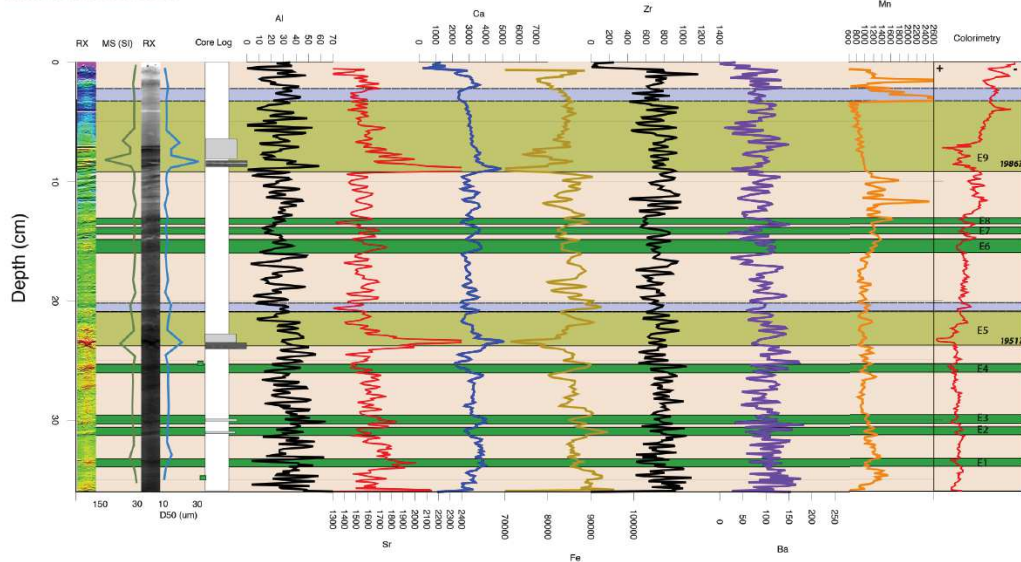


Figure C.4: XRF analysis of KS06-B and P

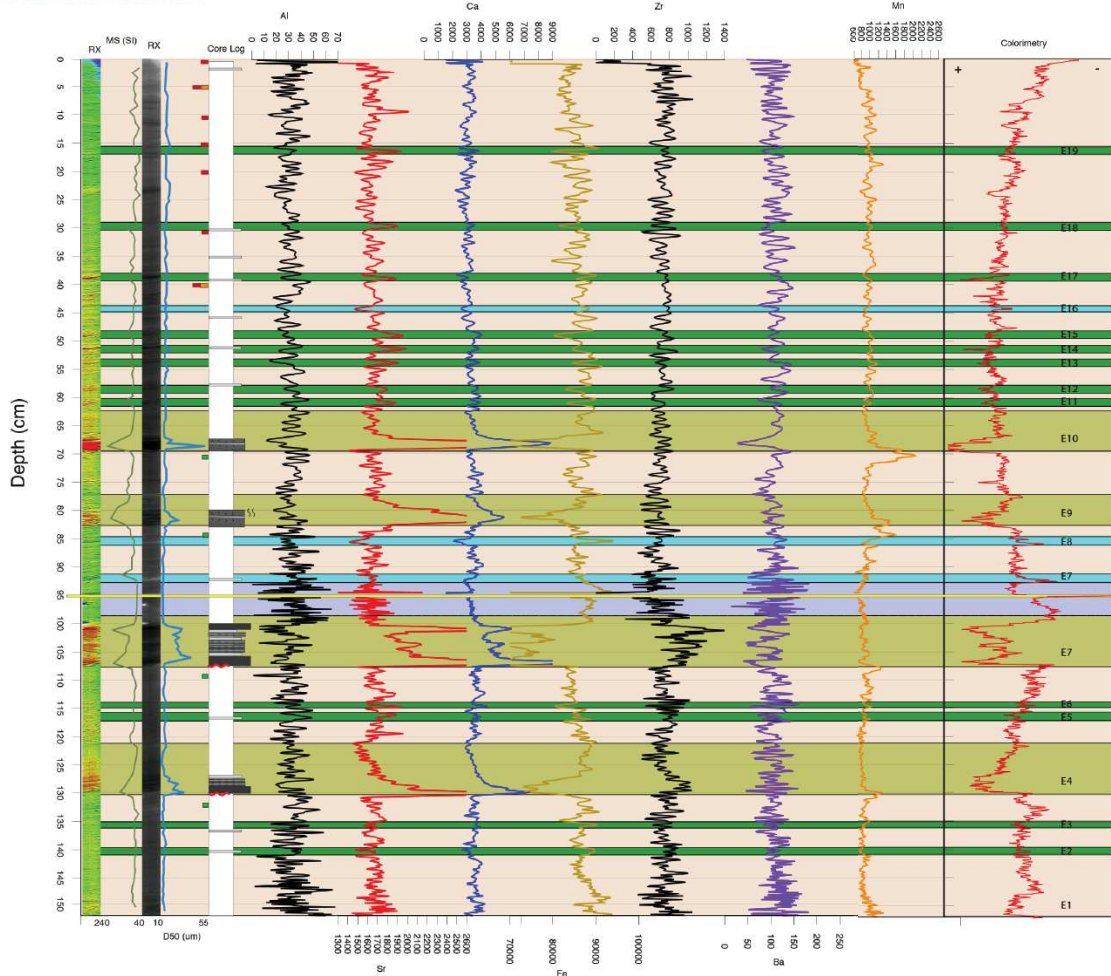
-SITE KS06- Luzon Volcanic Arc-

c.3-XRF data-

XRF data KS06-Box-Core



XRF data KS06-Piston Core



-SITE KS06- Luzon Volcanic Arc-

INDEX:

- Incertitude on the top of the sequence*
- High energy event identified as Turbidite sequence*
- Identified as Hemipelagite*
- Event non identified as Turbidite sequence*
- 14C samples sent for the 2nd batch*
- 14C samples sent for the 1st batch*
- 210Pb samples*
- E11 Event number*

Criteria of distinction between events:

Event	Colorimetry	Granulometry	Mag. Sus.	XRF	Type of event
	High	Graded	Sequence	Sr, Ca, Zr peaks	Turbidites
	High	No graded	No sequence	Sr, Ca, Fe peaks	Other
	Low	No graded	No sequence	Sr, Ca, Fe peaks	Other

Characterisation of turbidites:

KS06-Box-Core

Turbidites	Total thickness (cm)	Coarse unit (cm)	Tail (cm)	Sequence	Pulse	Base
E9	7+/-1	2	5+/-1	Truncated Bouma	2	Sharp, erosive
E5	4	1	3	Fining upward	1	Sharp, erosive

Zoom on turbidites-XR and XRF characterisation

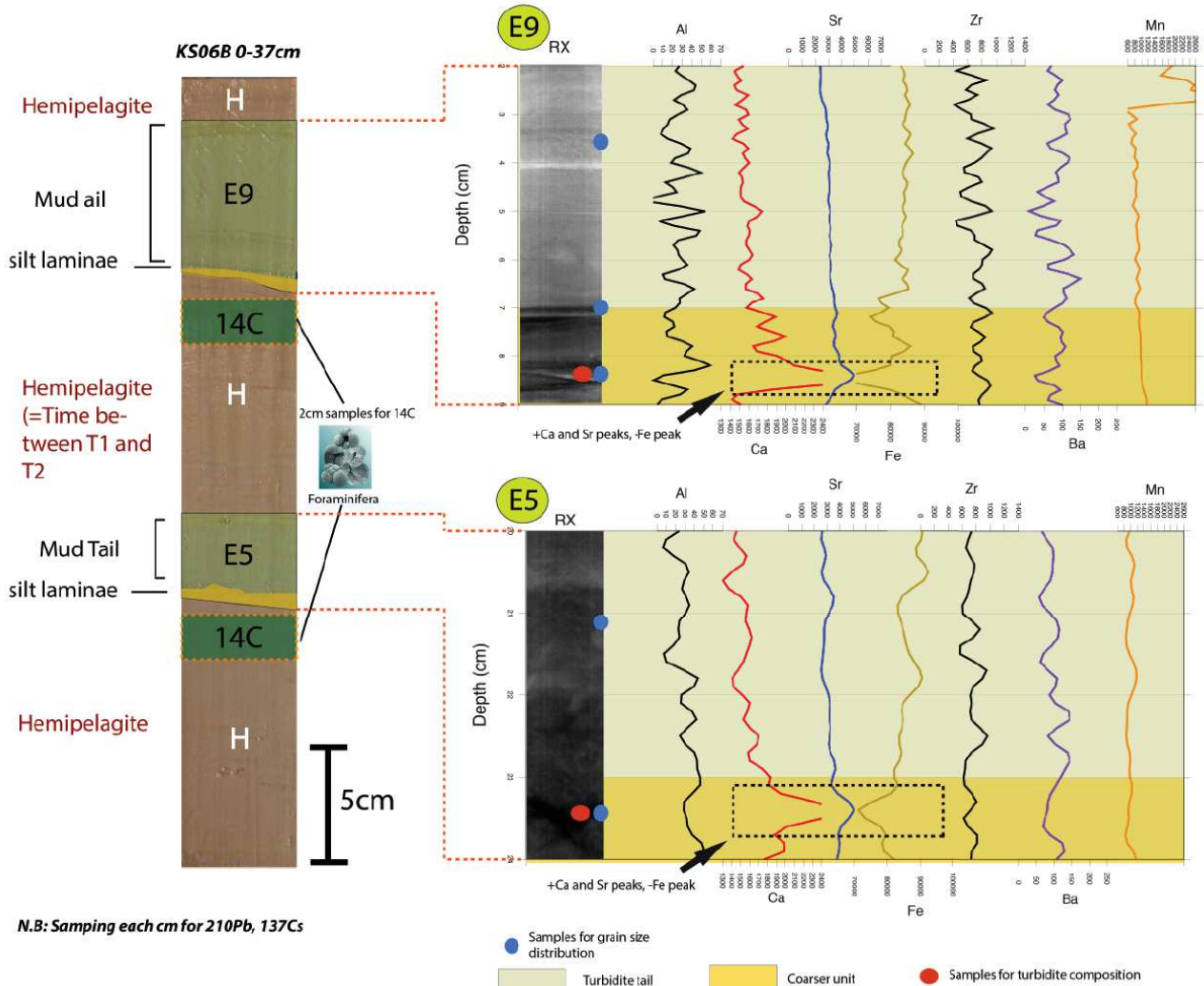


Figure C.5: Detailed analysis of turbidites layers-I

-SITE KS06- Luzon Volcanic Arc-

Characteristics of Turbidites from KS06 site:

KS06-Piston Core

Turbidites	Total thickness (cm)	Coarse unit (cm)	Tail (cm)	Sequence	Pulse	Base
E4	10	3	7	Truncated Bouma	3	Sharp, erosive
E7	15	7	8	Truncated Bouma	4	Sharp, erosive
E9	5	2.5	2.5	Fining upward	1	Sharp
E10	7	2	5	Truncated Bouma	2	Sharp

Zoom on turbidites-XR and XRF characterisation

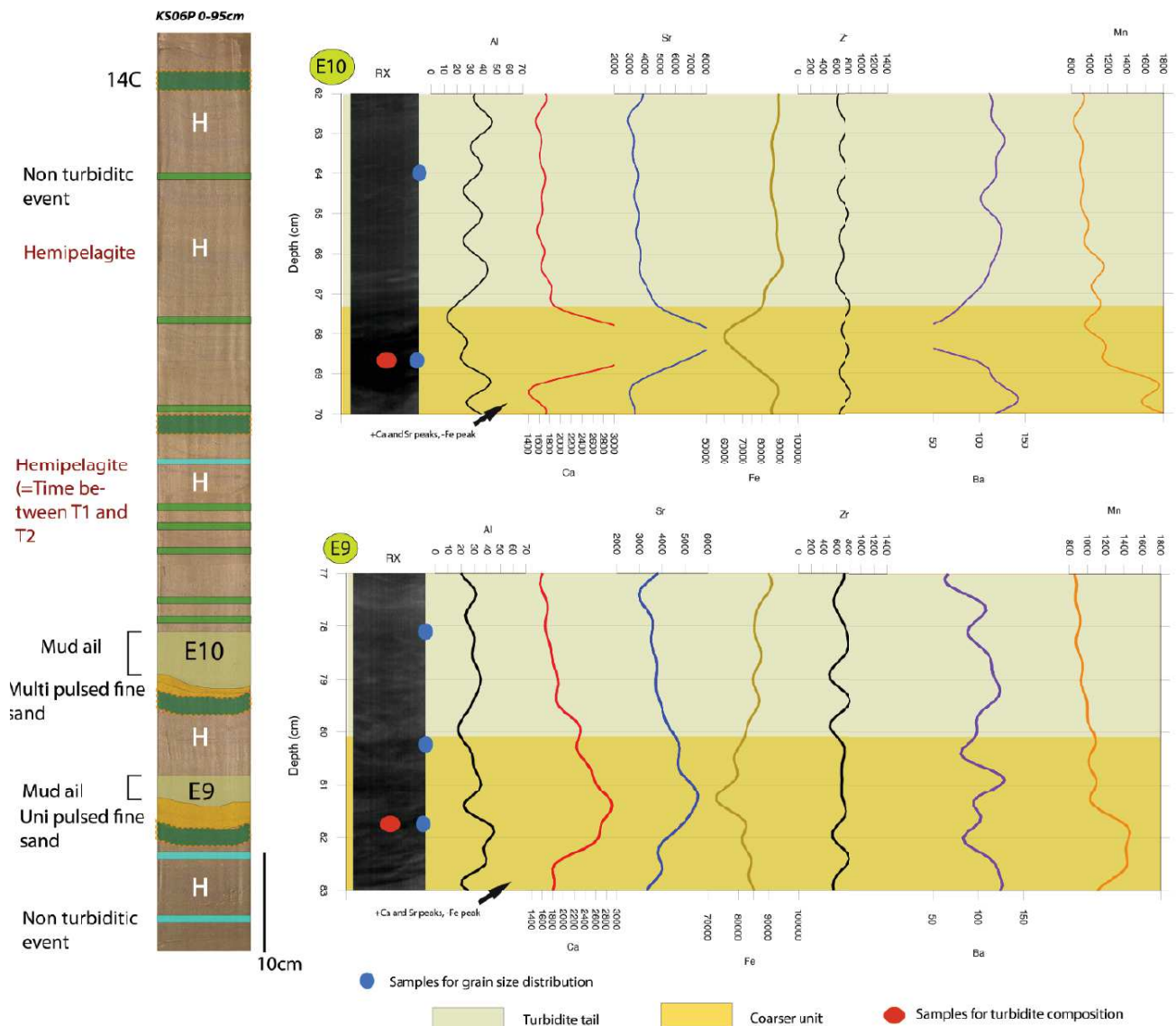


Figure C.6: Detailed analysis of turbidites layers-II

-SITE KS06- Luzon Volcanic Arc-

Characteristics of Turbidites from KS06 site:

KS06-Piston Core

Turbidites	Total thickness (cm)	Coarse unit (cm)	Tail (cm)	Sequence	Pulse	Base
E4	10	3	7	Truncated Bouma	3	Sharp, erosive
E7	15	7	8	Truncated Bouma	3	Sharp, erosive
E9	5	2.5	2.5	Fining upward	1	Sharp
E10	7	2	5	Truncated Bouma	2	Sharp

Zoom on turbidites-XR and XRF characterisation

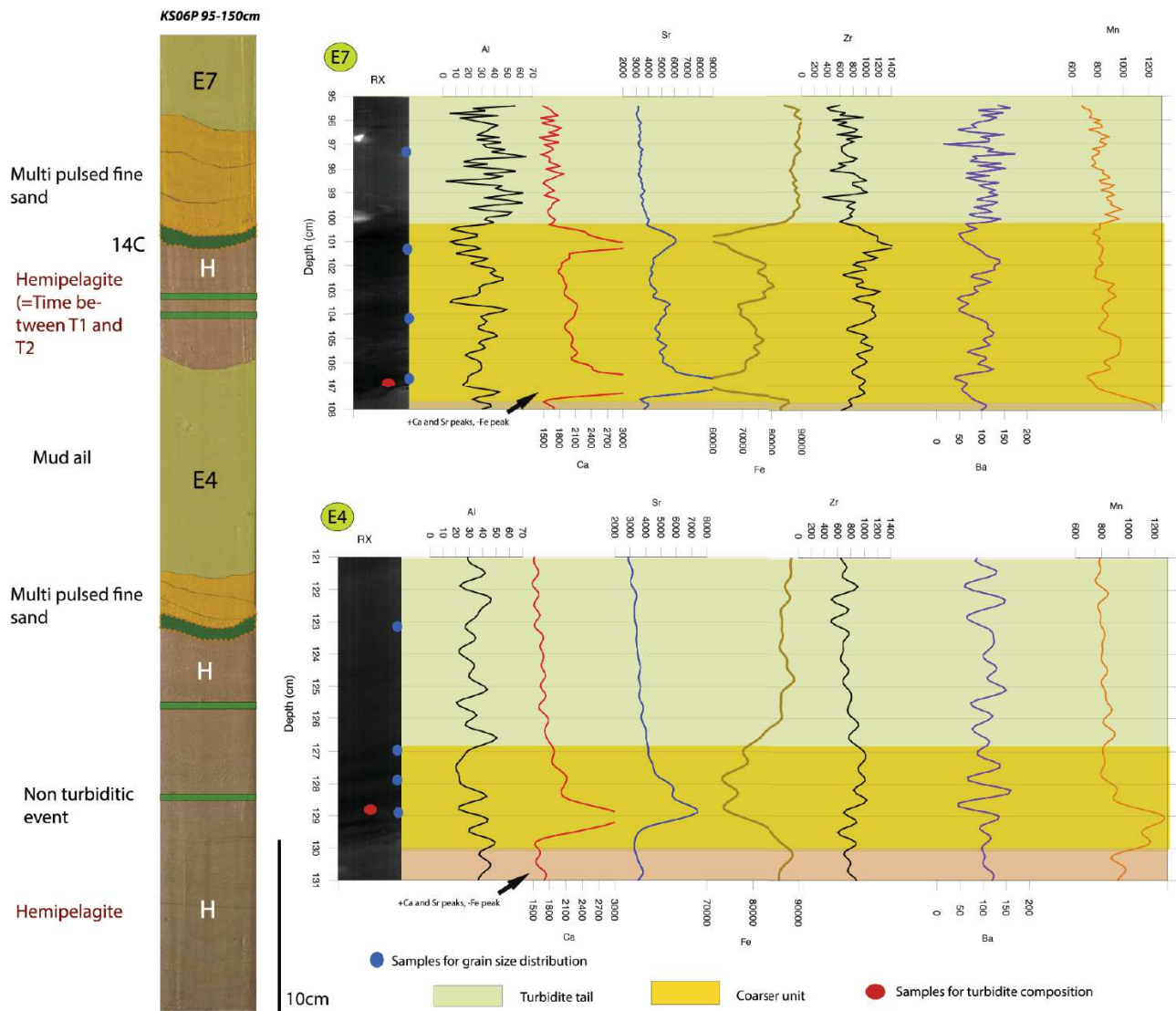
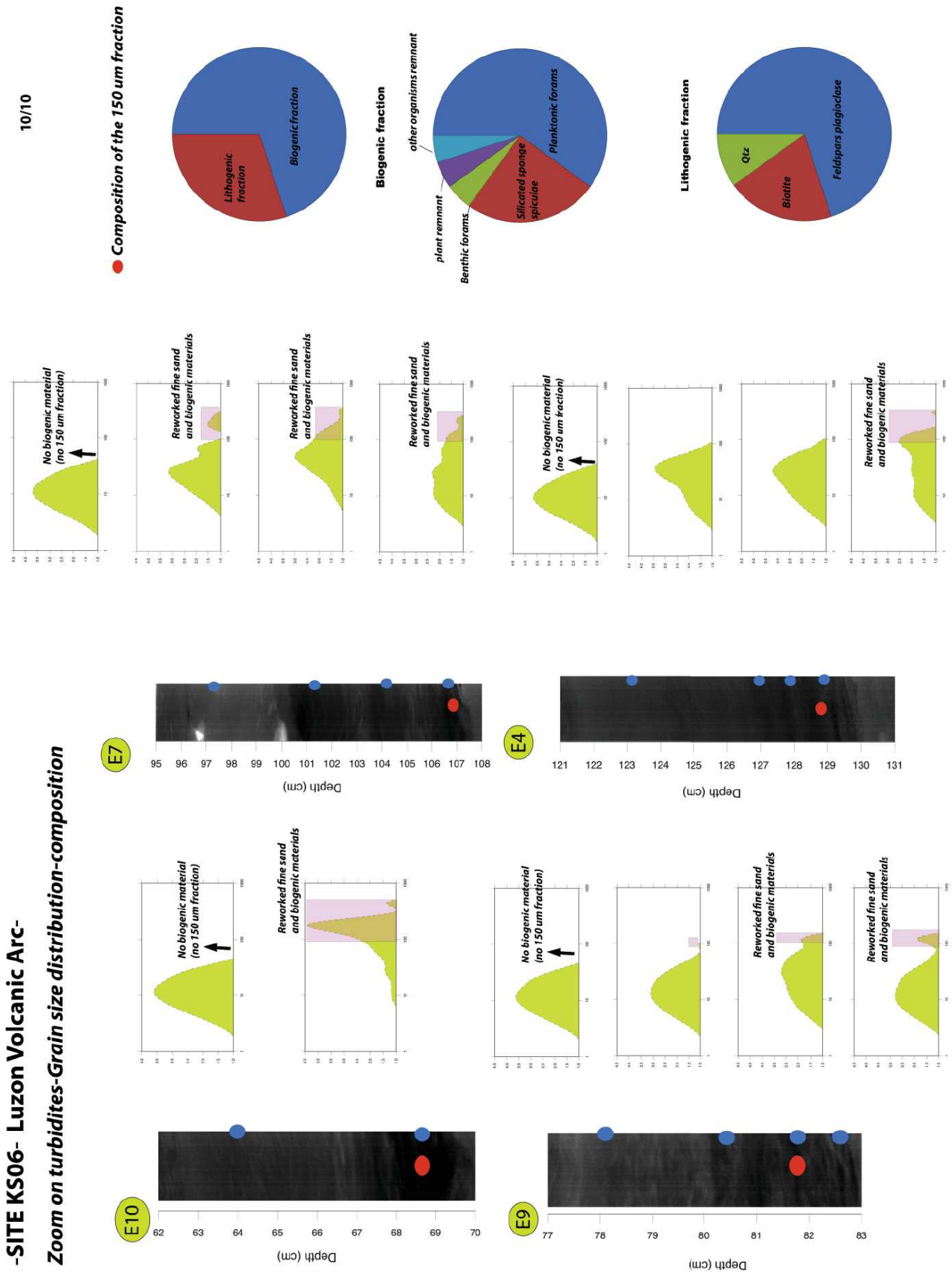


Figure C.7: Detailed analysis of turbidites layers-III

Figure C.9: Detailed analysis of turbidites layers-V



Coring sites KAS03/KR03: Morphology and core analysis

-SITE KR03-KAS03-Luzon Volcanic Arc-

2/8

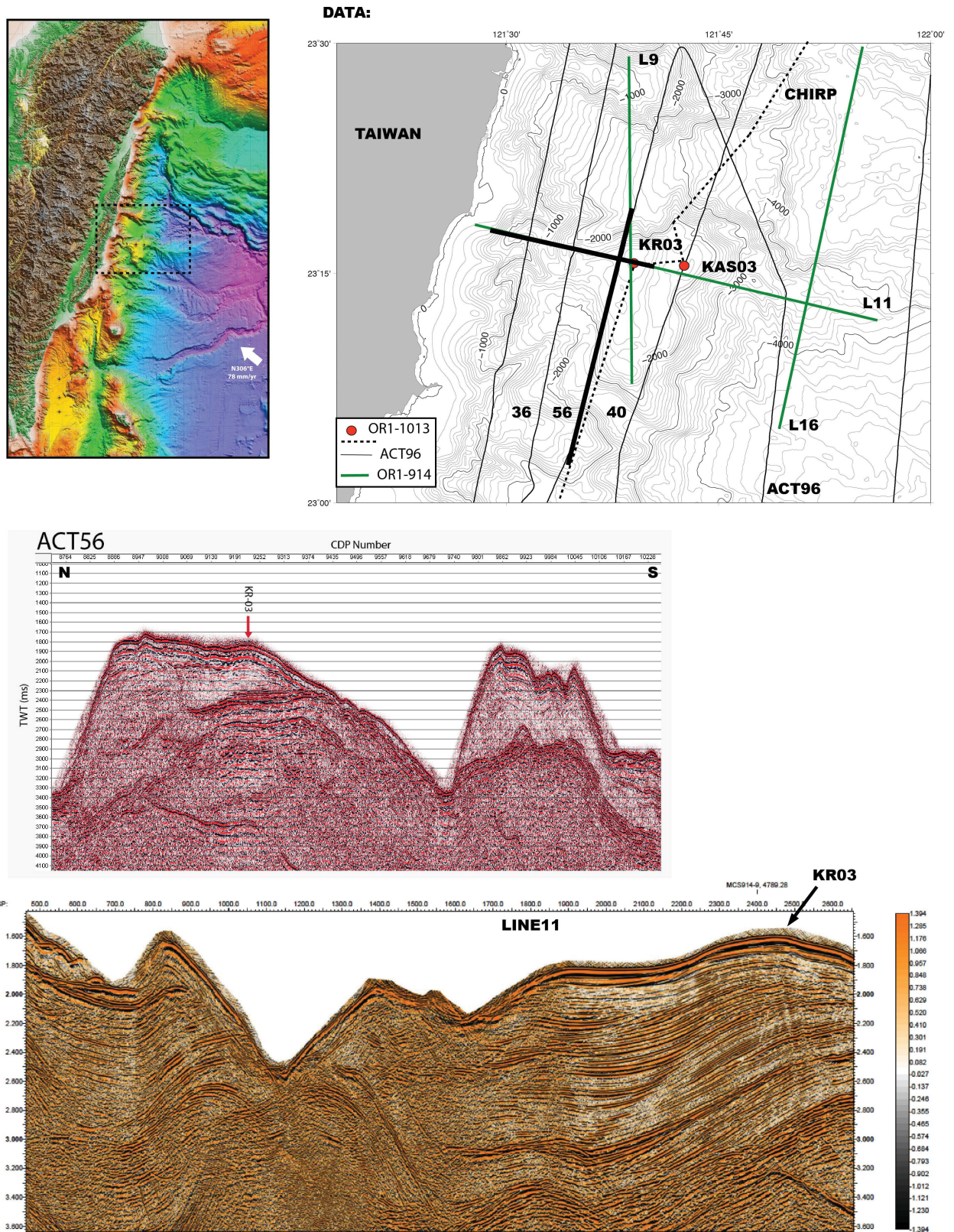


Figure D.1: Seismic profiles across KR03 site

-SITE KR03-KAS03-Luzon Volcanic Arc-

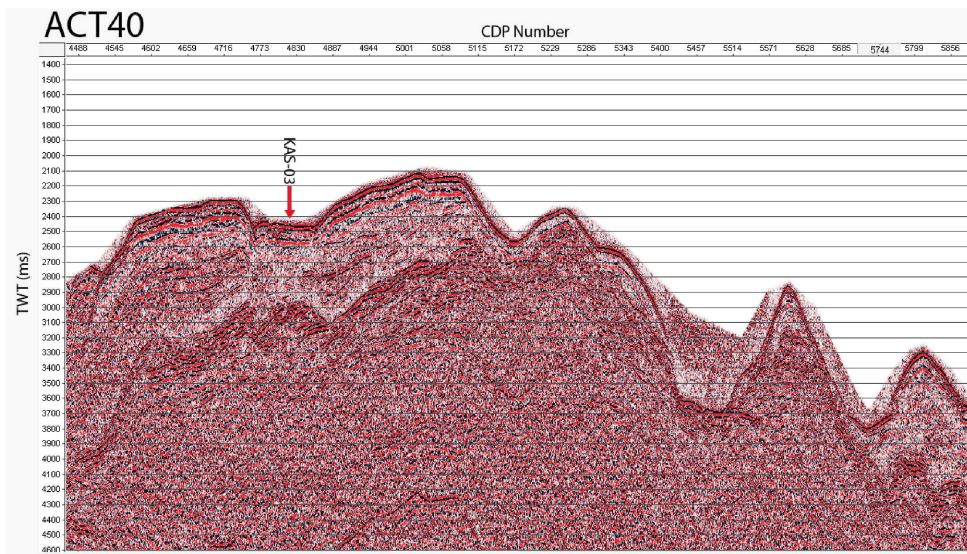
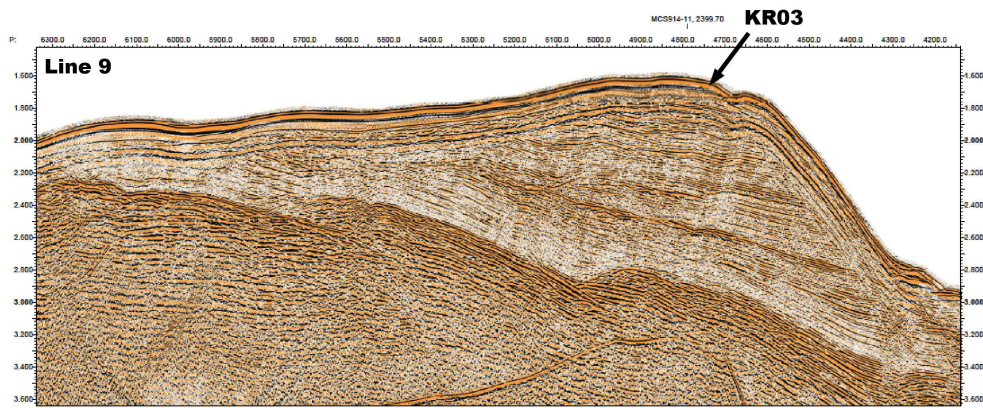
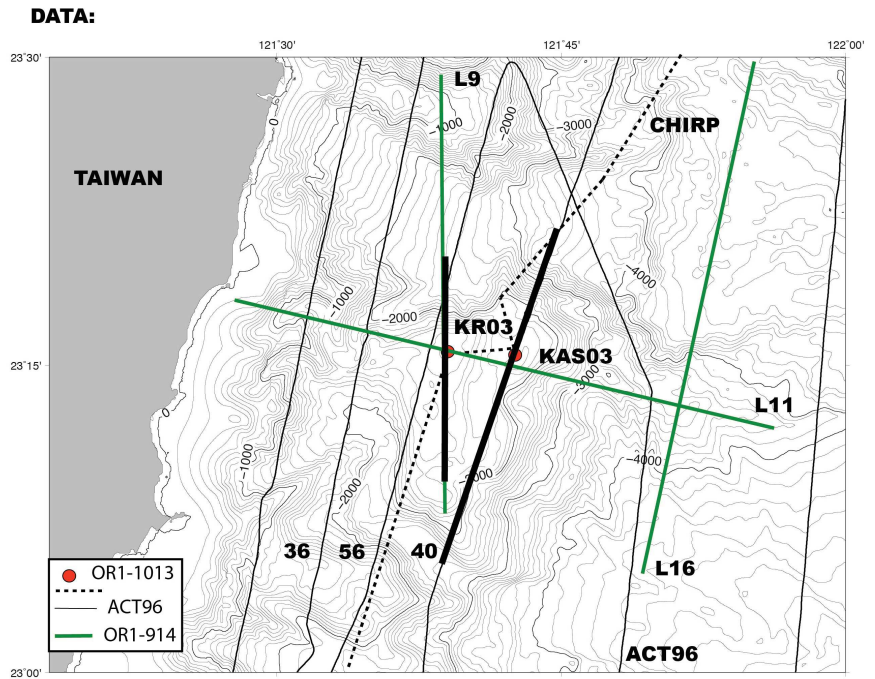
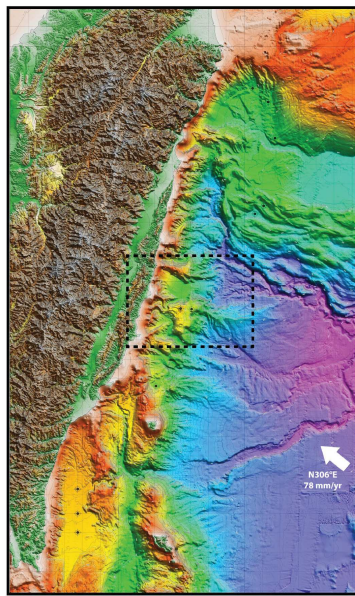
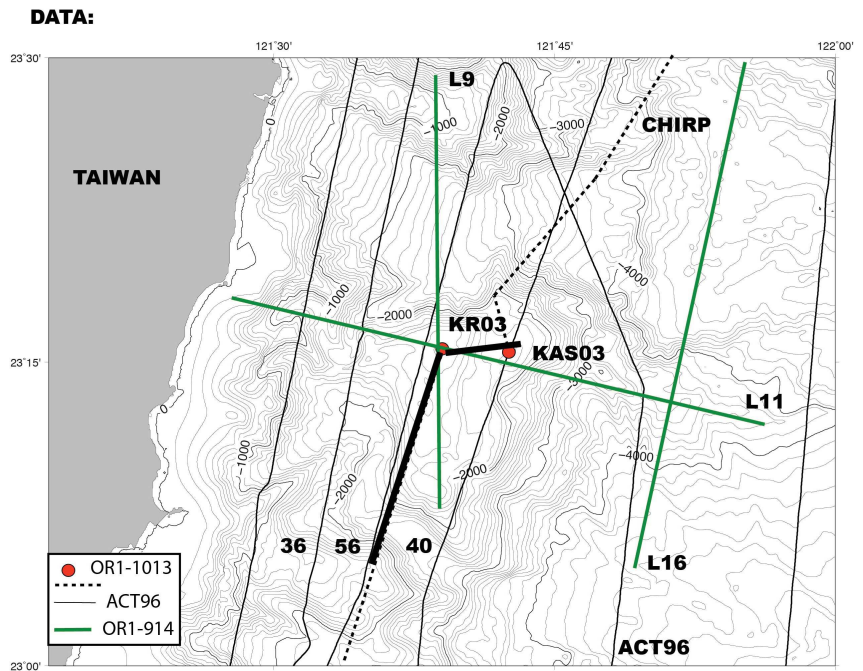
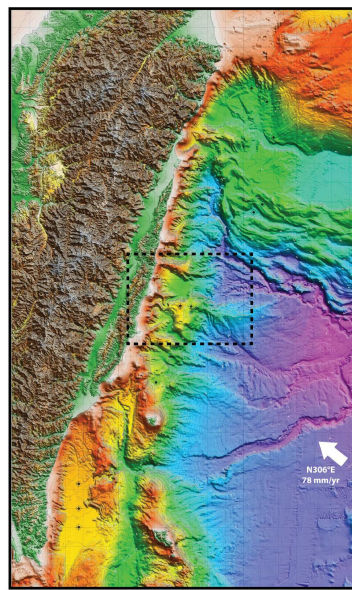


Figure D.2: Seismic profiles across KR03 site

-SITE KR03-KAS03-Luzon Volcanic Arc-

4/8



CHIRP:

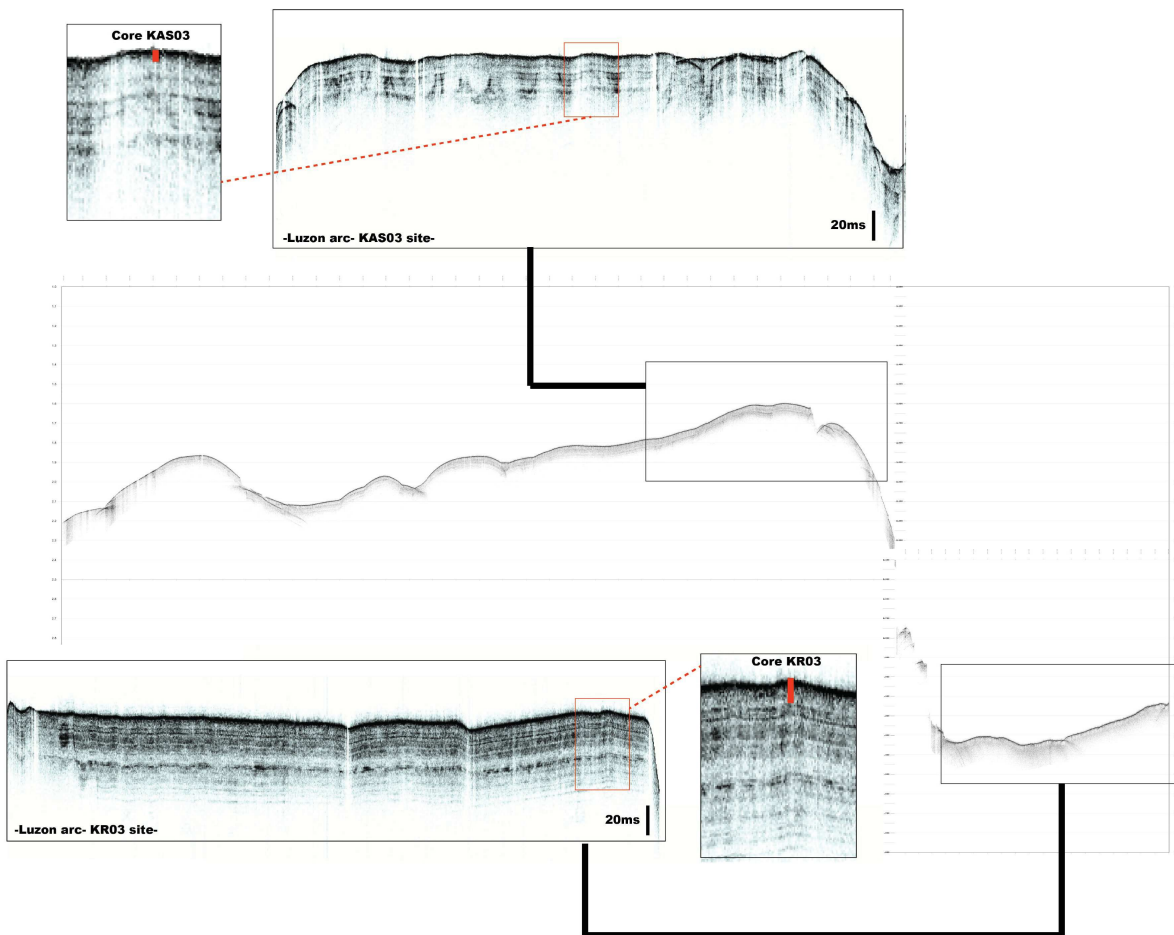
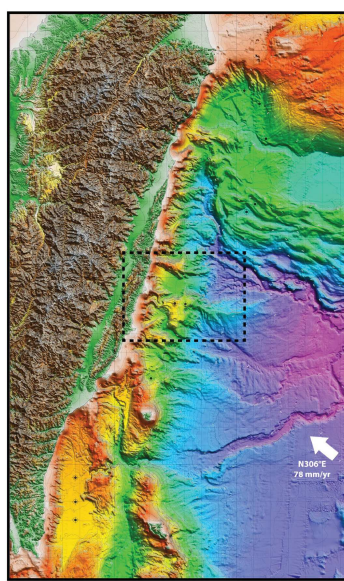


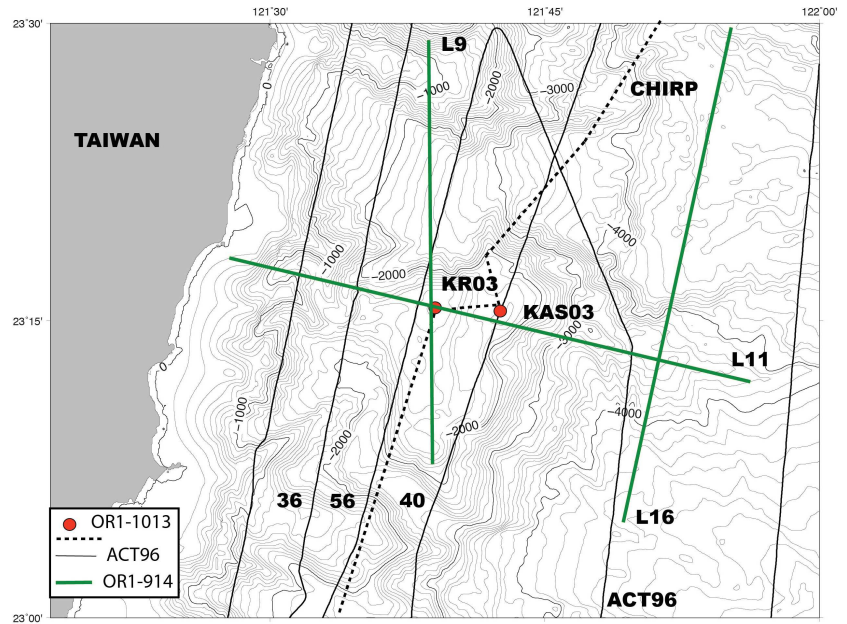
Figure D.3: Chirp profiles across KR03 and KAS03 sites

-SITE KR03-KAS03-Luzon Volcanic Arc-

5/8



DATA:



KAS03-Grain Size and High Resolution Magnetic Susceptibility

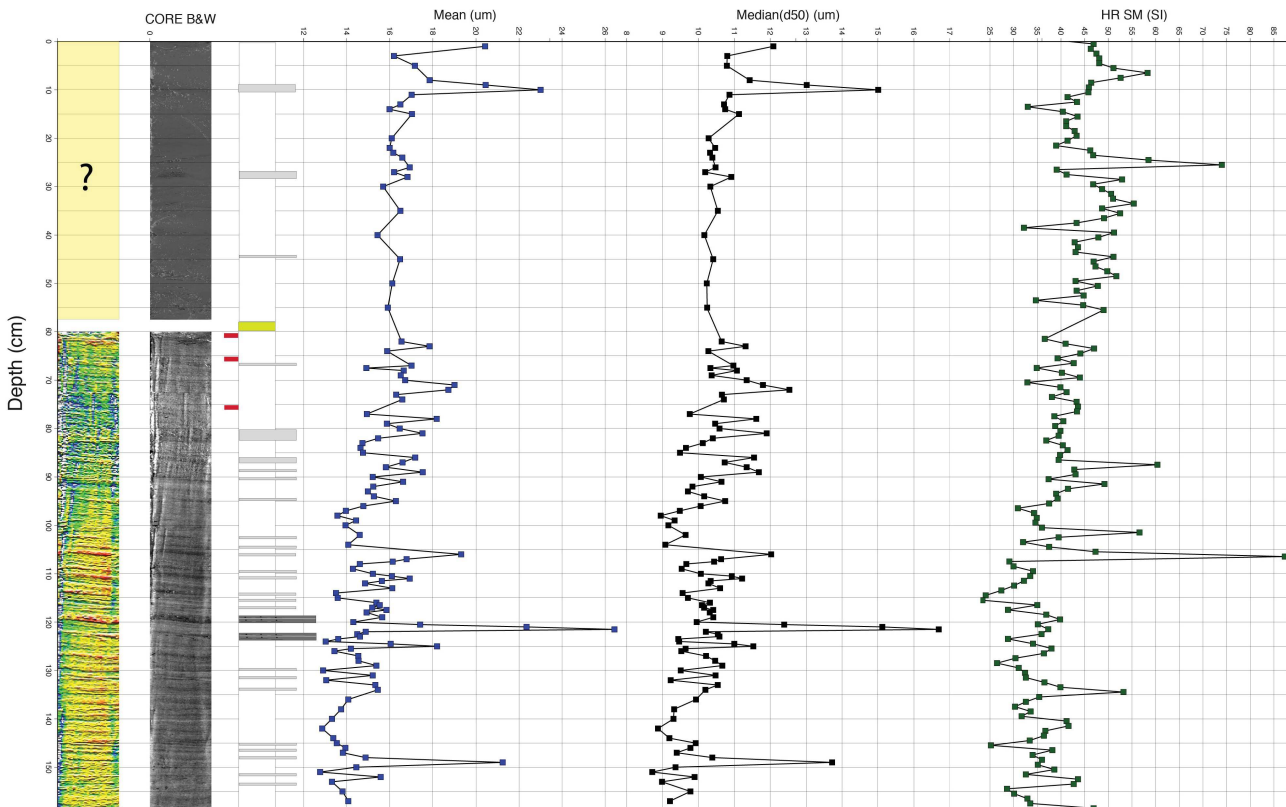


Figure D.4: Grain size analysis of core KAS03

KR03P-Grain Size and High Resolution Magnetic Susceptibility

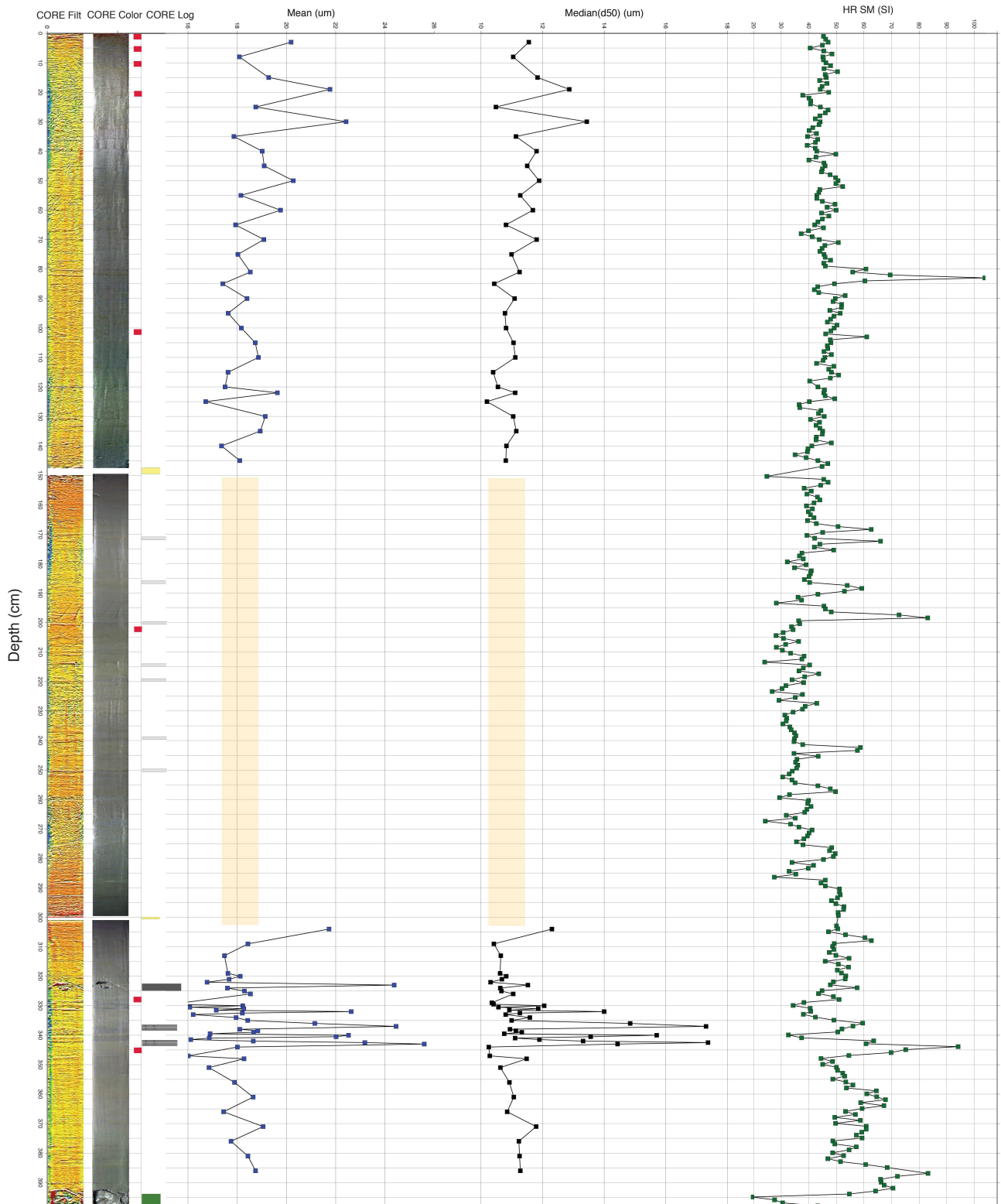


Figure D.5: Grain size analysis of core KR03

KAS03P-XRF DATA

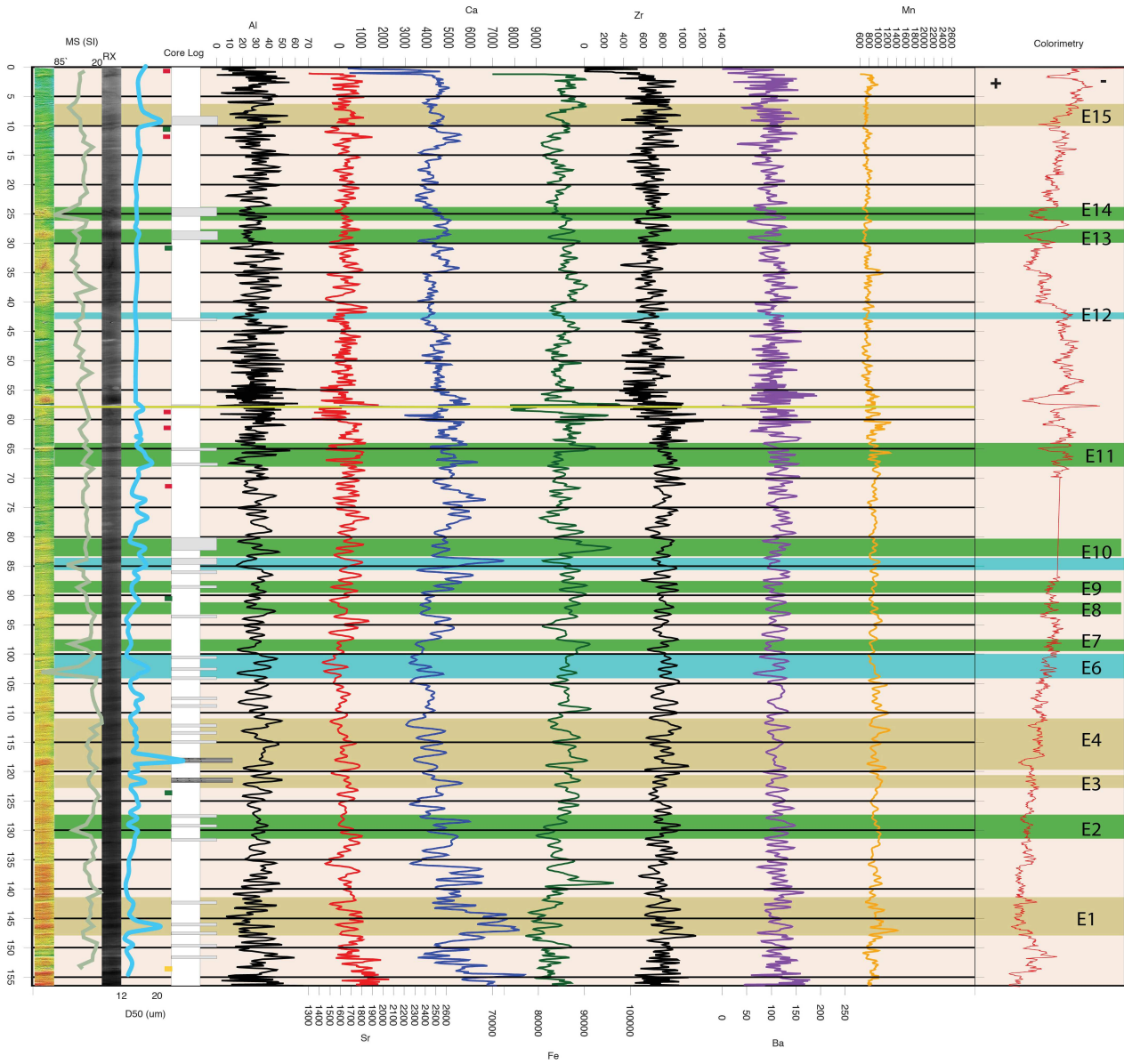
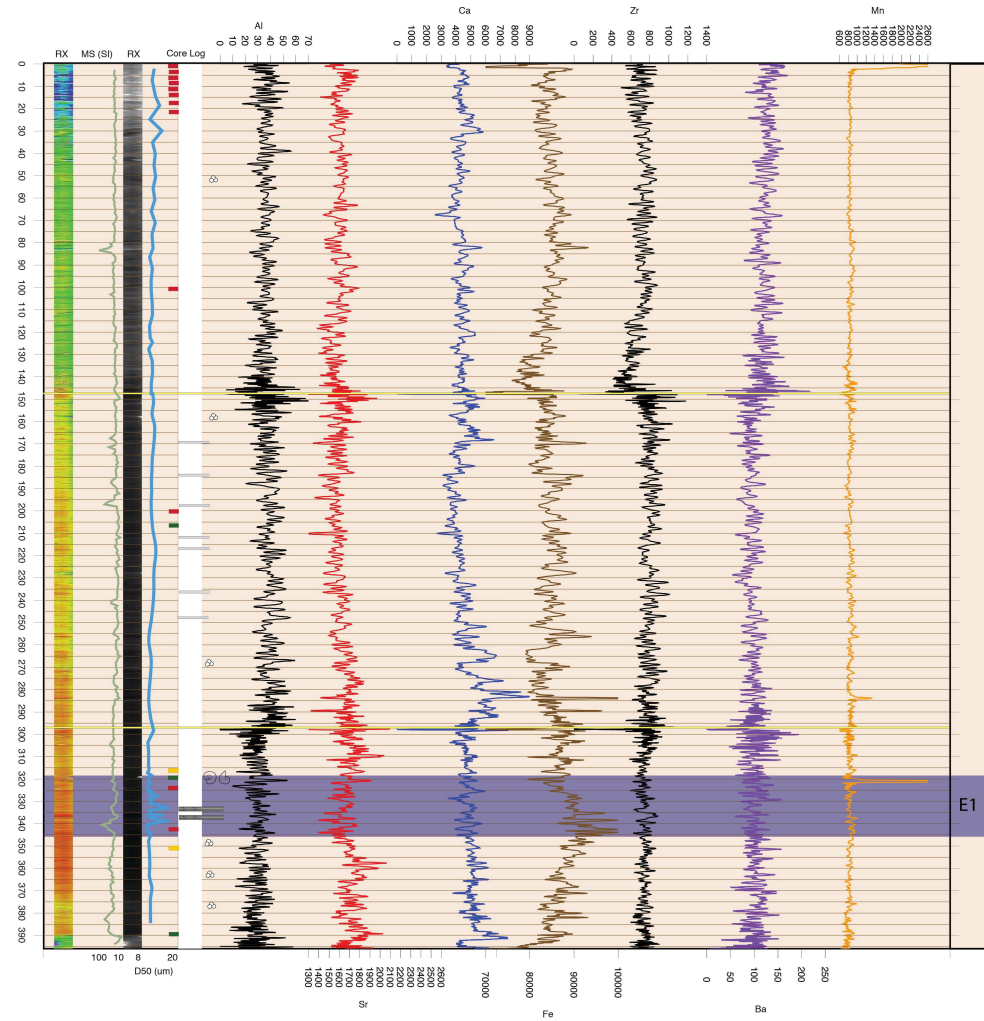


Figure D.6: XRF analysis of core KAS03

KR03P-XRF DATA



INDEX:

- Incertitude on the top of the sequence
- High energy event identified as Turbidite sequence
- Identified as Hemipelagite
- Event non identified as Turbidite sequence
- Other kind of event: tsunamite ??
- 14C samples sent for the 2nd batch
- 14C samples sent for the 1st batch
- 210Pb samples
- E11** Event number

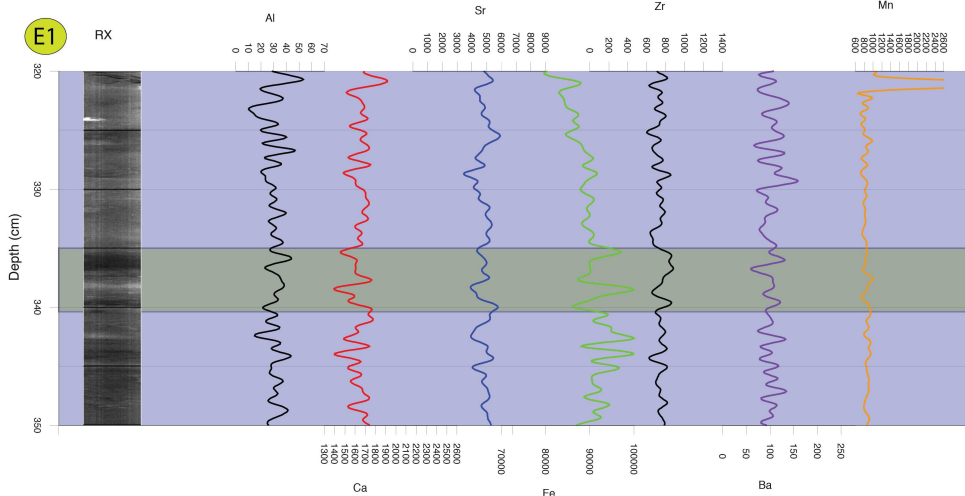
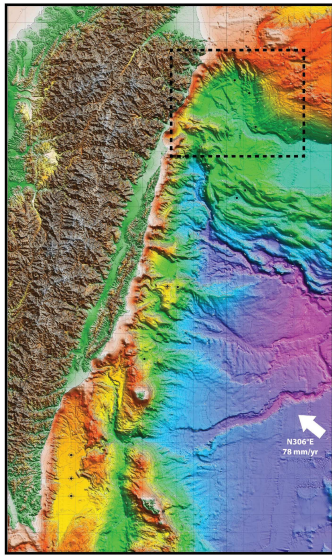


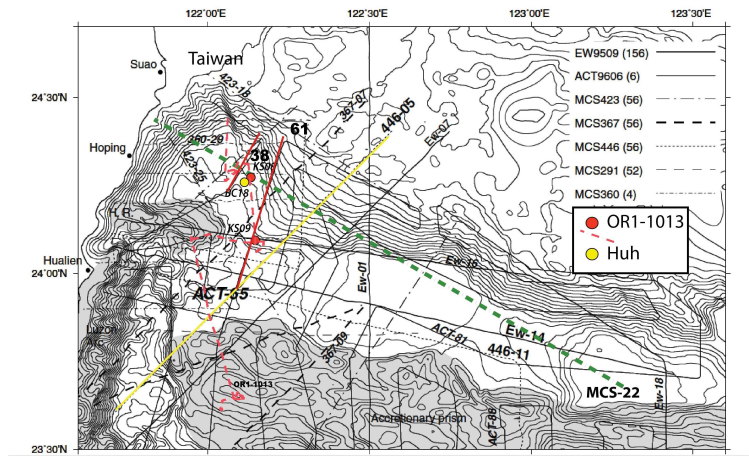
Figure D.7: XRF analysis of core KR03

Coring sites KS08/KS09: Morphology and core analysis

-SITE KS09&KS08- Ryukyu forearc-



Data:



MCS Lines:

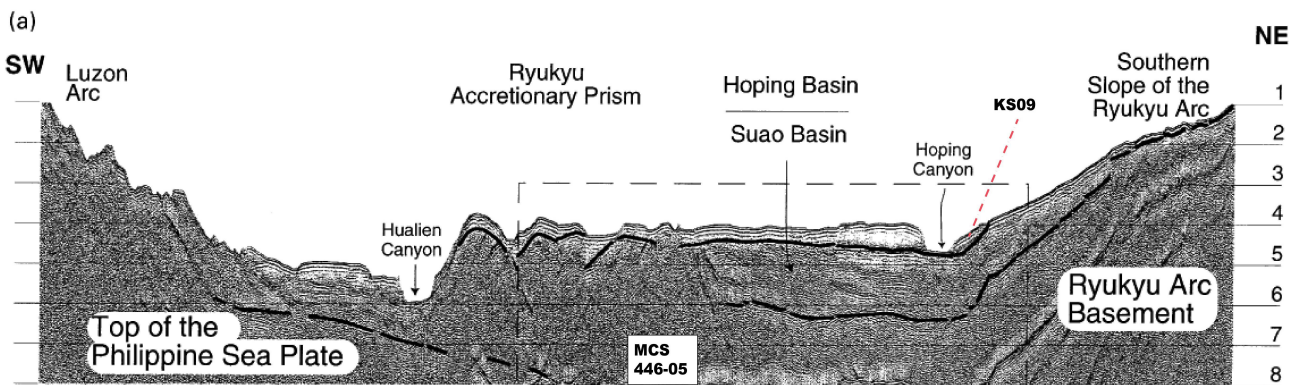
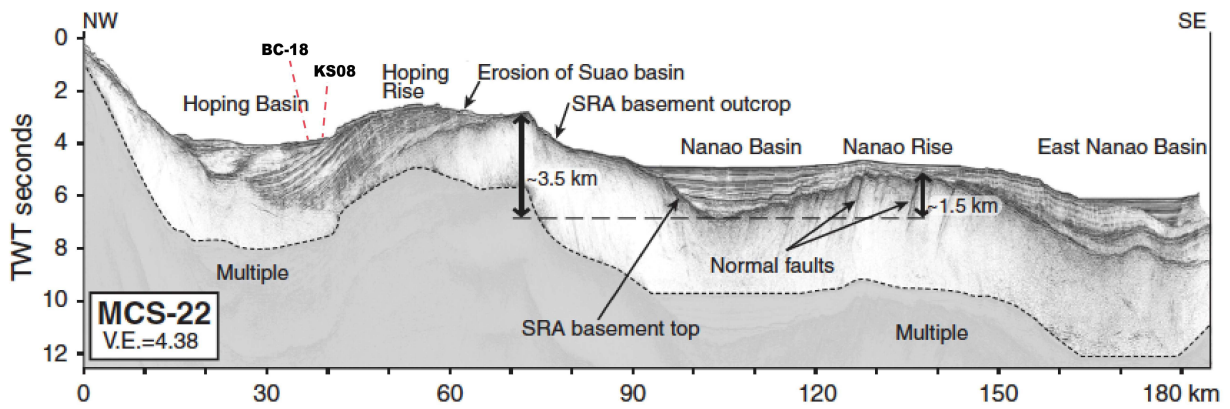
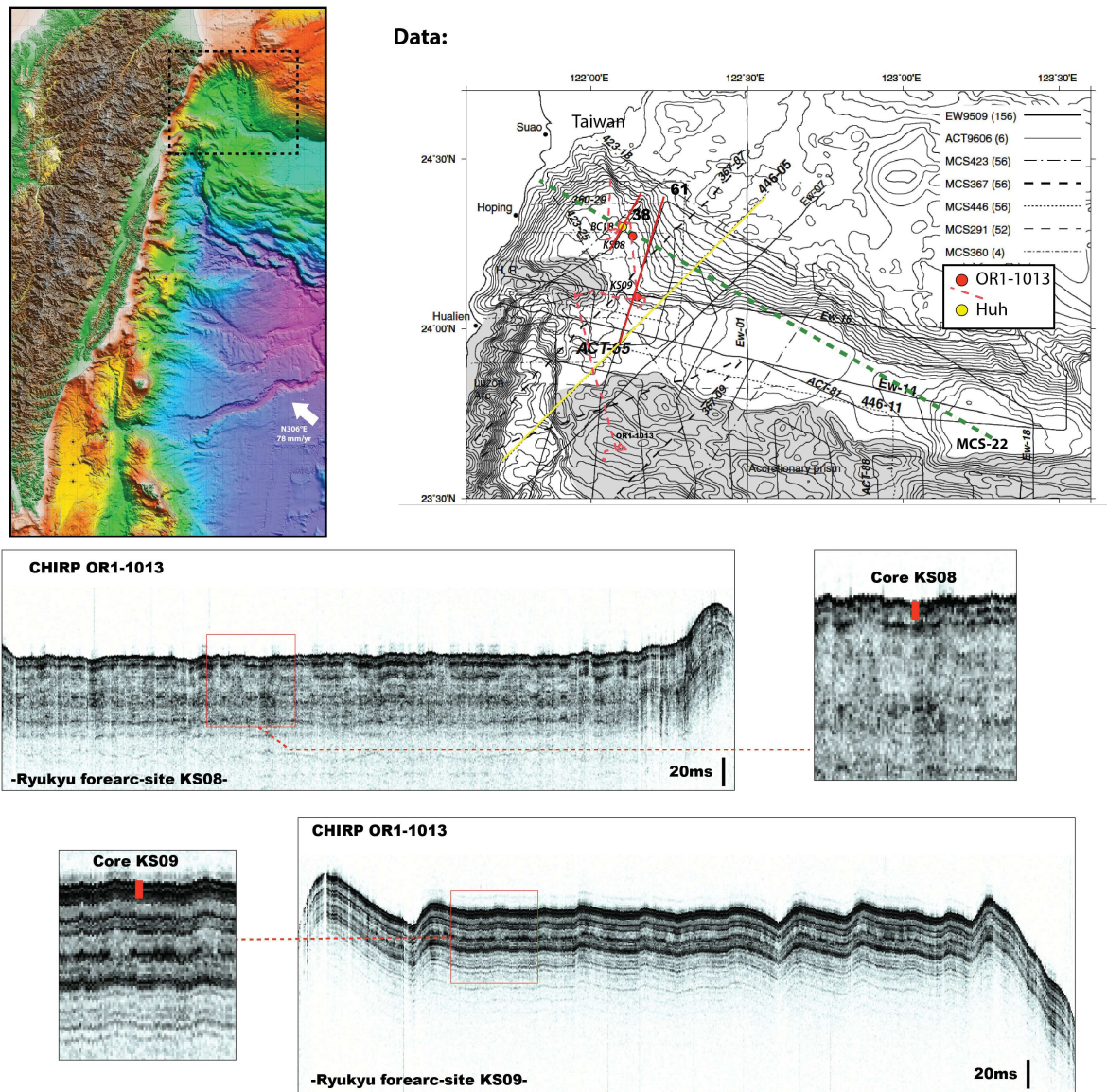


Figure E.1: Seismic profile across KS09 and KS08

-SITE KS09&KS08- Ryukyu forearc-



Source of instabilities

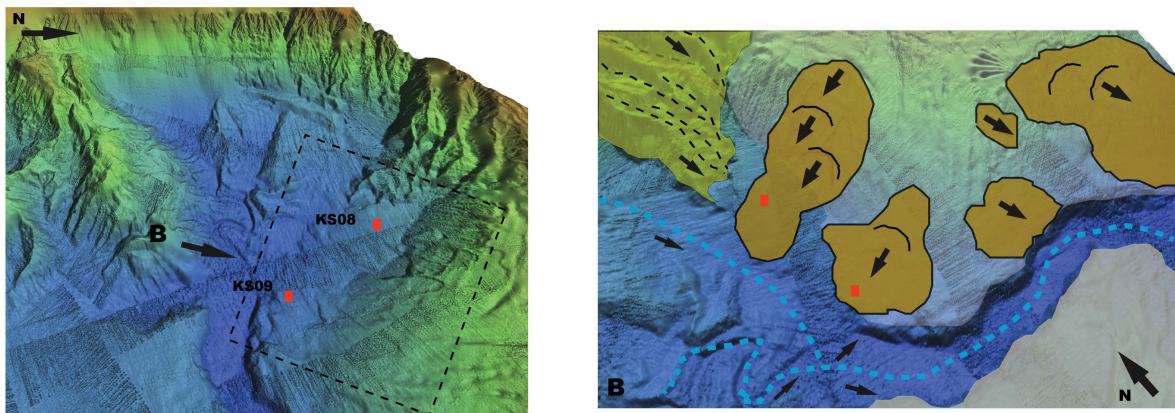
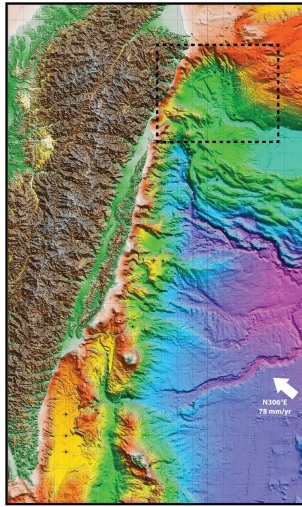


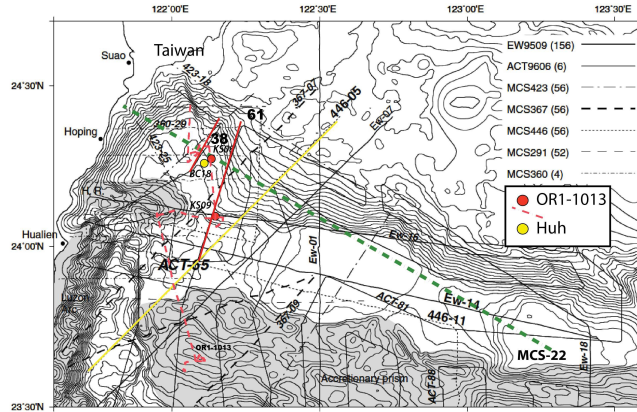
Figure E.2: Chirp profiles across KS08 and KS09, and slope instabilities around core sites

-SITE KS09&KS08- Ryukyu forearc-

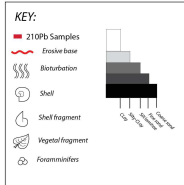
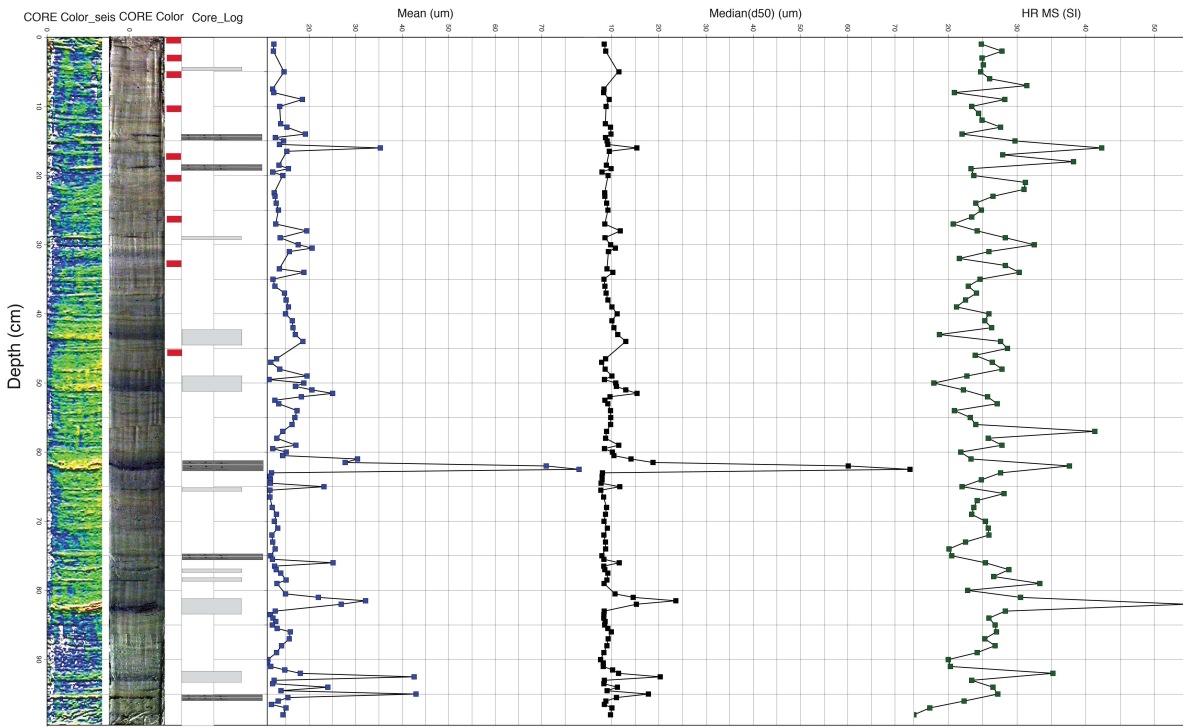
4/10



Data:



KS09P-Grain Size and High Resolution Magnetic Susceptibility

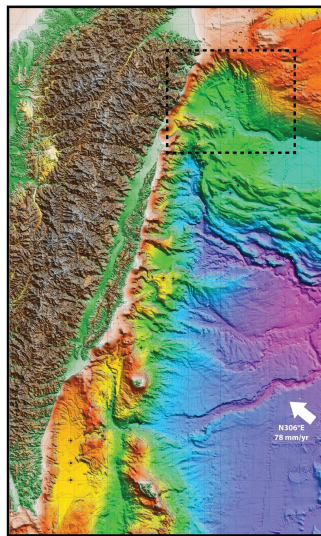


On the whole section:
 -Homogeneous clay with some oxydation (laminae)
 -Five silty laminae (turbidites?) with sometimes some bioturbation

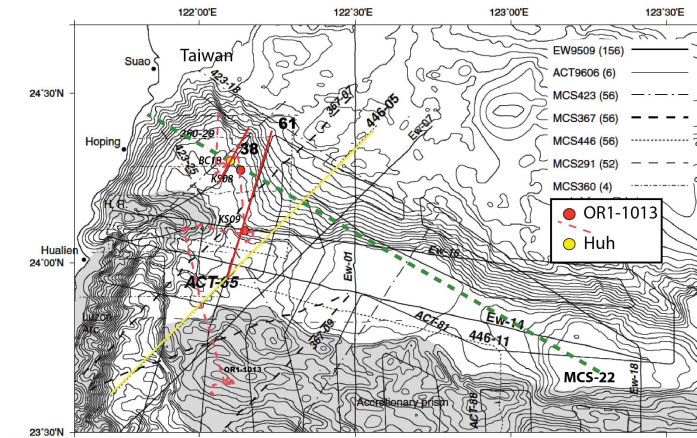
Figure E.3: Grain size analysis of core KS09

-SITE KS09&KS08- Ryukyu forearc-

5/10



Data:



KS08P-Grain Size and High Resolution Magnetic Susceptibility

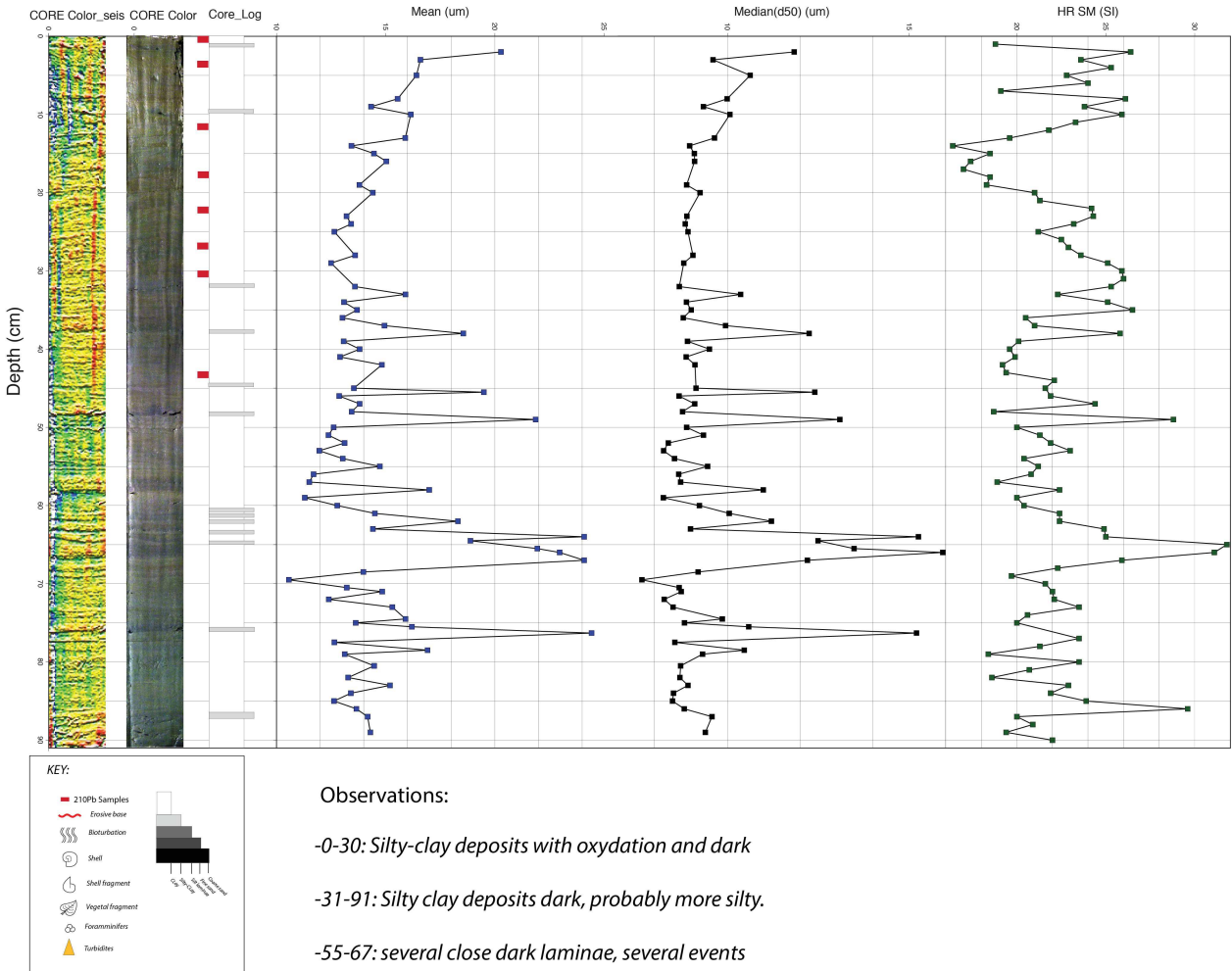
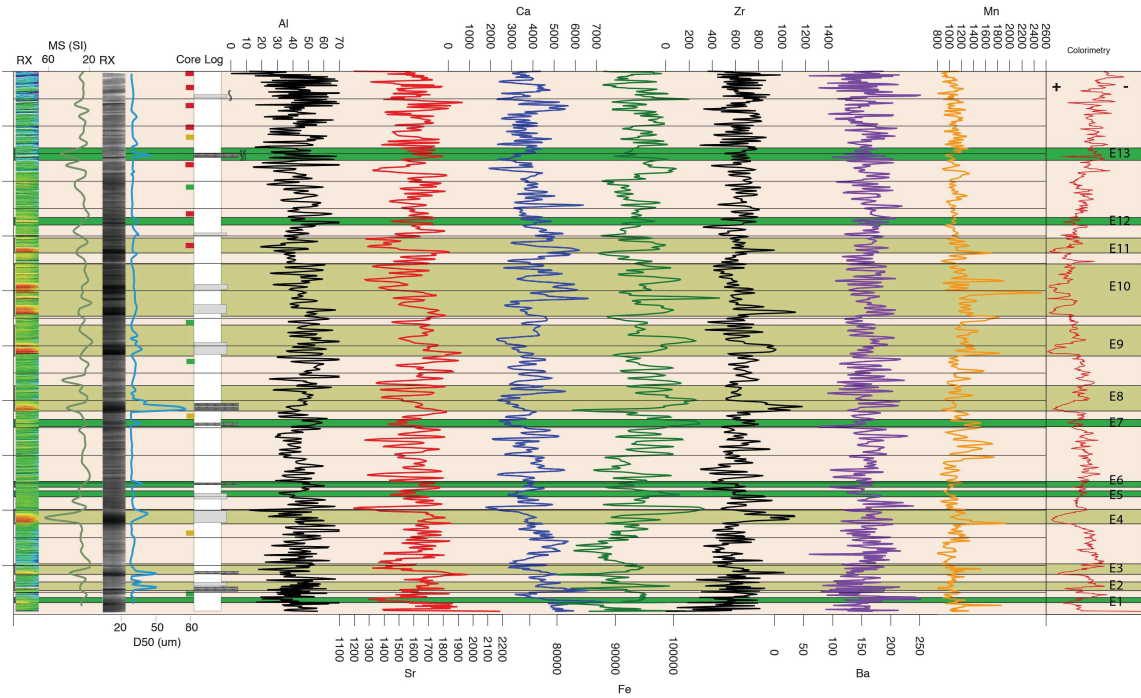


Figure E.4: Grain size analysis of core KS08

-SITE KS09-Ryukyu forearc-

c.3-XRF data- Turbidites characterization



-SITE KS08-Ryukyu forearc-

c.3-XRF data- Turbidites characterization

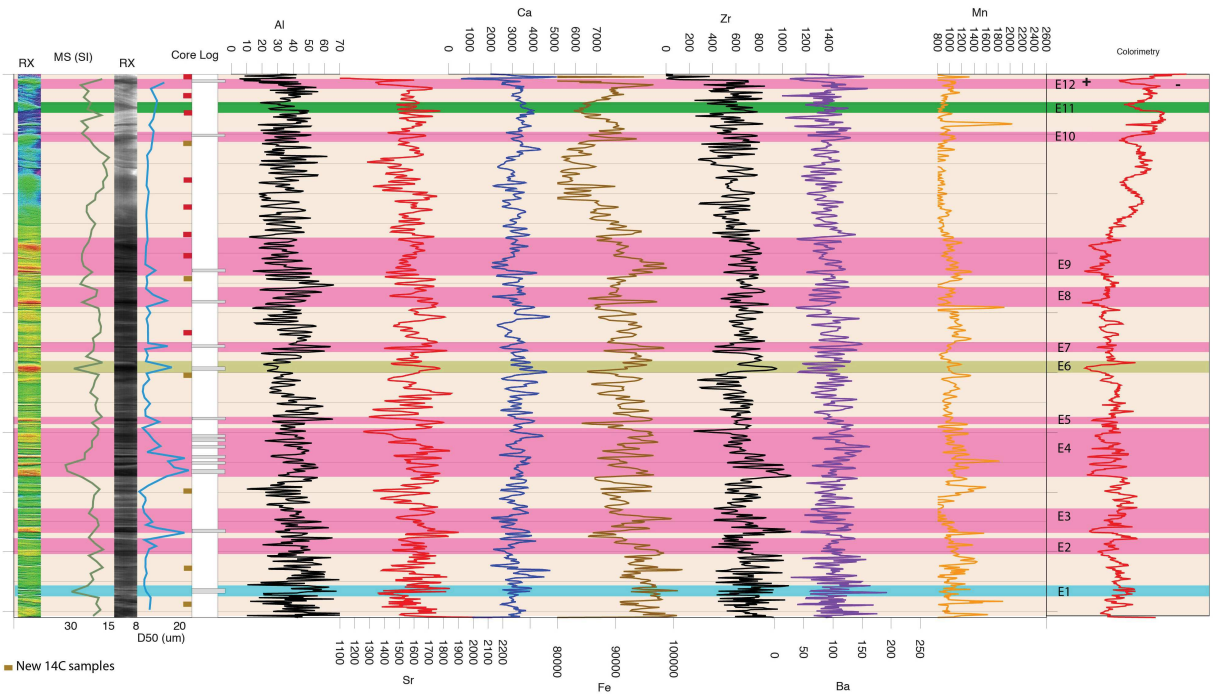


Figure E.5: XRF analysis of core KS09 and KS08

-SITE KS09- Ryukyu forearc-

INDEX:

- Incertitude on the top of the sequence*
- High energy event identified as Turbidite sequence*
- Identified as Hemipelagite*
- Event non identified as Turbidite sequence*
- 14C samples sent for the 2nd batch*
- 14C samples sent for the 1st batch*
- 210Pb samples*
- E11** *Event number*

Criteria of distinction between events:

Event	Colorimetry	Granulometry	Mag. Sus.	XRF	Type of event
	High	Graded	Sequence	Sr, Ca, Zr peaks	Turbidites
	High	No graded	No sequence	Sr, Ca, Fe peaks	Other
	Low	No graded	No sequence	Sr, Ca, Fe peaks	Other

Characterisation of turbidites:

Turbidites	Total thickness (cm)	Coarse unit (cm)	Tail (cm)	Sequence	Pulse	Base
E2	2	1	1	Fining upward	1	Sharp, erosive
E3	2	1	1	Fining upward	1	Sharp, erosive
E4	3	2	1	Fining upward	1	Sharp, erosive
E8	5	1	4	Truncated Bouma	2	Sharp, erosive
E9	6	2	3	Fining upward	1	Sharp, erosive
E10	10	5	5	Fining upward	1	Sharp, erosive
E11	3	1	2	Fining upward	1	Sharp, erosive

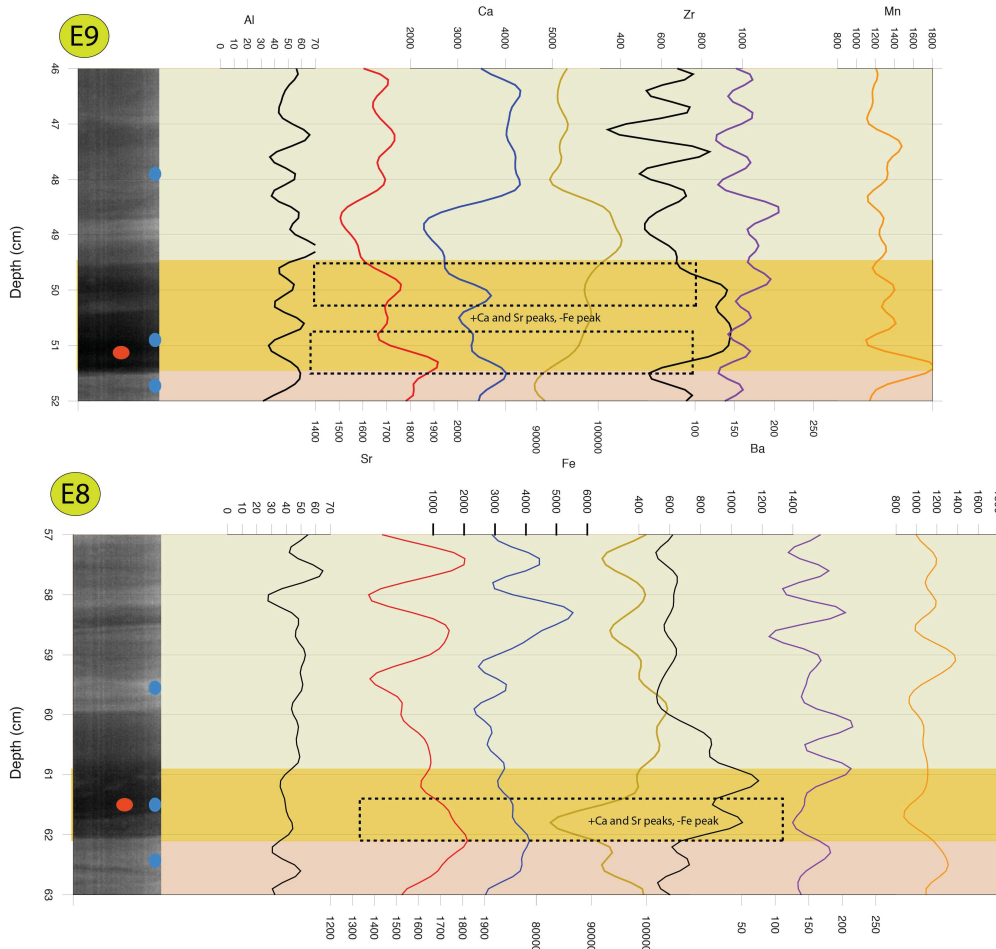


Figure E.6: Detailed analysis of turbidites layers-I

-SITE KS08- Ryukyu forearc-

8/9

INDEX:

- Incertitude on the top of the sequence
- High energy event identified as Turbidite sequence
- Identified as Hemipelagite
- Event non identified as Turbidite sequence
- 14C samples sent for the 2nd batch
- 14C samples sent for the 1st batch
- 210Pb samples
- E11 Event number

Criteria of distinction between events:

Event	Colorimetry	Granulometry	Mag. Sus.	XRF	Type of event
	High	Graded	Sequence	Fe, Zr peaks	Turbidites
	High	No graded	No sequence	Sr, Ca, Fe peaks	Other
	Low	No graded	No sequence	Sr, Ca, Fe peaks	Other

Characterisation of turbidites:

Turbidites	Total thickness (cm)	Coarse unit (cm)	Tail (cm)	Sequence	Pulse	Base
E2	4	1	3	Fining upward	1	Sharp, erosive
E3	5	2	3	Fining upward	1	Sharp, erosive
E4	8	4	4	Truncated Bouma	2	Sharp, erosive
E5	1	0.5	0.5	Fining upward	1	Sharp, erosive
E6	2	1	1	Fining upward	1	Sharp, erosive
E7	2	1	1	Fining upward	1	Sharp, erosive
E8	3	1	2	Fining upward	1	Sharp, erosive
E9	7	2	5	Fining upward	1	Sharp, erosive
E10	2	1	1	Fining upward	1	Sharp, erosive
E12	2	1	1	Fining upward	1	Sharp, erosive

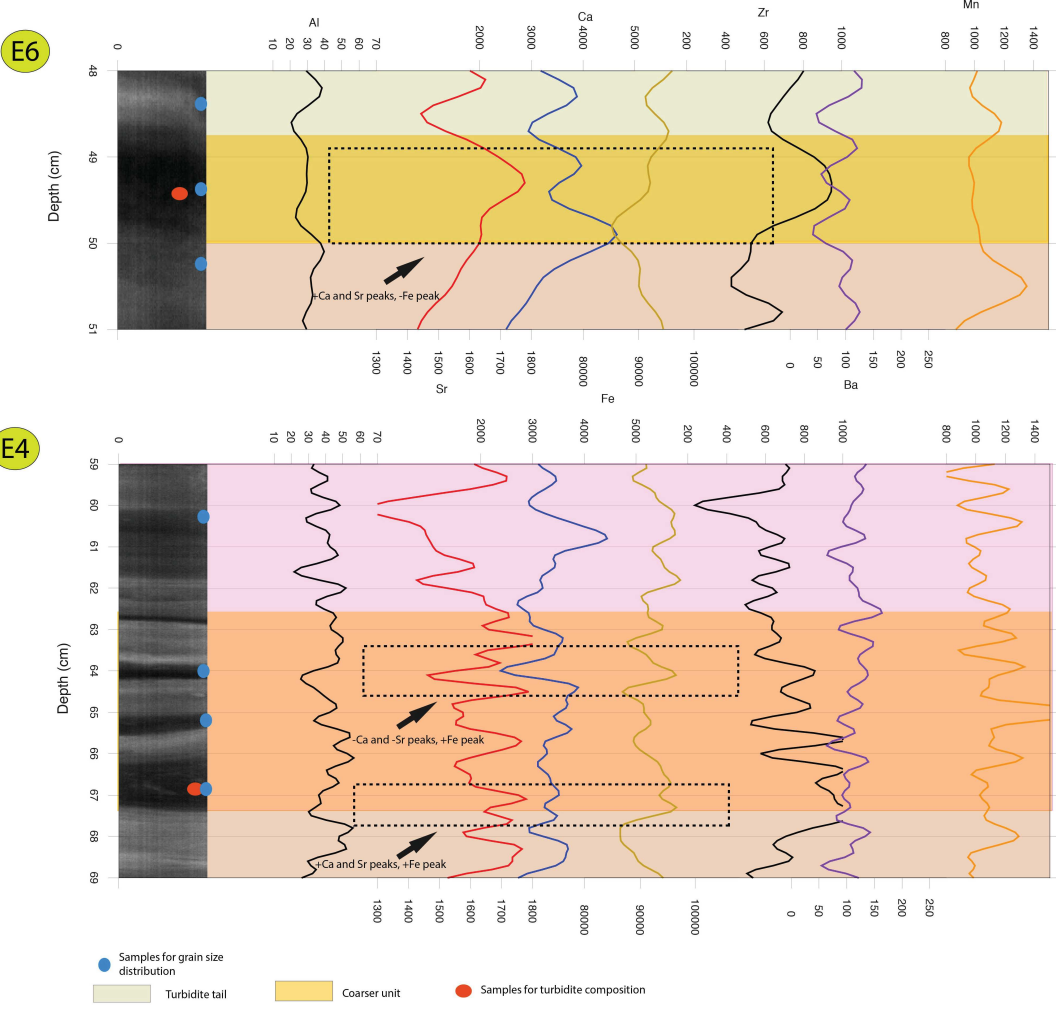


Figure E.7: Detailed analysis of turbidites layers-II

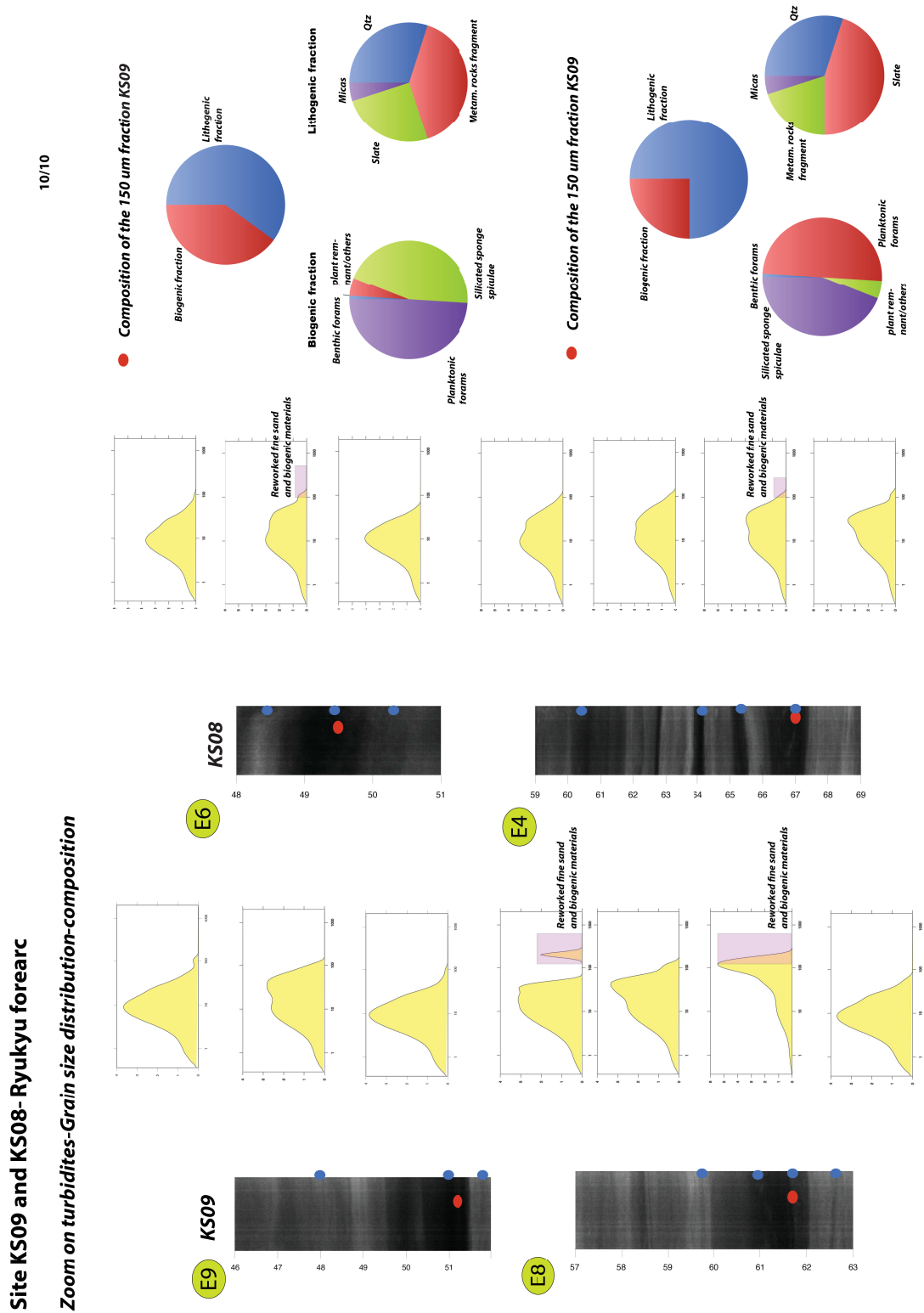


Figure E.8: Detailed analysis of turbidites layers-III

^{14}C and ^{210}Pb sampling

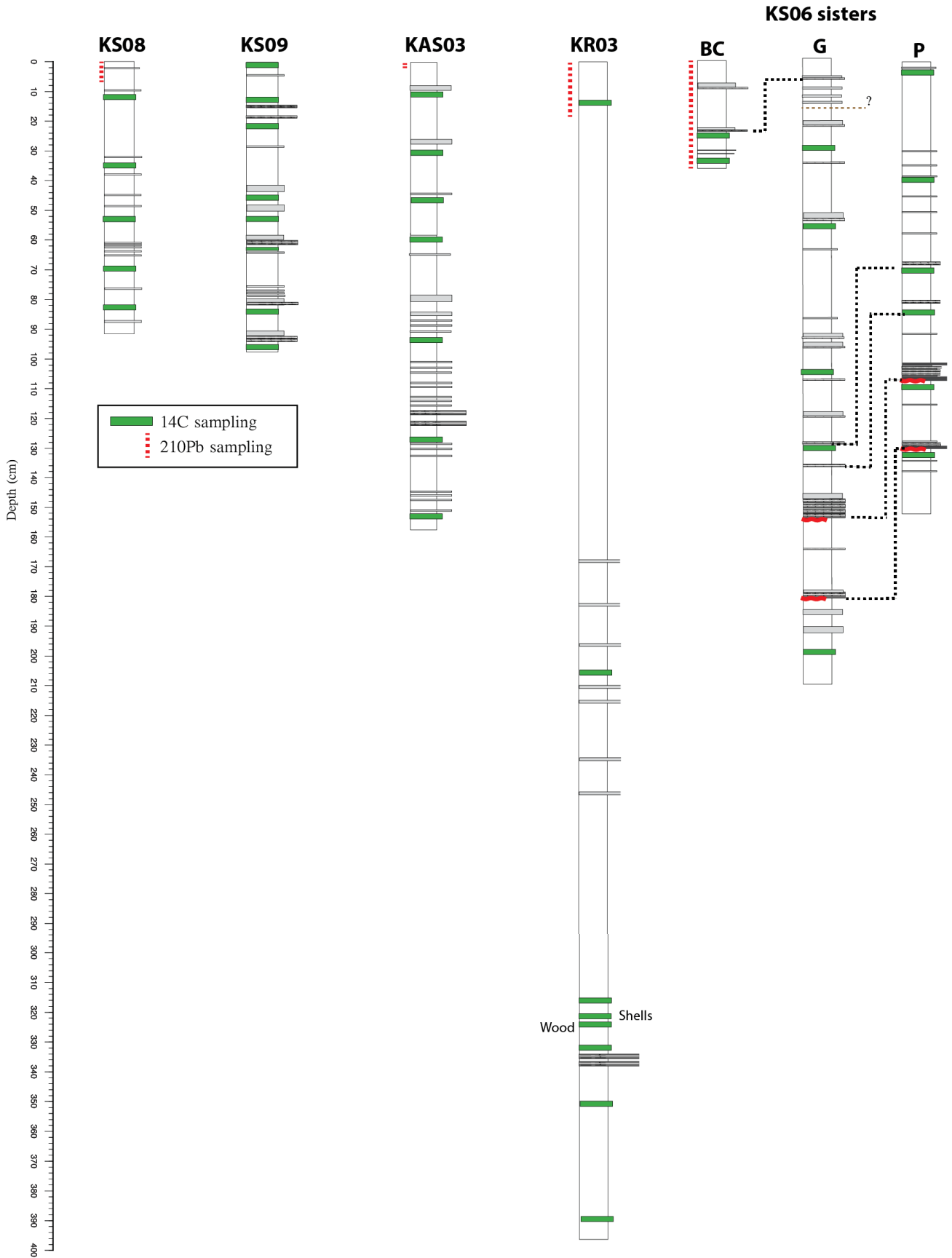


Figure F.1: ^{14}C and ^{210}Pb sampling

The P-Sequence in OxCal

```

Run: /KS06_B_G.oxcal

Plot()
{
  Curve("Marine13", "Marine13.14c");
  Delta_R("LocalMarine", 100, 40); ----- Reservoir correction
  P_Sequence(" ", 1, 1) ----- (Name, K parameter,
                                Interpolation value)

  {Boundary("Bottom") {z=156; ----- Model bottom depth
  };
  R_Date("A1", 1800, 30) {z=144;
  };
  Date("D") {z=130;
  };
  Date("D") {z=110;
  };
  Date("D") {z=102;
  };
  R_Date("E1", 1365, 30) {z=99;
  };
  Date("D") {z=98;
  };
  Date("D") {z=85;
  };
  R_Date("E1", 1045, 30) {z=82; ----- R_date (name, raw 14C, error)
  };
  Date("D") {z=77;
  };
  Date("D") {z=75;
  };
  Date("D") {z=68;
  };
  R_Date("E1", 585, 30) {z=41;
  };
  Date("D") { z=40;
  };
  Date("D") {z=26; ----- Date("D") = layer's age to be modelled at the z depth
  };
  R_Date("E1", 575, 30) {z=21; ----- z= corrected hemipelagite depth
  };
  Date("D") {z=18;
  };
  Date("D") {z=5;
  };
  Boundary("Core-top", AD(1996)) {z=0; ----- Model top depth
  };
  };
  }; ----- AD (date) = calibrated date input
};

```

Figure G.1: Example of P-Sequence code in OxCal for KS06G core

